

ROLE OF THE CATION IN HYBRID ORGANIC-INORGANIC PEROSKITE SOLAR MATERIALS

by

Christopher E Manspeaker, B.S., M.S., M.B.A.

A dissertation submitted to the Graduate Council  
of Texas State University in partial fulfillment  
of the requirements for the degree of  
Doctor of Philosophy  
with a Major in Material Science, Engineering and Commercialization  
August 2018

Committee Members:

Alex Zakhidov, Chair

Jennifer Irvin

Clois (Bert) Powell

Craig Swartz

Miguel Friedrich

**COPYRIGHT**

By

Christopher Manspeaker

2018

## **FAIR USE AND AUTHOR'S PERMISSION STATEMENT**

### **Fair Use**

This work is protected by the Copyright Laws of the United States (Public Law 94-553, section 107). Consistent with fair use as defined in the Copyright Laws, brief quotations from this material are allowed with proper acknowledgement. Use of this material for financial gain without the author's express written permission is not allowed.

### **Duplication Permission**

As the copyright holder of this work I, Christopher E Manspeaker, authorize duplication of this work, in whole or in part, for educational or scholarly purposes only.

## **DEDICATION**

The work presented here is in large part an effort to make a better tomorrow for our children and for that reason, I wish to dedicate this work to my children: Noah, Alexavier and Abigayle Manspeaker.

## ACKNOWLEDGEMENTS

I would like with my deepest thanks to Dr. Alex Zakhidov for accepting the role of advisor, without his efforts, my efforts would not have been so fruitful. It is very hard accepting a doctoral student into your group when they have outside focuses such as an existing career, but Dr. Zakhidov took that challenge and I was rewarded.

I am very grateful of the opportunities working in his lab has given me. Researching solar cells and power was a dream I was able to accomplish by working on this topic in his lab.

I wish to thank Dr. Jennifer Irvin for reviving my interest in chemistry and for being someone who you want to be better for. Some people inspire your best, and she inspired the best in me.

I wish to thank Dr. Powell for the effort in getting outside lectures and seminars in coming to Texas State. There was so much good learnings and perspectives that took place on a Friday afternoon.

I wish to thank Miguel Friedrich for the many insights from a business perspective. Being able to replace his position on a NSF Innovation Corp (I-Corp) project has given me more knowledge in commercialization efforts that any future endeavors

will be much easier to accomplish. I do appreciate your efforts in supporting someone so far away.

Lastly for my committee, I hardy thank you to Dr. Craig Swartz. It is always difficult in finding good committee members with the correct background to help your knowledge growth, especially considering the circumstances. I will always appreciate your desire to step up and assist an unknown person in their time of need. Many thanks are owed.

There are a so many supporting staff members at Texas State, especially in the ARSC that without their support I would not be here today. These members include Dr. Dmitry Lyashenko, Dr. Casey Smith, Nate England and Alissa Savage.

There are many people in the MSEC program who I have learned aside and either through helping them or they me I have learned much more, Raju Ahmed, Sadia Rab, Joyce Anderson, Jonathan Anderson, Rony Saha, Anwar Siddique, Beth LeBlanc and Fei Sun.

The commercialization effort with Dr. Gary Beall and my fellow MSEC students, Archana Gujjari with TX<sub>2</sub>O and Mariana Ocampo with ecoBOLT.

I also like to thank my fellow lab mates, Mehedhi Hasan, Joseph Sadler, Eric Welch, Johnathan Preiss, Patrick Scruggs, Garrett Merrion, Aureliano Perez and Kevin Lyon.

Also, special thanks is owed to Karla Pizana who's efforts make the MSEC program work and run!

Lastly, I would like to thank my wonderful family. This has been a difficult journey for all of us. The long commute, the long hours, always something to do it seems.

## TABLE OF CONTENTS

	PAGE
ACKNOWLEDGEMENTS.....	v
LIST OF TABLES.....	xii
LIST OF FIGURES.....	xiii
LIST OF ABBREVIATIONS .....	xxi
ABSTRACT.....	xxvi
CHAPTER	
1 INTRODUCTION .....	1
1.1 Perovskites Background.....	3
1.2 Perovskite Structure .....	5
1.3 Overview of the Perovskite Solar Cell.....	7
1.3.1 Junctions .....	7
1.3.2 Model of the Solar Cell.....	10
1.3.3 Figures of Merit.....	12
1.3.4 Power Conversion Efficiency.....	12
1.3.5 Short Circuit Current ( $J_{sc}$ ) .....	14
1.3.6 Open Circuit Voltage ( $V_{oc}$ ) .....	16
1.3.7 Fill Factor .....	16
1.4 Optical Properties .....	17
1.5 Defect Levels.....	21
1.6 Charge Carriers in Perovskites .....	24
1.6.1 Excitons .....	24
1.6.2 Polarons .....	27
1.7 Structure of the cell .....	29
1.8 Device Overview .....	32
1.8.1 Deposition Methods.....	35

1.8.2 Planar vs Mesoporous Structure.....	39
1.8.3 Hysteresis .....	40
1.8.4 Band Gaps .....	41
1.8.5 Stability.....	42
1.9 Device Structure .....	44
1.10 Motivation for Research .....	47
2 MEASUREMENT METHODS .....	50
2.1 FTIR .....	50
2.2 SEM-EDS.....	52
2.3 XRD.....	56
2.4 Profilometry .....	57
2.5 AFM.....	59
2.6 UV-VIS .....	61
2.7 XPS .....	63
2.8 IV Relation.....	65
3 COMMERCIALIZATION POTENTIAL.....	67
4 CHANGES TO DATA COLLECTION PLAN .....	72
5 CATION MEASUREMENT AND DISCUSSION .....	75
5.1 The Cations Overview .....	75
5.2 Cation Role in Perovskites .....	76
5.3 Spin Coating .....	77
5.4 Measurement Results.....	79
5.4.1 Thickness .....	79
5.4.2 XRD Results .....	85
5.4.3 AFM Results.....	91
5.4.4 UV VIS Data .....	97
5.4.5 SEM and EDS .....	99

5.4.6 KPFM .....	109
5.4.7 IV Measurements .....	117
5.4.8 XPS Data .....	124
5.5 Measurement Discussion .....	136
5.6 Summary .....	146
6 INTERFACES .....	148
6.1 Zinc Oxide .....	148
6.1.1 Background .....	149
6.1.2 Devices .....	149
6.1.3 Annealing .....	150
6.1.4 Metrology.....	151
6.1.5 Conclusions .....	153
6.2 PEDOT:PSS Poisoning.....	154
6.2.1 Overview .....	154
6.2.2 Background PEDOT:PSS.....	154
6.2.3 PEDOT:PSS Deposition and Storage.....	155
6.2.4 Mass Change .....	155
6.2.5 PEDOT:PSS Poisoning Summary.....	160
6.3 Lifetime .....	161
6.3.1 Results of Lifetime Testing.....	162
7 SCALABILITY SLOT DIE WORK .....	172
7.1 Overview .....	172
7.2 Background .....	172
7.3 Air Spin Coated .....	173
7.4 Slot Die Overview.....	177
7.5 Tests at nTact.....	179
7.6 XRD Data .....	183

7.7 Flexible Substrate .....	184
7.8 Scalability Discussion .....	185
7.9 Scalability Summary.....	187
8 CONCLUSIONS AND FUTURE WORK.....	188
8.1 Introduction .....	188
8.2 Conclusions .....	188
8.2.1 The Cation .....	188
8.2.2 Formamidinium.....	189
8.2.3 PEDOT:PSS.....	190
8.2.4 Slot Die .....	191
8.2.5 Ambient Conditions .....	191
8.3 Future Work.....	192
8.3.1 Hole Transport Layer .....	192
8.3.2 Electron Transport Layer.....	193
8.3.3 The Perovskite.....	193
APPENDIX .....	196
REFERENCES .....	257

## LIST OF TABLES

Table	Page
1-1. Calculated Goldschmidt Tolerance Factor ratios for pure halide perovskite Structures.....	6
1-2. Table of mobilities for alternative solar technologies.....	10
1-3. Alloy systems used in this study.....	20
4-1. Changes to the research plan.....	74
5-1. Sample cation properties.....	75
5-2. The perovskite alloys used in this work.....	77
5-3. Perovskite Alloy deposition recipe.....	77
5-4. Calculated lattice constants.....	87
5-5. Calculated Bandgaps based on UV-VIS data.....	97
5-6. KPFM potentials measured under illumination and in dark.....	111
5-7. Crystal sizes and surface roughness summary from AFM results.....	136
5-8. Calculated energies.....	141
5-9. Cation Alloy Masses.....	143
6-1. PEDOT:PSS test matrix.....	157
7-1. Ink formulations.....	173
7-2. Test matrix of initial samples done at nTact.....	180

## LIST OF FIGURES

Figure	Page
1-1. NREL Efficiency Chart [3] .....	2
1-2. Basic crystal structure of a perovskite crystal .....	4
1-3. Schematic highlighting crystal cage distortion for Goldschmidt tolerances outside ideal range of 0.8 to 1 [5].....	6
1-4. Models of the $\text{CH}_3\text{NH}_3\text{PbI}_3$ crystal structure.....	7
1-5. Differences between P-N and P-I-N junctions .....	8
1-6. Electrical model of a solar cell showing the Shunt and Series resistance .....	11
1-7. Spectral losses and AM1.5 [44] .....	13
1-8. The dependence of current and voltage in a device on based on the bandgap[47] .....	15
1-9. A) Temperature dependence of the bandgap for MAPBI films.....	20
1-10. A) Density of states for defects in perovskite solar cell .....	22
1-11. Charge carriers in perovskite solar cells .....	24
1-12. Exciton lifetimes and the effect on current density .....	26
1-13. Exciton binding energies as function of bandgap.....	27
1-14. Structure of $\text{CH}_3\text{NH}_3\text{PbI}_3$ , Colors are as follows: Grey- Lead (Pb), purple the halide (I) and green the organic ( $\text{CH}_3\text{NH}_3$ ) with a dipole moment indicated by the arrow from [79].....	28
1-15. Energy band alignment for the materials used in this work relative to MAPBI perovskite film .....	30

1-16. A) Basic structure of a perovskite solar device showing planar and mesoporous structures with n-type and p-type configurations.....	33
1-17. Assortment of deposition techniques A) Vacuum deposition, B) Dip method, C) Spin coating and D) vapor deposition [82].....	36
1-18. SEM images of as deposited perovskite film showing crystal sizes and film coverage and their corresponding device performance [99].....	37
1-19. SEM Images of mesoporous films, left and planar films on the right .....	40
1-20. A) Hysteresis seen in a representative perovskite device and B) the ideal IV curve [109].....	41
1-21. ITO patterned glass substrate.....	45
1-22. Solar Device patterning and film stack .....	46
1-23. The four devices on a typical solar device used in this research.....	47
2-1. FTIR basic operation principle and beam amplification effect of the ATR system.....	51
2-2. Incident electron beam radiation and the resulting emissions from the relative depth in the sample .....	54
2-3. SEM and EDS systems for detection .....	55
2-4. Schematic of a linear variable differential transformer used to on profilometers ..	58
2-5. Cartoon of a UV-VIS spectroscopy system .....	62
2-6. Cartoon of how XPS works with the x-rays interacting with the atoms electron orbitals and left the basic hardware setup highlighting he electron optics and the energy analyzer .....	64
3-1. Growth of the PV market, A) Current and predicted global install base [140] B) Domestic market [141] .....	68
3-2. Growth rate for three largest portable solar generator companies [143].....	70

4-1. UV-Vis data showing $\alpha$ -FAPbI <sub>3</sub> (175°C) phase to a $\delta$ -FAPbI <sub>3</sub> (25°C) phase .....	73
5-1. Evaporative rings on alloy perovskite samples from the application of the chlorobenzene solvent engineering step.....	78
5-2. A) Alloy Ink solutions, B) as deposited and C) annealed alloys .....	79
5-3. Alloy thickness results.....	80
5-4. Cesium concentration vs density of the ink solutions .....	82
5-5. XRD Pattern of 5% Cesium Alloy Sample .....	88
5-6. XRD Pattern of 25% Cesium Alloy Sample .....	88
5-7. XRD Pattern of 20% Cesium Alloy Sample .....	89
5-8. XRD Pattern of 10% Cesium Alloy Sample .....	89
5-9. XRD Pattern of 15% Cesium Alloy Sample .....	90
5-10. XRD Pattern of 15% Cesium (70% FA) Alloy Sample.....	90
5-11. AFM results, 5% alloy.....	91
5-12. AFM results, 5% Alloy .....	91
5-13. 10% Alloy AFM results .....	92
5-14. 10% Alloy, showing crystals that average ~168nm in size .....	92
5-15. 15% Alloy AFM results .....	93
5-16. 15% alloy, analysis of the images indicates an average crystal size close to 134nm.....	93
5-17. 20% alloy AFM results.....	94
5-18. The 20% alloy, analysis of image shows crystal diameter ~124nm.....	94

5-19. The 25% Alloy results.....	95
5-20. 25% alloy concentration .....	95
5-21. AFM results of the 15% Cesium (70% FA) alloy .....	96
5-22. AFM of 15% Cs alloy (70% FA) showing a crystal size of ~ 137nm .....	96
5-23. UV-VIS Curves of the alloy perovskites.....	97
5-24. Prepped sample for SEM, note the copper grounding strap.....	99
5-25. SEM image of a 5% cesium sample.....	100
5-26. Cs-I ratio in the alloy samples as measured by EDS .....	101
5-27. 5% Cesium Alloy SEM images .....	103
5-28. 5% Cesium alloy SEM images.....	103
5-29. 5% Cesium alloy SEM images .....	104
5-30. 10% Cesium alloy SEM image .....	104
5-31. 10% Cesium alloy SEM image .....	105
5-32. 15% Cesium (80% FA) alloy SEM images .....	105
5-33. 15% Cesium (80% FA) alloy SEM images .....	106
5-34. 20% Cesium alloy SEM images.....	106
5-35. 20% Cesium alloy SEM images.....	107
5-36. 25% Cesium alloy concentration .....	107
5-37. 25% Cesium alloy concentration .....	108
5-38. 15% Cesium (70% FA) SEM images.....	108

5-39. 15% Cesium (70% FA) SEM images.....	109
5-40. NIST AFM Sample Mounting Stack .....	110
5-41. 5% Cesium KFPM Images, Dark on top, under illumination on bottom.....	112
5-42. 10% Cesium, Dark on top, under illumination on bottom .....	113
5-43. 15% Cesium, Dark on top, under illumination on bottom .....	114
5-44. 15% (70% FA) Cesium, Dark on top, under illumination on bottom .....	115
5-45. 20% Cesium Content, Dark on top, under illumination on bottom .....	116
5-46. 25% Cesium, Dark on top, under illumination on bottom .....	117
5-47. All performance data for all alloy types, data includes non-yielding devices .....	118
5-48. Alloy efficiency of devices with proper IV-curves.....	119
5-49. Open Circuit Voltage (Voc) for yielding devices .....	120
5-50. Interface performance of PEDOT:PSS and the perovskite alloys .....	121
5-51. Short circuit current of the yielding devices.....	122
5-52. A) Short Circuit Current vs Cesium Concentration, B) Short circuit vs Bandgap .....	123
5-53. Alloy current vs thickness, graph shows importance on layer thickness .....	123
5-54. XPS Sample holder showing layout of samples 1-4 and the center position for run to run alignments.....	124
5-55. XPS results for the iodide peaks in the perovskite alloys .....	125
5-56. XPS results for the lead peaks in the perovskite alloys .....	126
5-57. XPS results for the carbon peak in the perovskite alloys .....	126

5-58. XPS results for the nitrogen peak in the perovskite alloys.....	127
5-59. XPS results for the oxygen peak in the perovskite alloys.....	127
5-60. XPS results for the cesium peaks in the perovskite alloys.....	128
5-61. Binding energy trend for iodide as a function of cesium concentration.....	129
5-62. Binding energy trend for lead as a function of cesium concentration.....	129
5-63. Binding energy trend for nitrogen as a function of cesium concentration.....	130
5-64. Binding energy trend for cesium as a function of cesium concentration.....	130
5-65. Iodide binding energy.....	131
5-66. Lead binding energy.....	132
5-67. Binding energy gap of cesium.....	132
5-68. Carbon XPS trend.....	134
5-69. XPS trend for oxygen.....	135
5-70. Growth of crystals based on transport kinetics.....	138
5-71. Growth model for crystals based on nucleation sites number and spacing.....	139
6-1. Work done at Texas State and published in the Journal of Physical Chemistry C [9].....	148
6-2. The n-i-p structure for ZnO perovskite.....	150
6-3. Annealing schema for the ZnO taken from work [9].....	150
6-4. FTIR sample setup schematic.....	152
6-5. FTIR experimental setup for collection of data in reference [9].....	153

6-6. The structure of PEDOT: PSS[187] and the conductivity of PEDOT:PSS compares to metals [188] .....	155
6-7. Change in mass of slides stored in fume hood and glovebox .....	156
6-8. Analysis of samples, top to bottom, EFF, Voc and Isc .....	158
6-9. Left, polarons under no bias experience no dipole resistance, Right panel, under bias induced dipole resistance [192] .....	161
6-10. Lifetime data showing cesium compounds (no dipole) performing better than dipole alloys [192] .....	162
6-11. Temperature Ramp of Lifetime Testing IV devices.....	164
6-12. Normalized lifetime current decay for the different alloys including MAPBI samples .....	165
6-13. Normalized Lifetime Voc for the alloy samples and MAPBI .....	166
6-14. Normalized efficiencies for the alloy samples and MAPBI.....	167
6-15. Normalized Fill Factor for the alloy samples and MAPBI .....	168
6-16. Decay of sample showing no interface breakdown, just dipole induced current loss.....	169
6-17. Decay IV curves of samples undergoing interface (PEDOT:PSS) break down .....	170
7-1. Difference in device parameters on one step 1:1:1 PbI <sub>2</sub> :MAI:MAAc ink spun coated in ambient and glove box conditions.....	175
7-2. Ambient inks solar device characteristics with different molar ratios of MAAc....	176
7-3. Best ambient 2.0 MAI concentration Device.....	177
7-4. A typical Slot Die Coater .....	178
7-5. Thickness trends for the different inks versus the dispense rate .....	181

7-6. Visual result of the sample with wood grain due to thickness non-uniformity .....	182
7-7. UV-VIS data for the different inks and samples performed at nTact .....	182
7-8. XRD data for the 1:1:1 ink at the different dispense rates.....	183
7-9. XRD Data for the 1:1.75:1 at different dispense rates left and the difference in apparent $PbI_2$ peak shown in purple circle on the right .....	184
7-10. Flexible substrate.....	185

## LIST OF ABBREVIATIONS

ABX<sub>3</sub> -- Generic formula for a perovskite, A cation, B cation, X halide/oxygen molecules

AFM -- Atomic Force Microscopy

AM1.5G -- Global Air Mass Standard 1.5

ATR -- Attenuated total Reflection

BCP -- Bathocuproine

C<sub>60</sub> -- Fullerene 60

C<sub>71</sub> -- Fullerene 71

CAGR -- Compound Annual Growth Rate

CDA -- Clean Dry Air

CdTe -- Cadmium Telluride, an alternative thin film solar cell material

CIGS -- Copper Indium Gallium Selenide, an alternative thin film solar cell material

Cs -- Cesium

CuI -- Copper Iodide

CuO -- Copper Oxide

DMF – Dimethylformamide (solvent)

DMSO -- Dimethyl Sulfoxide (solvent)

DOE -- Design of Experiments

EA -- Ethyl ammonium (cation candidate) ( $+NH_2CH_2CH_3$ )

EDS -- Energy Dispersive Spectroscopy

EFF -- Efficiency

EPA -- Environmental Protection Agency

ETL -- Electron Transport Layer

FA -- Formamidinium (cation) ( $+N_2H_4CH$ )

FAI -- Formamidinium Iodide ( $CHN_2H_4I$ )

FAPBI -- Formamidinium Lead Iodide ( $CHN_2H_4PbI_3$ )

FF -- Fill Factor

FTIR -- Fourier Transformed Infrared

FTO -- Fluorine Doped Tin Oxide

GaAs -- Gallium Arsenide, an alternative thin film solar cell material

HBr -- Hydrogen Bromide

HCL -- Hydrogen Chloride

HI -- Hydrogen Iodide

HTL -- Hole Transport Layer

I -- Iodide

IPA -- Isopropyl Alcohol

ITO -- Indium Tin Oxide

$J_{sc}$  -- Short Circuit Current Density

KPFM -- Kelvin Probe Force Microscopy

LANL -- Los Alamos National Laboratories

LEDS -- Light Emitting Diodes

LSD -- Least Significant Difference

MA -- Methylammonium (cation) ( $+NH_3CH_3$ )

MAI -- Methylammonium Iodide ( $CH_3NH_3I$ )

MAAc -- Methylammonium Acetate ( $NH_4CH_3CO_2$ )

MAPBI -- Methylammonium Lead Iodide perovskite ( $CH_3NH_3PbI_3$ )

NREL -- National Renewable Energy Laboratories

OFAT -- One Factor At a Time

Pb -- Lead

PCE -- Power Conversion Efficiency (EFF)

PEDOT:PSS -- poly(3,4-ethylenedioxythiophene) polystyrene sulfonate

PL -- photoluminescence

SEM -- Scanning Electron Microscopy

Si -- Silicon also an alternative thin film solar cell material

SnO -- Tin Oxide

Spiro-MeOTAD -- N7'-octakis(4-methoxyphenyl)-9,9'-spirobi[9H-fluorene]-2,2',7,7'-  
tetramine

SQ -- Shockley-Queisser Limit

TCO -- Transparent Conductive Oxide

TCPS -- Three characteristic parameter correlation

UV -- Ultra Violet

$V_{oc}$  -- Open Circuit Voltage

W -- Watts

XRD -- X-ray Refraction Diffraction

ZnO -- Zinc Oxide

## ABSTRACT

Climate change has renewed research into alternative power sources. One hot research topic is that of novel solar devices such as the hybrid inorganic-organic perovskite solar cell. Currently, hybrid perovskite solar cells are at 22.7% efficiency and are now exceeding all other thin film technology. The lone hurdle to wide spread adoption of hybrid perovskite solar cells remains thermal and water stability. Since the first reported perovskite solar cells using methylammonium lead iodide, researchers have been hard at work looking to address the stability issues. The use of different cations and the use of alloys of these cations have been proposed as solutions to the stability issues. One such alloy consisting of cesium, methylammonium and formamidinium is a leading candidate for commercialization of the perovskite solar cell. While the interactions of the lead cation and the halides are well understood, the role of the organic cation in the structure is not. This work examines the role of the cation in an alloy perovskite of cesium, methylammonium and formamidinium. This work uses SEM, XRD, XPS, AFM, KPFM, EDS, FTIR and IV measurements to highlight how the electronegativity, size and mass of the cations contribute to the resulting perovskite films in terms of solar characteristics, crystal sizes and film thickness. In addition, data will be presented to show how one of the underlying assumptions of perovskite manufacture, ambient processing, needs to be addressed to assure high quality

perovskite solar cells are manufacturable. The ambient processing condition results might provide insight into why so many researchers have a high range of reported values for perovskite solar cells made in labs across the globe. The role of interface stability on the hole transport layer will also be investigated as the degradation of the PEDOT:PSS hole transport layer has a marked impact on the ability of the perovskites to have the long term performance demanded by solar farms. Finally, some of the first films of perovskites deposited via slot die onto flexible substrates are initially reviewed as the use of slot die and flexible substrates are considered the next steps in commercialization of the hybrid perovskite solar cell system.

# 1. INTRODUCTION

The first observed photovoltaic effect was observed by Alexandre Becquerel 179 years ago in France. The young budding physicist discovered this effect working in his father's laboratory at the age of 19[1]. Almost half century later, the first patent for a solar cell would be awarded in 1888. At the dawn of the last century, even the great Albert Einstein would contribute to the knowledge of the photoelectric effect[2] , an effort which would eventually earn him the Nobel Prize in physics.

As with all things, work slowed due to two world wars, but work on solar cells began anew in the 1950s with Bell Labs and work on silicon-based cells. The Cold War and more importantly the Space Race would create a boom in research for solar cell devices, devices that can produce power directly from a material's interaction with the sun. Satellites, space probes and space stations all drove research into solar cells that were light weight, stable and highly efficient. Consequently, these devices were also expensive and had small niche market applications in space and remote areas where getting power to a remote military outpost or research station was not feasible. This model of deployment and market remained in place into the early 1970s.

Then in 1970, the Environmental Protection Agency (EPA) was established to control pollution. During the next 48 years, the EPA has championed the protection of the environment, whether through direct action or by pressure from the public. The EPA and the supporting research started identifying greenhouse gases as a problem in terms of climate change. Thea major source of these greenhouse gases are the from the

generation of electricity from fossil fuel plants (coal, oil, natural gas). One alternative to fossil fuel energy generation is from solar cells.

Research then began anew in solar cells with a focus for terrestrial power generation. The National Renewable Energy Laboratory (NREL) maintains a chart highlighting the maximum efficiency for each of the different devices under research since 1974 [3]. The most dominating feature of the chart, shown in figure 1-1, is the slow progress in efficiency gains over the past few decades. There is a notable exception in this chart for an innovative technology attracting much interest and the focus of this work, the perovskite solar cell.

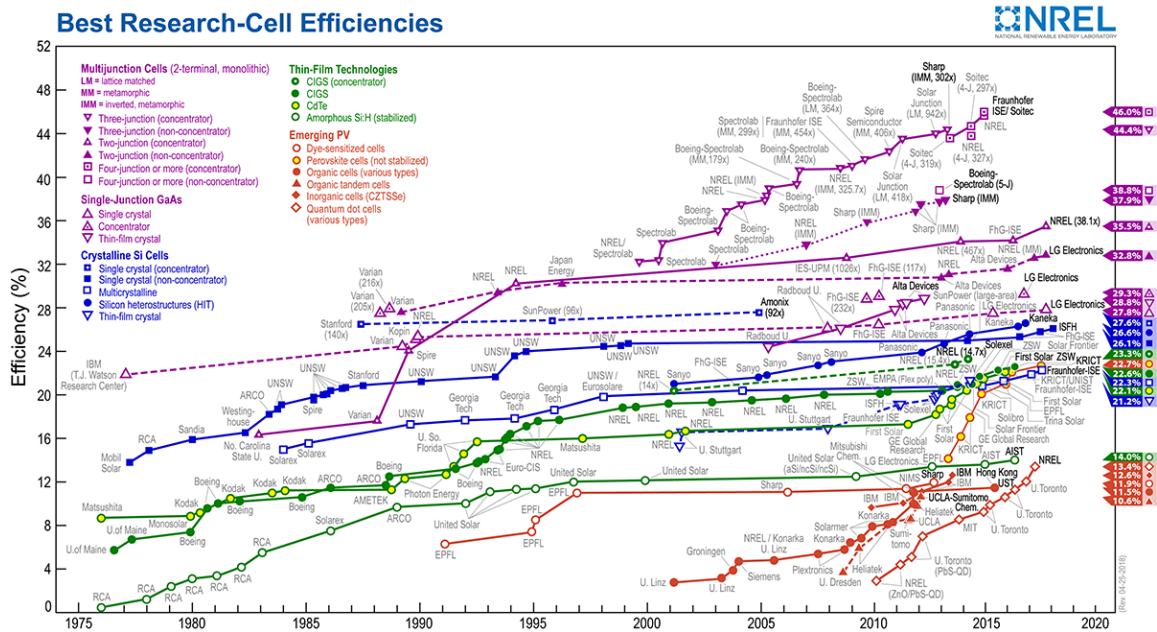


Figure 1-1: NREL Efficiency Chart [3].

Since its discovery a few years ago, measured and verified performance of perovskite based solar cells has them performing equivalently with technology with a head start of decades. However, unlike the other thin film perovskite are

competing with, the cost to manufacture a perovskite solar cell is a fraction of the cost of other thin films technology. The commercialization and realization of this technology would enable solar cells to begin to replace fossil fuel sources energy plants at a fraction of the cost of current thin film technology.

The work presented here is a small part of a larger effort on perovskite based solar cells. Perovskite solar cells use a hybrid of inorganic and organic cations to form the photoactive crystal. Chemistry has restricted the inorganic selection of the cations to lead, tin or germanium. The organic cation portion, however, is wide open and is the basis for this work.

## 1.1 Perovskites Background

Perovskites are a class of crystal minerals that were discovered in the Ural mountains of Russia in 1839 by Gustav Rose and named for Russian mineralogist, Lev Perovski[4]. Perovskite compounds have a characteristic structure denoted by  $ABX_3$  and seen in figure 1-2, where the A and B are cation type molecules and X have been traditionally oxides, but recently are halides[5], [6]. Despite the early discovery, it would be nearly a century before research began in earnest on perovskite materials starting in the 1940s. In the 75 years since the renewed interest, perovskites have become compounds demonstrating properties of superconductivity, light emitting, ferromagnetism, thermoelectric, piezoelectricity and of importance in this work, solar activity.

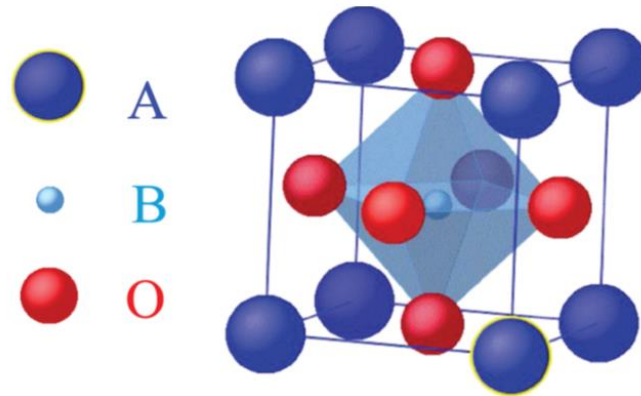


*Figure 1-2: Basic crystal structure of a perovskite crystal. A can be organic molecules, B are typical a metal ion and X can also be halides as I, Br and Cl [7].*

In the last 7 years perovskites have become a hot topic in the realm of solar cell devices. Since the first hybrid perovskite solar cell reported in 2009, solar efficiencies have climbed from 3.9% to over 24% even exceeding the efficiency levels of silicon based commercial solar cells. In addition, hot-carrier utilized perovskite based cells have been recently shown to have a theoretical limit of 66% efficiency[5], [7].

Despite the rocket like rise in device efficiency, the most compelling reason for the rise of perovskite solar cells is the relative ease and low cost of making an operational device. The manufacturing cost of producing a perovskite solar cell is estimated to be 75% less than a traditional thin film based solar cell [8]. This would make perovskite solar cells an instantly commercializable and profitable product. However, perovskites suffer from moisture and thermal instability.

Previous work done here at Texas State focused on thermal stability and a novel approach to increasing the thermal stability of a n-type perovskite solar cell utilizing a ZnO electron transfer layer was demonstrated[9]. Previous work also focused on the role of interfaces on stability and efficiencies [10].

## 1.2 Perovskite Structure

Perovskites can assume any of the 15 recognized crystal structures [11] and there has been over 376 compounds identified as perovskites with the  $ABX_3$  compound formula. The  $ABX_3$  formula signifies the relationship of the molecules in the crystal structure, with A and B being cations and X being an anion. Perovskite structures are neutral charged species hence the charges on A, B and X sum to zero. The structure additionally, has size constraints to fit into a stable crystal lattice. In general, the perovskite structure stability is predicted by the Goldschmidt relationship:

$$t_{IR} = (R_A + R_X)/(\sqrt{2} * (R_B + R_X)) \quad (1-1)$$

Where  $R_A$ ,  $R_B$  and  $R_X$  are the ionic radius of the species A-B-X. For an ideal perovskite structure, the Goldschmidt relationship value is taken to be 1 and most experimental data has shown that real perovskites are in the range of 0.8 – 0.9 [11], [12]. Values outside this tolerance range tends to distort the lattice preventing crystal lattice creation or inherently unstable crystals and example of this is shown in figure 1-3.

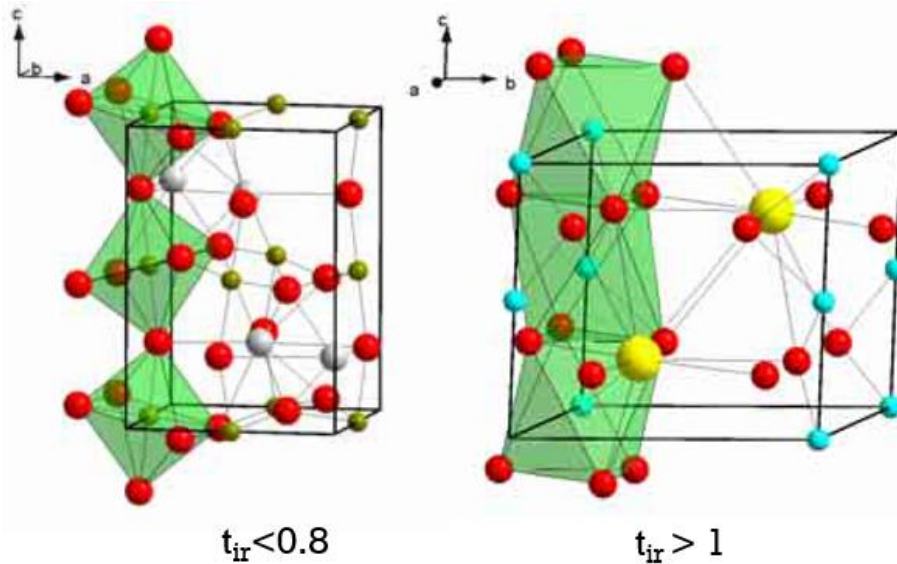


Figure 1-3: Schematic highlighting crystal cage distortion for Goldschmidt tolerances outside ideal range of 0.8 to 1 [5].

For the perovskites that have gained much attention in recent years, the Goldschmidt ratio tends to border on the small side of the ratio which generally speaks to the long-term stability of the crystal. The Goldschmidt ratio for pure halide perovskites are calculated and are shown in table 1-1.

Table 1-1: Calculated Goldschmidt Tolerance Factor ratios for pure halide perovskite structures.

Perovskite	Halide	Goldschmidt TF
CH <sub>3</sub> NH <sub>3</sub> PbI <sub>3</sub>	Iodide (I)	0.912
CH <sub>3</sub> NH <sub>3</sub> PbCl <sub>3</sub>	Chlorine (Cl)	0.938
CH <sub>3</sub> NH <sub>3</sub> PbBr <sub>3</sub>	Bromine	0.927

The cation selection of methylammonium (MA) which is +NH<sub>3</sub>CH<sub>3</sub> is the driving factor in the low Goldschmidt tolerance values. Figure 1-4 shows several models of the CH<sub>3</sub>NH<sub>3</sub>PbI<sub>3</sub> crystal lattice. In each figure within Figure 1-4, the +NH<sub>3</sub>CH<sub>3</sub> is represented by a cloud of uncertainty in its location within the crystal lattice. Figure 1-4A highlights the size difference between the components of the perovskite which contributes to the

high uncertainty with the MA location [13]. It should be noted that the uncertainty in the MA location is larger than the size of the cation by almost an order of magnitude.

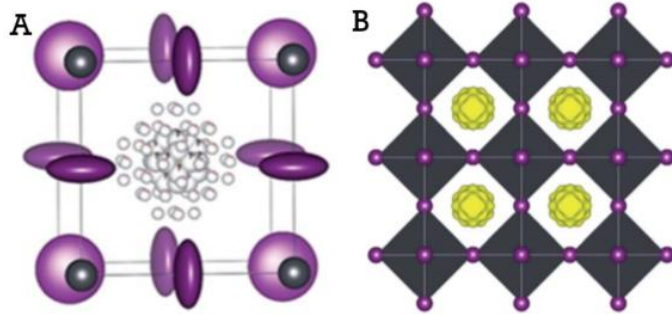


Figure 1-4: Models of the  $\text{CH}_3\text{NH}_3\text{PbI}_3$  crystal structure. A) Electron shell model [13], B) Crystal lattice positioning [13]. Note in both the high uncertainty of the  $+\text{NH}_3\text{CH}_3$  cation represented by the cloud of circles in both models.

There is some evidence that the small MA size contributes to high carrier lifetimes within the crystal [14]. Thus a larger cation might reduce the portion of the cation that rotates within the crystal thus reducing carrier lifetimes and reducing the Rashba effect [14].

## 1.3 Overview of the Perovskite Solar Cell

### 1.3.1 Junctions

Solar cells and semiconductors share a common root in that they are descendants of the effect of junctions of dissimilar materials that form P-N junctions. The P-N junction is widely understood and is found in use in many semiconductor materials and thin film solar devices such as silicon, copper indium gallium selenide (CIGS), cadmium telluride (CdTe) and gallium arsenide (GaAs). The device physics can be tuned via doping which influences potentials, diffusion lengths and depletion widths.

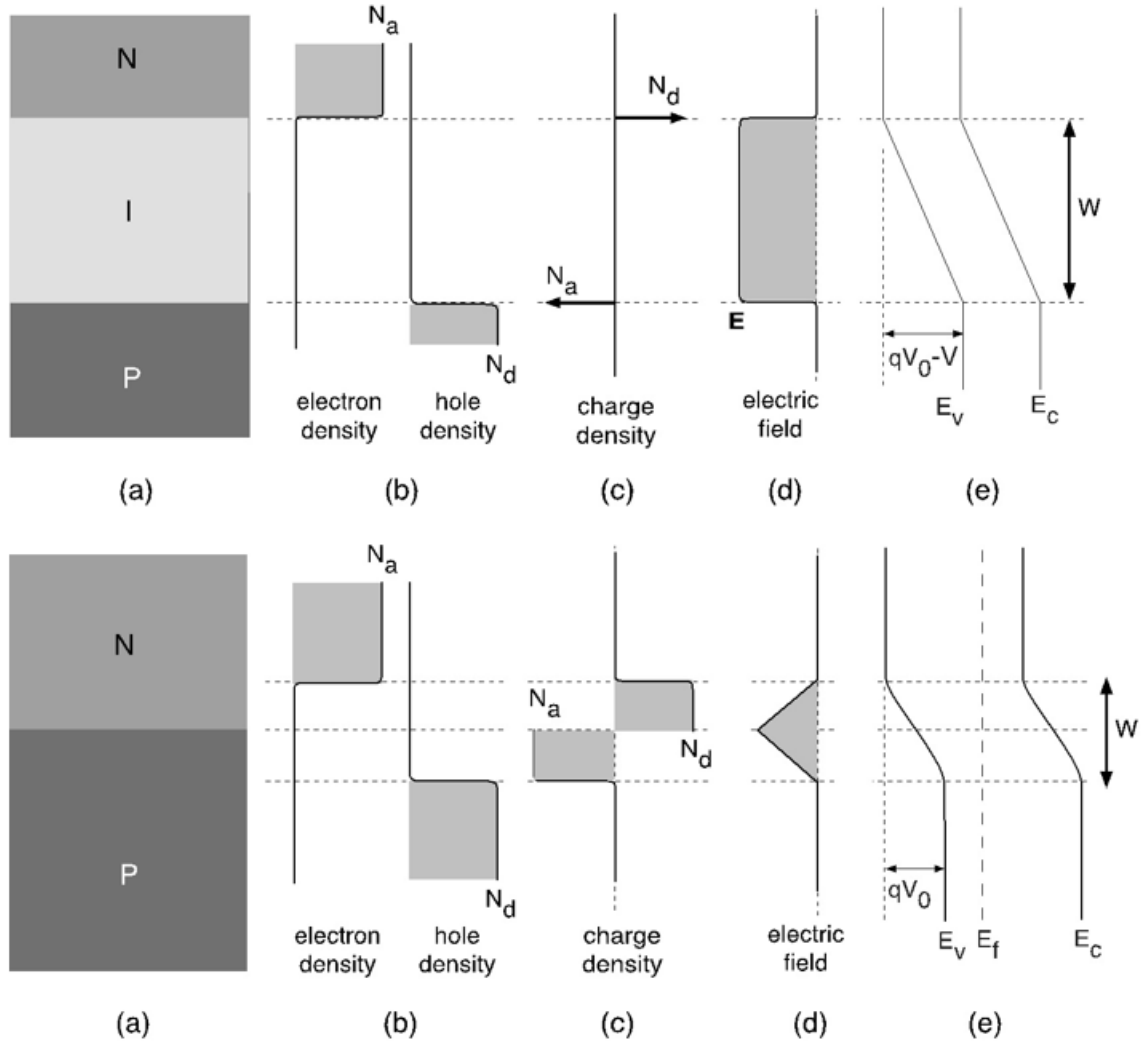


Figure 1-5: Differences between P-N and P-I-N junctions. a) Structure, b) Carrier distribution, c) Charge distribution, d) Electric field, e) band diagram under reverse bias [15]. The following nomenclature is used,  $N_a$ , acceptor concentration,  $N_d$ , donor concentration,  $E$  electric field,  $E_v$ - valence band level,  $E_c$ -conduction band level,  $E_f$  Fermi energy level,  $W$ - width of the depletion region (PN) or thickness of intrinsic layer (PIN),  $V_0$  is the built in voltage and  $V$  is the applied voltage [15].

Perovskite devices differ from these traditional materials in that the resulting device is not a P-N junction, but a P-I-N junction. Here, the P and N portions of the P-N junction remain, that is the p-type material has a higher concentration of holes while the n-type material higher electron concentrations. The difference is the intrinsic

material, which is electrically neutral in terms of charge carriers. The differences in the operational effects are shown in figure 1-5. Perhaps the biggest difference in the operation is seen in figure 1-5D where the electric field in the intrinsic layer is uniform.

The operation of the solar device differs slightly between the P-N and P-I-N junctions. In a traditional thin film device, the incoming photon needs to interact with the device creating both majority and minority carriers. As in other P-N devices, the increase in minority carriers dictates the performance of the system. In a P-I-N device, the photon interaction creates both types of carriers as well, however, both carriers influence the device physics.

For the P-I-N junction to outperform the P-N junction, the created carriers need to have three characteristics. The first, the carriers need to have a long lifetime, secondly, they need to have good mobility within the intrinsic layer and lastly, they need to have long diffusion lengths. All of these characteristics are related:

$$L = \sqrt{D\tau} \quad (1-2)$$

Where L is the diffusion length (m), D is the diffusivity (m<sup>2</sup>/s) and τ is the lifetime (s)

The mobility is then related to equation 1-2 via the Einstein relation:

$$D = \mu_q \frac{k_B T}{q} \quad (1-3)$$

Where  $k_B$  is the Boltzmann's Constant,  $\mu_q$  is the electron mobility, q is the electron charge and T is the temperature. If these values are sufficiently large, then the intrinsic layer can be made dimensionally large as carriers created would both survive long enough

and move to the P/N material to extract the charge in terms of current. As can be predicted, maximizing the intrinsic layer thickness results in a higher number of carriers being created and extracted provided that the carriers have long lifetimes and mobilities. This happens since a thicker absorber material allows for more interactions between the incoming photons and the absorber, increasing carrier generation.

The P-I-N structure becomes an ideal structure for solar cells when these conditions are true, (high lifetimes, high mobilities and long diffusion lengths) and these properties exist within perovskite materials and are shown in table 1-2.

*Table 1-2: Table of mobilities for alternative solar technologies.*

<b>Material</b>	<b>Mobility <math>\mu</math> (<math>\text{cm}^2/\text{Vs}</math>)</b>	<b>Diffusion Length</b>	<b>Lifetimes</b>	<b>Reference</b>
Perovskites	20-600 for both 2.5 -1620 for holes 0.7 – 282 for e-	22.9-37.3 ( $\mu\text{m}$ ) 100 nm–1 $\mu\text{m}$	21-54 ( $\mu\text{s}$ ) 108-133 (ps)	[16]–[22]
CdTe	100-1000	6-14 ( $\mu\text{m}$ )	0.5-1 (ns)	[23]–[26]
CiGSe	2-40	3 ( $\mu\text{m}$ )	8ns	[27]–[30]
Si	0.001 - 0.05	60-300 $\mu\text{m}$	5-200 ( $\mu\text{s}$ )	[31]–[36]
GaAs	$10^3$ - $10^7$	5-6 ( $\mu\text{m}$ )	3.7-6ns	[37]–[40]

### 1.3.2 Model of the Solar Cell

There are several different electrical models of solar cells, the simplest and most popular model is that of a simple single diode [41],[42]. The model of a diode is used as current is modeled to flow in one direction due to the photo generated current while under illumination and is shown in figure 1-6. This is a valid assumption as solar cells are useful only when generating current. It should be noted that it is possible to apply a

current to generate photon emission from perovskites, creating light emitting diodes (LEDs). This can be done using the same perovskites material presented here albeit with a different layer stack that maximizes the current input into the perovskite as opposed to removal [43].

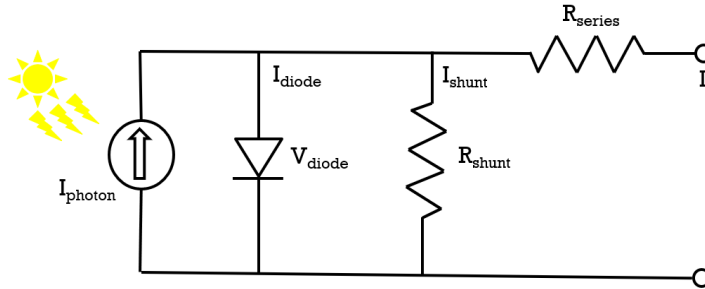


Figure 1-6: Electrical model of a solar cell showing the Shunt and Series resistance.

In the electrical model, shown in figure 1-6, there are two resistances that are factors in device performance, the series resistance ( $R_{\text{series}}$ ) and the shunt resistance ( $R_{\text{shunt}}$ ).  $R_{\text{series}}$  is the mostly made up of resistances that occur while getting the current out from the device and has three main components. The first is known as the contact resistance which is the results of interfaces. As the carriers move to the metal, they encounter resistance as the transfer from one layer to the next. Band alignments, interface quality, layer thickness, interface type (meso vs planar) all contribute to the series resistance. The next portion of resistance occurs within the perovskite material. Carriers generated within the absorber must transport to the hole and electron transport layers. This is anomalous to the emitter-base resistance found in typical P-N junction solar devices. Resistance to transport within this layer can be tied to crystal quality, defect traps, impurity levels and crystal density. Therefore, it is modeled

differently than the interface resistance as it gives an indication of absorber quality. The last resistance is the resistance of the top and bottom metal contacts. This resistance can be adjusted through use of better quality metals such as gold and better transparent conductive oxides (TCO). Regardless of the source of  $R_{series}$ , the goal of any device is to have  $R_{series}$  approach zero.

$R_{shunt}$  is the other primary resistance. Unlike  $R_{series}$ ,  $R_{shunt}$  needs to be as high as possible. The reason for wanting a high  $R_{shunt}$  is that a high shunt resistance prevents parasitic current loss. Devices with low  $R_{shunt}$  lose much of their current by providing an alternative path for the photo generated current to go. Low  $R_{shunt}$  has the effect of reducing both open circuit voltage of the device ( $V_{oc}$ ) and the short circuit current ( $J_{sc}$ ) and is seen primarily in poorly built devices.

### 1.3.3 Figures of Merit

To properly characterize a solar cell, there are four figures of merit, power conversion efficiency (PCE) often times just referred to as efficiency (EFF), short circuit current ( $J_{sc}$ ), open circuit voltage, ( $V_{oc}$ ) and finally the fill factor, FF. Together these four figures of merit are used to classify how well a solar cell is converting photons into useful energy.

### 1.3.4 Power Conversion Efficiency

Power conversion efficiency (PCE) measures how well the solar cell converts photons from the sun into electrical power. A measurement is made using a solar simulator that is calculated to an air mass 1.5 spectrum (AM1.5) which accounts for

the different wavelengths of light that are present at the surface of the earth. In addition, the simulated light is calculated to have an energy of  $100\text{mW}/\text{cm}^2$ . In short, the PCE measurement is made with light consisting of the wavelengths present in sunlight at an intensity of  $100\text{mW}/\text{cm}^2$ . This implies that a 20% efficient device would have a power density of  $20\text{mW}/\text{cm}^2$  or having produced a maximum power output of only 20% the input or incident sunlight. Figure 1-7 shows the solar spectrum and highlights some of the losses due to photon interactions with the gases in the atmosphere.

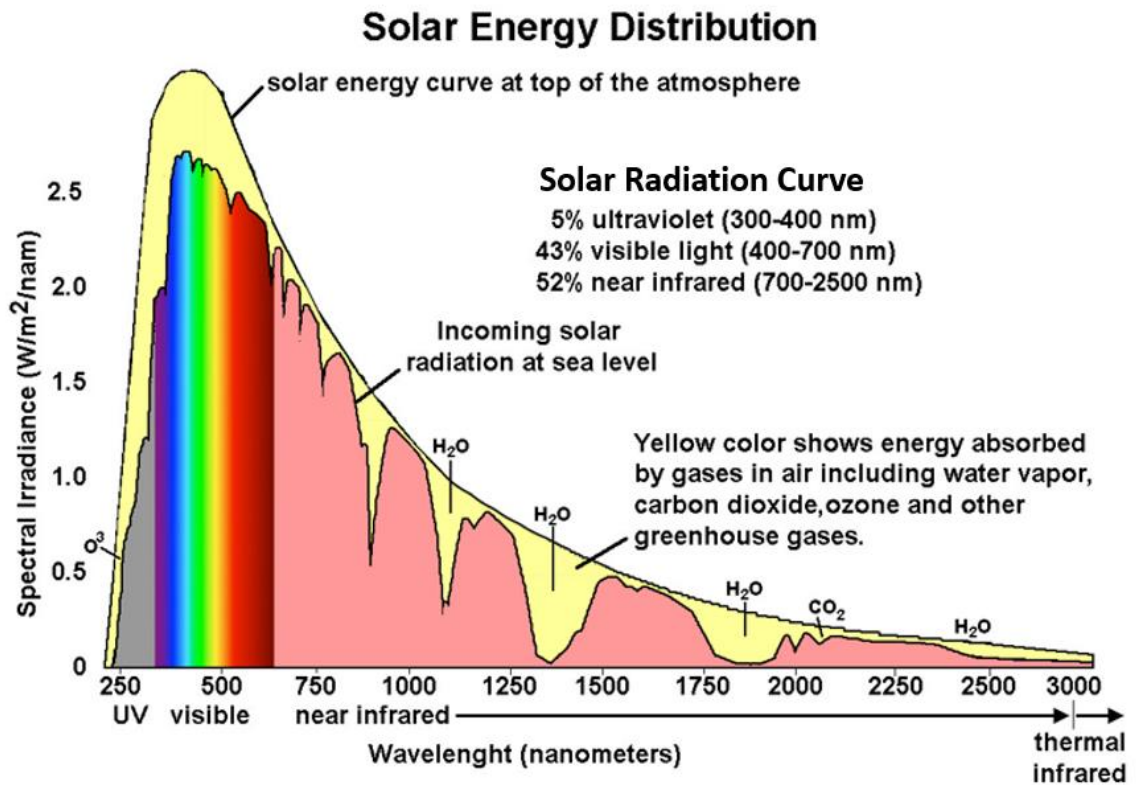


Figure 1-7: Spectral losses and AM1.5 [44].

Of all the figures of merit, high PCE is the most sought-after characteristic of solar cells. Solar cells with high efficiencies demand higher prices on the market and are

the goal of many researchers [45]. However, there is a limit to PCE as dictated by Shockley-Queisser (SQ) limit. The SQ limit places limits on the maximum PCE possible due to non-desirable interactions of the incoming photons and the device. These losses that are not possible to engineer out and include: carrier recombination, scattering and reflection and the largest loss, heat generation. As a result, the highest possible PCE on a device is predicted to be ~33%, with a majority of the incoming photons (almost half) lost to heating effects of the material [46].

There are some devices that perform better than Shockley-Queisser limit, but these are not single junction cells, but have been enhanced somehow, either from the use of mirrors or concentrators which increase the incoming light, thus the incoming light is not  $100\text{mW}/\text{cm}^2$ , but 2 to 10 times higher. Other options include using multi-junction cells that are basically stacks of solar cells that are designed to best capture certain wave lengths of light. The multijunction cells are typically high dollar devices and are found on many space-based machines.

### 1.3.5 Short Circuit Current ( $J_{sc}$ )

The short circuit current ( $J_{sc}$ ) is the current through the solar cells when the voltage across the solar cell is zero and under illumination. The  $J_{sc}$  is a measure of the devices ability to generate carriers from the incoming photons, however there are many factors that influence the measurement. Items like carrier lifetime, carrier diffusion lengths, interfaces and materials all effect a solar cell's  $J_{sc}$  measurement. In this study, the biggest factor effecting  $J_{sc}$  is the ability of the hole and electron transport layers to transport carriers and the interface of the perovskite with those layers.

The  $J_{sc}$  has a maximum ideal value for any device and that is depended on the AM1.5 spectrum. At 100% efficiency and under ideal conditions (meaning no losses to Shockley-Queisser) an incoming photon should produce one carrier in the device. Additionally, as seen in figure 1-8, the current is also depended upon the bandgap of the device. The bandgap dependence is a result of the lack of energy of the incoming photons to generate a carrier resulting in the decrease in current density with increasing bandgap. Additionally, photons with higher than needed energy generate carriers, but the excess energy is lost to heating. For perovskites, expect a max current density in the range of 25-40mA/cm<sup>2</sup> depending on the composition[46].

For the devices under investigation here,  $J_{sc}$  depends on many factors. The two biggest factors encountered here are film quality and interface problems. The first is encountered with aged ink, aged perovskite material (possible decomposition) and/or HTL-perovskite layer contamination. In addition, the multi-crystalline perovskite material gives rise to a high number of grain boundary which can cause problems if not properly annealed in ideal conditions (humidity levels and temperature).

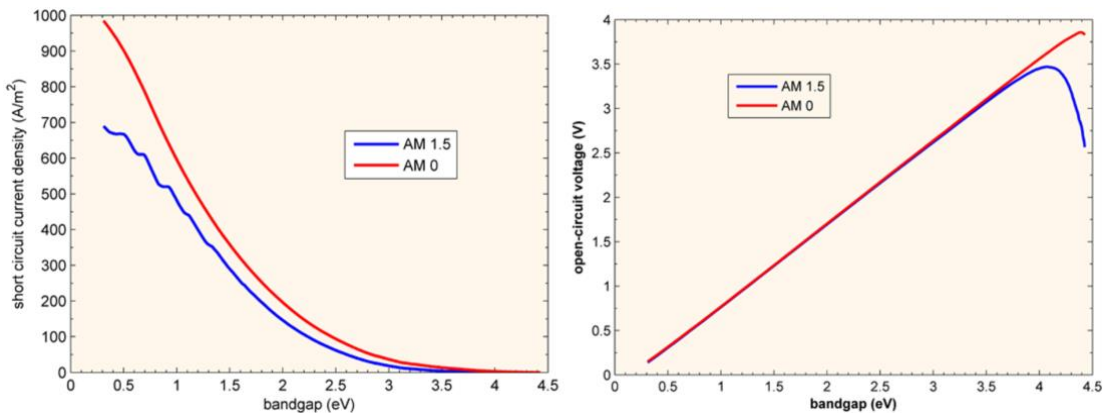


Figure 1-8: The dependence of current and voltage in a device on based on the bandgap[47].

### 1.3.6 Open Circuit Voltage ( $V_{oc}$ )

The open circuit voltage ( $V_{oc}$ ) is the maximum available voltage on a solar device under illumination and this occurs at zero current. The  $V_{oc}$  is caused by the biasing of the cell via the photon induced current in the cell. The  $V_{oc}$  is the measurement of the recombination of carriers in the device.  $V_{oc}$  is also dependent upon the bandgap of the device. In addition, there is a maximum value for  $V_{oc}$  that is based on the bandgap in much the same way as  $J_{sc}$ . As the bias in the cell is dependent upon the carrier concentration,  $V_{oc}$  has a max value and that relationship is seen in figure 1-8.

For the devices under investigation here, the  $V_{oc}$  is also dependent upon crystal quality and the band alignment structure of the film stack. For example, we can increase  $V_{oc}$  in the studied devices by replacing the hole transport layer (HTL) with another material that allows for closer band alignment between the perovskite and HTL.

### 1.3.7 Fill Factor

The fill factor is an abstract concept that describes the ideality of the power curve. The fill factor arises from the fact that there are two power points for a solar cell. The first is the theoretical max power of the device given by  $V_{oc}$  and  $J_{sc}$ . The second is the actual device performance which produces a max power at a value less than the theoretical prediction. The points on the IV curve where actual max power exists are known as  $V_{mp}$  and  $I_{mp}$ . The fill factor then is then the ratio of the actual max power to the theoretical max power given by  $V_{oc}$  and  $J_{sc}$ :

$$Fill\ Factor = \frac{I_{mp} * V_{mp}}{J_{sc} * V_{oc}} \quad (1-4)$$

Under ideal conditions, the fill factor is one and the max power would equal the theoretical max power of the device. However, in practice the fill factor is typically below 0.8 for most devices driven by resistive (both shunt and series) losses and the diode effect. For devices with high  $J_{sc}$  and  $V_{oc}$  but having low efficiencies, the fill factor is what drives the poor performance or rather the combination of the shunt and series resistance.

For devices under investigation here, fill factors do approach 0.8 for well performing devices [46]. Fill factors tend to die off for devices that are decomposing as parasitic losses increase in the absorber material to HTL interface. Fill factors also tend to decrease if the perovskite material undergoes a crystal lattice change as seen in the  $FAPbI_3$  perovskite materials.

#### 1.4 Optical Properties

The properties of perovskites are determined by the crystal structure and constituents within its structure as well as the environmental conditions. For example,  $CH_3NH_3PbI_3$  (MAPBI) optical properties are effected by temperature[48][49] which effects bandgap and photoluminescence (PL). Driving some of these properties is the crystal phase transitions that occurs at 330K where the crystal structure moves from cubic to tetragonal and again at 163K where the crystal transitions from tetragonal to orthorhombic[48]. Reported bandgaps of MAPBI range over a narrow window, but are close to 1.57eV [50] which is close to the ideal Shockley-Queisser bandgap of 1.34eV.

The crystal phase transitions also influence the PL spectra observed by shifting the signal. In addition, perovskites observe random PL emissions from on and off states known as PL blinking [48], [51]–[53]. The blinking is seen on a variety of perovskite structures from quantum dots to nanoparticles. For the films in this study, two theories are present on what the underlying mechanism is. One states that ion migration contributes to non-radiative recombination events similar to Auger processes[52], while the other attributes this to defects (both structural and chemical) within the perovskite creating trap states that contribute to the non-radiative recombination events[51][53].

Other optical properties show expected behavior that comes with a tunable bandgap. One such behavior is the refractive index of MAPBI which has shown a dependence on the halide concentration ratio[54]–[57] as well as the organic concentration ratio[58], with a reduction in the refractive index observed by the addition of Cl to the film[49] with little effect on the extinction coefficient[49]. Lastly, MAPBI also has a high thermal expansion coefficient, about 50 times greater than silicon[48]. This high thermal expansion could be a problem with interfaces within a perovskite layer stack as the heating cycle can separate the material [59].

MAPBI films optical properties are desirable in a solar cell as they are easily tunable and are shown in figure 1-9. However, the crystal phase transitions occur at temperatures that would be considered normal operational conditions for a solar cell. In addition, the deposition method has shown to have an effect on the optical and band gap properties as well[60]. In support of this, we will show that deposition technique also effects the resulting yield of the devices prepared at Texas State (appendix 9.2).

Lastly, the large thermal expansion coefficient will be challenge to solar cell lifetime as large coefficients can cause thin films to delaminate reducing or killing the cells effectiveness. These are just some of the challenges to the use of MAPBI as a solar cell.

FAPBI films also show multiple crystal phases, known as  $\alpha$  and  $\delta$  phases (sometimes reported as the  $\beta$  -phase). The  $\alpha$ -phase is the more desirable phase (cubic), however, this phase exists at temperatures above temperatures of 348K [61]. FAPBI films have a better bandgap than MAPBI films with 1.48eV being reported [50]. As can be expected, the  $\alpha$  and  $\delta$  phases have different PL peaks [62]. FAPBI films also have tunable bandgaps from the changing of the halide ratio [63] much like MAPBI films. The thermal expansion coefficient is similar to MAPBI films in the  $\alpha$ -phase, but nearly 2x that in the  $\delta$ -phase. However, due to the  $\alpha$ -phase existing at elevated temperatures, FAPBI films are not well studied and the effect of the phase transition will be reviewed later.

Figure 1-9 shows some of the effects on the bandgap of perovskite materials based on A) temperature of the MAPBI film, B) alloying effect of FA and MA on the perovskite film and C) which shows the effect of the deposition technique has on the resulting film's performance. All these factors are a challenge to consistent performing films.

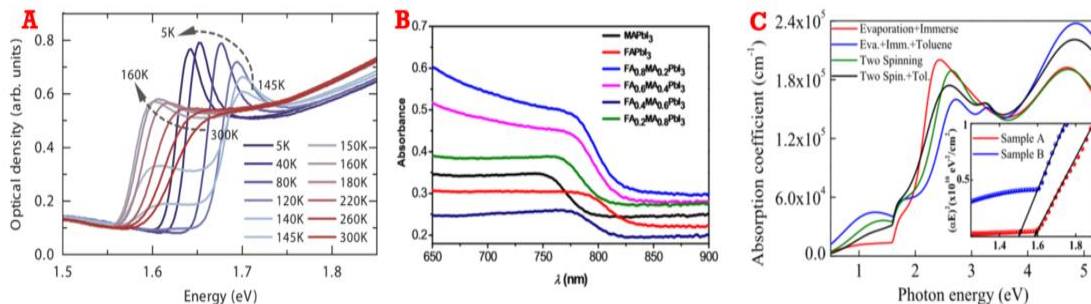


Figure 1-9: A) Temperature dependence of the bandgap for MAPbI<sub>3</sub> films [48]. B) Optical absorbance (bandgap) differences in alloy films of MA and FA perovskites [64]. C) Bandgap differences observed from deposition techniques [60].

To overcome the crystal phase problems with both MAPbI<sub>3</sub> and FAPbI<sub>3</sub> films, researchers are alloying the films resulting in films such as MA<sub>x</sub>FA<sub>1-x</sub>PbI<sub>3</sub> [64][65]. In addition, researchers are looking at the ABX<sub>3</sub> and allowing for A cation to include Cs, MA, FA and other cations and the B cation to include Pb and Sn to help address the crystal stability. In this study, six alloys are examined and are listed in table 1-3. Alloys of FA<sub>x</sub>MA<sub>y</sub>Cs<sub>z</sub>PbI<sub>3</sub> will be studied and these systems are identified by the cesium content found in each as shown in the table 1-3.

Table 1-3: Alloy systems used in this study.

System	Alloy
5% Cesium	FA <sub>0.8</sub> MA <sub>0.15</sub> Cs <sub>0.05</sub> PbI <sub>3</sub>
10% Cesium	FA <sub>0.8</sub> MA <sub>0.1</sub> Cs <sub>0.1</sub> PbI <sub>3</sub>
15% Cesium	FA <sub>0.8</sub> MA <sub>0.05</sub> Cs <sub>0.15</sub> PbI <sub>3</sub>
20% Cesium	FA <sub>0.7</sub> MA <sub>0.1</sub> Cs <sub>0.2</sub> PbI <sub>3</sub>
25% Cesium	FA <sub>0.7</sub> MA <sub>0.05</sub> Cs <sub>0.25</sub> PbI <sub>3</sub>
15% Cesium (70% FA)	FA <sub>0.7</sub> MA <sub>0.15</sub> Cs <sub>0.15</sub> PbI <sub>3</sub>

## 1.5 Defect Levels

Defects in semiconductors at the band level are energy states that trap carriers (electrons or holes) and prevents those carriers from operation in the device. The defect levels in semiconductors are classified as either deep or shallow with the difference being the energy level required to remove a carrier from the trap. Deep level traps are traps are states that require more energy than what is available at room temperature ( $kT$ ) to escape, while shallow require less than  $kT$  to escape. Shallow level traps are easy to overcome as sufficient energy is available at room temperature ( $kT$ ) for the carriers to escape. The deep level traps, however, keep carriers from moving into the valence or conduction bands, isolating those carriers from being of use to the device. As a result, devices that have a high level of deep level traps have problems operating as intended. For solar devices, these traps effectively remove phonon generated carriers from the device, reducing device efficiency.

Perovskites have an advantage due to the unique direct bandgap nature of the crystal and the fact that electrons can be promoted from both the lead and halide atoms[55] as shown schematically in Figure 1-10B. The direct bandgap nature also gives rise to shallow level defects within the crystal. Figure 1-10A, shows a DFT model of the density of states for a bulk MAPBI film and the grain boundary defects. The absence of states within the bandgap is attributed to the shallow nature of the defect levels observed in perovskites[55] .

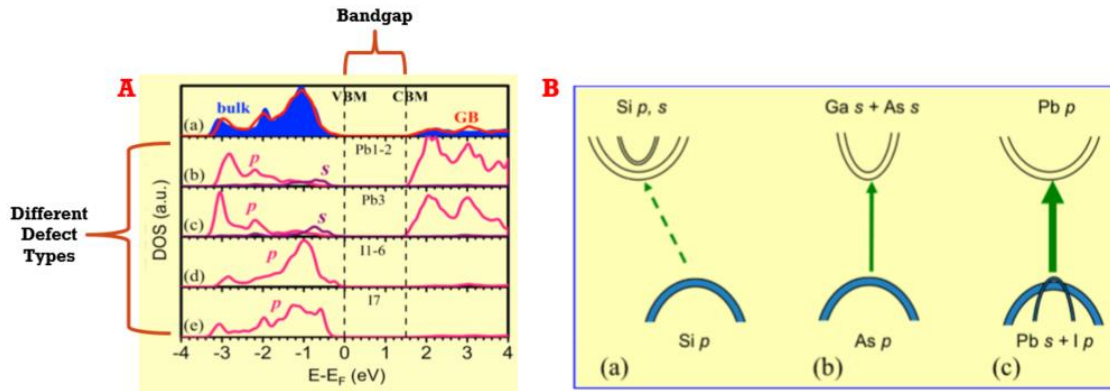


Figure 1-10: A) Density of states for defects in perovskite solar cell. B) Direct bandgap highlighting dual promotion from both Pb and I orbitals [55].

Defect levels and states in perovskites are typically modeled and compared to experimental data to confirm the model based on actual performance. A common defect state occurs along the grain boundaries where an interruption in the crystal is encountered. Crystal boundaries especially perovskite boundaries are particularly challenging giving the range of terminal ends that can be encountered such as Pb, I, H, C and N atoms which gave rise to 13 different scenarios for the crystal edge along the grain boundary [66]. Interestingly, this model showed that Pb-rich conditions, which create more Pb areas along the grain boundary, are better than the I-rich conditions based on carrier lifetimes and better hysteresis performance [66] [67]. The Pb rich conditions are what is present when a two-step deposition method is used to create the perovskite film. The challenge at Texas State is the addition of acetate and cesium to this crystal boundary.

To help fight defect levels, especially along the boundary, many researchers are attempting to reengineer the crystal growth [67]–[69]. One method adds ethanol to the

MA cation solution for vapor assisted perovskite formation [67]. In context of the former discussion, the ethanol addition still leaves the perovskite in a rich Pb environment, which reduces the defect levels along the crystal boundary. Solvent engineering methods are also being explored to reduce crystal defects. In one example, the use of different solvents helps with film coverage and produced larger crystals [68]. The larger crystals had increased performance which was attributed to a decrease in the defect states associated with the grain boundaries as larger crystals have less grain boundaries than smaller crystals.

Mobility of defects within a perovskite has also been probed [70]–[72]. In one study the mobility of  $ABO_3$  ions were modeled via DFT and it was shown that A cation and O interstitials diffuse via both 1D and 2D diffusion mechanisms while B vacancies tend to be immobile [71]. We can extrapolate this data to show that Pb and the halide are more likely to be mobile within the crystal than the cation, regardless of cation choice (MA, FA, Cs or alloy of two or more). The ion migration has also been shown to be a contributing factor to observed hysteresis with devices with lower carrier mobilities (higher defect states) exhibiting more hysteresis[70].

In summary, perovskites have shallow level defects, with most attributed to grain boundaries. Different chemistries used during perovskite crystal formation can reduce the effects of defects by using excess Pb or by increasing crystal size. Hysteresis seen in perovskites can be attributed to defect sites produced by ion migration (iodide) and localized charging effects that hinder movement of the ions under reverse bias[73]–[76]. Despite these issues, shallow defects levels are ideal as carrier movement is only

hindered due to the sufficient energy at room temperature for the carriers to free themselves from the shallow level traps.

## 1.6 Charge Carriers in Perovskites

In traditional thin film solar cells such as silicon, charge carriers are modeled as a p-n junction. For a p-n junction, incoming photons induce the creation of electrons and holes that drift which produce a current and this is well known and understood phenomena. For hybrid systems, there is a difference in carriers and how they are created and how they move to create current. In addition, the hybrid perovskite systems are p-i-n junctions and these behave differently than a p-n junction. For hybrid perovskites, the charge carriers are excitons and polarons are shown in figure 1-11.

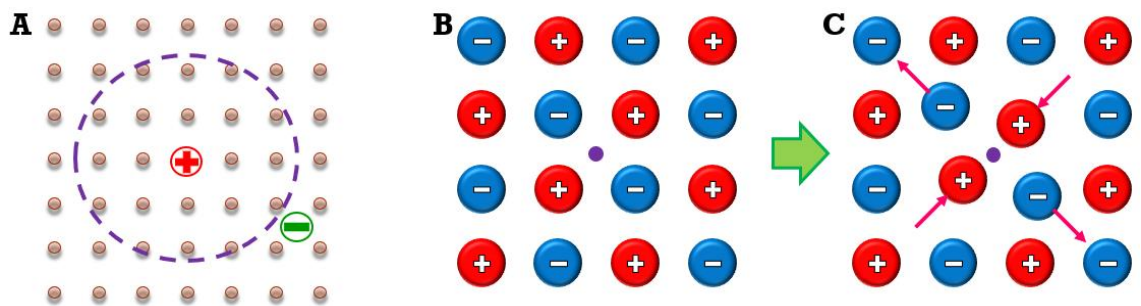


Figure 1-11: Charge carriers in perovskite solar cells. A) An Exciton charge pair. B) and C) The effect of an electron (purple dot) on a crystal lattice creating a polaron in C).

### 1.6.1 Excitons

Excitons are coupled charges that are created when a phonon interacts with the crystal. These are electron and hole combinations and they move through the crystal lattice as a coupled pair and are considered quasi-particles[77]. There are two types of excitons, Frenkel excitons that are charged pairs localized at a position in the crystal

lattice and Wannier-Mott excitons that are a coupled pair that diffuse through the lattice.

Exciton density and contribution to the current is depended upon the lifetime of the exciton[78]. For excitons, the life times are measured in their dissociation time. Hence, short lifetime excitons are quickly separated into holes and electrons and longer lifetime excitons move together as the quasi particle. Figure 1-12 highlights the effect of exciton lifetime on the density of excitons. Short life time excitons are created ( $x=0$  in figure 1-12A) and the concentration falls off exponentially meaning less excitons diffuse to the contact. As to be expected from this behavior, the contribution to the total current  $J_p$  is negligible (figure 1-12C). This type of device is known as an excitonic solar cell. In the opposite scenario, long life excitons build in density at the contact ( $x=300$  in figure 1-12B) and as a result, the contribution to the total current is significant (figure 1-12D). These types of devices are known as bipolar cells. Excitonic transport devices are not influenced by voltage biasing as excitons are a neutral quasi particle. As a result, perovskites are bipolar p-i-n devices and are influenced by external fields [78].

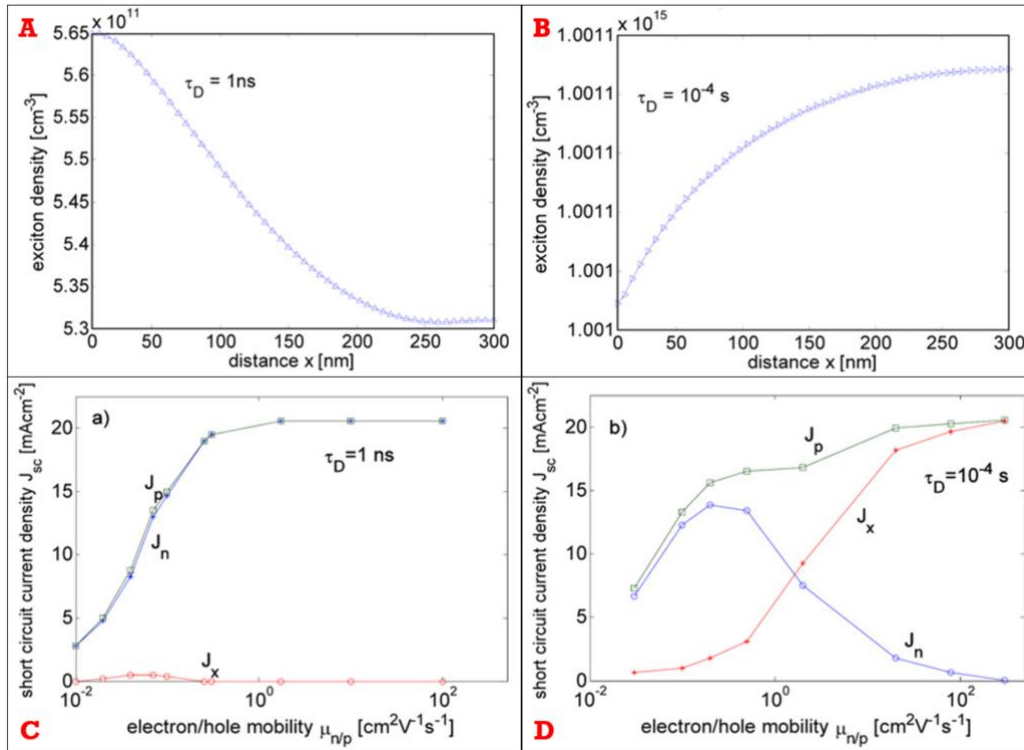


Figure 1-12: Exciton lifetimes and the effect on current density. A) Short lifetime, B) Long lifetime, C & D) Contribution to the current observed [78].

Excitons are not free to generate and require energy to generate. In one modeling study, the binding energy of excitons were calculated using a simulation using different models for the excitons and are shown in figure 1-13. The interesting result from this work is that the excitons have a binding energy greater than  $kT$  (at 300K is  $\sim 25.9 \text{ meV}$ ). Thus in order to operate, the excitons must quickly dissociate into hole and electron polarons[69] or the excitons would be created and unable to move at room temperatures. This model keeps supports the bipolar theory of perovskite functioning.

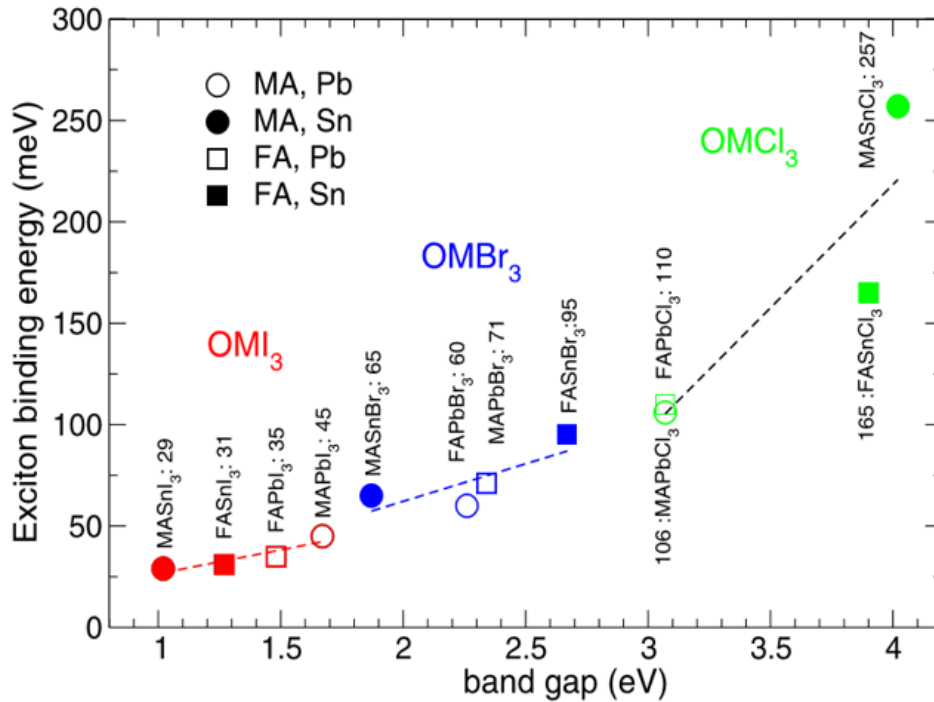


Figure 1-13: Exciton binding energies as function of bandgap [69].

### 1.6.2 Polarons

Polarons are quasi-particles that are used to describe the interaction of electrons with atoms in a crystal lattice. The interesting feature of a polaron is shown in figure 1-11 A and B shows that the polaron causes a distortion in the crystal lattice caused by an electron created in figure 1-11 B. This distortion is caused by the charges on the cation and anion species within the lattice. The creation of polarons in a crystal lattice influences carrier mobilities due to coulombic forces arising with the electron in the crystal matrix. Thus, for an electron to move through the crystal, the lattice must distort to enable transport.

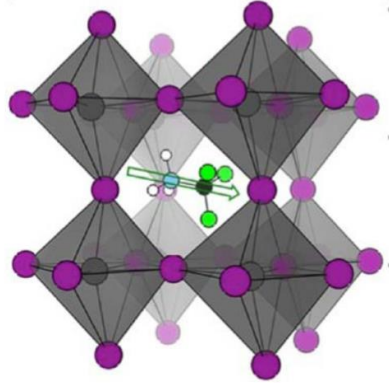


Figure 1-14: Structure of  $\text{CH}_3\text{NH}_3\text{PbI}_3$ , Colors are as follows: Grey- Lead (Pb), purple the halide (I) and green the organic ( $\text{CH}_3\text{NH}_3$ ) with a dipole moment indicated by the arrow from [79].

The distortion caused by the polaron and the need of the crystal lattice to flex to allow movement of the polaron results in the lower mobilities measured on perovskite solar devices [79]. To explain the modest mobilities in perovskites, polarons are modeled as having large masses [79]–[81]. In one model, the large mass polarons are due to the possible dipole created by the organic portion of the perovskite within the crystal lattice[79]. The effective masses are estimated to be in the range of  $10m_e \sim 300m_e$  [79], [82] with a volume of 3-6 unit cells ( $\sim 900 \text{ \AA}^3$ ). The advantage of the large polaron is that the carriers are protected from defects and phonons which cause scattering in other materials [80].

In an alternative study, polarons seem to be more contained at the interfaces, especially holes[69]. The abundance of polarons at the interfaces reduces the need of the dipole stabilization mentioned previously. Regardless of the stabilization effect, charged polarons are separate in the crystal matrix (either in the bulk or at the

interfaces). This separation helps explain the high lifetimes and diffusion lengths observed in these materials[69].

Regardless of the modeling of polarons are the unique charge carrying species within perovskites. The heavy masses predicted by model to explain the slow mobilities of carriers provide benefits to the perovskite. It should be noted, that higher mobilities were obtained when a single crystal perovskite were used[82] which would support interfaces influencing the polarons. The heavy mass allows the polaron to be less effected with scatter centers from defects and phonons. This enables the polaron to have high lifetimes and diffusion lengths while explaining the low mobilities all good traits for a solar cell [69], [77], [79]–[84].

## 1.7 Structure of the cell

The solar cells under investigation are built on standard glass substrates with a patterned coating of a transparent conductive oxide (TCO) acting as the anode. The structures under investigation here use indium tin oxide (ITO) as the TCO. For many devices, there is a choice for the anode, including fluorine tin oxide (FTO). FTO currently outperforms ITO for many solar cell applications [85]–[87]. The energy level of FTO is slightly less than ITO, 4.4eV vs 4.7eV [87] which helps in hole extraction efficiency resulting in much better  $J_{sc}$  currents for FTO over ITO [85]–[87]. The use of  $TiO_2$ , which requires a high temperature sintering process also drives the use of FTO over ITO in standard n-i-p devices[88]. However, the use of ITO has favor with the inverted p-i-n structures like those used in this work [10] as the systems are typically not heated.

Figure 1-15 shows the energy band alignments of the materials used in this work in relationship to MAPBI.

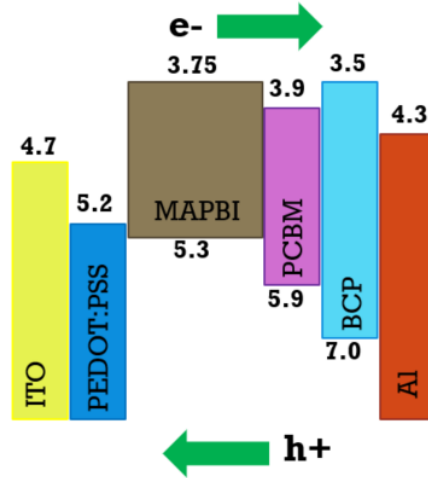


Figure 1-15: Energy band alignment for the materials used in this work relative to MAPBI perovskite film.

Poly(3,4-ethylenedioxythiophene) polystyrene sulfonate (PEDOT:PSS) is used as the hole transport layer (HTL) in this work. PEDOT:PSS has the advantage of being low cost and easily deposited via spin coating. Other more effective HTL are available such as octakis (4-methoxyphenyl)-9-9'-spirobi[9H-fluorene]-2-2',7,7'-tetramine (spiro-MEOTAD) and poly(triaryl amine), poly[bis(4-phenyl)(2,4,6-trimethylphenyl)amine] (PTAA) [10] to name a few, however the inverted structure limits the use of spiro-MEOTAD as perovskite cannot be spin coated onto this layer. However, PEDOT:PSS can be doped or modified via simple methods such as addition of solvents [89][90] or ammonia[91] to modify the pH level of the surface and increase the current output.

The next layer in the structure is the electron transport layer (ETL). Currently, the most popular ETL for perovskite materials is  $\text{TiO}_2$  [10]. Other popular choices include

SnO<sub>2</sub>, NiO<sub>x</sub> and ZnO, however ZnO has stability issues when used[9] and has fallen from favor despite excellent electrical properties. The use of the inverted device structure limits the choices of ETL as the deposition method must not damage the perovskite layer it will be deposited upon. In this work the use of C<sub>60</sub> and C<sub>71</sub> fullerenes were used to construct devices. The use of C<sub>60</sub> and C<sub>71</sub> fullerenes are a good choice for perovskites as fullerenes can be deposited either via spin coating (dissolved in chlorobenzene) or via evaporator. Fullerenes have great band alignment with the MAPBI films allowing for excellent electron collection, high mobilities and conductivities all contributing to higher J<sub>sc</sub> [92].

Hysteresis is modeled to occur in perovskites as a result of ion migration. As mentioned above, polarons and ions migrate under bias, resulting in a buildup of charges at the interfaces with the ETL/HTL [73]–[76]. Once the bias is reversed, the accumulated charges impede the flow of carriers resulting in the hysteresis seen in many perovskite devices. In the test structure under investigation, the use of fullerenes have been shown to reduce hysteresis[93][94] in the inverted structure. The model for reduced hysteresis is based on the migration of the fullerene into the perovskite grain boundaries and passivating defect sites [93].

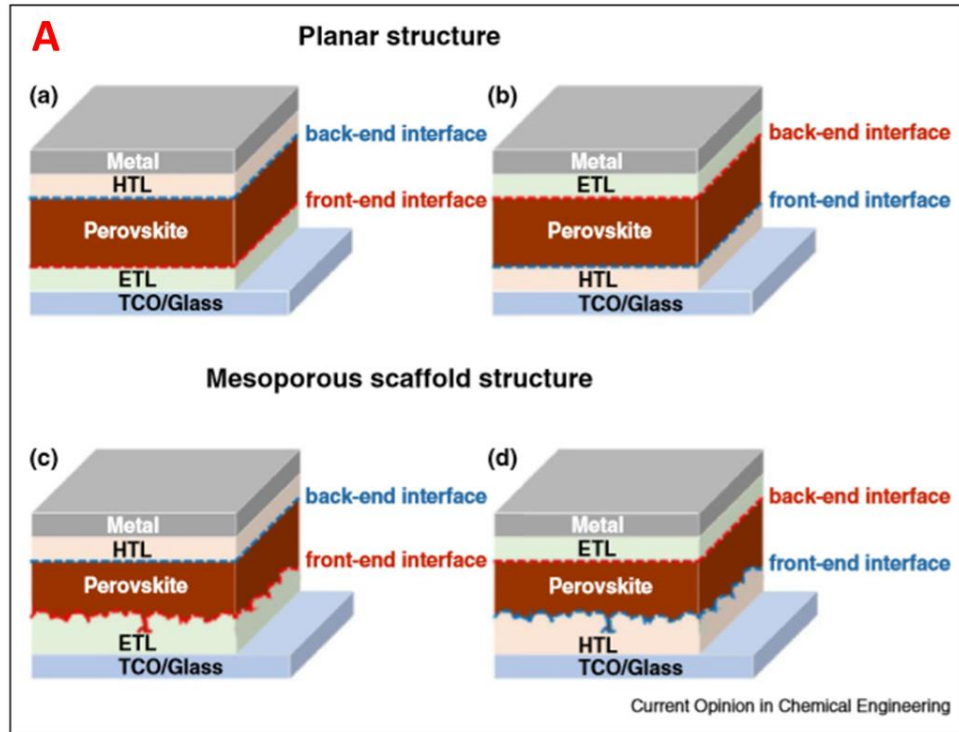
The next layer used is bathocuproine (BCP) in the layer stack. BCP is an interfacial layer used at the cathode interface to reduce the gaps and voids that exist as a result of the nature of the polycrystalline perovskite film [95][96]. BCP is an ETL with a lower electron level than the fullerenes hence the use of BCP as the sole ETL would result in poorer performance[97]. Instead, the BCP creates a bridgework or pathway

between the perovskite and cathode metal that is not bridged by the fullerene by filling in the holes. Thus, despite the poor performance of BCP relative to the fullerenes, the addition of BCP allows for better overall contact and electron transport than what would exist with fullerenes alone based on the poor coverage of fullerenes on the perovskite.

The last layer used is the cathode. There are many options for materials such as aluminum, silver, gold and carbon nanotubes. Copper has also been tried, however the mobility of copper atoms leads to the creation of CuI salts which degrade performance in the perovskite cell. Silver possesses the highest conductivity of these materials while aluminum the lowest, however silver has a much higher cost. Aluminum is used in this research as the cathode for the perovskite layer as a cost consideration.

## 1.8 Device Overview

There are four basic device structures for perovskite devices as shown in Figure 1-16, n-type (n-i-p) and p-type (p-i-n) configurations built upon planar and mesoporous perovskite films as seen in figure 1-16A. The perovskite film acts as the intrinsic absorber sandwiched between an electron transport layer (ETL) and a hole transport layer (HTL). Figure 1-16B shows a small sampling of the high number of different device layer stacks of just n-type devices.



**B**

Interface type	Device structure	PCE %	$V_{OC}$ V	$I_{SC}$ mA/cm <sup>2</sup>	FF %	Lifetime* hours	
Front-end n-type	Meso FTO/TiO <sub>2</sub> /MAPbI <sub>3</sub> /Carbon	9.08	0.8	21.02	0.54	2000	
	FTO/TiO <sub>2</sub> /MAPBr <sub>3</sub> /PTAA/Au	9.3	1.1	12.31	0.69	2000	
	FTO/TiO <sub>2</sub> /ZrO <sub>2</sub> /5-AVA-MAPbI <sub>3</sub> -Carbon	12.84	0.858	22.8	0.66	1000	
	FTO/TiO <sub>2</sub> /MAPbI <sub>3</sub> /PDDPDBTE/Au	9.2	0.855	14.4	0.749	1000	
	ITO/TiO <sub>2</sub> /MA <sub>x</sub> FA <sub>1-x</sub> Pb(I <sub>x</sub> Br <sub>1-x</sub> ) <sub>3</sub> /spiro-MeOTAD/Au	20.8	1.16	24.6	0.73	800	
	IZO-PET/TiO <sub>2</sub> /MAPbI <sub>3</sub> /spiro-MeOTAD-t-bp-LITFSI/Au	12	1.02	16.8	0.69	600	
	FTO/TiO <sub>2</sub> /MAPbI <sub>3</sub> /spiro-MeOTAD/Au	15	0.993	20	0.73	500	
	FTO/TiO <sub>2</sub> /MAPb(I <sub>x</sub> Cl <sub>1-x</sub> ) <sub>3</sub> /spiro-MeOTAD/Au	4.2	0.64	18.3	0.36	435	
	FTO/TiO <sub>2</sub> /meso-Al <sub>2</sub> O <sub>3</sub> -IPFB-MAPb(I <sub>x</sub> Cl <sub>1-x</sub> ) <sub>3</sub> /spiro+buffer/Au	13.07	1.03	20.62	0.62	350	
	ITO/TiO <sub>2</sub> /FAPbI <sub>3</sub> /PTAA/Au	20.1	1.06	24.7	0.775	-	
	FTO/TiO <sub>2</sub> /MAPbI <sub>3</sub> /spiro-MeOTAD/Ag	19.71	1.086	23.83	0.76	-	
	FTO/TiO <sub>2</sub> /MAPbI <sub>3</sub> /spiro-MeOTAD/Au	18.36	1.094	21.21	0.78	-	
	Planar	ITO/TiO <sub>2</sub> -PCBM/MAPbI <sub>3</sub> /spiro-MeOTAD/Au	17.6	1.11	21	0.77	2300
		FTO/SnO <sub>2</sub> /(MAPbBr <sub>3</sub> ) <sub>0.15</sub> -(FAPbI <sub>3</sub> ) <sub>0.85</sub> /spiro-MeOTAD/Au	18.4	1.14	21.3	0.74	720
		ITO/TiO <sub>2</sub> /PCBB-2CN-2C8/MAPbI <sub>3</sub> /spiro-MeOTAD/Au	16.45	1.06	19.85	0.78	500
		FTO/SnO <sub>2</sub> /MAPbI <sub>3</sub> /spiro-MeOTAD/Au	16.02	1.11	22.83	0.64	500
		FTO/ZnO/MAPbI <sub>3</sub> /spiro-MeOTAD/Ag	14.99	1.08	20.04	0.7	500
		FTO/TiO <sub>2</sub> /MAPb(I <sub>x</sub> Cl <sub>1-x</sub> ) <sub>3</sub> /DERDTS-TBDT/MoO <sub>3</sub> /Ag	16.2	1.05	21.2	0.73	220
FTO/TiO <sub>2</sub> /MAPb(I <sub>x</sub> Cl <sub>1-x</sub> ) <sub>3</sub> /spiro-MeOTAD+Li-TFSI+TBP/Ag		12.66	0.974	19.7	0.65	168	
Front-end p-type		Meso FTO/TiO <sub>2</sub> /ZrO <sub>2</sub> /NiO/MAPbI <sub>3</sub> -carbon	14.9	0.917	21.36	0.76	100
		FTO/TiO <sub>2</sub> /Al <sub>2</sub> O <sub>3</sub> /Ni/MAPbI <sub>3</sub>	13.6	0.953	19.1	0.75	-
		ITO/NiOx/NiOnc-MAPbI <sub>3</sub> /PCBM/BCP/Al	9.44	1.0	14.65	0.64	-
	SnO <sub>2</sub> F/MAPbI <sub>3</sub> -NiO/PCBM/Al	1.5	0.83	4.9	0.35	-	
	Planar	ITO/NiOx/MAPbI <sub>3</sub> /ZnO/Al	16.1	1.01	21	0.76	1440
		FTO/NiMgLiO/MAPbI <sub>3</sub> /PCBM/Ti(Nb)Ox/Ag	16.2	1.072	20.62	0.748	1000
		ITO/PEDOT:PSS/MAPbI <sub>3</sub> /ZnO ALD/Ag	16.15	1.02	20.73	0.76	960
		ITO/PEDOT:PSS/MAPb(I <sub>x</sub> Cl <sub>1-x</sub> ) <sub>3</sub> /PCBM/BCP/Ag	15	0.99	20.8	0.73	720
		ITO/PEDOT:PSS/MAPbI <sub>3</sub> -D/PCBM/MUTAB/	16.5	1.03	20.06	0.8	360
		ITO/Cu:NiOx/MAPb(I <sub>x</sub> Br <sub>1-x</sub> ) <sub>3</sub> /PCBM/C <sub>60</sub> -SAM/Ag	15.4	1.11	19.01	0.73	250
		ITO/Cu:NiOx/MAPb(I <sub>x</sub> Br <sub>1-x</sub> ) <sub>3</sub> /PCBM/Ag	14.98	1.11	18.75	0.72	250
		ITO/PEDOT:PSS/MAPbI <sub>3</sub> /PCBM/Ca-Al	18	1.03	20.6	0.85	96

Figure 1-16: A) Basic structure of a perovskite solar device showing planar and mesoporous structures with n-type and p-type configurations. B) Table of different layer stacks in producing perovskite solar devices [10].

In the most common n-type device (a in figure 1-16A), an ETL is deposited upon a transparent conductive oxide and this acts as the growth layer for the film stack. This configuration defines the front-end as the TCO-ETL-perovskite and the back-end as the perovskite-HTL-anode. The anode in most cases is a metal such as aluminum, gold or silver. In the p-type structure, these interfaces are reversed, that is the front-end interface consists of the TCO-HTL-perovskite and the back-end as the perovskite-ETL-metal. The basic requirements for ETL and HTL layers are as following: 1) energy level matching, 2) easy carrier transport from perovskite to anode/cathode, 3) low optical absorption, 4) mechanical flexibility and finally 5) low cost [10].

One feature to notice in the Figure 1-16B is the difference in ETL and HTL layers between n-i-p and p-i-n devices. The reason for the difference in these layers is that the order of the processing steps matter in the construction of the device[10]. An organic HTL such as spiro-MeOTAD (and other organic transport layers) cannot support the growth of a perovskite film as film growth requires a hydrophilic surface. The growth of transport layer films is the challenge of depositing  $\text{TiO}_2$ , ZnO and/or PEDOT:PSS which either utilizes high temperatures which decomposed the perovskite film or uses solvents which can dissolve the perovskite film [9]. Thus, while a wide selection of ETLs and HTLs are available, solvents, hydrophilicity, and temperature dictate their use, structure and placement on perovskite films.

As can be seen from the table in figure 1-16B, the most popular ETL layer is  $\text{TiO}_2$ . However, ZnO has much better properties transport properties as an ETL than  $\text{TiO}_2$  [10],

however ZnO based perovskite films tend to decompose at a higher rate than TiO<sub>2</sub> based films. Work done previously at Texas State demonstrated an annealing processing step that could improve thermal stability of ZnO-perovskite layers[9]. Later work showed that the hydroxide groups found on the ZnO contributes to the decomposition of the perovskite deposited on ZnO and small buffer layers had little effect in preventing decomposition[98] while larger layers created insulating layers, impeding device operation. Thus, the annealing processing step was as at least as effective in reducing decomposition as an additional layer.

### 1.8.1 Deposition Methods

Perovskites have a huge advantage over other solar devices in one area while they are similar in performance/efficiencies to other devices, they are the clear winner in terms of production costs. There are several ways to produce a perovskite thin film such as spin on substrates, slot die casting, solution based processing and evaporative methods as shown in figure 1-17. All these methods are much more cost effective than similar thin film technologies.

These processing methods show the real advantage for perovskites: inexpensive, low temperature atmospheric deposition processes. The perovskite devices can be grown on several different substrates and lattice matching is not required for a functioning device.

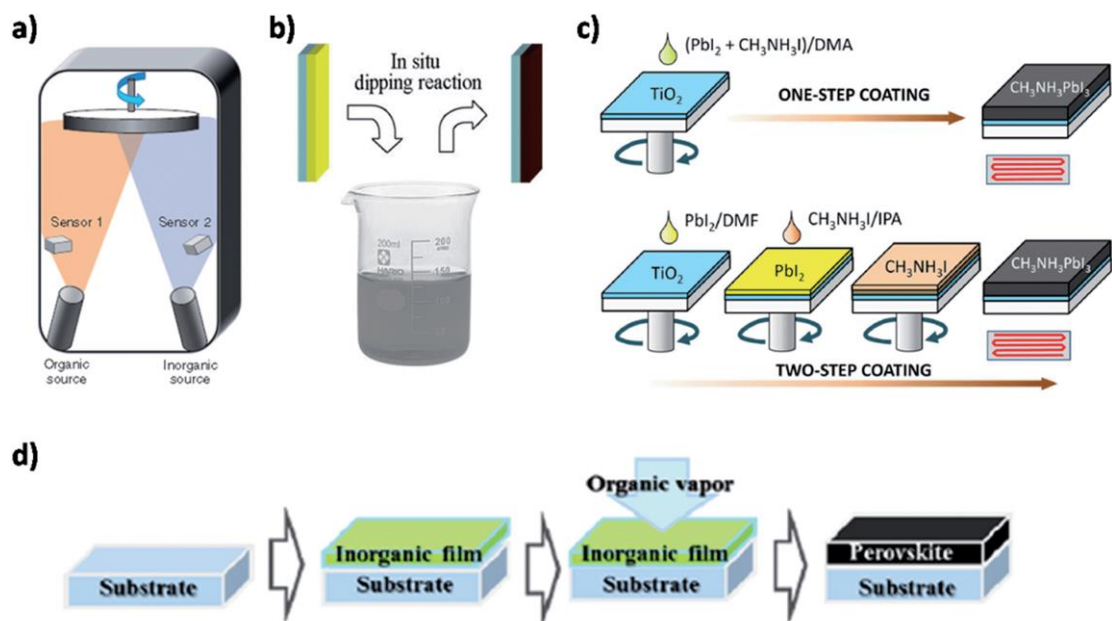


Figure 1-17: Assortment of deposition techniques A) Vacuum deposition, B) Dip method, C) Spin coating and D) vapor deposition [82].

Currently spin coating is the dominant method for depositing a perovskite film, and there are several different techniques within spin coating. The first is a one-step spin coating, where the  $BX_2$  and  $AX$  materials are dissolved in a solvent. The materials are then deposited onto the substrate and then spun at high speeds to mix and remove the solvent resulting in the formation of the  $ABX_3$  film. The second technique is a two-step method in which the  $BX_2$  portion is deposited/grown on the substrate. The  $AX$  portion is then deposited on top of the  $BX_2$  film and spun to mix and remove the solvent, creating the  $ABX_3$  film. A third technique is the use of acetate adduct method in which methylammonium acetate (or formamidinium acetate) is added to the ink and the system deposited as a one-step coating. The last technique used is a solvent engineering method. Here, a one-step ink in DMF or DMSO (or a combination of the solvents) are prepared and spun on as a one-step ink, however, in the last seconds of the spin coat, a second solvent,

chlorobenzene, for example, is added to the spinning substrate adding a evaporation cap, slowing solvent removal rates and allowing for better crystal formation.

The biggest challenge with spin coating is controlling crystal growth. The one-step technique requires the crystals to grow while the solvent is being removed. This presents problems as crystals tend to agglomerate creating a plethora of crystal sizes and film coverage problems [99], [100]. An example of the difference that film coverage and crystal growth have on perovskite performance can be seen in figure 1-18. The large crystals shown in figure 1-18a should perform better, however the poor film coverage limits conversion efficiency. In contrast, the small crystals in figure 1-18c, have good film coverage, but a high concentration of defects preventing high efficiencies.

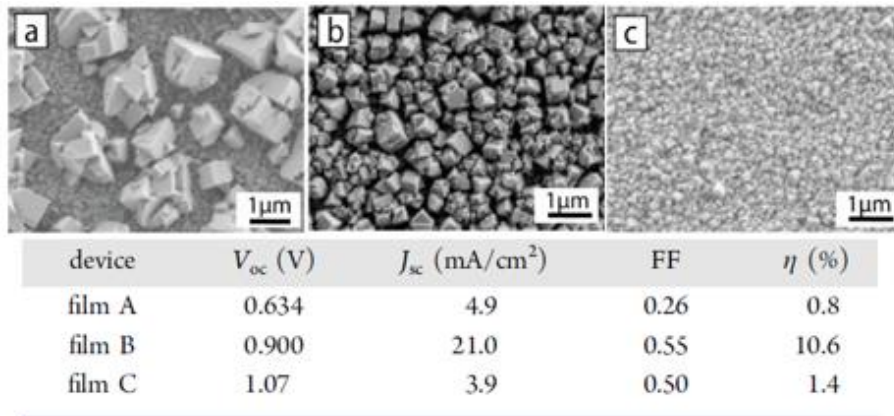


Figure 1-18: SEM images of as deposited perovskite film showing crystal sizes and film coverage and their corresponding device performance[99].

The two-step technique attempts to address these issues by having the AX<sub>2</sub> film act as a scaffold for growing the perovskite. The result is better uniformity since the perovskite crystals are growing from a scaffold and not from a liquid suspension. The

disadvantage of this method is that  $AX_2$  film thickness must be kept thin or the BX deposition step will not completely diffuse into the  $AX_2$  film, leaving unreacted  $AX_2$  at one interface and unreacted BX at the other interface which limits device performance. Hence, performance is driven by ability of BX precursor to diffuse into the  $AX_2$  matrix.

The acetate adduct and solvent engineering techniques look to allow maximum time for the crystals to grow by reducing primary solvent evaporation. The acetate adduct method is the easier of the two methods to properly perform, however, lab results at Texas State shows that the acetate salt can become part of the crystal. The solvent engineering method prevents incorporation into the crystal, however, the addition of excess counter solvent at the end of the spin cycle is a skilled art to perform properly leading to more variation in the outcome of the devices.

The downside to spin coating techniques (and all atmospheric methods) is that the resulting film is highly disordered. The high disorder of any film contributes to the increase in defectivity seen in materials. In particular, disordered films suffer from multiple interface surfaces due to grain boundaries, increased crystal defects and a higher number of intrinsic defects that degrade the performance of the device [55], [100]–[102].

In order to combat both the coverage and crystal size issues, many researchers have turned to other solvent engineering techniques [100], [103]–[106]. In these cases, other solvents or chemicals are added to the deposition process which effects the crystal growth. For example, halogen acid additives (HCl, HI, HBr) can be added to the

spin coating solvents improving film coverage and crystallinity[106]. However, it should be noted that adding HCl or HBr to the solvent increases the likelihood of a mixed halide perovskite ( $\text{ABl}_{3-x}\text{Cl}_x$  or  $\text{ABl}_{3-x}\text{Br}_x$ ) which modifies the bandgap and performance of the device.

After the deposition of the perovskite, the perovskite needs an annealing step to help drive off the solvents used in keeping the precursors in solution. The annealing process is also a factor in device performance[57] and improper annealing can lead to device reliability issues. The team at Texas State has reported on a modification to the annealing step for perovskites grown on ZnO substrates that helped improve the thermal stability of the devices [9].

### 1.8.2 Planar vs Mesoporous Structure

Perovskite solar devices have two primary structures, mesoporous and planar, and two secondary structures known as p-type or n-type [10] and are seen in figure 1-19. The mesoporous structure has to date the highest efficiency currently at over 20% using an n-type mesoporous structure. The best planar device is also an n-type device with an 18% efficiency[10]. The advantage of the mesoporous device structure over planar has been attributed to shorter electron diffusion lengths in the mesoporous films compared to planar films as well as possible incomplete conversion of starting materials into planar perovskite films [107]. An interesting note on device performance, mesoporous films currently out perform planar films even with the same film stack [10], [107].

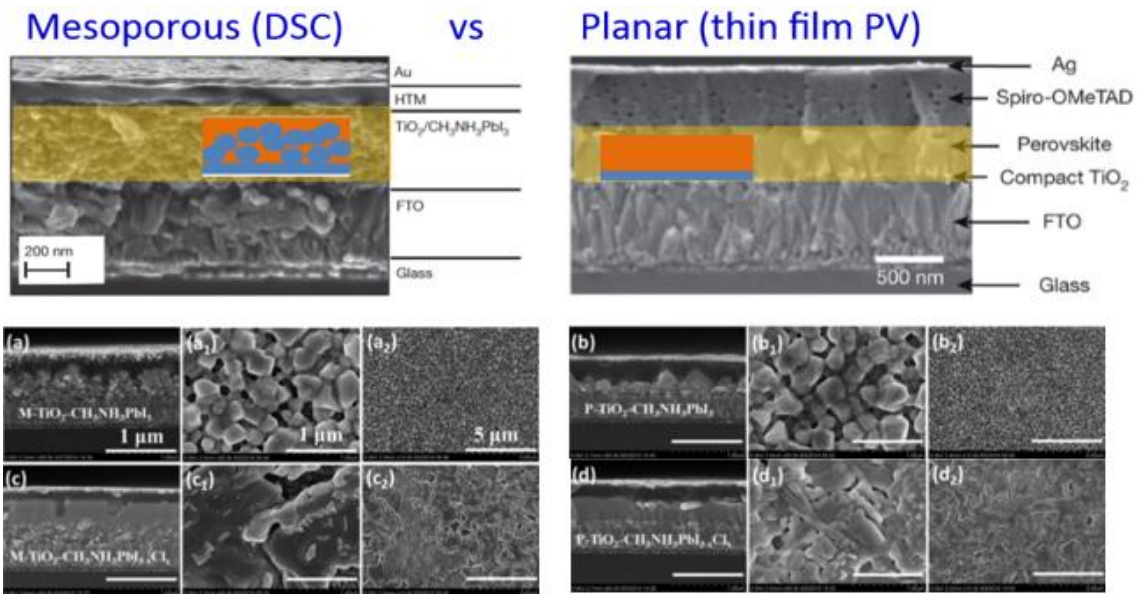


Figure 1-19: SEM Images of mesoporous films, left and planar films on the right [107], [108].

The fact that mesoporous devices outperform their planar counterparts contribute to the potential benefit of perovskite devices. Mesoporous films are much easier to construct than planar films and are a primary reason for the cost advantage of perovskite devices [8].

### 1.8.3 Hysteresis

Perovskites have also shown a strong hysteresis problem which is hampering the commercialization effort of these devices [57]. Hysteresis is the phenomena seen while tracing the current to voltage relationship of the cell and seen in figure 1-20. The large difference, depending on whether the potential is decreasing or increasing represents a design challenge to engineers as well as an efficiency problem [109]. This is since power output from the device depends on how the device gets biased, so an increasing load

requirement would result in less power output, while a decreasing load requirement would result in a greater output. While both problems are solvable with the correct circuit design, the solution adds complexity to the cell, increasing its cost. In addition, temperature and solar gain have been shown to create hysteresis in perovskite cells [109].

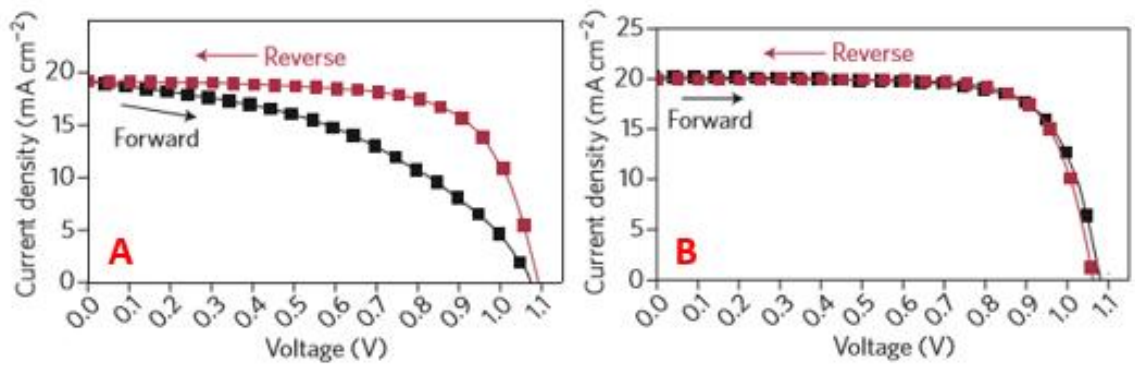


Figure 1-20: A) Hysteresis seen in a representative perovskite device and B) the ideal IV curve[109].

Hysteresis can be controlled with grain size, with larger crystals showing less tendencies to demonstrate hysteresis [100], [110]. While the causes of the hysteresis are still under investigation, it has been shown that higher defect levels and grain boundaries contribute to the hysteresis seen in perovskites [100], [110].

#### 1.8.4 Band Gaps

Within the ABX<sub>3</sub> perovskite crystal structure, it has been determined that the bandgaps of the perovskite solar devices are driven by the p-orbital differences between the B cation and the X anion, thus the band gaps are driven by the energy difference

between the lead atom and the halide (iodide) [55]. In addition, it has been shown that the A cation does not seem to contribute to the bandgap nor to the transfer of the phonons/electrons within the crystal [55].

At the present, there are two ways to tune the bandgap. The first way to tune the bandgap is to use a two-step deposition technique and vary the concentration of BX deposited onto the AX<sub>2</sub> film. This process has shown to reduce the bandgap of the CH<sub>3</sub>NH<sub>3</sub>PbI<sub>3</sub> perovskite from 1.7eV to 1.46eV while keeping an uniform crystal size of ~35nm [56].

The second approach is to use a mixed halide approach, that is, to create a perovskite with a AB(X<sub>z</sub>Y<sub>3-z</sub>) structure, where X and Y are two different halides. In the case of the perovskite CsPb(I<sub>x</sub>Br<sub>3-x</sub>) changing the fractional iodide concentration from 0.65 to 1.0, results in a reduction of the bandgap from 1.92eV to 1.76eV [57], [111]. In addition, the mixed halide perovskites have shown better stability over single halide versions [106].

### 1.8.5 Stability

Stability, as previously mentioned, is the Achilles' heel of these devices. PbI<sub>2</sub> based perovskites suffer from both thermal and moisture related stability problems. Solar devices need to survive operational conditions that routinely reach 85°C in operation environments. These devices also need to survive high humidity that can exist in those same operation environments

Humidity is a problem for all solar cells, regardless of type. Solar cells need to be protected from moisture damage to the cell as water vapor can corrode contacts, provide short circuit paths and reduce efficiency. The easiest way to combat humidity challenges is to encapsulate the device [112].

There are two ways that researchers attempt to encapsulate the perovskite. The encapsulation methods vary from a simple encasement of the entire cell, which is done here at Texas State, to altering the film stack by using different layers that operate as a water barrier [113]–[115]. The layer stack solution has been successful, however, there is a general decrease of device performance and increased cost and complexity with the use of these barriers. As there are several solutions to water incorporation into the cell, humidity is not a going concern giving the encapsulation techniques to prevent water penetration into the film and the fact that all solar cells are encapsulated to prevent water damage.

Of the two stability issues, temperature remains the most challenging reliability issue for the perovskite solar cell. Work done here at Texas State has already shown a simple method for annealing the perovskite that increases its lifetime under high temperatures [9]. As seen previously, crystal size also effects thermal stability with larger crystals showing better stability [116].

For thermal stability, work has also focused on changes in the layer stack, in particular with the ETL and HTL. The initial discovery of perovskite solar cells was made by groups looking at organic-inorganic systems, hence many of the devices have had

organic based layers acting as ETL and HTL such as spiro-MeOTAD, poly(3-hexylthiophene-2,5-diyl) (P3HT), poly[bis(4-phenyl)(2,4,6-trimethylphenyl)amine] (PTAA) and PEDOT:PSS. These organic layers as well as the methylammonium cation portion of the perovskite tend to decompose at elevated temperatures experienced at the upper operational temperatures of solar cells which has been calculated to be as high as 119°C [117], [118].

As a result, many have begun looking at carbon nanotubes, fullerenes and even eliminating the ETL/HTL layers to improve stability and have had some success in terms of stability [119]–[125]. At the present, the search for different ETL/HTL has not increased the device performance and in general a lack of stability testing still persists on many configurations [10]. This means that temperature stability remains a challenge for perovskite devices.

## 1.9 Device Structure

The solar cells used in this work are built on a glass substrate with a pre-patterned ITO coating as shown in figure 1-21. The ITO coating is  $15\Omega/\text{sq}$ , is 120nm thick and the glass slides are 25mm by 25mm, or one-inch square glass slides.

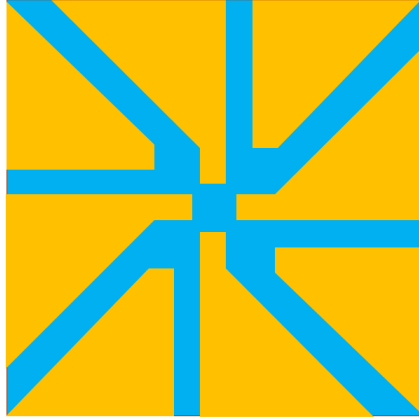


*Figure 1-21: ITO patterned glass substrate. ITO pattern is represented by the yellow portions of the figure and the blue being the underlying glass substrate. Note: Pattern is not to scale nor are colors correct.*

The devices are then built on this substrate creating 4 devices from the single substrate. Figure 1-22 shows a typical construction of a solar cell using a two-step deposition technique, however a single-step deposition would skip step #3. Figure 1-22 also shows a visible cartoon representation of what the substrate looks like after each processing step.

Using Figure 1-22 as a reference; in step 1 the substrate is cleaned. Step 2: PEDOT:PSS is spin coated to the desired thickness and annealed in ambient. Step 3: The first of the two-step deposition process, in this example,  $\text{PbI}_2$  is spin coated in a controlled atmosphere glove box with 0ppm of oxygen and water. In a single-step deposition process, this step is skipped. Step 4: The second deposition ink is spin coated creating the perovskite inside the controlled atmosphere. Samples are then annealed either in the controlled environment or in humidity-controlled atmosphere. Step 5: Samples have the ETL,  $\text{PC}_{70}\text{BM}$ , deposited inside a controlled atmosphere via spin coating and annealed. Step 6: The perovskite film is etched back using a manual

etch technique where the unneeded portions of the film are removed via a knife. The resulting film is a cross as shown in figure 1-22-6. Step 7: BCP is deposited at the desired thickness via a shadow mask with the pattern shown in figure 1-22-7. Thicknesses are controlled via quartz crystal microbalance (QCM) control within the evaporator. Step 8: Samples are then coated with a metal, in this case, aluminum is used and is deposited using the evaporator to the desired thickness. The pattern used is an 'L' which allows it to contact the ITO pads. Step 9: Substrate is removed from the evaporator and the devices are encapsulated via an UV cure epoxy and a glass slide cover resulting in an environmentally sealed device. Step 10: the devices are further etched using a knife in the areas shown in figure 1-22-10 and silver paste applied via a paint brush to enable good contacts.

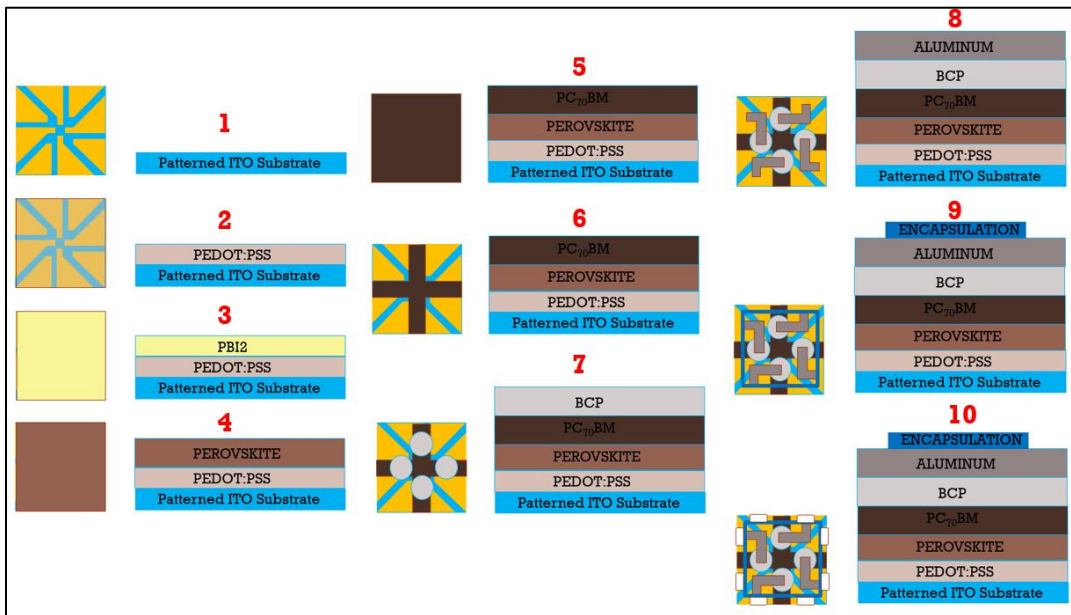
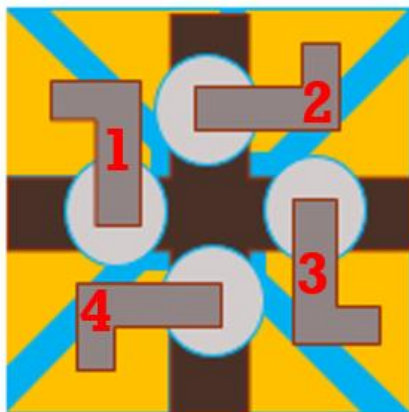


Figure 1-22: Solar Device patterning and film stack. See text for description of process steps.

The resulting sample has four devices as shown in figure 1-23. These devices have an active area of  $\sim 6.5\text{mm}^2$  each. The radial pattern of the devices helps reduce uniformity problems associated with spin coating techniques.



*Figure 1-23: The four devices on a typical solar device used in this research.*

## 1.10 Motivation for Research

While power conversion efficiency of perovskite PV is exceeding that of the other thin film PV technologies, stability remains the major issue. To address this challenge and to formulate a predictive model for the device reliability under stress (thermal, mechanical, electrical current cycling, UV, moisture, etc.) the fundamental understanding of the structure-property relations in organohalide lead perovskite is badly needed. Specifically, the role of the A - cation remains largely unknown.

Considerable research has been done in selecting cations. However, much of this work is done on satisfying the Goldschmidt ( $G_{\text{tf}}$ ) tolerance factor. Thus, the selection of a new cation for use in a perovskite structure focuses on the molecule size and not much else. The push here is to increase the  $G_{\text{tf}}$  factor of the perovskite material

to a larger value than that of MAPBI films. The overall hope is that device performance will remain while thermal and water stability improves.

The cation choice should have an impact on the perovskite device performance and the characteristics of the cation, relative to other one another, should allow for a prediction on the performance of the perovskite based on that cation selection.

The purpose of this work is to investigate the role of the cation in the perovskite structure. To understand the role of the cation, a difference is needed in the cation structure. Current perovskite like MAPBI and FAPBI use organic molecules made up of nitrogen and carbon. The challenge becomes the carbon and nitrogen are next to impossible to distinguish in a crystal lattice structure as is the case in current devices.

The current rise of alloys of different cation materials using cesium, methylammonium and formamidinium will be thus be used to investigate the role of the cation in the perovskite material. The addition of cesium will allow testing to judge how the incorporation of the size, mass and ionic nature of this atom has on the resulting perovskite material and its performance as a solar material.

To properly judge the resulting perovskite material, all processing conditions will be same, thus different ratios of the cation alloy will receive the same deposition conditions (same spin cast recipe), annealing and film stack, allowing then for the role in the perovskite structure to be elucidated.

The following techniques will be used to shed light on the role of the cation:

- Profilometry- this will give film thickness values
- AFM – crystal sizes, film coverage and surface roughness of resulting films
- XRD – crystal lattice types and ink conversion rates
- SEM – crystal sizes, film coverage
- UV-VIS – bandgap position
- EDS – chemical composition of the cation
- KPFM – work potentials and grain boundary information
- XPS – chemical shifts and the binding energies of the species in crystal lattice
- FTIR—chemical signature of the species as well as any shifts in bonding (vibrational) energies of atoms within the cation
- IV Curves – material performance as a solar device

The information gathered in this study will then be attempted to be modeled to predict how a different cation system will perform based on the mass, size and ionic nature of the cation species.

## 2. MEASUREMENT METHODS

In this work there were a variety of different measurement techniques to characterize the perovskite solar cell devices used in this work. One of the largest hurdles in the research in perovskite materials is the measurement techniques. Hybrid perovskite materials, especially the hybrid systems in this work, can degrade during measurement. Techniques such as scanning electron microscopy (SEM), energy dispersive spectroscopy (EDS), X-ray photoelectron spectroscopy (XPS) and X-ray Diffraction (XRD) which use high energy incident radiation sources can damage the sample, altering the results of the measurement [126]–[128].

### 2.1 FTIR

Fourier transformed infrared spectroscopy (FTIR) is an analytical technique that uses incident radiation in the IR spectrum. The IR spectrum includes wavelengths of light from  $12800$  to  $10\text{cm}^{-1}$  and is typically divided into three regions, the near infrared ( $12800\text{--}4000\text{cm}^{-1}$ ), the mid-infrared ( $4000\text{--}200\text{ cm}^{-1}$ ) and the far-infrared region ( $50\text{--}1000\text{ cm}^{-1}$ ). The most common measured region is the mid-infrared due to most molecules absorbing IR radiation at these wavelengths.

Infrared radiation causes bonds between atoms to vibrate and the wavelength are characteristic of specific bonds. Thus, the FTIR spectrum of a molecule provides information about the organic functional groups present in a molecule such as alcohols, ketones, amines and others. The IR energy changes the dipole moment found between bonding atoms as well as increases the vibrational energy of the bonds. Since each

bonding pair has the same energy, the resulting IR spectrum gives a unique fingerprint of a molecule.

A common FTIR setup is shown in figure 2-1. The incident light enters a Michelson interferometer where the light is split into two beams. The movable mirror then translates through the wavelengths and an interferogram is created by the detector. A Fourier transformation is then performed on the data to translate the interferogram into spectrum of wave numbers.

To aid in signal strength and detection for thin films an attenuated total reflectance (ATR) crystal is often used. The principle for ATR is that the incident beam is sent into the sample many times to boost signal strength. ATR enhances signal strength by allowing the incident beam to interact with the sample multiple times. The incident IR beam is sufficiently high power to allow multiple interactions despite having multiple absorption events, this increasing the signal to noise ratio. The ATR crystal and beam path are shown in figure 2-1.

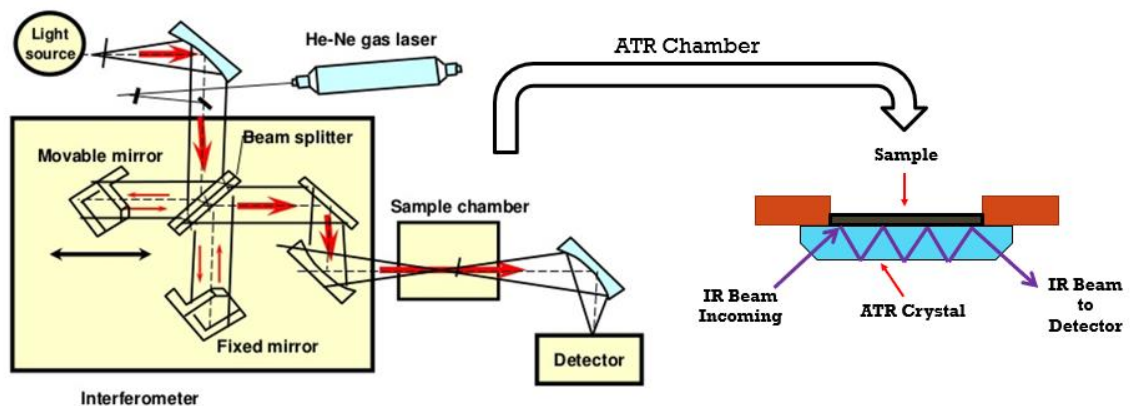


Figure 2-1: FTIR basic operation principle and beam amplification effect of the ATR system[129].

FTIR was used to analyze perovskite films grown using different methods. In particular, the one step methylammonium acetate method, the two-step methylammonium acetate methods and traditional two step lead iodide methods. Residual methylammonium acetate present in the final film could signal a different crystal compound. In addition, solvent-precursor complexes could be identified giving information on formation kinetics.

FTIR spectra were acquired using a Nicolet 6700 with a liquid cooled detector. Background spectra taken at the beginning and end to ensure no artifacts were introduced. Samples were taken using attenuated total reflection (ATR) mode which is common for analyzing thin films. Samples were torqued to the same setting for each sample.

## 2.2 SEM-EDS

Scanning electron microscopy (SEM) and energy dispersive X-ray (EDS) are two related techniques for producing information about a sample. The former produces images of samples down into the nanometer range while the later gives information on the elemental composition of the sample. The technique can also produce secondary electrons, back-scattered electrons and cathodoluminescence, however these other techniques require dedicated detectors which are not available with the system in use.

SEM is a high vacuum technique and samples need to be stable in high vacuum. For this technique, electrons are produced in an electron gun on the top of a large column. The electron gun is responsible for the beam current or the number of

electrons in the beam. The electrons are then gathered and accelerated in the condenser lens (see figure 2-2) which consists of a bias plate beam and magnetic fields. The bias plate is responsible for the final energy of the electron beam. The magnetic field or lens is there to align the beam as it travels the column as electrons are a charged species and an unmagnetized field would cause the beam to spread.

The beam then encounters the sample. Texas State's SEM-EDS system has three detectors: the backscattered electron detector, the secondary electron detector and the energy dispersive X-ray detector. The secondary electrons are among the shallowest energy emitted from a sample (Auger is the least), followed by backscattered electrons and then characteristic X-rays. Figure 2-2 has a reference for the sources of signals that arise when a sample is illuminated by an electron beam. Figure 2-3 shows the components of the SEM and EDS systems. Note, many SEM systems have a EDS detector to allow collection of this information.

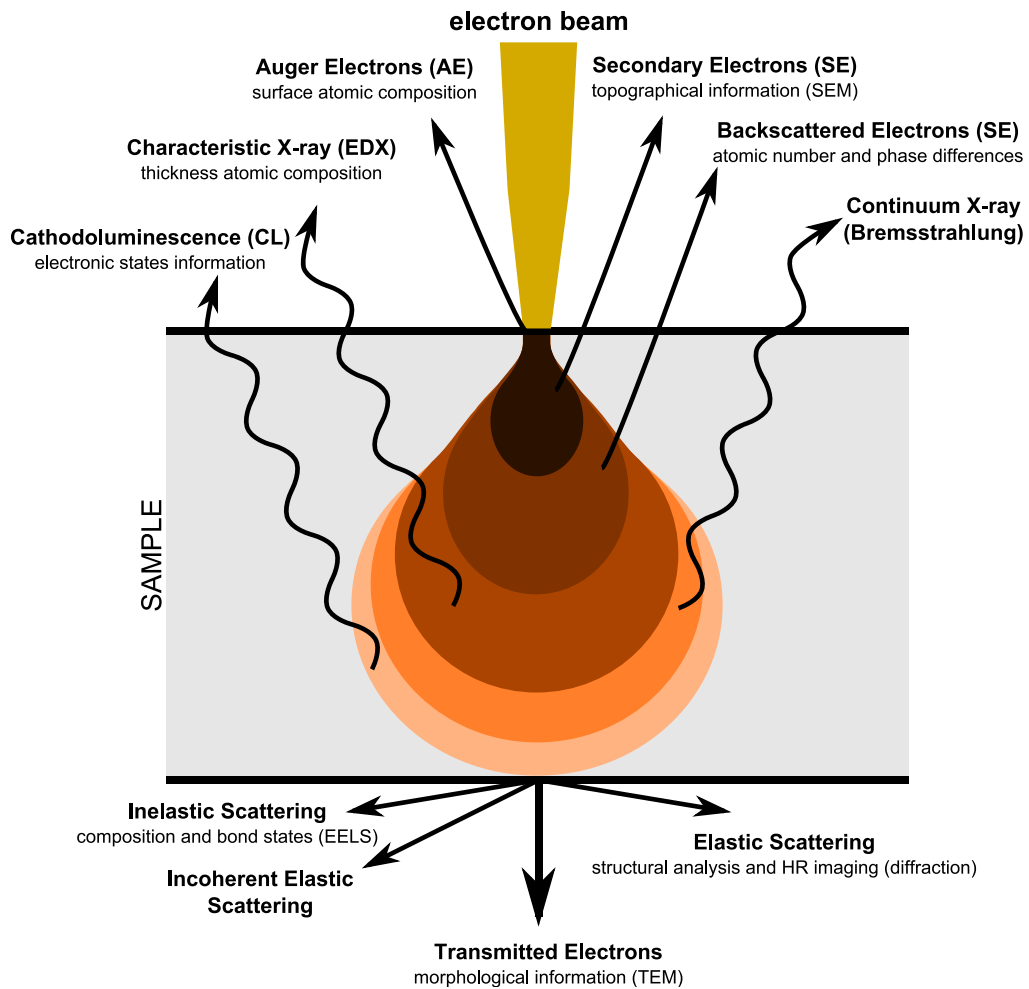


Figure 2-2: Incident electron beam radiation and the resulting emissions from the relative depth in the sample [130].

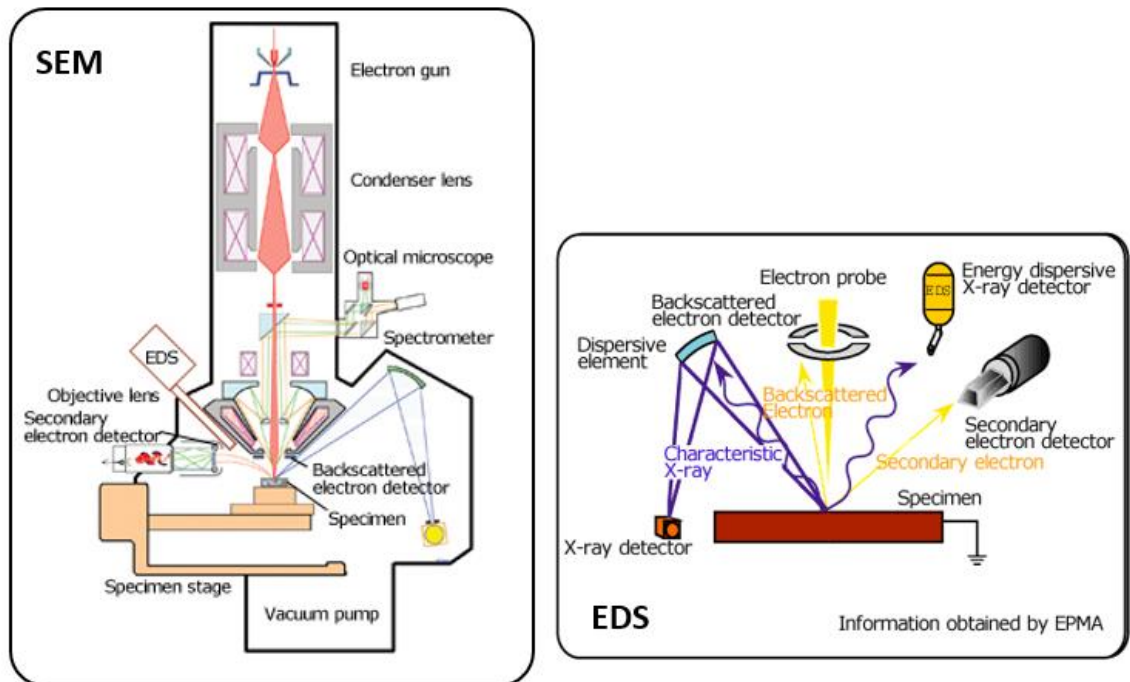


Figure 2-3: SEM and EDS systems for detection [131].

The SEM is typically used in imaging mode where secondary electrons are used to generate images of the perovskite sample. The information in the images gives indications of crystal quality and coverage. Backscattered electrons are seldom used in imaging of perovskites as the higher energy beam tends to damage the sample more than in secondary electron mode. Finally, EDS is used to help characterize crystals as to their chemical ratios. This helps judge whether the correct alloy compositions are present in the sample as well as if the imaged area contains perovskite decomposition products such as  $\text{PbI}_2$  or higher than expected amounts of organics.

Images taken using the SEM were done on a FEI Helios NanoLab 400 DualBeam field emission scanning electron microscope that has focused ion beam capabilities. The system has incident energy potential in the range of 350V – 30kV for the beam and has

image resolution in the nanometer range. The system is also equipped with an energy dispersive x-ray (EDS) system to provide elemental analysis.

### 2.3 XRD

X-ray Diffraction (XRD) is a spectroscopy technique that gives information on the crystal structure of a sample. XRD is unique in that the technique only gives information on structure of a sample, that is the crystal lattice. This information includes lattice spacing, crystal structure and crystal sizes (for polycrystalline material). XRD does this by illuminating a sample with X-rays at different angles and observing the scattered and reflected X-rays from the sample[132].

X-rays within a sample interact with the regular lattice spacing within the sample resulting in a diffraction pattern. The diffraction pattern behaves according to Bragg's law and the combination of rotation around the sample gives rise to the information needed to characterize a sample. Bragg's law is given by:

$$2d\sin\theta = n\lambda \quad (2-1)$$

XRD spectrum will have a series of peaks at certain values of  $2\theta$  which arise from the X-rays encountering many different planes of atoms and these signals combine constructively. There are only two unknowns in Bragg's law since the wavelength  $\lambda$  is determined by the wavelength of the source X-rays, leaving only  $d$  to be determined since  $\theta$  is measured/determined by the peaks[132]. Using the peak location, it is then possible to construct a series of Miller Index planes (hkl). From the Miller Indices it can

be determined which the crystal configuration type the crystal has and the lattice constant using simple math[132].

In this work, XRD was used for two main purposes. The first was in identifying the crystal lattice type and configuration. This is the basic operation of the XRD, create a spectrum of peaks for identification. The different alloys under investigation will have slightly different lattice constants and peak distributions. The second was to look for decomposition or incomplete conversion into perovskite. This was done by observing the absence or presence of the  $\text{PbI}_2$  in the spectrum.

XRD measurements were conducted using the Rigaku Smart Lab X-Ray Diffractometer using the Smartlab Guidance software. A Cu x-ray source operating at 40kV and 44mA was used as the incident radiation source and operated in the Bragg-Brentano high resolution configuration. The spectrum scanned with a  $2\theta$  range of 10-65°.

## 2.4 Profilometry

Profilometry is perhaps the simplest of the measurement techniques used in this work. In a profilometer, a small stylus is dragged across a surface and the deflection of the stylus both up and down gives a surface profile. Data from profilometry can reveal the surface roughness and topography of the surface. The limitation of profilometry is in the size of the stylus as a large stylus will miss much surface topography.

The system uses a diamond tipped stylus that is drawn over the sample per the a programable speed, distance and force[133]. Differences in the topographical features

are measured via the stylus linked to a linear variable differential transformer[133] (figure 2-4) which translates the small movements of the stylus into voltage.

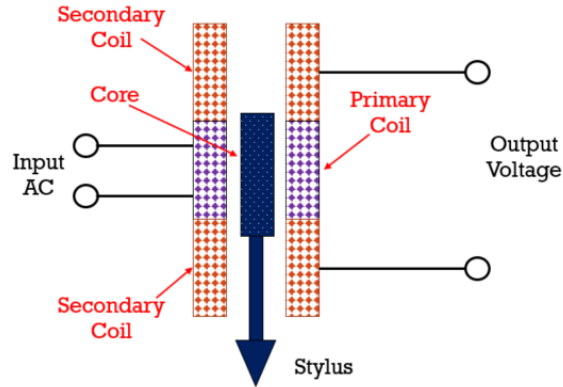


*Figure 2-4: Schematic of a linear variable differential transformer used to on profilometers.*

Profilometry was used to measure layer thicknesses for each of the layers used in this work. All layers were deposited upon a bare glass surface. The samples were then scribed down to the bare glass. The stylus was then moved across the scribe mark revealing the topographical feature of a trench. The depth of the trench was then interrupted as the thickness of the film. Several scribes were created in different places and a minimum of five measurements were taken and the results from the points were then averaged to obtain a film thickness.

The profilometer used in this work was the Bruker DektakXT with nanometer resolution utilizing a  $2\mu\text{m}$  tip radius using a stylus force of 3mg. Length of the measurement was between 500 and  $1000\mu\text{m}$  which was much larger than the trench scratched into the samples.

## 2.5 AFM

Atomic force microscopy (AFM) is a measurement technique that uses a stylus to measure the surface of a sample. AFM is a profilometry measurement and only differs from profilometry in the size of stylus, resolution and how the system measures surface topography. AFM systems also have a variety of other techniques that can be used to gather information beyond that in profilometry systems.

The biggest difference is in the size of the stylus used, in the profilometer the stylus is  $2\mu\text{m}$ . For an AFM tip, the tip has a radius of  $\sim 8\text{nm}$  (depending upon the tip used) resulting in a 1000-fold reduction in size. Depending upon the technique and tip size used, individual molecules can be resolved.

The measurement system for AFM differs as well. Whereas the stylus system uses differences in resistance as the stylus deforms over a sample, the deformation at this scale is not sufficient to produce a strong enough signal above the background noise. To combat this, a laser is used. The laser is reflected off the AFM cantilever into a 4-quadrant photo detector. The photo detector data is then interpreted by the computer to give information on cantilever movements and translated into surface topography.

There are two primary modes of measuring surface topography with an AFM, contact mode and tapping mode. Contact mode is the same mode used in the profilometry described above. The AFM tip is dragged across the sample and deflections in the tip movement is then processed into an image of the surface.

Tapping mode is the other mode to measure the topography of the surface. In this mode, the tip is oscillated up and down near its resonance frequency (the cantilever can be thought of as a spring) and is brought in close proximity of the surface. When in close proximity, Van der Waals forces, dipole-dipole interactions, electrostatic forces and magnetic forces interact with the oscillating tip changing the frequency. The change in frequency is then processed by the computer and the results displayed as the topography of the surface.

Regardless of modes, both tapping mode and contact mode can be used to effectively measure perovskite surfaces. AFM can give many of the same information as SEM, but in the case of perovskites, AFM does so without damage to the crystals.

The further advantage of AFM systems can be found in the forces that influence the tapping mode data collection and that those forces can then be used to get more information from a sample surface. Kelvin Probe Force microscopy (KPFM) for example is a technique that can measure the work function and surface potential. The technique uses a metalized or conductive cantilever and the tip or sample is then biased. Potential differences between the tip and the surface can then be measured. A related measurement technique used is called peak force tunneling AFM (TUNA) where instead of a potential measurement (voltage) a current profile can be measured.

In this work, AFM in tapping and KPFM were used to help characterize the perovskite system. AFM tapping gives information on surface topography including

crystal sizes, surface roughness and density of the crystals. KPFM was used to examine defect levels within the crystals and along the grain boundaries.

The AFM used in this work is the Bruker Dimension ICON. The system was used using the Scan Asyt software feature which enables the system to adjust measurement parameters via feedback information to produce images. The system was used in contact mode, tapping mode and KPFM using the following probes:  $\mu$ masch HQ-NSC14/AL BS.

KPFM was also performed on the NIST AFM system. The KPFM mode worked better on the NIST system than the Bruker for reasons not yet fully understood (believed to be an issue with the Bruker system). However, both systems should have yielded comparable results. The NIST AFM was used in the low voltage high sensitivity mode which reduced the scan area to  $\sim 1\mu\text{m}$ . Probe tips used was  $\mu$ masch HQ-NSC18/Pt.

## 2.6 UV-VIS

Ultraviolet-visible spectroscopy (UV-Vis) that utilizes light in the 190 to 1100nm wavelength range (UV and visible light) [134]. The technique is a simple one, a light source with an output spectrum in 190-1100nm illuminates the sample and is shown in figure 2-5. A detector then scans the wave lengths of transmitted or absorbed light and presents a plot of the resulting spectrum (intensity vs wavelength).

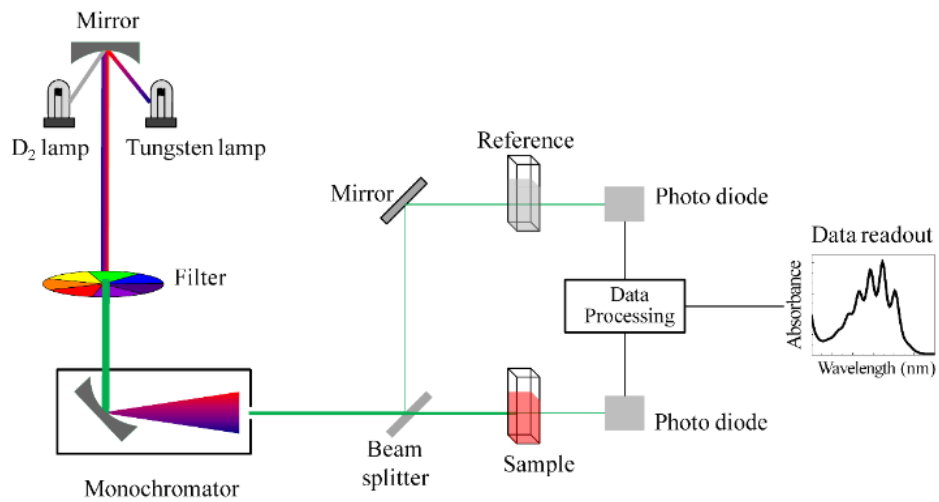


Figure 2-5: Cartoon of a UV-VIS spectroscopy system[135].

UV-VIS gives information on the electronic structure of the sample. This technique gives information on the ability of electrons within the sample to absorb the incident light and excite electrons between highest occupied molecular orbitals (HOMO) and lowest unoccupied molecular orbital (LUMO) states. For solar devices, this information reveals the bandgap of the device since the incident wavelength of light is related to energy via the relation below:

$$E = hc/\lambda \quad (2-2)$$

Where E is energy, h is Planck’s constant, c the speed of light and  $\lambda$  the wavelength. This measurement then gives the bandgap of perovskite materials used in this work.

The UV-VIS instrument used in this work was a Shimadzu UV-2501(PC) using a range of 200-900nm. This system has a resolution of 0.1nm with a beam height of

12mm and width of 1mm. A blank glass slide was used as the reference sample to account for any influence from the glass substrate during measurement.

## 2.7 XPS

X-ray photoelectron spectroscopy (XPS) is a technique that uses X-rays to generate a photoelectron response from the sample. The photoelectrons contained in the sample possess a binding energy to the orbital shell in which they reside. The energy of the emitted photoelectrons are unique to each element and the resulting spectrum can be used to identify the elemental composition of an unknown sample[136],[137]. XPS can give both qualitative and quantitative information about a sample[137].

In an XPS, incident monochromatic X-rays are incident onto a sample (See figure 2-6). The incident radiation incites photo emission of electrons from the orbital shell of the atom under X-ray illumination. These emissions are both characteristic of the element and are collected through electron optics and run through the energy analyzer on the tool before becoming incident on a detector where they are measured[136]. A characteristic of XPS systems is that they have a domed or half sphere energy analyzer to measure the energy levels of the photoelectrons. The energy analyzer is biased (the pass energy) and eliminates higher or lower energy photo electrons as a result. The input to the analyzer is (known as the electron optics) collects a portion of the emitted photoelectrons using magnetic lens and/or electrostatic lens. Resulting electrons are

collected at the detector and current systems give better than millielectron volt resolution.

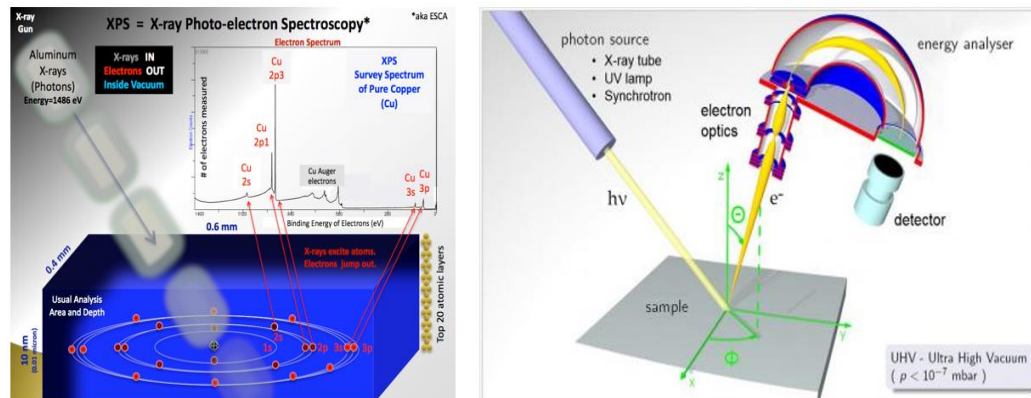


Figure 2-6: Cartoon of how XPS works with the x-rays interacting with the atoms electron orbitals and left the basic hardware setup highlighting the electron optics and the energy analyser[138], [139].

The power in XPS is that it can give information on the energy level of the bonds within a sample[137] known as the chemical shift. This is valuable information in crystal formation and can give insight into how stable a crystal can be and is used in this work to estimate the effects of the cation selection on the  $ABX_3$  perovskite cage. In particular, XPS is giving information on the effect of the cation on the lead and halide energy levels. This information will be used to examine effects on bandgap and potential crystal stability in an alloy matrix.

The XPS measurements were conducted using a high resolution Gammatdata Scienta SES-2002 operating in an ultrahigh vacuum and using SES software 1.2.5. A monochromatic Al x-ray source (1486.6eV, anode operating at 12kV and 150W) was used as the incident radiation source. Survey scans were done on each sample at a pass

energy of 100eV prior to the elemental scans. Pass energy for the elemental scans was varied from 20eV to 50eV depending on the sample.

## 2.8 IV Relation

The current-voltage curves (IV curves) were generated by measuring using a Keithley 2400 SourceMeter in conjunction with an Oriel ABA solar simulator with an AM 1.5G filter that is calibrated to a 100mW/cm<sup>2</sup>. The Keithley 2400 was controlled via a customer LabView program that sets the voltage sweep window and interval. The typical window used was voltage sweep between -0.1 to 1.1V. Current measured was depended upon the device under illumination. The system generates the IV relationship of the solar cell under AM1.5G illumination. This data gives the  $J_{sc}$ ,  $V_{oc}$ , Fill Factor and efficiency of each device.

Samples were measured in a custom designed and 3D printed device jig which allowed for fast measurements between the four samples. Currently, only one device can be measured at a time due to program constraints and jig setup. However, the use of a second Keithley 2400 SourceMeter and a separate LabView program allows for two devices to be tested simultaneously, although this was only used during lifetime testing.

Lifetime testing was also performed on alloys. The lifetime testing is performed while a device is under constant illumination for a period of several hours (days). There are three modes for lifetime testing, constant voltage, constant current or max power. Constant voltage keeps the device under  $V_{oc}$  bias at all times. Constant current keeps the device biased at max current (no bias). For max power testing, the device is kept

under bias conditions that reflect the max power. The LabView program collects IV relationships every minute for the first 10 minutes and then every 10 minutes thereafter till the program is stopped or the programmed number of sweeps is performed (user defined). All bias conditions mentioned previously are updated after each sweep.

### 3. COMMERCIALIZATION POTENTIAL

Perovskite solar cells are considered the holy grail of solar cells as they are a cheap, highly efficient and easily made solar cell. This characteristic is a common preamble to many research papers and states that the ability to make these cells with basic laboratory equipment in ambient conditions is a driving factor in the pursuit of solar cells.

Currently, perovskites are demonstrating the same kinds of efficiencies seen on silicon,  $\text{SiGe}$  and  $\text{CdTe}$  devices (>20%) which are widely available commercially. The key advantage of perovskites over other traditional solar energy power generation is the manufacturing costs of the panel. Perovskites need less expensive processing steps, such as the high vacuum processing steps that are needed for the silicon,  $\text{SiGe}$  and  $\text{CdTe}$  devices. In fact a recent study suggests that the cost of a similar perovskite solar cell would be 75% less than a traditional solar cell [8]. In addition, the amorphous nature of the perovskite absorber material further reduces material costs as less costly and pure starting materials are needed to form the absorber material.

The remaining hurdle is the long-term stability of perovskite solar devices. A recent review of the current devices show both a lack of long term testing and a uniform long term testing methodology[10]. As a new comer to the market space, perovskites have an inherent disadvantage when competing with other thin film technologies when it comes to lifetime testing. Other thin film devices have decades of results based on installation data coupled with lab-based testing, perovskites currently have none. As a

result, there will be a higher risk associated with deploying large scale terrestrial solar farms using perovskites given the lack of the 20 years of lifetime experience the other thin film technologies have.

The US market for solar cells was estimated to be \$4 billion USD as of 2015 and was projected to have a compound annual growth rate (CAGR) of 14%[140]. In fact, globally, the solar cell market is projected to reach \$100 billion by the year 2024. One of the driving factors in the fast growth rates is government investment in projects in nations like Brazil, India and in countries in many parts of Africa. These investments represent these nations’ efforts to bring clean power to their people. Add to this movement the recent decision by California to mandate solar cells on new builds and the state of the market is very good. Figure 3-1A shows the global growth rate of solar installation and 3-1B the US share of that growth.

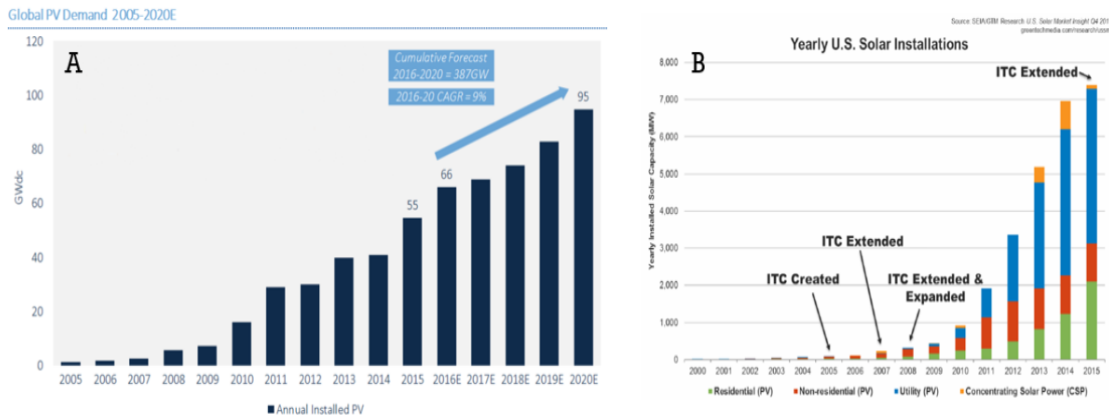


Figure 3-1: Growth of the PV market, A) Current and predicted global install base[140] B) Domestic market [141].

Because so many governments are mandating the use of solar, the market opportunity for perovskite solar cells becomes more viable. The reduced cost of manufacture can be appealing to many governments, especially in the third world, where cost is going to be a large factor in technology selection. Thus, large scale terrestrial installations can be viable given the government investment and the low cost and high efficiency of the cells compared to other thin film technology. There is still considerable risk in terrestrial installations, only since the reliability and lifetimes of perovskites are still unknown. A market entry similar to First Solar's [142] introduction of CdTe solar cells into the market place might be a viable, however, considerable investment would be required.

The best option for perovskite solar cells is the portable electronic market. The portable solar panel market is estimated to be around \$34 billion with a projected CAGR of nearly 86%[141]. Many potential markets are in this space including military hardware and smartphones/tablets being the most lucrative [143]. The best fit would be in portable chargers for cell phones. Cell phones have a replacement rate of about 26 months, with cell phone carriers looking to add upgrade cycle plans at 12 month periods [144]. This market would allow perovskite solar cells a fantastic opportunity to learn and earn as the portable electronic market has high product turnover rates meaning that there is little expectation that these devices should last more than a few years before the technology advances and makes the older generation obsolete. This reduces the risk to perovskite solar cell device manufactures as short-term devices pose

little risk. Figure 3-2 shows the forecasted sales and growth rate for the three largest portable solar generator companies, which shows good growth rates and demand.

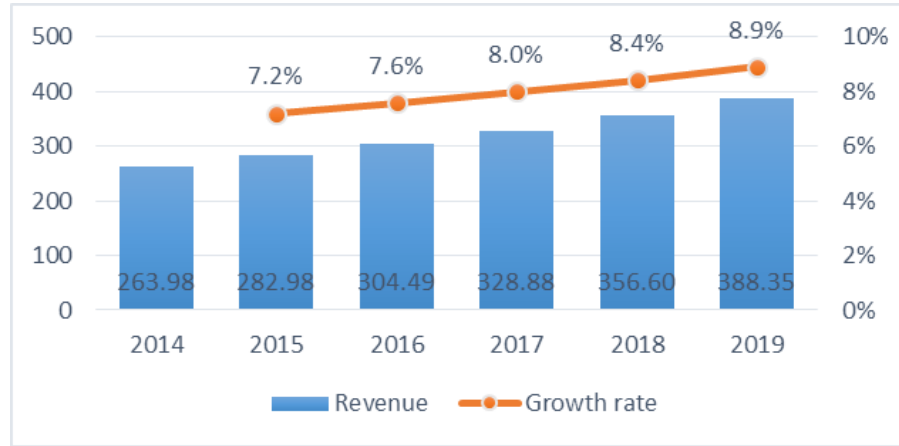


Figure 3-2: Growth rate for three largest portable solar generator companies [143].

Regardless of the ultimate length of ownership, the portable solar panel market is the best place to test perovskites for long term operation. Customers will have their devices in harsh conditions and a recycling program for obsolete products (driven by smart phone changes) can yield good data from usage. In addition, perovskite solar cells paired with a smart phone/tablet can also provide immediate feedback via data messaging (provided the customer agrees and can be made so by reducing the cost of the device in exchange for the data). Lessons learned can be applied directly into large scale terrestrial sized panels reducing the long-term risk for this technology.

Lastly, the importance of the new California law cannot be understated. The inexpensive nature of perovskite solar cells paired with the flexible and light weight substrates can be an answer to architectural problems incorporating solar cells into new

housing and building design. Panels can be made into any shape, allowing unique design elements to be incorporated into buildings. Reduced weight means less structure supports are needed, reducing building costs. Lastly, the use of perovskite paints to apply solar cells to the structure itself is also a possibility. Color choices would be limited to darker colors to take advantage of solar spectrum absorption, but other colors choices could be possible albeit at a cost of efficiency.

## 4. CHANGES TO DATA COLLECTION PLAN

The proposal for this work was to evaluate the role of the cation by examining systems of methylammonium and formamidinium based perovskite cells. Consirable work was done on the FAPbI systems, however, one issue remained. FAPbI perovskite systems are not thermally stable preferring to relax from an desirable  $\alpha$ -FAPbI phase to a  $\delta$ -FAPbI phase which happens at temperatures below 100°C [145]. The  $\alpha$ -FAPbI phase has a reported efficiency of over 20% [145].

However, it was observed that the transition between  $\alpha$ -FAPbI phase to a  $\delta$ -FAPbI phase happens too quickly in the labs at Texas State University to yield reliable data on the IV relationships and with most of the other measurement techniques used. The desirable phase could be recovered as shown in figure 4-1 using UV-Vis data by reheating the sample to 175°C. However, for SEM, AFM, XRD, XPS, FTIR, heated stages and constant heating of the sample are required and not possible. The evaporated steps of BCP and aluminum on devices take ~60 minutes and reheating of the finished device stack destroyed the devices. Thus in the observed ~15 minutes of time it took to transition from  $\alpha$ -FAPbI phase to a  $\delta$ -FAPbI phase, it was deemed that this approach was not feasible.

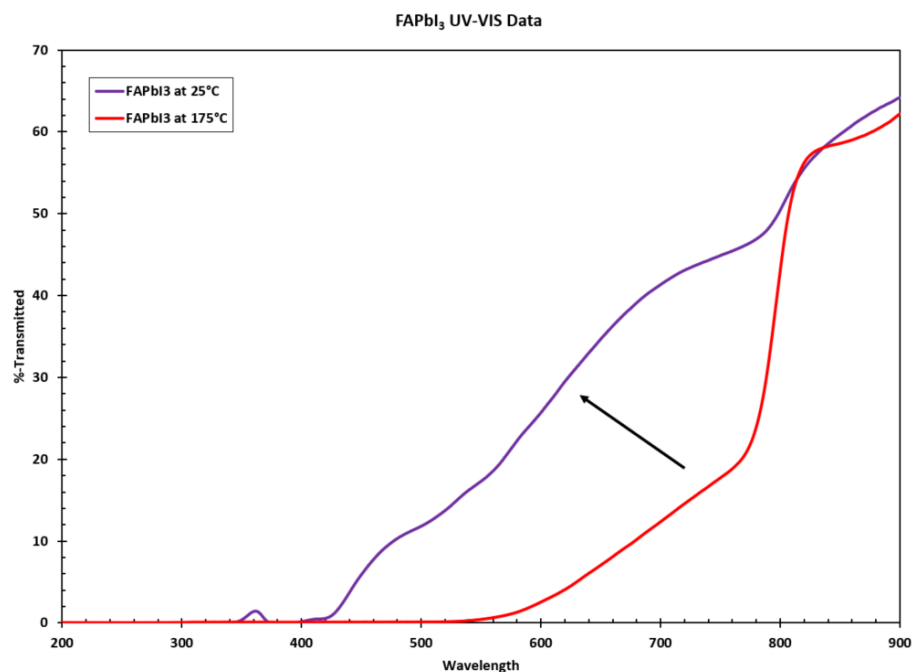


Figure 4-1: UV-Vis data showing  $\alpha$ -FAPbI<sub>3</sub> (175°C) phase to a  $\delta$ -FAPbI<sub>3</sub> (25°C) phase.

To combat this problem, an alloy was selected of cesium, methylammonium and formamidinium. This is a popular alloy[146] has the benefit as being room temperature stable. The second advantage this choice gives is the ability to investigate the cesium in relation to the lead and iodide. With the former choice, both organic cations contain carbon and nitrogen and few analytical techniques could distinguish between the two. Here, the role can be more readily examined in the alloys. The changes to the initial data collection plan are listed in table 4-1:

Table 4-1: Changes to the research plan.

Research Goal	Old Plan	New Plan
Maximize crystallite sizes	Optimize for each system	Each system (alloy) receives same treatment
Film coverage		
Optimization of film thickness		
Device Characterization	No change. IV curves and UV-VIS measured for each system	
Characterization of the interface	No change. Done via SEM, EDS and AFM	
Thermal Decomposition	Characterize thermal decomp	Not performed, alloy is stable to elevated temperatures
Defect Density Characterization	CL and KFPM	Done via KFPM
Energy Levels	Not performed	Done via XPS
Device Lifetimes	Not Performed	Measured through illuminated stress testing

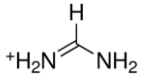
The increased device stability under elevated temperatures allowed for the use of XPS as a characterization tool for the perovskites, a first at Texas State. Furthermore, the higher temperature stable devices allowed for the testing of device lifetimes under constant  $V_{oc}$  biasing under illumination under AM1.5G.

## 5. CATION MEASUREMENT AND DISCUSSION

### 5.1 The Cations Overview

In this work, the alloys were constructed from cations of methylammonium (MA), formamidinium (FA) and cesium. Each of these cations have the same charge (+1) but have different electronegativities (dipole moments), sizes and compositions. Table 5-1 has a summary of the different basic parameters of the cations that are used in this work. For this work, the terms electronegativity and dipole moments will be used interchangeably. While technically incorrect as an atom, cesium in this case, cannot have a dipole moment, the electronegativity of cesium is being extended as a basis of comparison to the dipole moment of the MA and FA cations. This assumption is being used since electronegativity of each atom is used to calculate the dipole moments in a molecule.

*Table 5-1: Sample cation properties.*

Property	Cesium	Methylammonium	Formamidinium
Structure	Cs <sup>+</sup>	CH <sub>3</sub> -NH <sub>3</sub> <sup>+</sup>	
Size (pm)	298	217 [147]	253[147]
Dipole	--	1.54 Debye [148]	3.19 Debye[148]
Electronegativity	0.79 Paulings	--	--
Mass (g/mol)	132.91	32.07	45.06
Goldschmidt Ratio (based on pure cation)	0.807 Pure CsPbI <sub>3</sub>	0.911 Pure MAPbI <sub>3</sub>	0.987 Pure FAPbI <sub>3</sub>

## 5.2 Cation Role in Perovskites

The role of the cation's role in the perovskite is being evaluated in this work using an alloy system of methylammonium (MA), formamidinium (FA) and cesium. Current work on this topic has shown that an alloy of these cations has good stability and solar characteristics such as efficiency (PCE), open circuit voltage ( $V_{oc}$ ), short circuit current ( $I_{sc}$ ) and fill factor (FF)[149]–[152].

Work done at the National Renewable Energy Laboratory (NREL) is focusing on a one particular alloy composition for its current work in scaling perovskites from the lab to the fab. Using this alloy composition as a starting point, different alloy mixtures were then created to test the contribution of the cation to the system. Of the three choices of which to examine, cesium was the clear-cut favorite for further testing as the two remaining cations of MA and FA are comprised of the same species of carbon, nitrogen and hydrogen. As a result, when looking at the contribution or data from the carbon or nitrogen in the alloy, there would be no way to distinguish between the contributions from the MA carbon or the FA carbon.

Table 5-2 shows the alloy concentrations used in this work. The NREL system is listed and comprises a system of 5% Cs, 15% MA and 80% FA. A difference of Cs concentrations of at least 5% was used to show a measurable difference in the systems. As the FA was the dominated cation in the NREL system, effort was made to keep the FA composition as high as possible and not to drop the MA concentration below 5%. The resulting alloys are then described in table 5-2.

Table 5-2: The perovskite alloys used in this work.

<b>MA<sub>x</sub>FA<sub>y</sub>Cs<sub>z</sub>PbI<sub>3</sub>, (x + y + z = 1)</b>			
<b>System</b>	<b>Cesium Z</b>	<b>Formamidinium (FA) Y</b>	<b>Methylammonium (MA) X</b>
5%	5%	80%	15%
10%	10%	80%	10%
15%	15%	80%	5%
20%	20%	70%	10%
25%	25%	70%	5%
15% (70% FA)	15%	70%	15%

### 5.3 Spin Coating

The NREL alloy perovskite is deposited using a two-stage spin coupled with a solvent engineering step. The recipe and procedure are listed in table 5-3. This recipe is a two-stage spin recipe coupled with a solvent engineering step. As with many solvent engineering recipes, the solvent engineering portion, step 5, is as much art as it is science. As highlighted in appendix 9.2, the dynamic application of ink to the spinning sample causes many problems. Those issues with the dynamic application of ink also applies to the dynamic application of solvent. To better elucidate the role of cesium, all alloy systems were deposited using the recipe shown in table 5-3 and not optimized for maximum IV performance.

Table 5-3: Perovskite Alloy deposition recipe.

<b>Step 1</b>	<b>Step 2</b>	<b>Step 3</b>	<b>Step 4</b>	<b>Step 5</b>	<b>Step 6</b>
Prep Ink	Deposit ~80μl Ink	Spin to 1000 RPM for 10sec	Ramp to 6000RPM for 20 seconds	Deposit ~100μl Chlorobenzene dynamically in last 8 sec of spin	Anneal for 10min at 100°C inside glovebox

The application of chlorobenzene is performed in the last 8 seconds of the spin cast cycle. If chlorobenzene is applied too quickly, the devices behave differently than devices with slow application rates. However, visually, the faster application of chlorobenzene allows for less visible rings brought on by the interaction of sample cooling with the spin chuck as well as the lack of coverage due to the evaporation of chlorobenzene from the surface as seen in figure 5-1. Since humans are performing the solvent engineering step via the use of pipettes, the solvent rings are not preventable. Solvent rings can be visible after deposition, however, they are much more defined after the perovskite has undergone step 6 and been annealed.

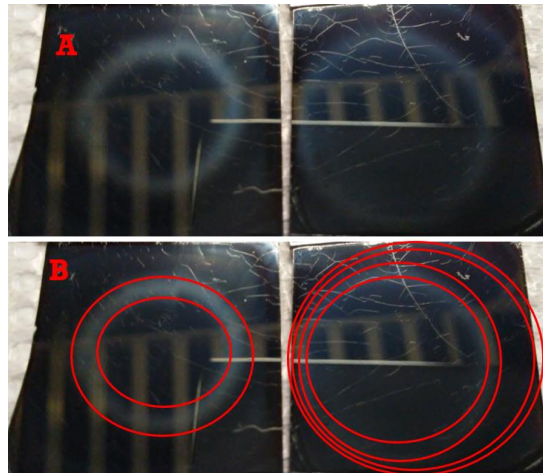


*Figure 5-1: Evaporative rings on alloy perovskite samples from the application of the chlorobenzene solvent engineering step. A) As seen. B) Rings highlighted for clarity.*

The alloy systems all anneal to the desired color, a deep and shiny black. However, the as deposited films have a slight difference in color and is shown in figure 5-2. The 5% NREL alloy has a slight yellow tinge and cracks are seen throughout the deposited film. The cracks are seen on all the remaining alloy systems with the systems getting

progressively darker in color with higher cesium content. Figure 5-2 shows the ink color for each of the systems as well as the as deposited film appearance prior to anneal. The inks used in these systems show no visible difference and all are yellow in color as seen in figure 5-2.

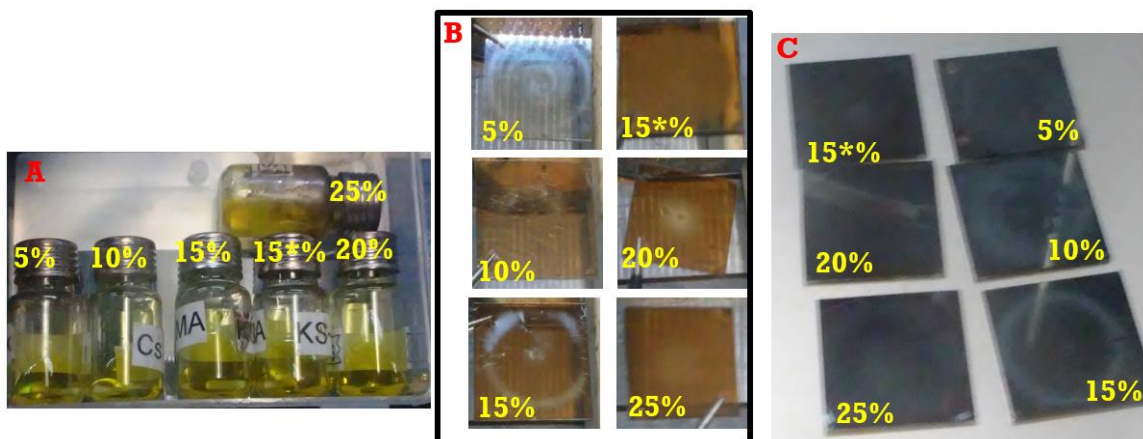


Figure 5-2: A) Alloy Ink solutions, B) as deposited and C) annealed alloys.

## 5.4 Measurement Results

### 5.4.1 Thickness

The thickness results for the alloy systems are shown in figure 5-3. The thickness was measured using the profilometer described earlier. The results show a trend in the thickness based on cesium concentration. Increasing the cesium concentration reduces the film thickness. The 5% cesium concentration samples had the thickest films and were  $\sim 530\text{nm}$ . These 5% Cs films are also thicker than the One-Step MAPBI perovskite which are typically  $\sim 450\text{nm}$ .

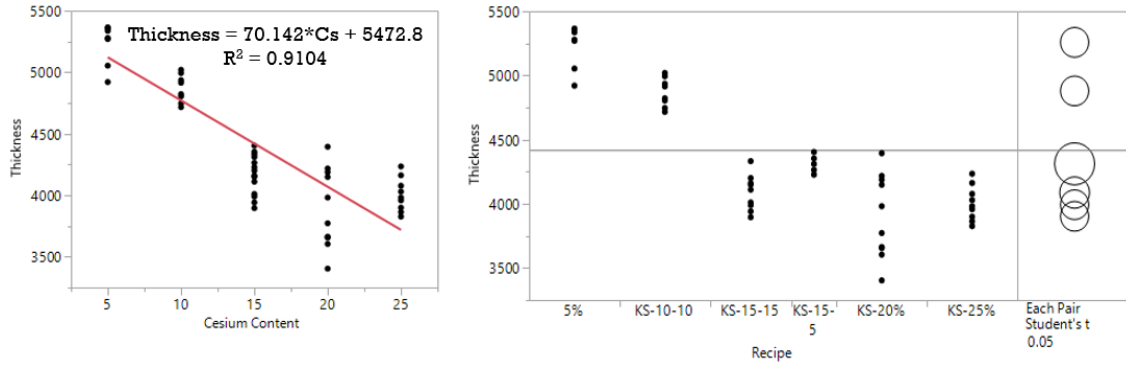


Figure 5-3: Alloy thickness results. Fitted curve showing strong linear relationship and right panel highlighting the statistical differences in thickness.

As can be seen from figure 5-3, there was a trend in the data with the higher cesium concentration alloys tending to result in thinner layers under the same deposition conditions.

A review of spin coating techniques reveals that the final thickness is driven by two primary factors, spin speed and fluid viscosity and this relationship is given by [153][154]:

$$\frac{h(t)}{h_0} = \sqrt{\frac{3\eta}{2\rho\omega^2 h_0^2}} \quad (5-1)$$

Where  $h(t)$  is final film thickness at time  $t$ ,  $h_0$  is the initial film thickness,  $\eta$  is absolute viscosity,  $\rho$  is the fluid density and  $\omega$  is the angular velocity and the final thickness as:

$$h(t) = 3 \left[ \frac{3C^3(t)\vartheta_0\phi}{2(1-C_0(t))\omega^2} \right]^{1/3} \quad (5-2)$$

Where  $h(t)$  is final film thickness at time  $t$ ,  $C(t)$  is the concentration of the solids at  $t$ ,  $C_0$  is initial solid concentration,  $\phi$  is the liquid evaporation rate and  $\nu$  is the kinetic viscosity ( $\nu = \eta/\rho$ ).

Since all films were deposited using the same spin coat recipe, the angular velocity is the same for all alloy systems. We can then reduce and rearrange equation 5-1 to get a relationship between the final thicknesses based on this equation as follows:

$$\frac{h(t)_x}{h(t)_y} = \frac{\eta_x \rho_y}{\eta_y \rho_x} = \frac{v_x}{v_y} \quad (5-3)$$

The relationship in equation 5-3 can give us an idea of the difference in kinetic viscosity of the different inks based on cesium concentration. The first thing to noticed is that the density of the fluid increases with increasing cesium concentration and is shown in figure 5-4. The increase in density is strongly correlated with cesium concentration as indicated by the linear fit depicted in the figure 5-4, despite the reduction in mass from the MA cation as the cesium atom is so much heavier. If we use the ratio in equation 5-3, the difference seen in densities at the 5% and 25% cesium concentration is ~1.6%, yet the thickness difference is about 25%. Thus, the density of the inks would not be driving the thickness trend observed.

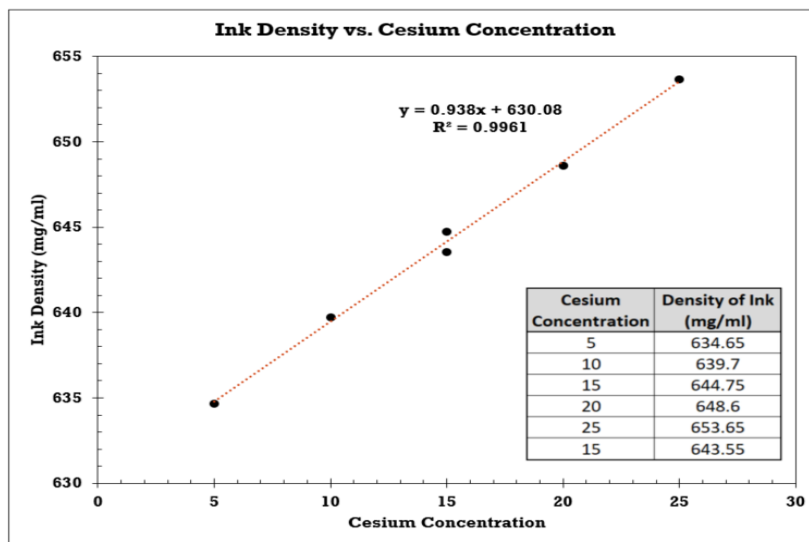


Figure 5-4: Cesium concentration vs density of the ink solutions. Based on calculations based on mole ratios predicted for each concentration.

The next parameter in equation 5-3 is the viscosity of the inks. All inks are ~1M solutions in a 4:1 ratio of DMF to DMSO solvents. Viscosity can be readily measured using a graduated cylinder, a ball bearing and a stop watch. However, the volumes needed to measure this parameter, even in a 5mL graduated cylinder, are quite large based on typical volumes normally used in the lab, which are typically < 2mL. In addition, there is simply not enough distance in a 5mL graduated cylinder to measure accurately the difference in fall times. As a result, we need to estimate the viscosity.

We can estimate viscosities using the Jones-Dole equation[155]:

$$\frac{\eta}{\eta_o} = 1 + AC^{\frac{1}{2}} + BC \quad (5-4)$$

Where  $\eta$  is the viscosity, C is the solute concentration, A is a coefficient from the Debye-Hückel theory and B is based on solute-solvent interactions. It should be noted that all

parameters and ratios are all at the same temperature and pressure. From Debye-Hückel [156]:

$$A = \gamma \frac{C}{C^o} \quad (5-5)$$

Where C are the concentrations and  $\gamma$  is the activity coefficient.

The 'B' coefficient is a measure of the interactions between the solute and solvent[157][158]. Reviewing the data and methods of determining this value a few things become clear. The 'B' coefficient is highly depended upon temperature and for low concentrations (below 1M) the 'B' is considered a constant[158]. This is an important observation as the alloy systems are nothing more than different concentrations of the same solutes in the same solvent. Here, the MA, FA, Cs, Pb and I are the solutes in a 4:1 DMF:DMSO solvent. As none of the individual concentrations are above 1M, the solute-solvent interactions can be considered to be the same in each system and the Jones-Dole 'B' coefficient can be considered a constant.

To calculate the Jones-Dole 'A' coefficient, the use of Debye-Hückel theory is required to calculate the activity coefficient. One popular approximation, as these parameters are modeled based on data, of the activity coefficient that is given by [159]:

$$\ln\gamma_i = -z_i^2 \frac{A\sqrt{I}}{1+B\sqrt{I}} + CI \quad (5-6)$$

Where A, B and C are adjustable model parameters, z is the ionic charge on species i and I is the molal strength given by:

$$I = \frac{1}{2} \sum_i m_i z_i^2 \quad (5-7)$$

Where  $m_i$  is the molal concentration of species i and z is still the ionic charge on that species.

Equation 5-7 gives insight on the relationship observed between the cesium concentration and the thickness observed. The higher ionic/molal strength, represented by the increase in concentration of the cesium atom should have the effect of resulting in thicker films, however, in our systems, that is not the case. This discrepancy can be explained not by the role of the Cs but rather, by the role of the MA. The dipole moment on MA is greater than the electronegativity on the Cs as discussed above. As the Cs concentration is reduced, the MA concentration is generally increasing and as a result, is driving the thicker films observed.

In summary, the thicknesses of the films were observed to have an inverse relationship with cesium concentration, that is higher Cs concentration films were generally thinner than their lower Cs concentration films. The use of spin coating relationships, the Jones-Dole relationship and Debye-Hückel theory all give insight into the role of the cations in the alloys. The MA cation, with a large dipole moment ( $\sim 2 \times$  Cs), drives the general thickness relationship given in equation 5-3 by use of the strong molal concentration given by equations 5-6 and 5-7.

From this information, we then can predict future perovskite thicknesses based on this relationship presented here. Perovskite formulations containing cations with smaller dipole moments than MAPBI films will have generally thinner films when processed under similar conditions.

#### 5.4.2 XRD Results

XRD was performed on the six alloy samples on the Rigaku Smartlab XRD system. A 'Quick theta/2-Theta Scan (medium resolution) was selected to measure these samples. The XRD measurement was discussed earlier. Data from the XRD gives crystal structure and lattice size. The samples were made just prior to XRD analysis (<5 minutes) to assure as little atmospheric related decomposition occurred. The samples were prepared in two ways, one perovskite deposited on bare glass and the second with the perovskite deposited on PEDOT:PSS coated bare glass samples.

Reviewing the PEDOT:PSS and bare glass substrates, there were slight differences in the XRD pattern was observed between the substrates on all systems. However all crystal lattice planes resided at essentially same  $2\theta$  value, or within the tolerance of the XRD system. Given the highly disordered nature of the perovskite systems, this was not unexpected [132]. XRD results are reported in the figures below.

All systems were observed to have a simple basic cubic structure regardless of the alloy composition. Calculated lattice constants did vary between the alloys and are shown below in table 5-4. Unlike the other parameters, no obvious trends are observed with the lattice constant based on the XRD results, however, there is a general trend

with the data. For clarity, only the XRD patterns for the alloys deposited on bare substrate alloys are reported with the corresponding identifiable lattice planes identified for each composition. The lattice constants for each system were calculated with data from both substrate preparations and are consistent.

Interestingly enough, while the lattice constant does appear to be slightly different between the alloy samples, it compares very closely with that of pure cubic  $\text{MAPbI}_3$  (6.391 Å) [160] and that of pure cubic  $\text{FAPbI}_3$  (6.362 Å)[161]. The reported  $\text{FAPbI}_3$  structure, which is actually smaller than the reported  $\text{MAPbI}_3$  structure, despite the difference in cation size ( $\text{MA} = 217\text{pm}$  vs  $\text{FA} = 253\text{pm}$ ). This is probably a result of the difference in electronegativity in the MA and FA cation as they interact with the large lead cation. The like charges repulse one another increasing the lattice spacing between the atoms. This would explain why the incorporation of the large Cesium atom into the matrix does not greatly expand the lattice structure as the poor electronegativity (cesium is the least electronegative atom known) does not affect the lattice constants in any meaningful way. However, a similar composition system of 15% MA and 85% FA did report a smaller lattice constant (6.224Å) than the 15% MA systems in the systems observed here. It can be theorized then, that the large cesium atom did have the predicted effect of increasing the lattice spacing to accommodate it.

Table 5-4: Calculated lattice constants.

Sample	Lattice Constant BARE (Å)	Lattice Constant PEDOT:PSS (Å)	Average (Å)
5%	6.345	6.351	6.348
10%	6.345	6.347	6.346
15%	6.373	6.372	6.373
20%	6.313	6.312	6.313
25%	6.356	6.355	6.356
15% (70% FA)	6.341	6.340	6.341

In summary, the XRD results show that the alloys all exhibit a simple cubic structure with lattice constants reported in table 5-4. Lattice constants and cubic structure correspond well with reported structures for FAPbI<sub>3</sub> and MAPbI<sub>3</sub> films. Differences in reported lattice constants observed in the results are the combined effect of cation electronegativity and size interacting with the remaining cation (Pb<sup>2+</sup>) and the anion (I<sup>-</sup>).

5.4.2.1 5% Cesium Alloy XRD Results

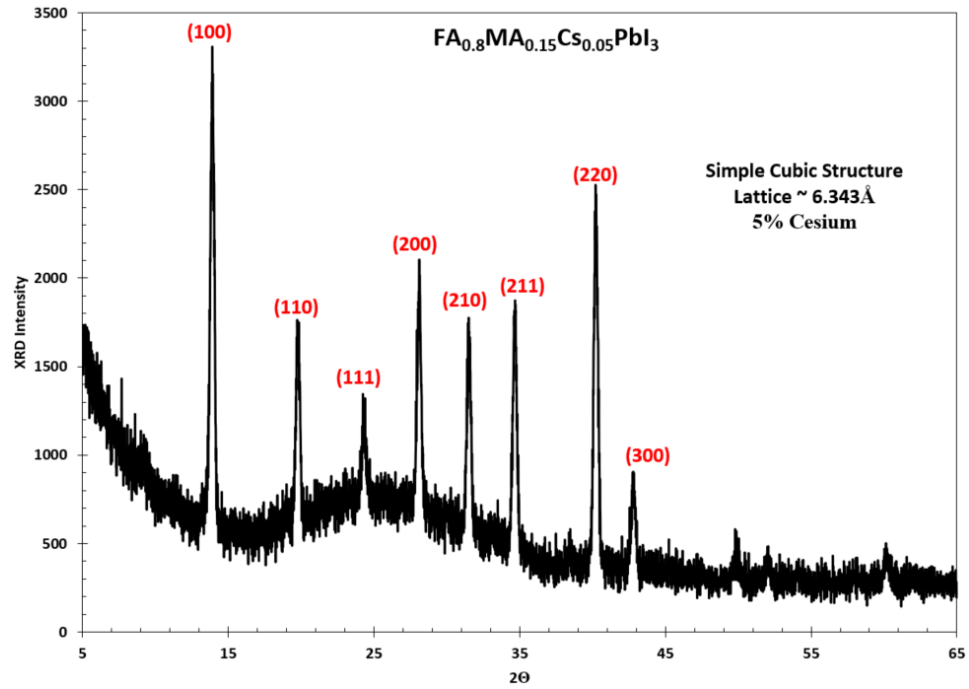


Figure 5-5: XRD Pattern of 5% Cesium Alloy Sample.

5.4.2.2 25% Cesium Alloy XRD Results

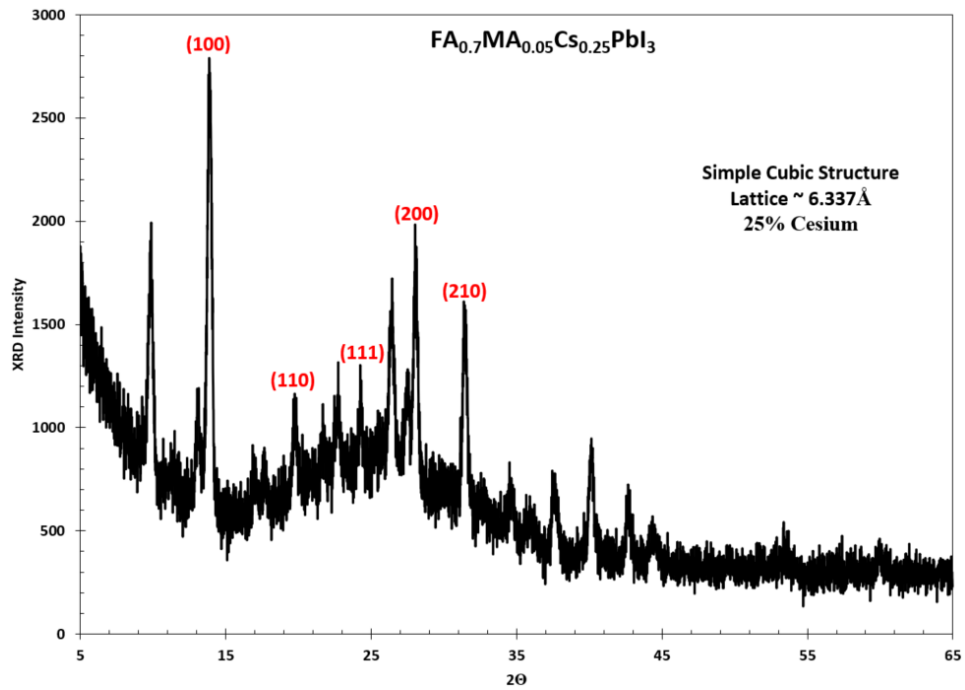


Figure 5-6: XRD Pattern of 25% Cesium Alloy Sample.

#### 5.4.2.3 20% Cesium Alloy XRD Results

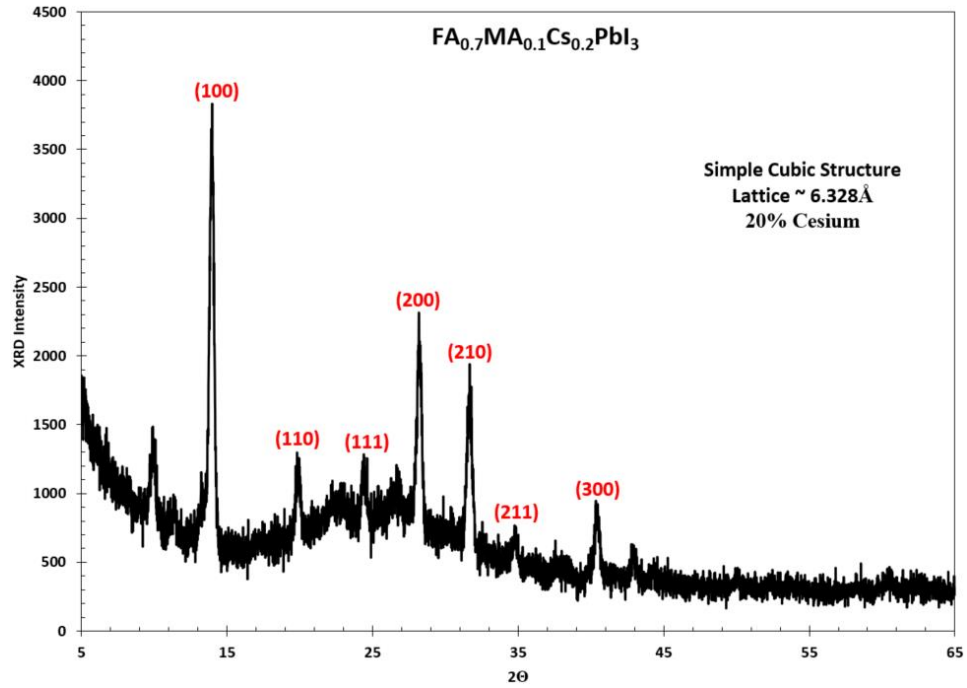


Figure 5-7: XRD Pattern of 20% Cesium Alloy Sample.

#### 5.4.2.4 10% Cesium Alloy XRD Results

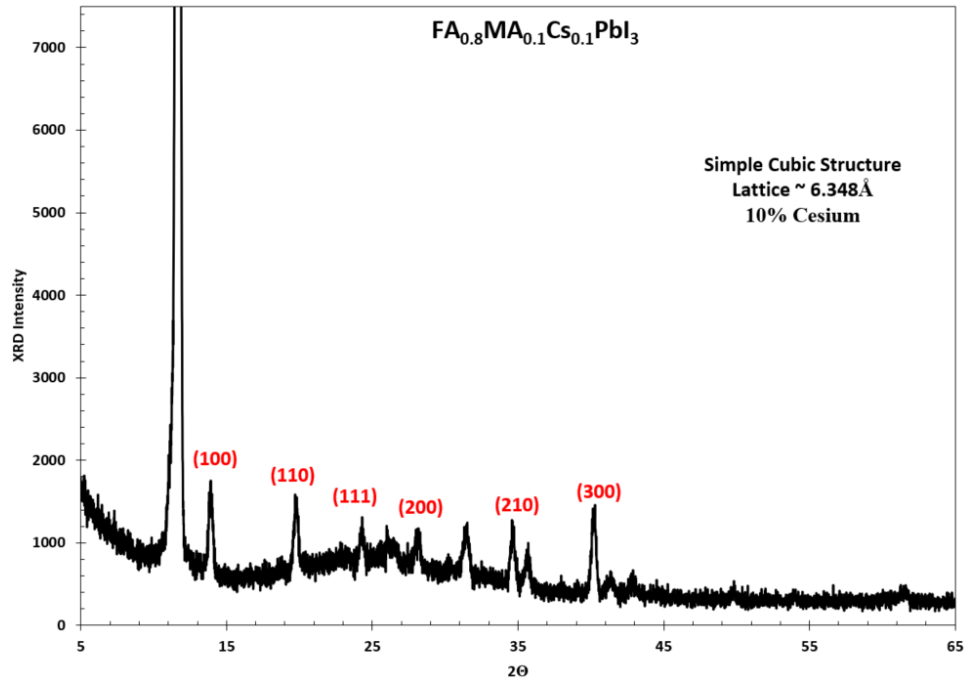


Figure 5-8: XRD Pattern of 10% Cesium Alloy Sample.

#### 5.4.2.5 15% Cesium Alloy XRD Results

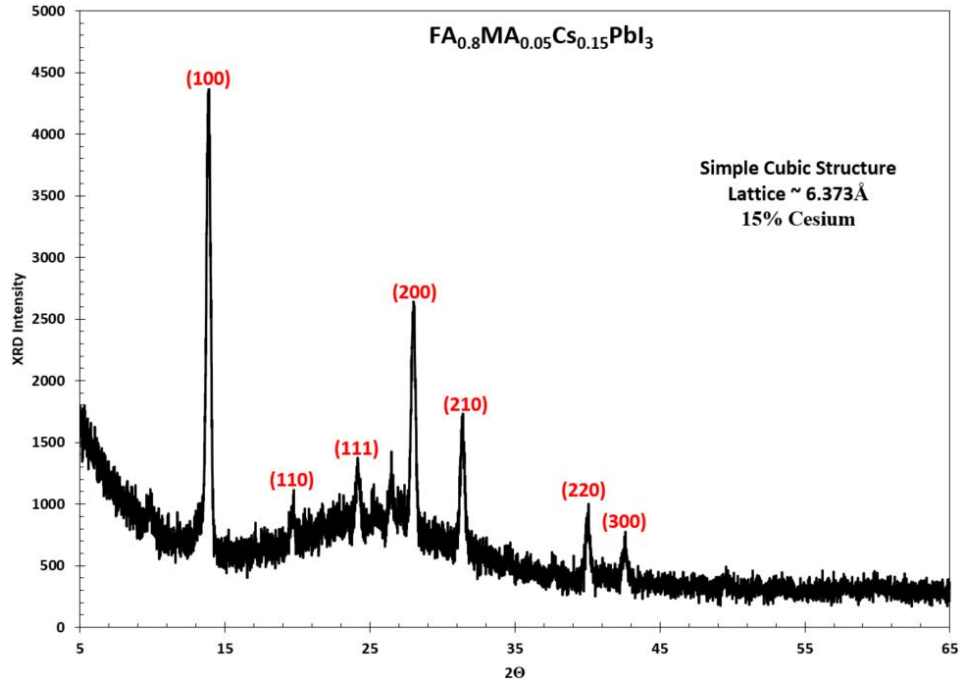


Figure 5-9: XRD Pattern of 15% Cesium Alloy Sample.

#### 5.4.2.6 15% Cesium (70% FA) Alloy XRD Results

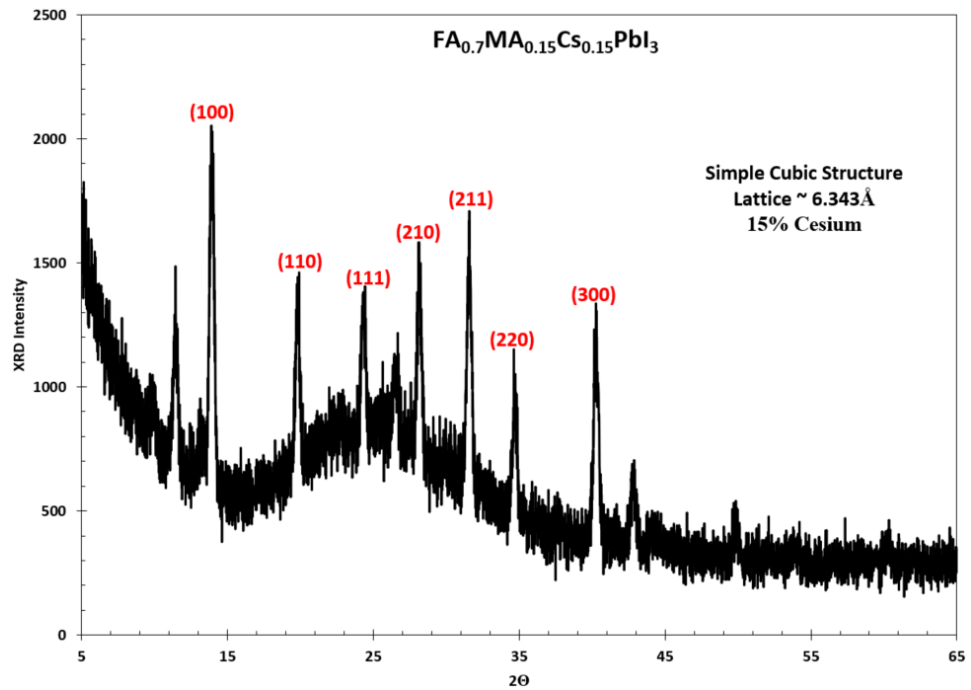


Figure 5-10: XRD Pattern of 15% Cesium (70% FA) Alloy Sample.

### 5.4.3 AFM Results

#### 5.4.3.1 5% Cesium Alloy Results

The AFM results for the 5% Cesium alloy samples are shown in figure 5-11 and figure 5-12. From these figures it is clear to see that this alloy yields very good coverage ('pin' hole free) with a very uniform crystal size distribution. Those crystal sizes from analysis of the images in figure 5-12 show crystal sizes of about 219nm in diameter.

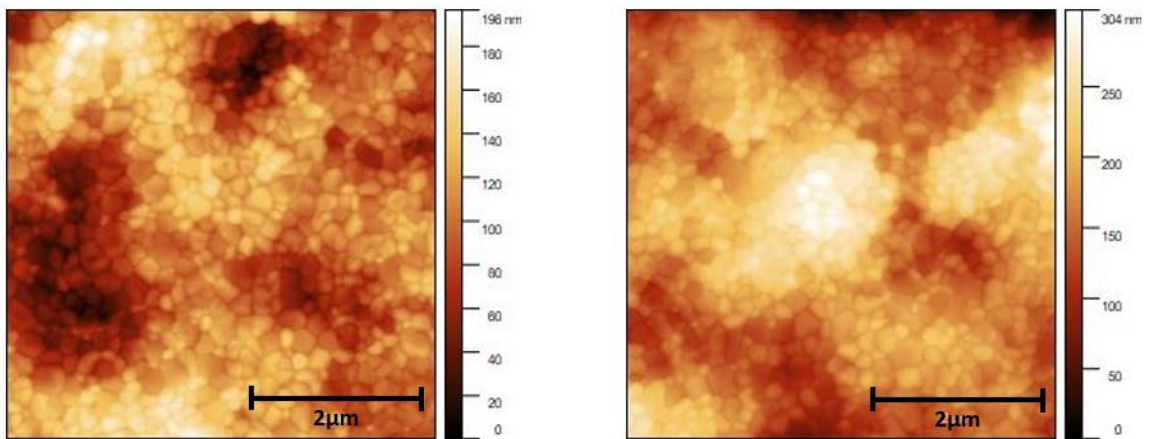


Figure 5-11: AFM results, 5% alloy.

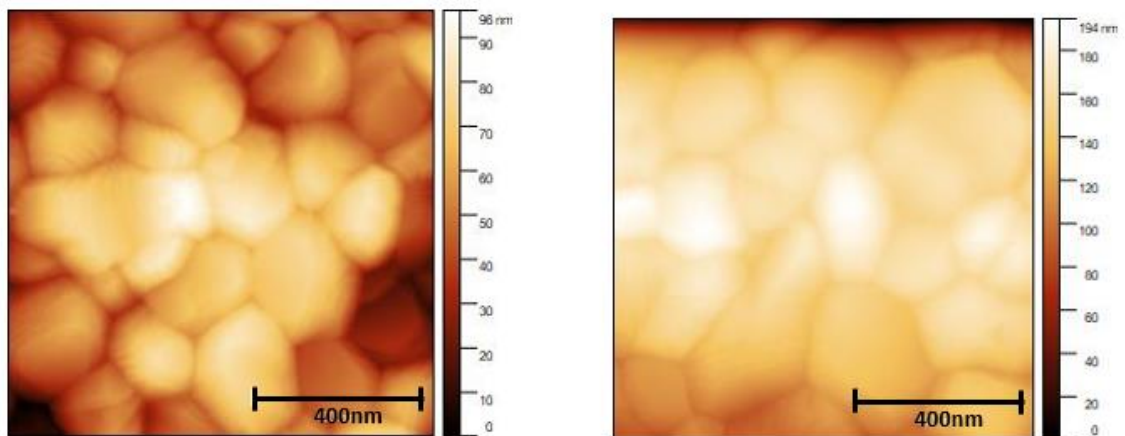


Figure 5-12: AFM results, 5% Alloy. Shows average grain sizes of ~219nm.

#### 5.4.3.2 10% Cesium Alloy

AFM results for the 10% alloy are shown in figures 5-13 and 5-14. As with the 5% alloy film, the 10% alloy film has good surface coverage and a good pin hole free coverage of the surface. However, the average crystal sizes for the 10% alloy are smaller and average  $\sim 168\text{nm}$  in diameter.

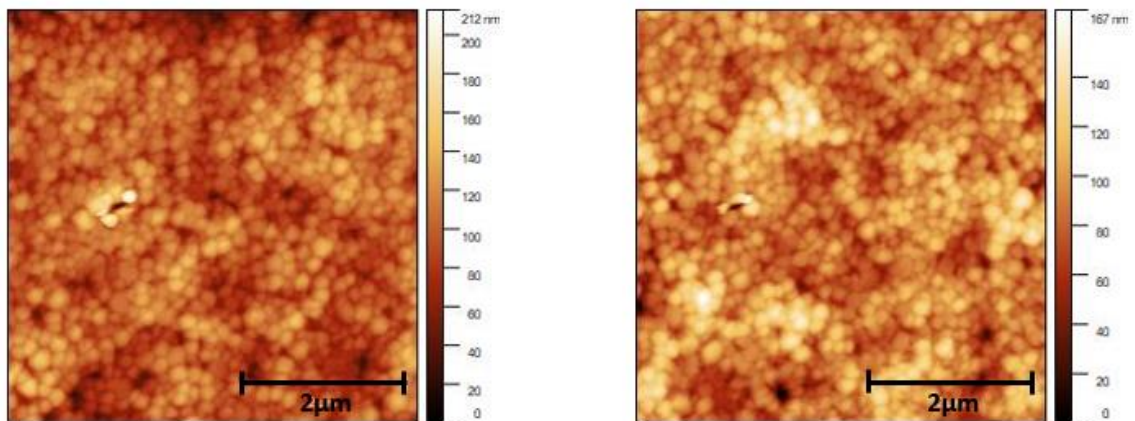


Figure 5-13: 10% Alloy AFM results.

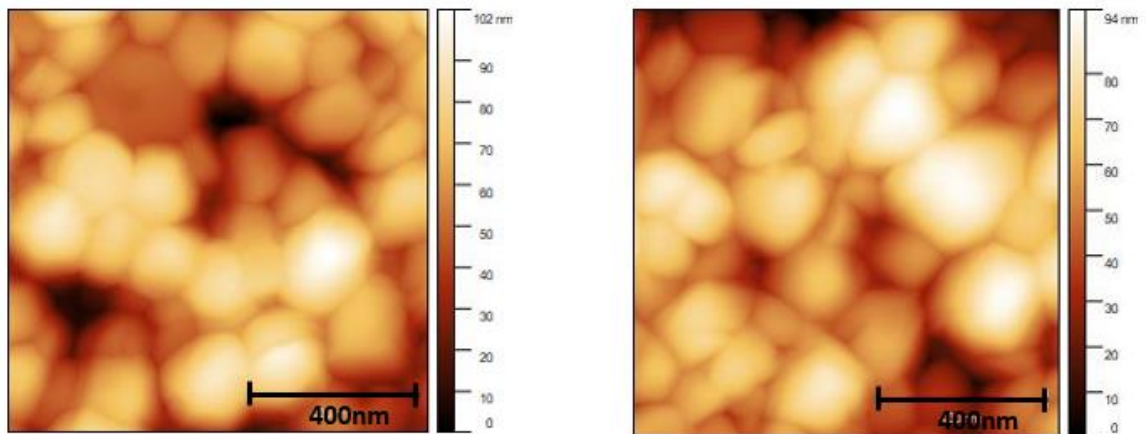


Figure 5-14: 10% Alloy, showing crystals that average  $\sim 168\text{nm}$  in size.

### 5.4.3.3 15% Cesium Alloy

AFM results for the 15% alloy are shown in figures 5-15 and 5-16. As can be seen in figure 5-15, the morphology of the surface changes slightly. Coverage is still very good and uniform, however, islands are seen in the AFM images. Examining the islands closer indicate them to be areas of poor coverage. From the images in figure 5-16, the downward trend of crystal sizes continues with this alloy averaging about 138nm.

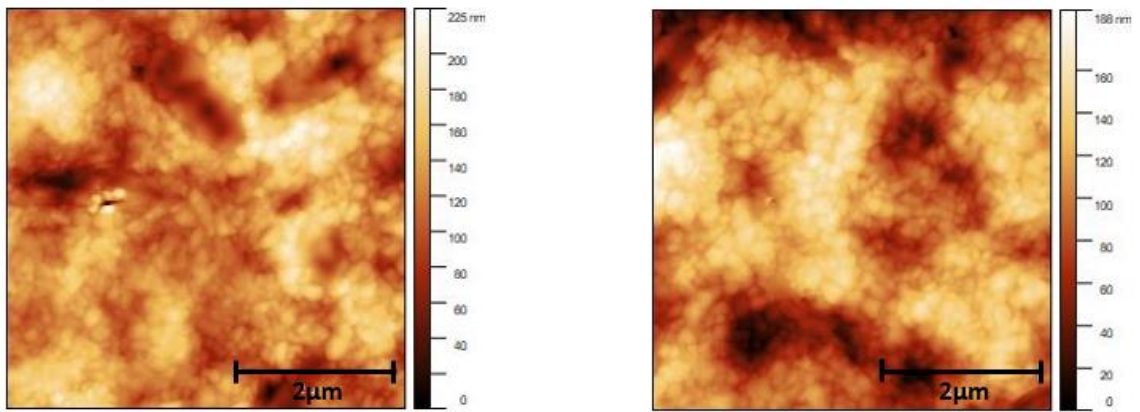


Figure 5-15: 15% Alloy AFM results.

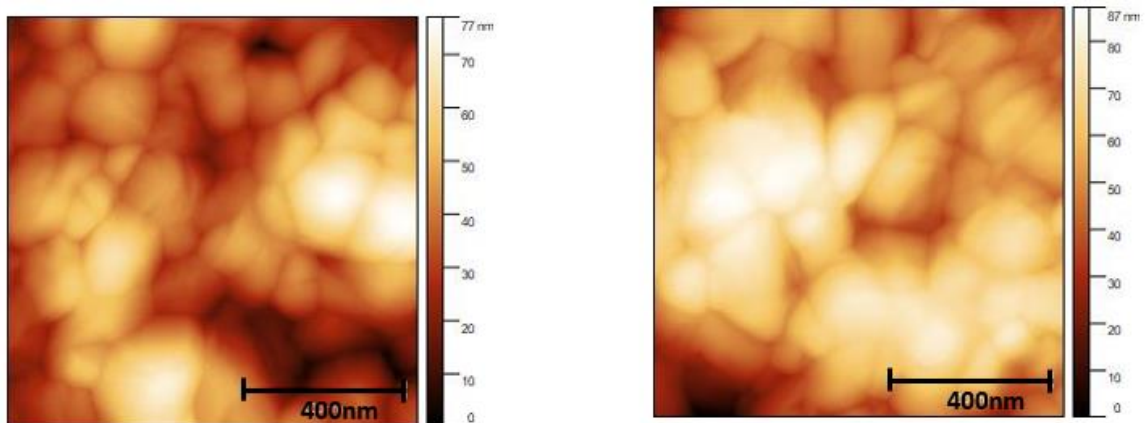


Figure 5-16: 15% alloy, analysis of the images indicates an average crystal size close to 134nm.

#### 5.4.3.4 20% Cesium Alloy

AFM results for the 20% alloy are shown in figures 5-17 and 5-18. Morphology of the films are very good and pin hole free. Crystal sizes are at  $\sim 124\text{nm}$  based on analyzing the images in figure 5-18.

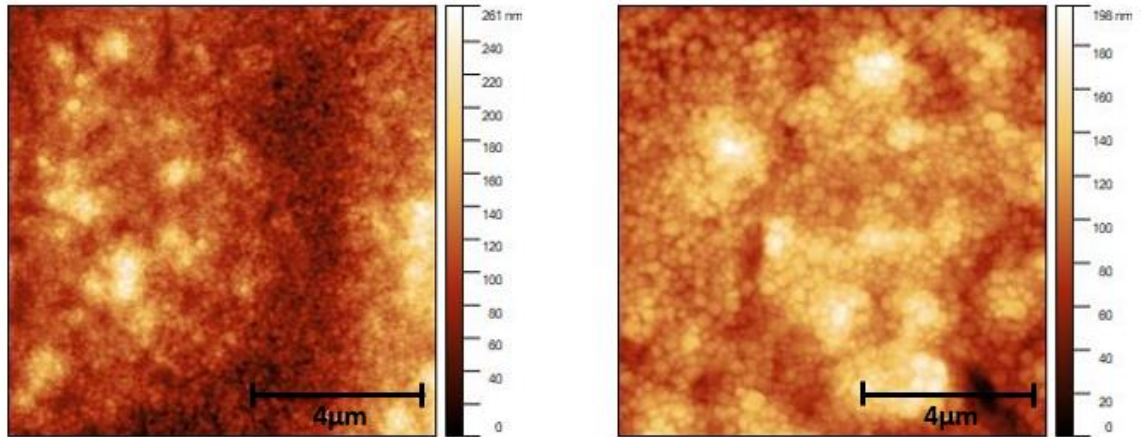


Figure 5-17: 20% alloy AFM results.

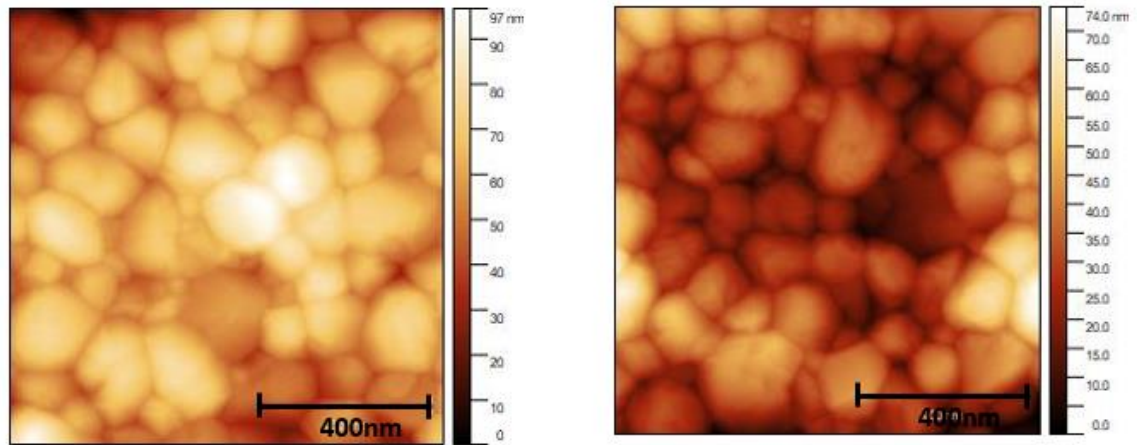


Figure 5-18: The 20% alloy, analysis of image shows crystal diameter  $\sim 124\text{nm}$ .

#### 5.4.3.5 25% Cesium Alloy

AFM results for the 25% alloy are shown in figures 5-19 and 5-20. Morphology of the films are very good and pin hole free. Crystal sizes are at  $\sim 138\text{nm}$  based on analyzing the images in figure 5-20.

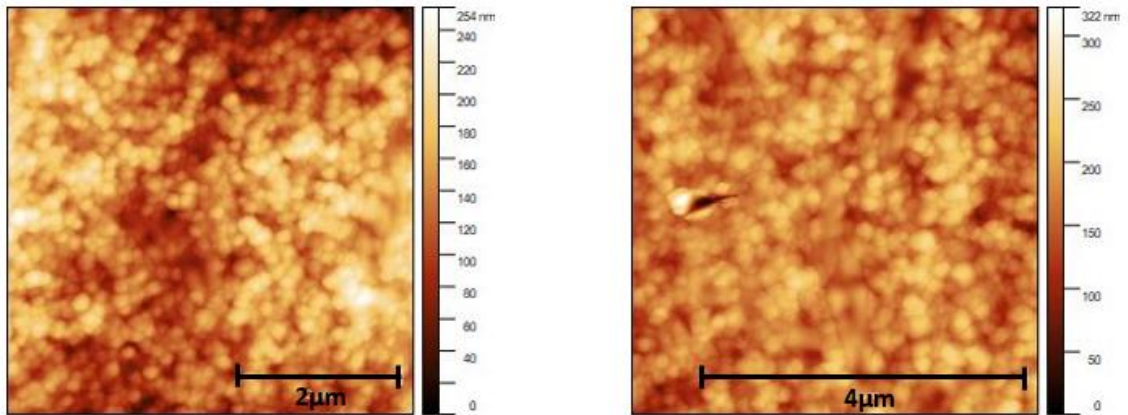


Figure 5-19: The 25% Alloy results.

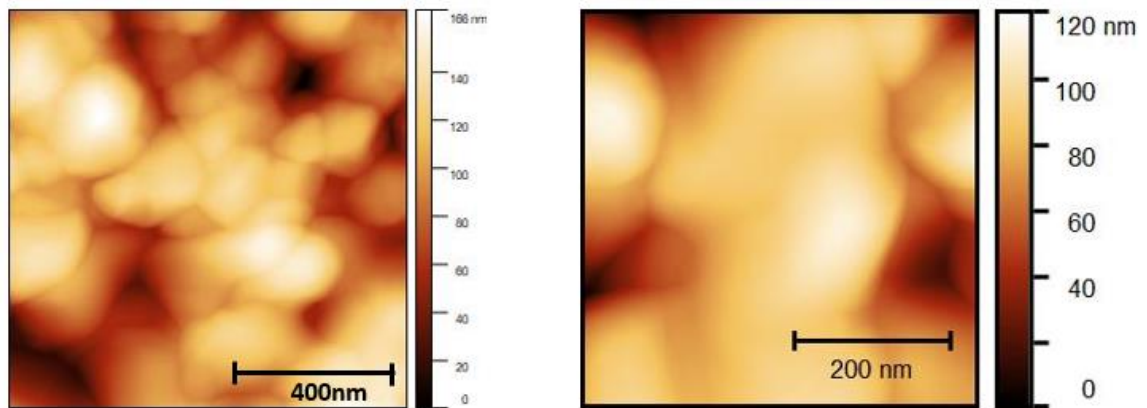


Figure 5-20: 25% alloy concentration. Image analysis indicates  $\sim 138\text{nm}$  crystal size. Note, right image is smaller area than left.

#### 5.4.3.6 15% Cesium (70%FA) Alloy

AFM results for the 15% Cesium (70%FA) alloy are shown in figures 5-21 and 5-22. Morphology of the films are very good and pin hole free. Crystal sizes are at  $\sim 137\text{nm}$  based on analyzing the images in figure 5-22.

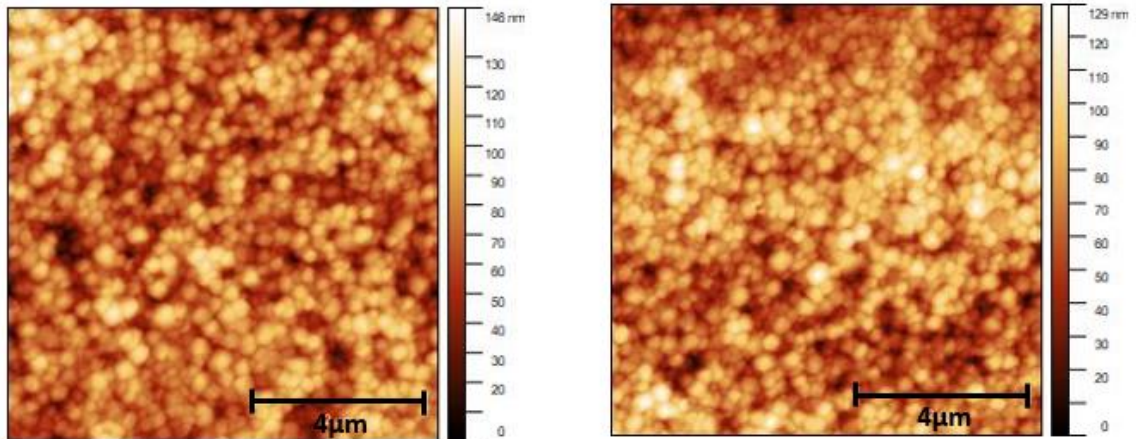


Figure 5-21: AFM results of the 15% Cesium (70% FA) alloy.

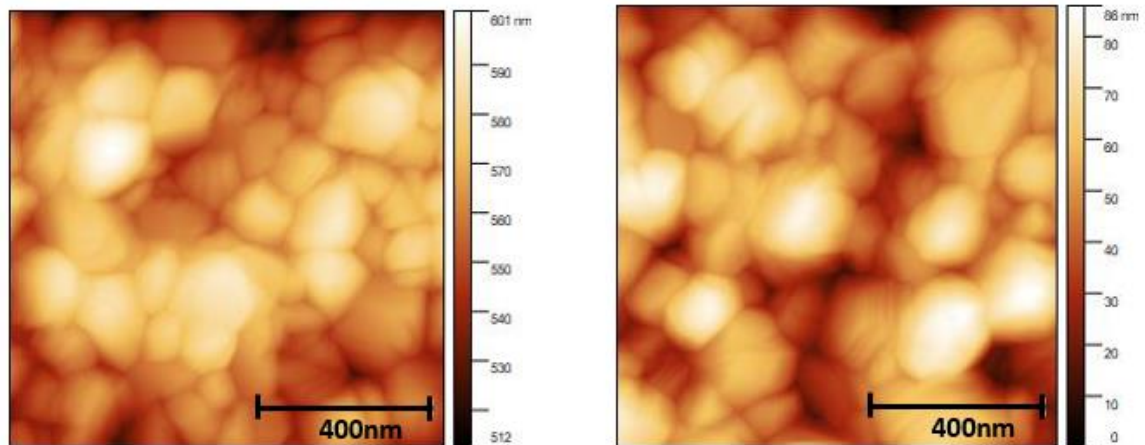


Figure 5-22: AFM of 15% Cs alloy (70% FA) showing a crystal size of  $\sim 137\text{nm}$ .

#### 5.4.4 UV VIS Data

UV-VIS data was collected on the alloy samples using a Shimadzu UV-2501(PC) UV-Vis Spectrometer described earlier. The data from this instrument is used to calculate the bandgap and absorption spectra of the perovskite samples. UV-Vis measurement data is presented in figure 5-23. Data is separated into FA of 70% and 80% to help highlight the trend seen in the data. Bandgaps estimated from this data are shown in table 5-5.

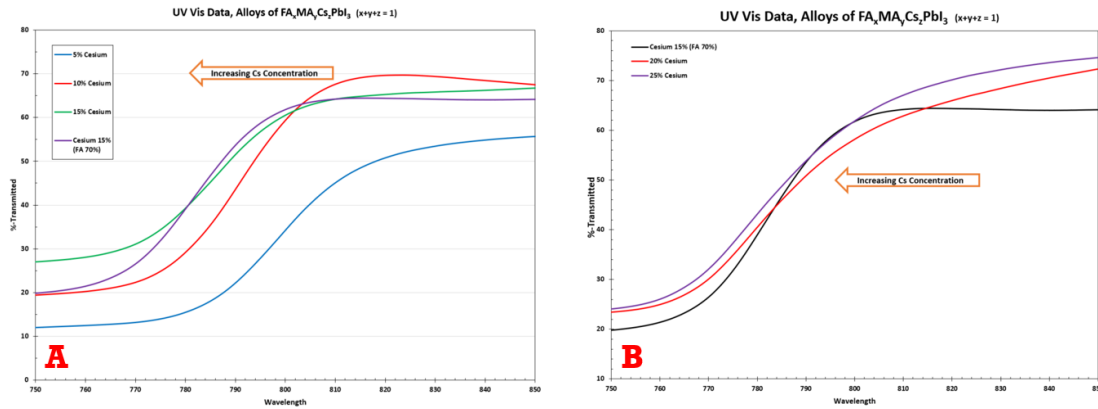


Figure 5-23: UV-VIS Curves of the alloy perovskites. A) 80% FA alloys, B) 70% FA alloys.

Table 5-5: Calculated Bandgaps based on UV-VIS data.

Sample	Calculated Bandgap (eV)
5% Cesium	1.550
10% Cesium	1.570
15% Cesium	1.575
15% Cesium (70% FA)	1.582
20% Cesium	1.586
25% Cesium	1.588

One item to notice in the table 5-5 is there is clear trend of increasing bandgap with cesium addition. The higher the cesium, the higher the bandgap. The trend is more pronounced for the higher 80% FA content samples than the 70% FA samples. The bandgaps observed for the alloy samples are in similar in energy levels for their pure phase systems ( $\text{MAPbI}_3 \sim 1.53\text{eV}$ ,  $\text{FAPbI}_3 \sim 1.4\text{-}1.5\text{eV}$ ,  $\text{CsPbI}_3 \sim 1.73\text{eV}$ ) [162]. As the cesium level increases, the trend is towards the higher bandgap level reported for the pure phase  $\text{CsPbI}_3$  perovskite.

The selection of a cation atom then can affect the bandgap as much as the selection of the anion in perovskite systems. It is well known that using a different mix of halides allows researchers to tune the bandgap of the system[56][57]. In using the halide substitution method, the halide shrinks in radius, but gains much more electronegativity in the process. The result is the greater electronegativity of the halide atom causing a shift in the bandgap to higher energies. The higher energies are needed to help remove the electron from the more electronegative halide. This gives  $\text{MAPbI}_3$  the best bandgap in terms of Shockley-Queisser of the mixed  $\text{MAPbI}_{3-x-y-z}\text{Br}_y\text{Cl}_z$  series.

Reviewing the data on the cation contribution to the bandgap a similar phenomenon is seen. As the overall electronegativity contribution of the cations are reduce, the bandgap increases. The trend toward higher bandgap is seen with the pure phase  $\text{CsPbI}_3$  structure compared to the  $\text{MAPbI}_3$  structure and reviewing the electronegativity of the Cs (low) compared to the MA (high), the ionic strength of materials have shown a relationship with bandgaps [163],[164]. The less electronegative

cation has less attraction towards the electrons allowing them to stay in their shell on the anion.

#### 5.4.5 SEM and EDS

SEM and EDS were run on the alloy samples. SEM images were created, and the EDS was used to verify composition of the samples. The FEI SEM was used to generate this data and the operation was discussed previously.

Samples were prepared fresh and stored in a sealed vial prior to SEM imaging. To help combat the charging effect on the perovskite samples, the perovskite was deposited on unpatterned ITO substrates. A corner of the sample was then scrapped clean of perovskite and silver paste deposited on the exposed corner. A piece of tape was used as a diffusion barrier to keep the water from the silver paste from infiltrating the perovskite sample. Copper tape was then affixed to the silver paste and wrapped around the to the substrate holder. Figure 5-24 shows the sample prep. Finally, a multimeter was used to assure proper grounding of the sample to the SEM holder.

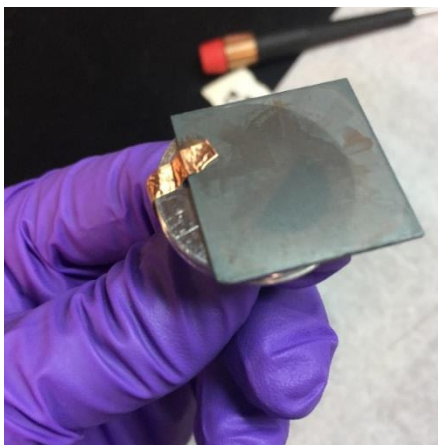


*Figure 5-24: Prepped sample for SEM, note the copper grounding strap. Similar setup used for KFPM.*

EDS for the samples were done at 8kV energy. Cesium's L line is at 4.285keV and iodide's L line is at 3.938 keV, however, iodide also has an L line at 4.221keV which gives a large error for identifying systems with both cesium and iodide given the resolution of the system. Additionally, the use of the 8kV energy to generate the spectrum also damages the sample, burning holes into the samples, introducing boron, indium, silicon, tin and oxygen into the spectrum. Figure 5-25 shows the pre and post EDS SEM image on a perovskite sample showing the damage to the sample.

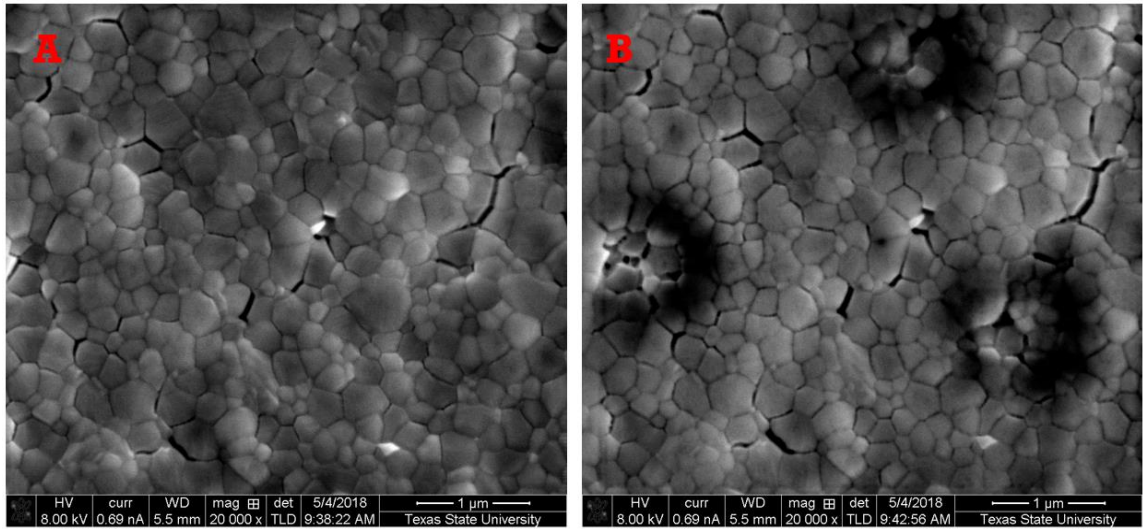


*Figure 5-25: SEM image of a 5% cesium sample. A) Pre EDS-measurement. B) Post EDS measurement where damage is clearly seen in the three sample areas.*

To combat the high error in measurement, multiple areas were measured using an area scan as opposed to point scans. The area scans returned consistent values compared with the point scans. The EDS beam was scanned in random areas of the sample for a min of 50 seconds for each sample. The higher scan times can increase accuracy, but also created much more damage.

To determine the proper ratios of alloys in each sample, the ratio of cesium to iodide was chosen. The ratio of iodide in each sample is the same while cesium varies. The only other variable portion of the sample was the nitrogen content, however, the potential to contaminate the sample with carbon and nitrogen sources made this to unreliable for a good measurement. Thus, the ratio of cesium to iodide was used to gauge alloy samples. Figure 5-26 shows the results of the EDS measurements and the ratio.

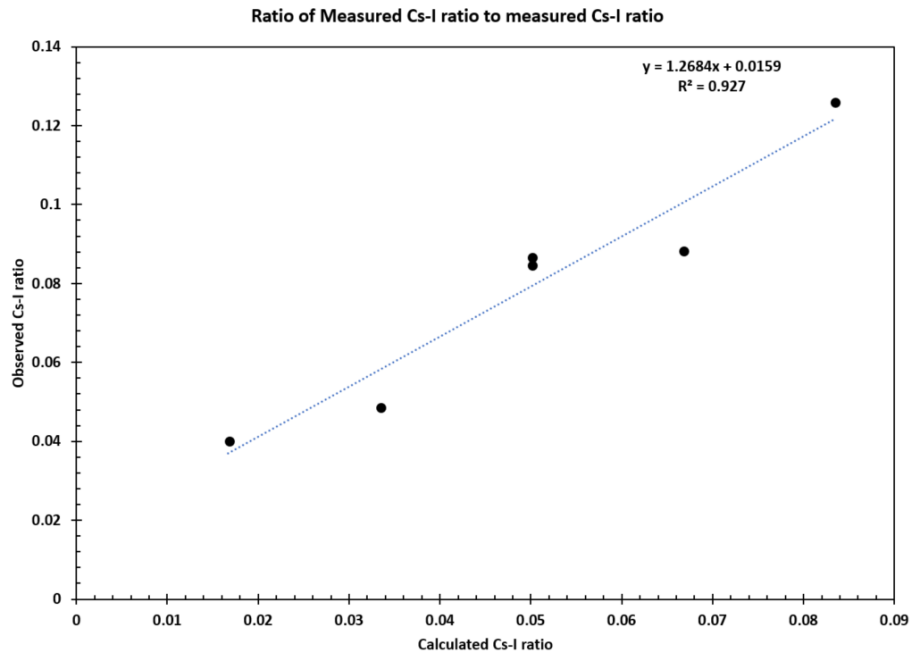


Figure 5-26: Cs-I ratio in the alloy samples as measured by EDS.

The results in figure 5-26 show very good agreement with predicted ratios of cesium and iodide and actual measured ratios. This data confirms that there are differences in the ratios of the cesium in the different alloy samples. Additionally, there is good agreement with the two 15% cesium samples, one at 80% FA and the other at 70% FA content.

SEM images were also taken of several regions of each alloy sample. The big challenge with perovskite samples and imaging is that while the destruction of the crystal is acceptable for EDS measurements, they make for poor images. Also, the best known method (BKM) method for MAPbI films imaged at Texas State called for the use of 5kV and a current of 5pA. Unfortunately for the alloy samples, this was not enough current to generate any images. Also, the 5kV was insufficient for the EDS measurements. The images captured here at thus at 8kV and at currents in the nano-amp range. The higher current results in sample damage and this makes getting clear images of perovskites a tough task. The BKM is to focus on a spot, then rapidly move to another position on the sample and take an image. As the perovskite film is not planar, this can lead to some less than ideal images.

One unique feature of many of the samples were the bright crystals that were present in many portions of the SEM images regardless of alloy. Initially, it was thought that these might be  $\text{PbI}_2$  regions, or potentially other salt compounds within the perovskite. However, upon using EDS on these regions, they returned a composition no different than the bulk film. This could be just a result of the random crystal orientation reflecting more electrons towards the detector.

#### 5.4.5.1 5% Cesium Alloy SEM Images

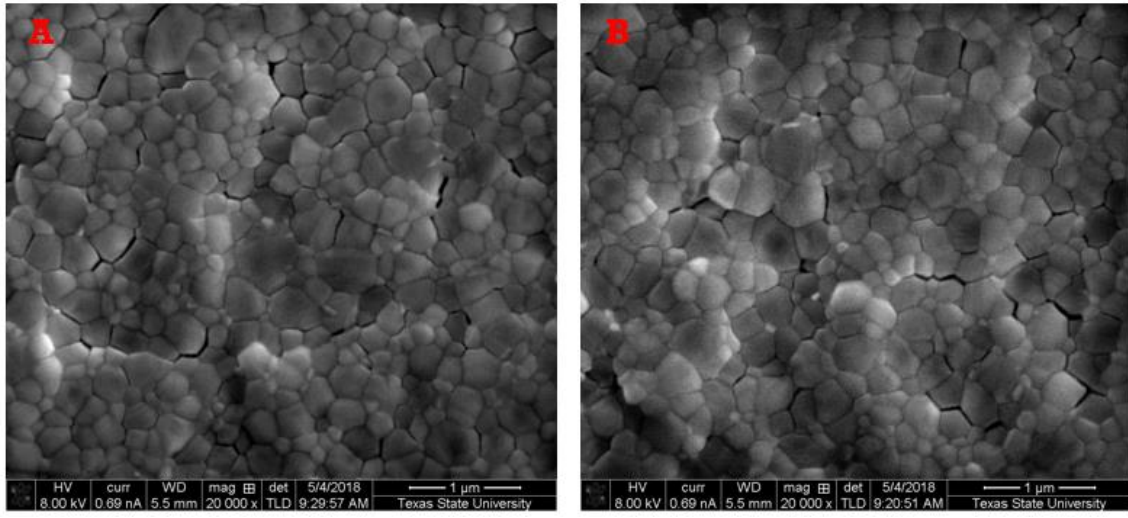


Figure 5-27: 5% Cesium Alloy SEM images.

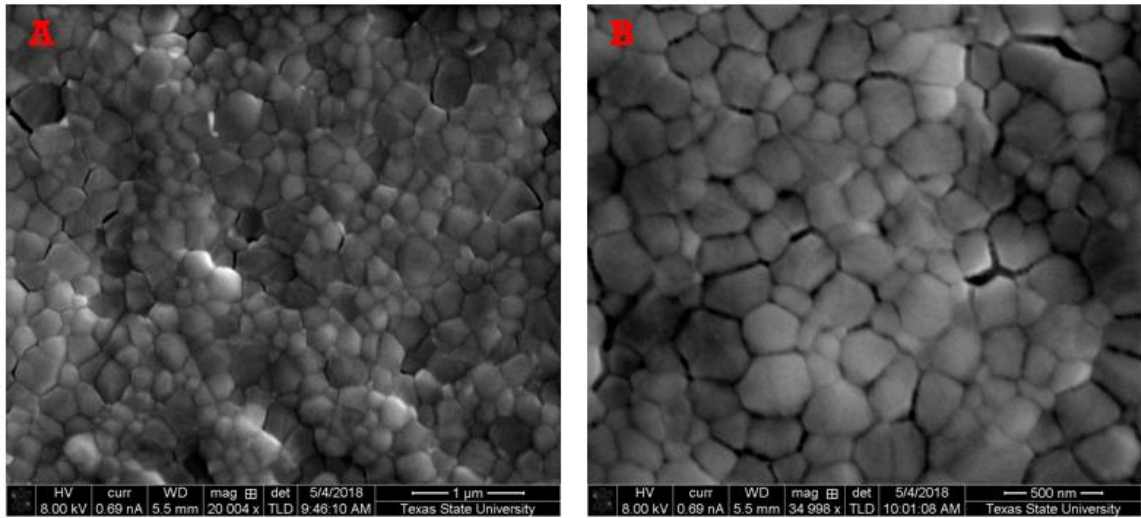


Figure 5-28: 5% Cesium alloy SEM images.

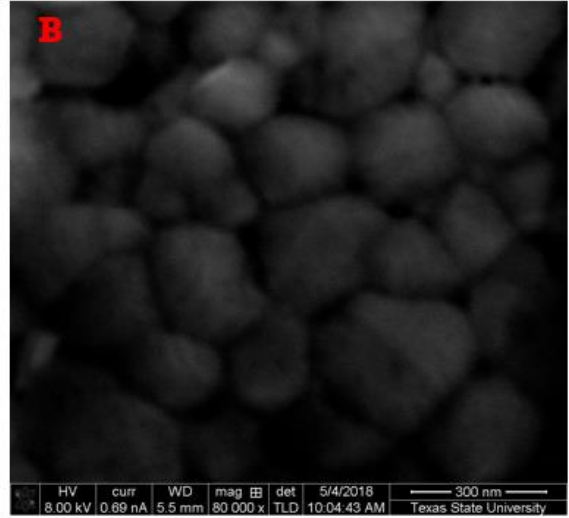
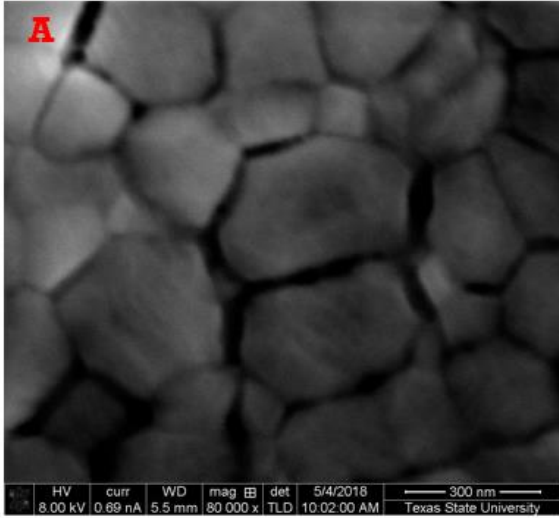


Figure 5-29: 5% Cesium alloy SEM images.

#### 5.4.5.2 10% Cesium Alloy SEM Images

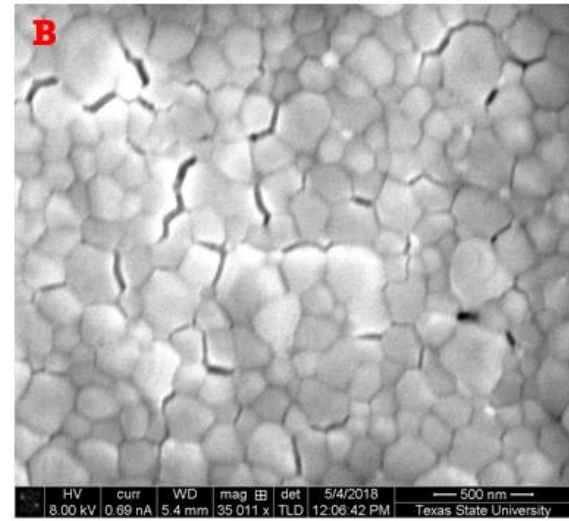
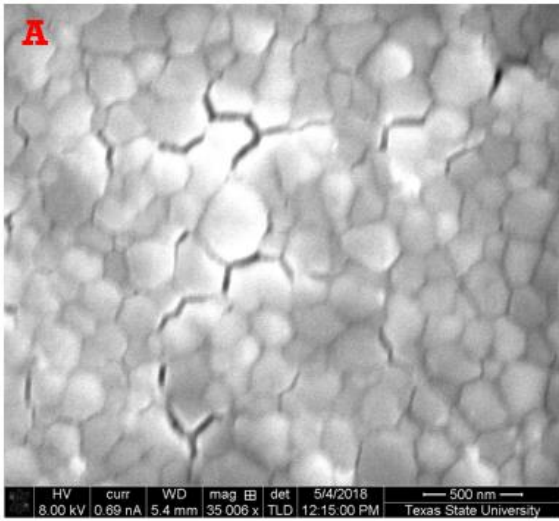


Figure 5-30: 10% Cesium alloy SEM image.

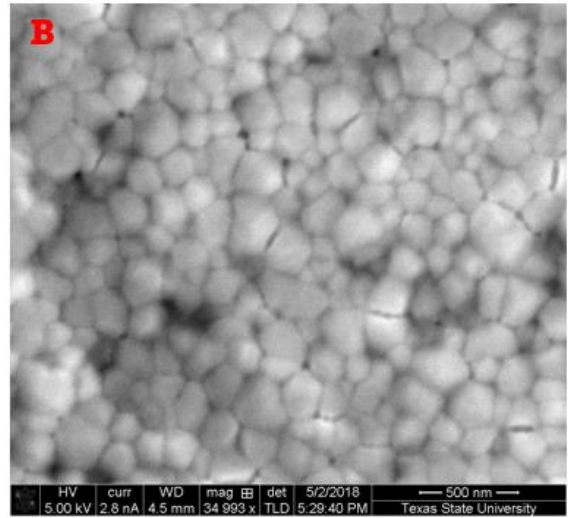
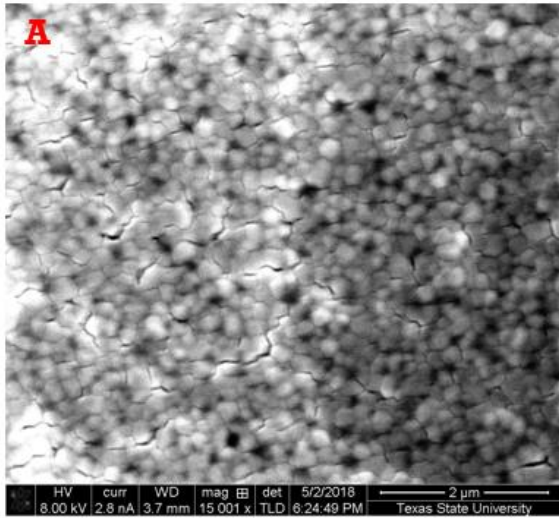


Figure 5-31: 10% Cesium alloy SEM image.

#### 5.4.5.3 15% Cesium Alloy SEM Images

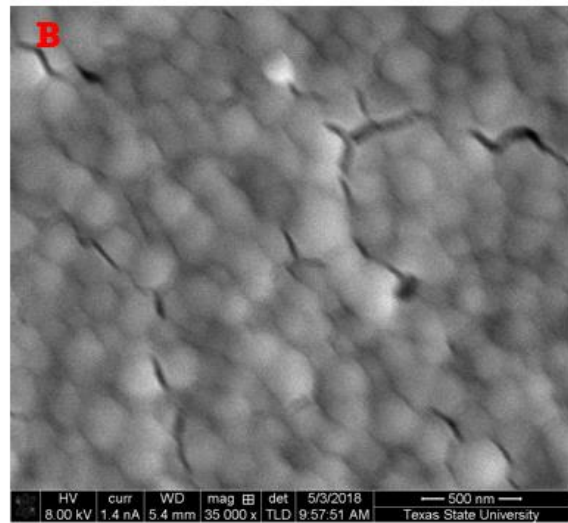
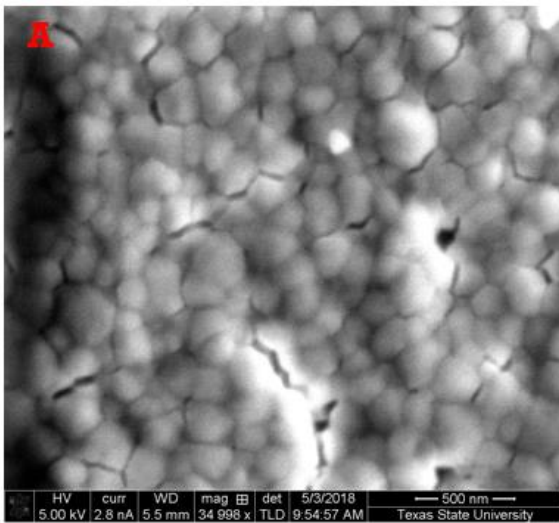


Figure 5-32: 15% Cesium (80% FA) alloy SEM images.

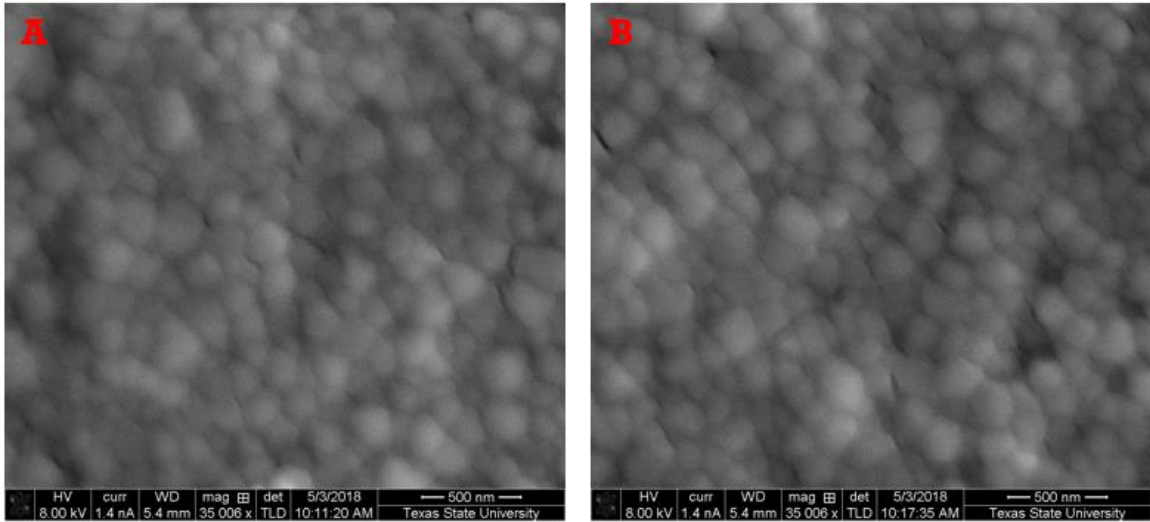


Figure 5-33: 15% Cesium (80% FA) alloy SEM images.

#### 5.4.5.4 20% Cesium Alloy SEM Images

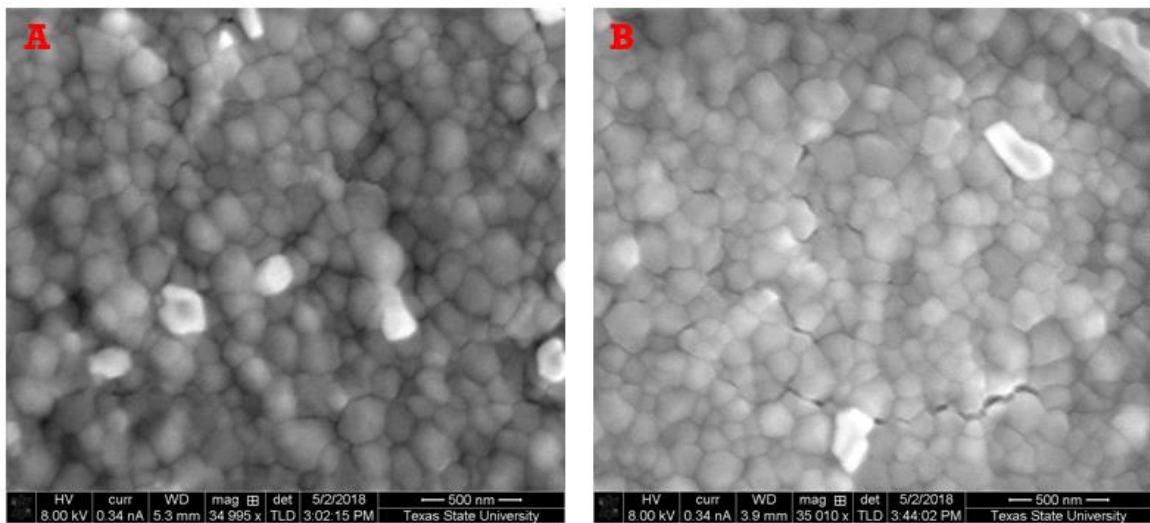


Figure 5-34: 20% Cesium alloy SEM images.

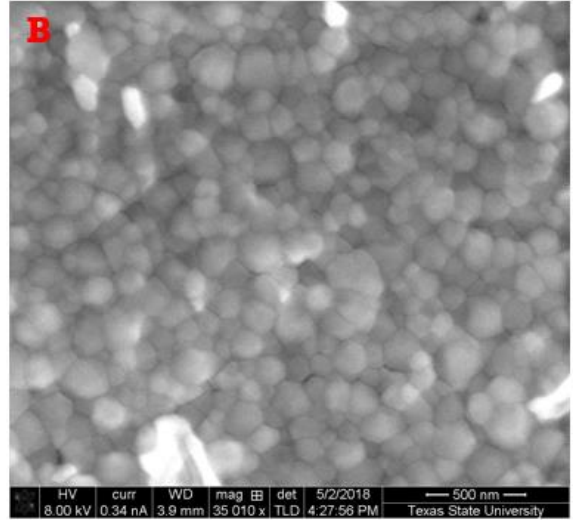
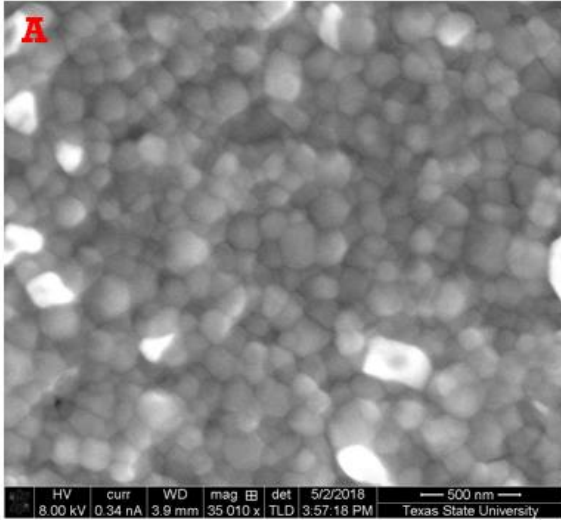


Figure 5-35: 20% Cesium alloy SEM images.

#### 5.4.5.5 25% Cesium Alloy SEM Images

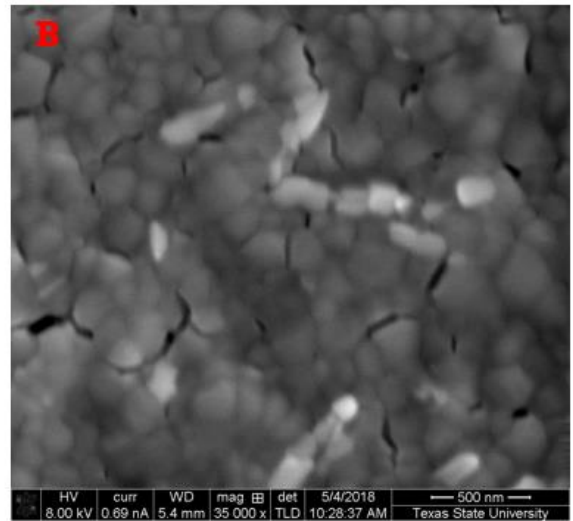
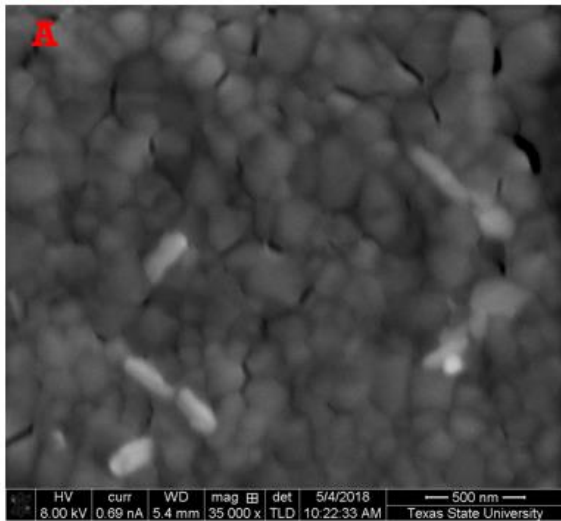


Figure 5-36: 25% Cesium alloy concentration.

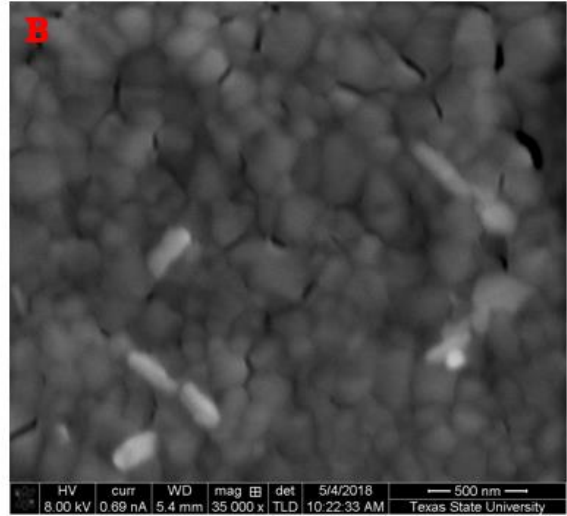
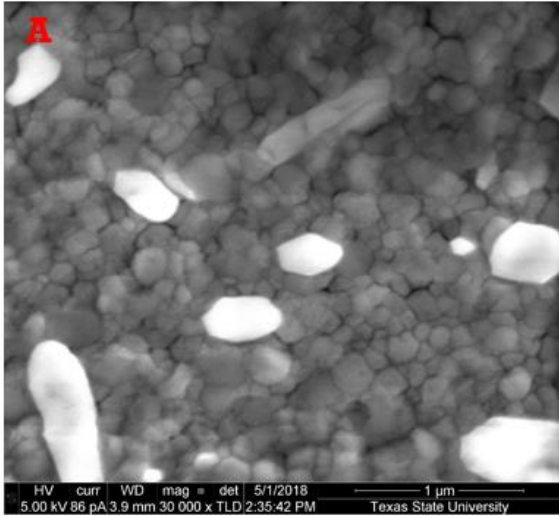


Figure 5-37: 25% Cesium alloy concentration.

#### 5.4.5.6 15% Cesium (70% FA) SEM Images

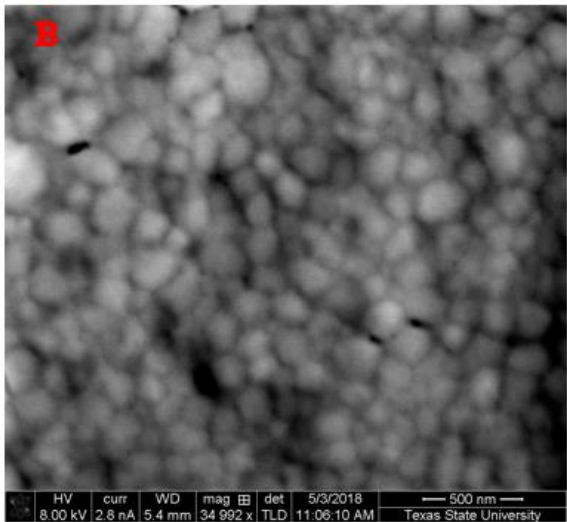
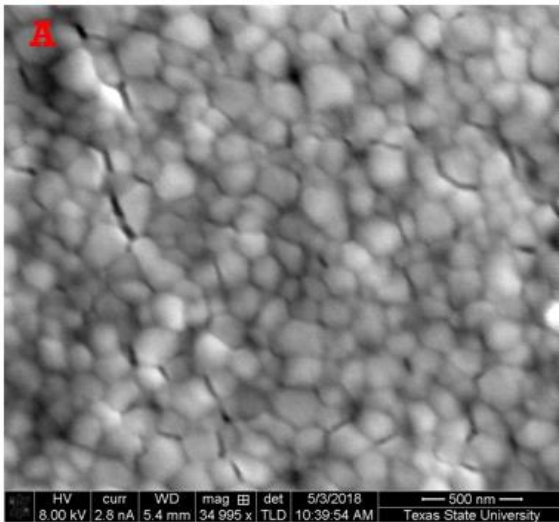


Figure 5-38: 15% Cesium (70% FA) SEM images.

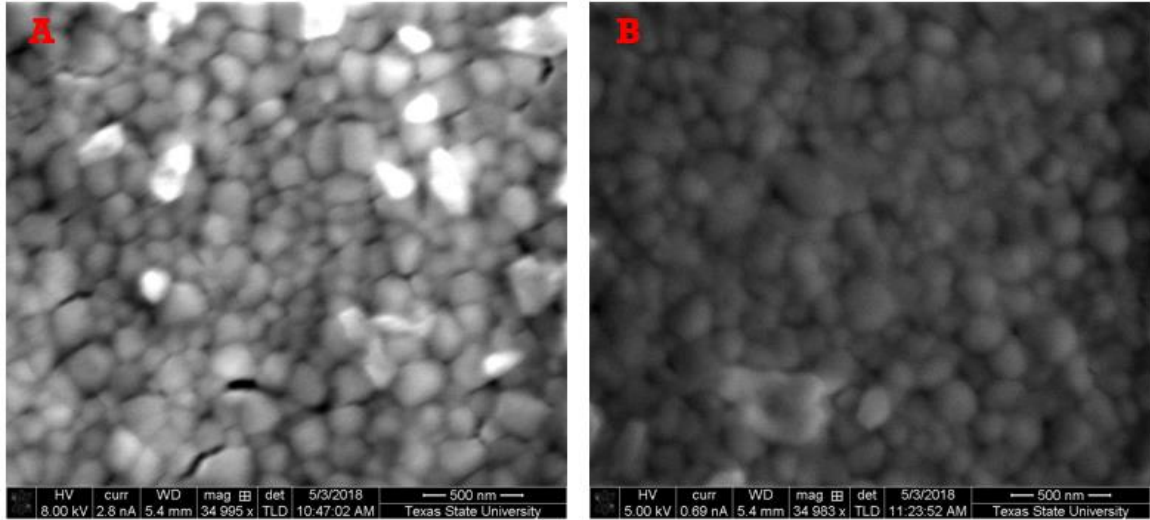


Figure 5-39: 15% Cesium (70% FA) SEM images.

#### 5.4.6 KPFM

Kelvin force probe microscopy (KPFM) was performed on the alloy samples. This AFM measurement was performed on the NIST AFM instrument. KPFM was attempted on the Bruker AFM instrument, however, the resolution on the NIST system was much better, even for the reference sample supplied by Bruker.

The NIST system operates in the same way the Bruker system does for KPFM measurements with two exceptions. The first is the sample mounting conditions are different for the NIST system. The Bruker system uses a vacuum chuck, hence the samples are mounted and grounded directly to chuck. The NIST system uses a special sample holder that provides the grounding path and uses a system of magnets to mount a sample. This setup provided a challenge to collecting data as the sample stack was subject to creep during the measurements. Care was given to minimize the effect, but creep was observed on most samples. The sample stack is highlighted in figure 5-40. As

can be seen, the high number of connections (2 magnets and 2 adhesives) contributed to the creep. The other change was that the samples had to be smaller than the 25mm x 25mm square glass substrates which required cutting the samples to a smaller size for analysis. Other than unavoidable debris caused by the cutting of samples into smaller samples, no effect to the measurements were observed for the topographical measurements performed.

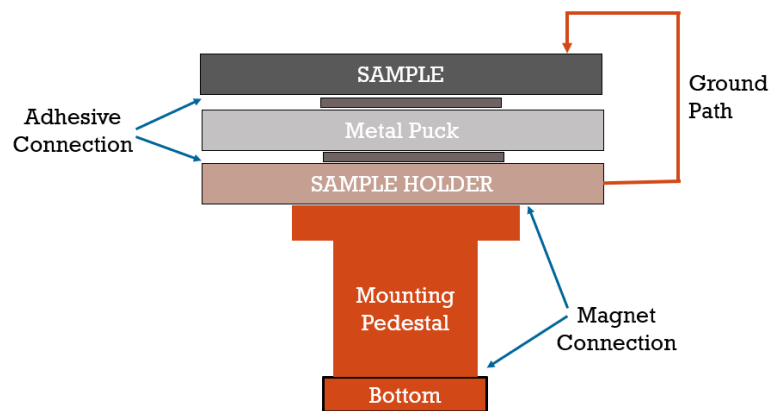


*Figure 5-40: NIST AFM Sample Mounting Stack. The stack has four connections that can cause creep.*

Samples for the NIST AFM were prepared on un-patterned ITO substrates. These substrates were then isolated to the metal puck via silver paste and copper tape. The silver paste posed additional challenges as it is a water-based solution which can degrade the alloy samples. Additionally, the use of copper tape might have also contributed to the creep effect seen on some of the samples shown below.

Results from the KPFM showed consistent data for each area tested and differences in the levels measured between alloy samples. Included in the measurements were samples measured under illumination and under dark conditions.

Note: illumination conditions were under LED lights the NIST AFM system is supplied with and are not traceable to AM1.5. All alloy samples did show marked differences between the light and dark KPFM modes. The results from the KPFM testing are summarized in table 5-6 below.

*Table 5-6: KPFM potentials measured under illumination and in dark.*

<b>SAMPLE</b>	<b>Dark (v)</b>	<b>Light (v)</b>	<b>Photo Effect (v)</b>
<b>5%</b>	<b>-0.1348</b>	<b>-0.2136</b>	<b>-0.0788</b>
<b>10%</b>	<b>-0.0890</b>	<b>-0.1928</b>	<b>-0.1037</b>
<b>15%</b>	<b>-0.1254</b>	<b>-0.1633</b>	<b>-0.0380</b>
<b>15% (70%FA)</b>	<b>-0.0106</b>	<b>-0.0825</b>	<b>-0.0719</b>
<b>20%</b>	<b>-0.2656</b>	<b>-0.3450</b>	<b>-0.0794</b>
<b>25%</b>	<b>-0.2472</b>	<b>-0.3788</b>	<b>-0.1316</b>

The KPFM images from the NIST AFM are shown in the figures below. In each case, a topo image of the area is shown next to the KPFM image. The images are in a four pack, with the dark images above and the illuminated images below. The additional topo image is there to demonstrate how much creep was encountered during the measurements.

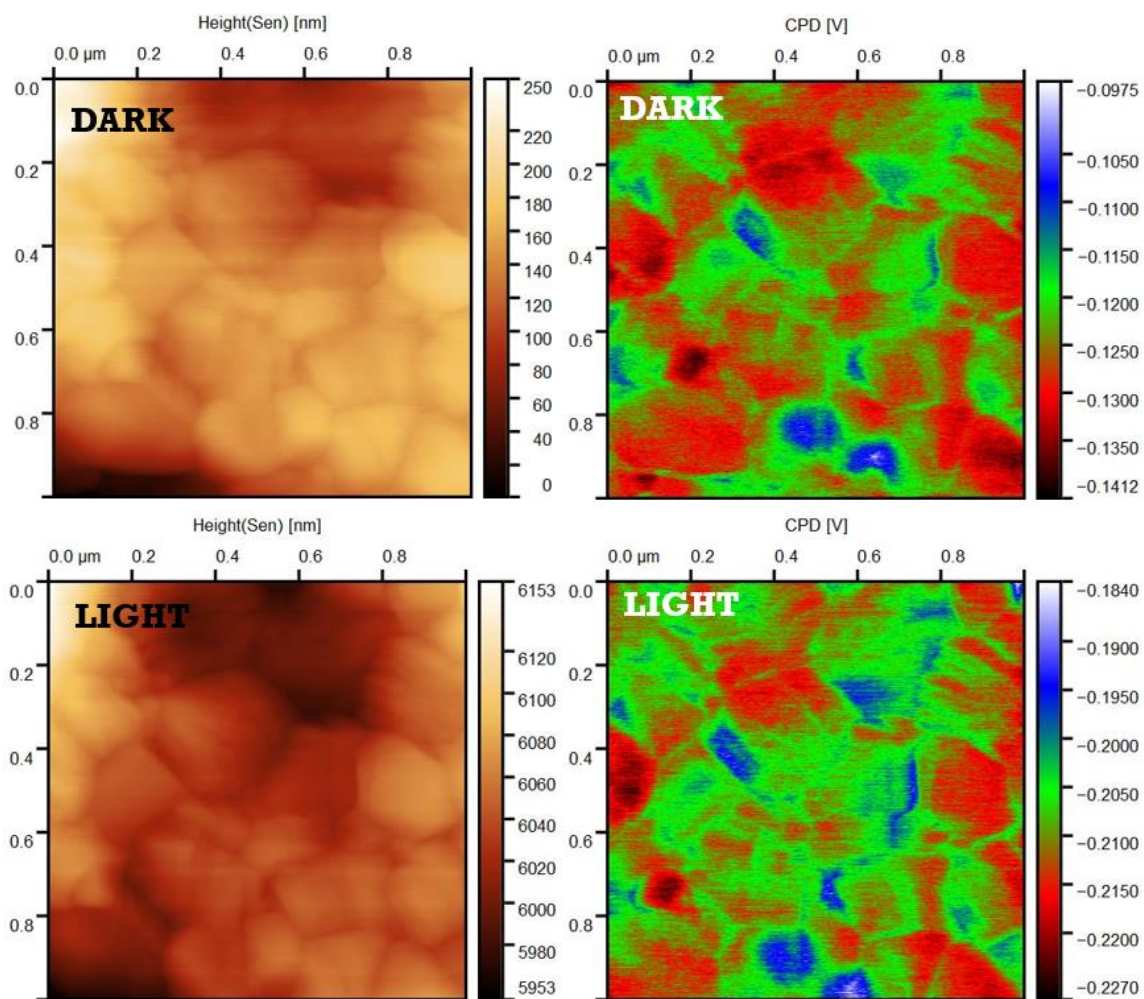


Figure 5-41: 5% Cesium KFM Images, Dark on top, under illumination on bottom.

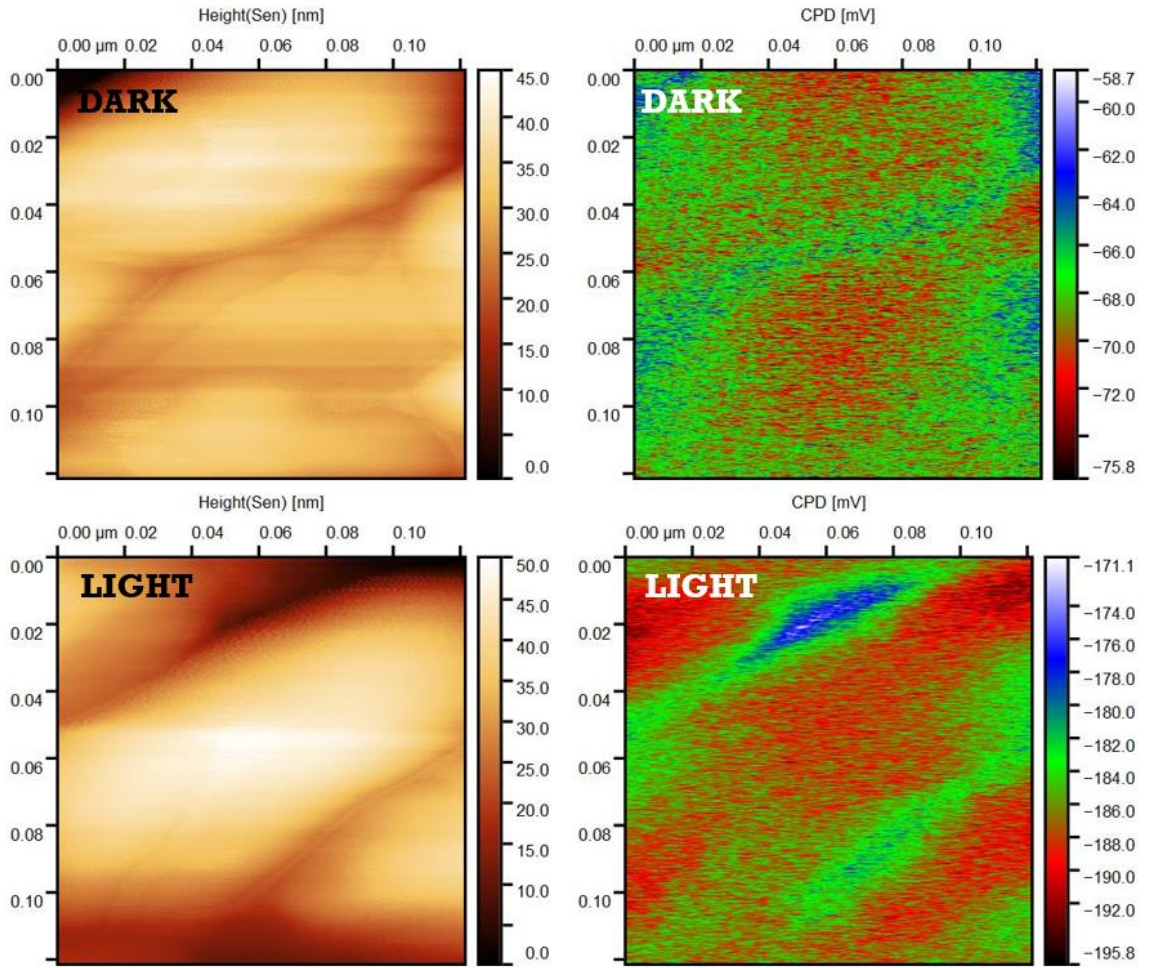


Figure 5-42: 10% Cesium, Dark on top, under illumination on bottom. Note the excessive creep on these samples.

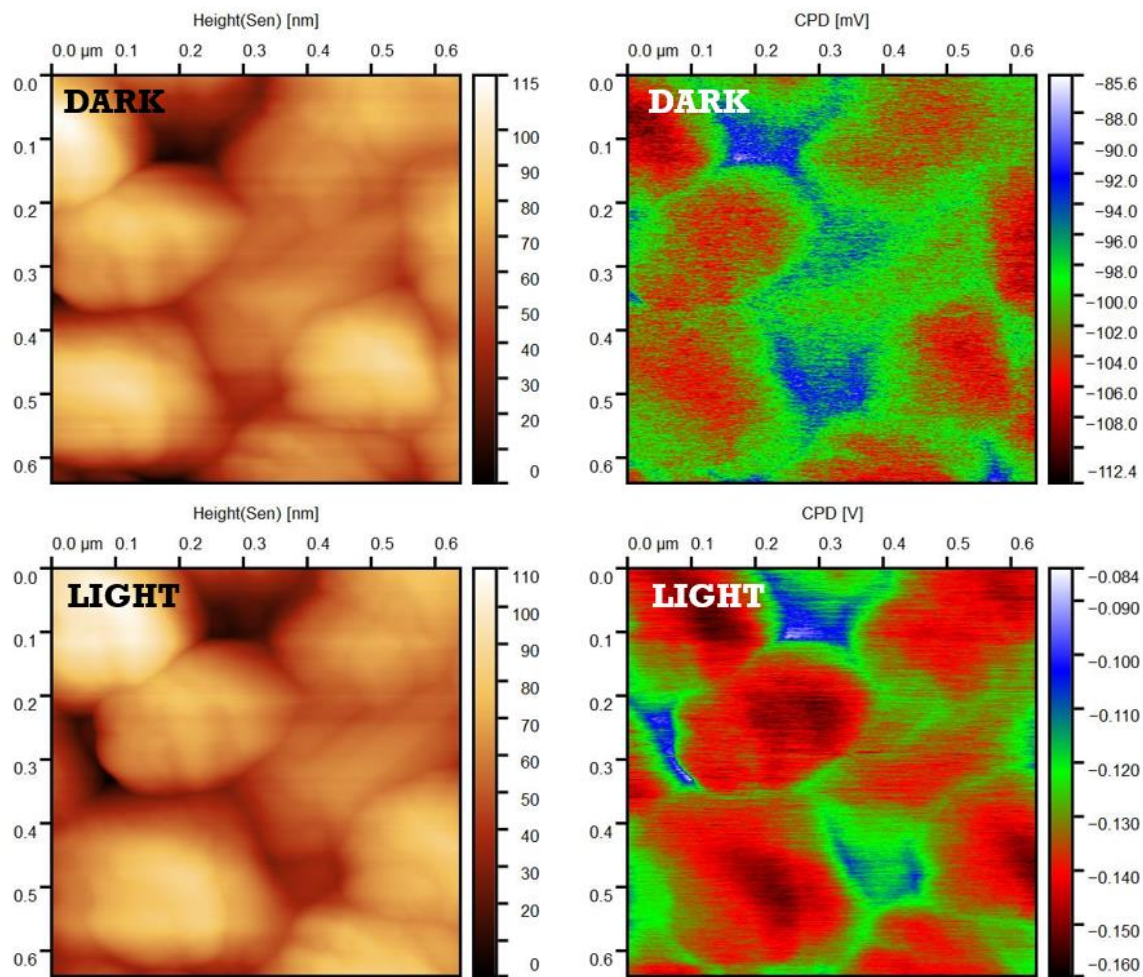


Figure 5-43: 15% Cesium, Dark on top, under illumination on bottom.

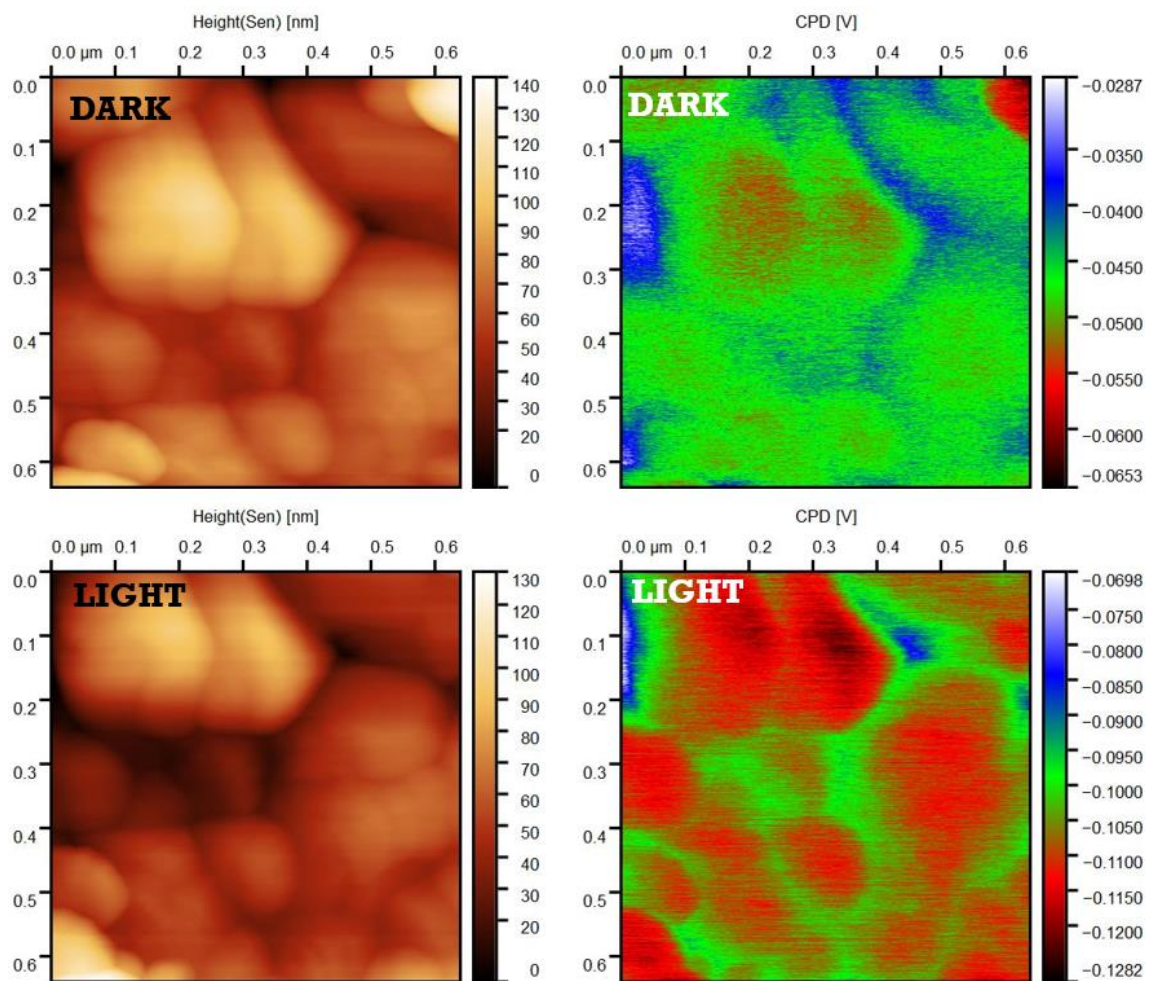


Figure 5-44: 15% (70% FA) Cesium, Dark on top, under illumination on bottom.

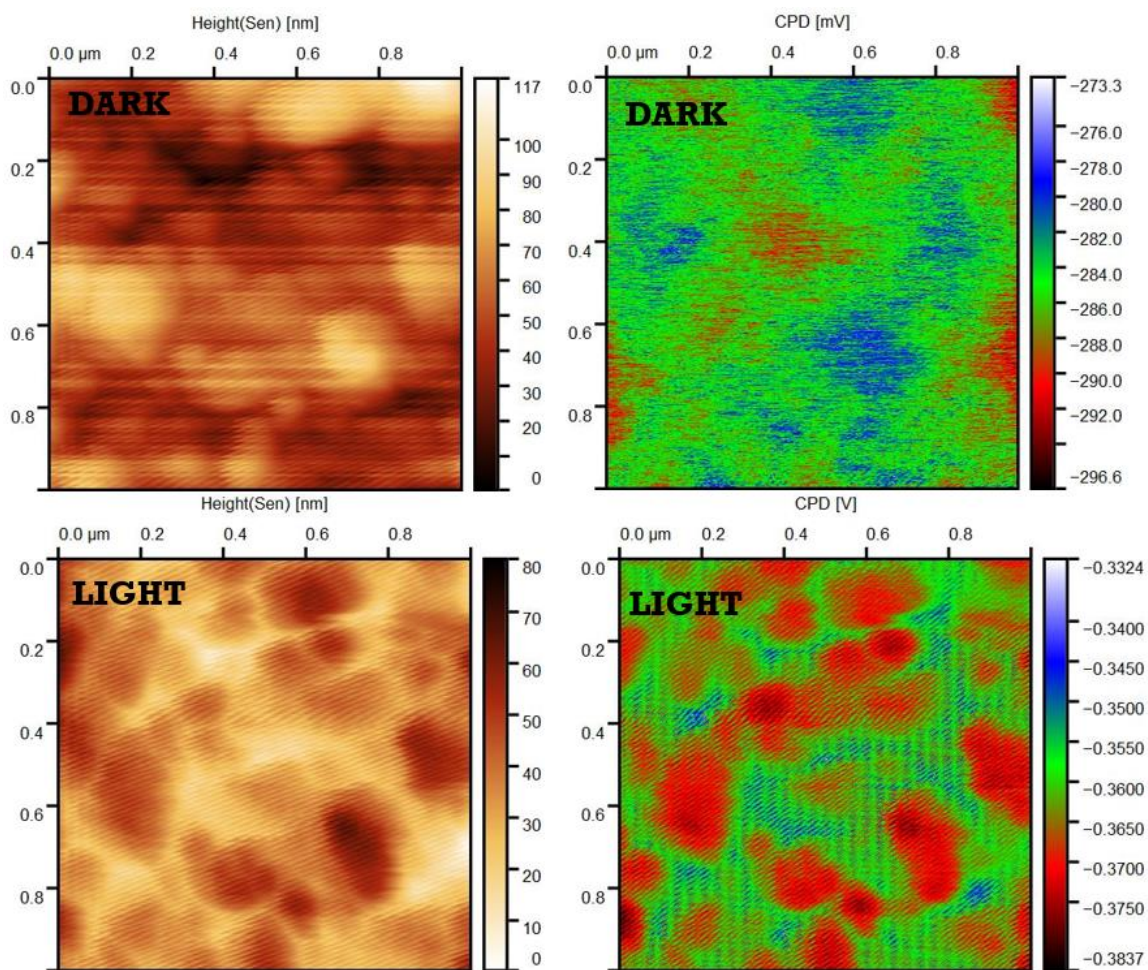


Figure 5-45: 20% Cesium Content, Dark on top, under illumination on bottom.

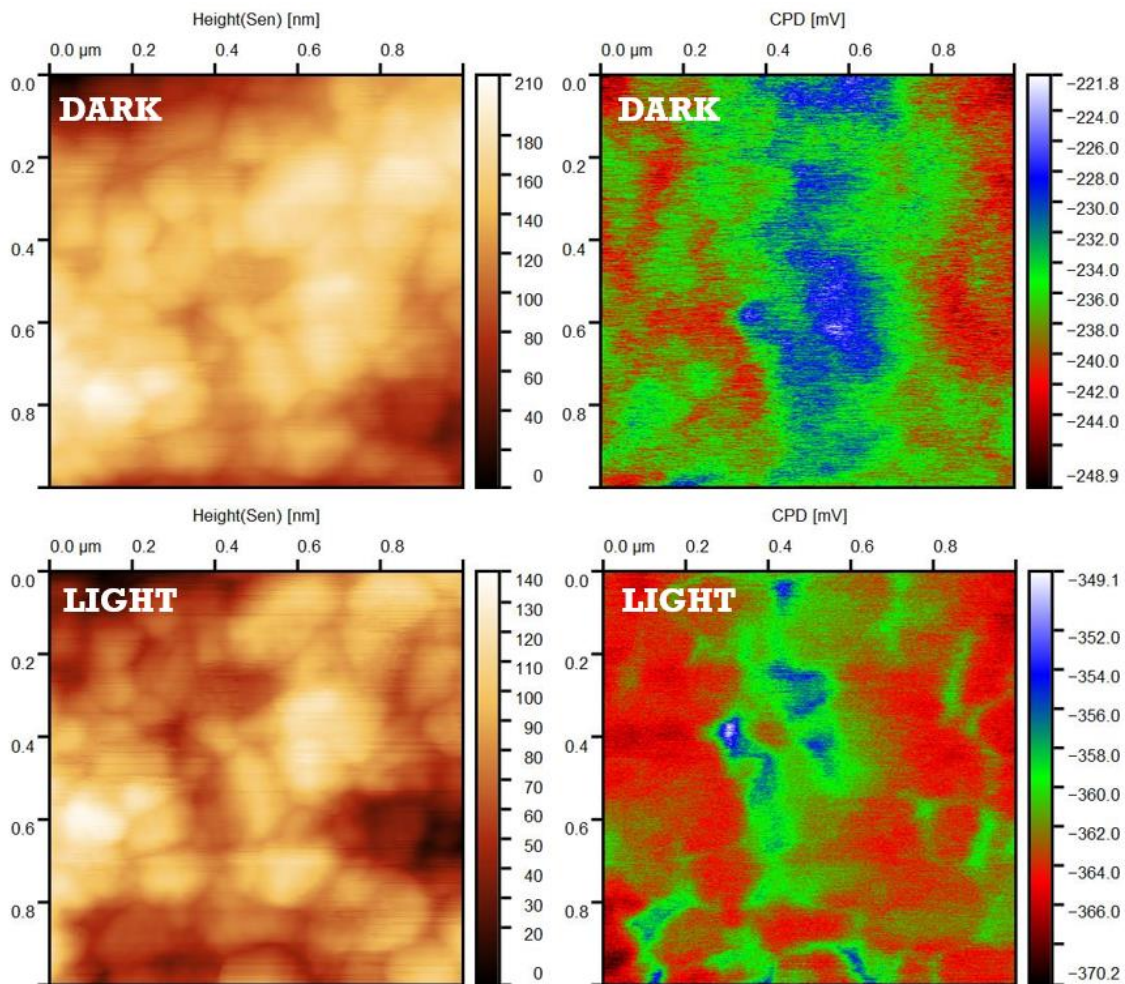


Figure 5-46: 25% Cesium, Dark on top, under illumination on bottom.

#### 5.4.7 IV Measurements

Next, IV measurements were made on the alloy samples. Over the course of testing for lifetime measurements multiple sets of alloys were created from fresh inks and cover the range of the different environmental problems observed in appendix 9.4. This allowed for considerable amount of data to be collected and statistically analyzed. Included in this data set is data for the one-step MAAC adduct method for creating MAPbI<sub>3</sub>. This method is a popular method for creating high performing devices in the

lab at Texas State University and has been reported by others in the lab[165]. For this reason, the IV data for this formulation is included as a reference to compare the alloys against.

The results of all alloy runs, regardless of performance, can be seen in figure 5-47. As can be seen here, poor performing devices are abundant for all alloy types. To clean this data up, any devices performing below 5% EFF and/or 6V  $V_{oc}$  were removed for statistical analysis. These parameters were selected as the IV curves for these devices tend to show non-photovoltaic performances, i.e., they behaved as a diode or a short or had other performance problems as to be able to rule them out.

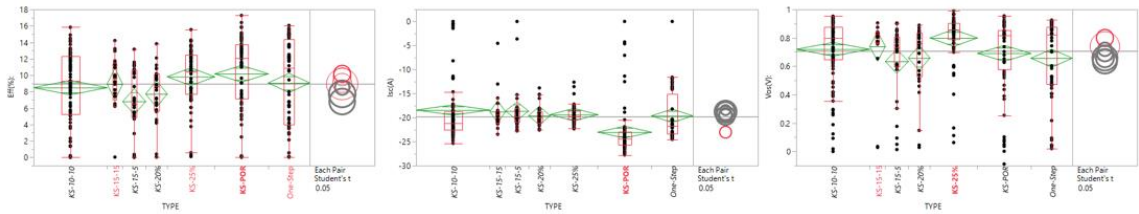


Figure 5-47: All performance data for all alloy types, data includes non-yielding devices.

The scrubbed data is shown in the following three figures: figure 5-48 the efficiency, figure 5-49 the open circuit voltage and figure 5-51, the short circuit current. The best performing device tested to date is the 5% cesium device with a ~17.3% PCE. Overall, based on efficiency, the  $\text{MAPbI}_3$  and cesium 5% alloy devices outperform the remaining alloys, handily. The 15% cesium (FA 80%) content alloy performed the worse of all the systems under investigation.

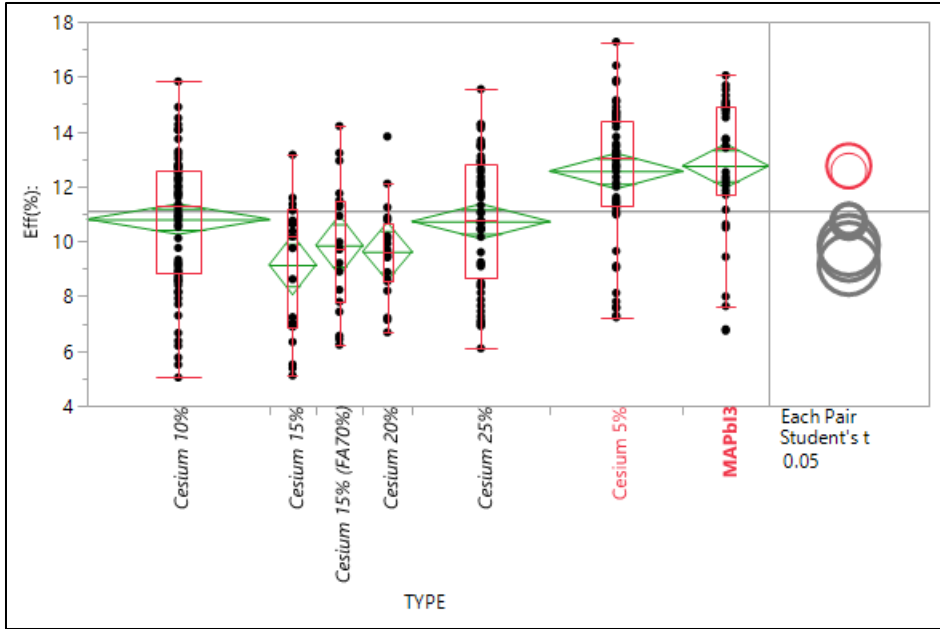


Figure 5-48: Alloy efficiency of devices with proper IV-curves.

Figure 5-49 shows the open circuit voltage measurements for the devices under investigation. Here there was more similarity between the devices. This should be expected as the measured bandgap for these devices are similar and  $V_{oc}$  is related to bandgap as given in generalized rule of thumb expression below[166]:

$$V_{oc} = 0.95E_g - 0.232 \quad (5-8)$$

Essentially, the expression in 5-8, indicates that there is a maximum value for  $V_{oc}$  that is related to the bandgap as well as the interaction with the transport layers. In these p-i-n devices, the transport layer affecting the  $V_{oc}$  is the PEDOT:PSS layer. Using the rule of thumb in equation 5-8, the range of  $V_{oc}$  expected for these devices and based on

bandgaps in table 5.5 should be 1.2405 ~ 1.2766V. The maximum reported  $V_{oc}$  was 0.99V and that was for a cesium 25% alloy.

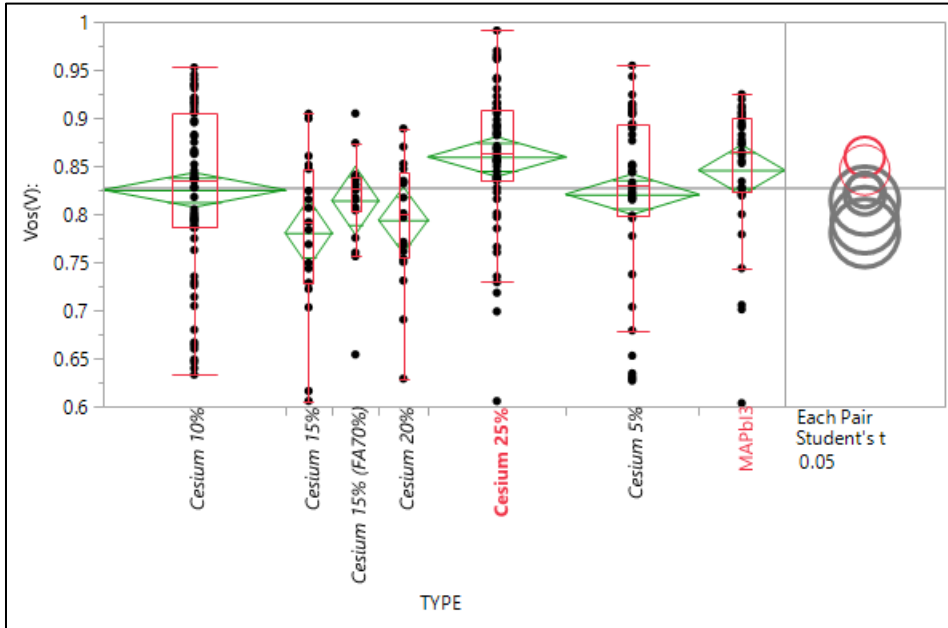


Figure 5-49: Open Circuit Voltage ( $V_{oc}$ ) for yielding devices.

As mentioned prior, the interface between the perovskite and PEDOT:PSS is considered to be the reason the  $V_{oc}$  is performing so poorly for these devices. An active area of research at Texas State is looking to replace the PEDOT:PSS with another hole transport layer to address this. For example the use of copper iodide can increase the observed  $V_{oc}$  by ~6% [167] or by ~12% using copper oxide[168]. Previous work done at Texas State highlights the importance of interfaces[10] on device performance. Despite the fact that PEDOT:PSS is not a good hole transport layer, it is possible to ascertain how well of an interface exists between the HTL and alloy by examining the difference between the observed  $V_{oc}$  and theoretical  $V_{oc}$ . The voltage gap can measure how well the interface between the two materials are actually performing [169]. Figure 5-50

shows the voltage gap. There is a clear trend with the data showing a larger gap and poorer performance with increasing cesium concentration. That gap disappears for the 25% cesium alloy. The measured  $V_{oc}$  is independent of observed crystal size, lattice size and layer thickness. There is a similar trend seen in the dependence of  $V_{oc}$  on the ionization potential defined earlier. The 25% cesium concentration has the highest value and that might be contributing to the performance of the alloy for  $V_{oc}$ .

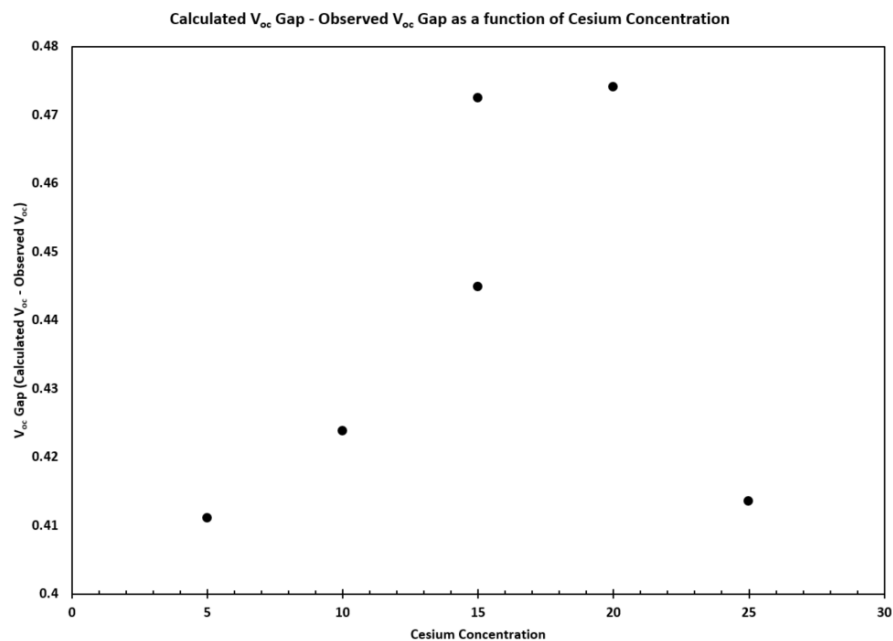


Figure 5-50: Interface performance of PEDOT:PSS and the perovskite alloys.

Figure 5-51 shows the short circuit current. This data shows the performance of the alloys and the differences between them in the most clarity. The first thing to notice in figure 5-51 is the 5% cesium current performance. The 5% cesium current performance is not only statistically outperforming the other alloys, it does so by a wide margin, almost an outlier of the group. The current performance of the 5% alloy is what drives its efficiency performance.

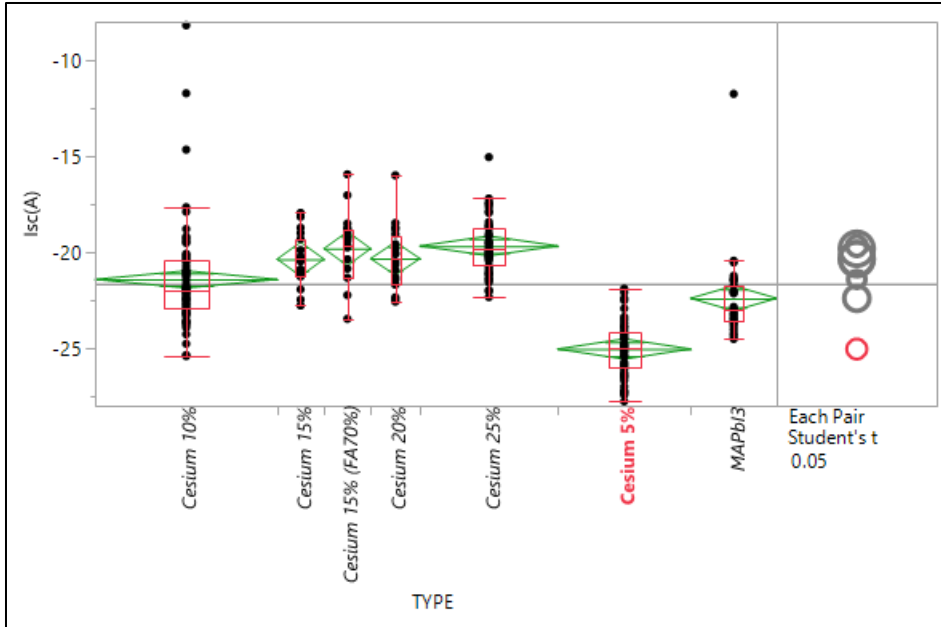


Figure 5-51: Short circuit current of the yielding devices.

One of the interesting trends seen in the IV data is the trend of cesium content and current and is shown in figure 5-52A. Figure 5-52 shows a second order trend with a high  $R^2$  value (95.5%) for the current as a function of cesium concentration. This trend is another data point highlighting the importance of the cation in the alloy of perovskites. However, care should be used in evaluating current performance and cesium content as this trend can be related to the differences in the performance based on bandgap as seen in figure 5-52B.

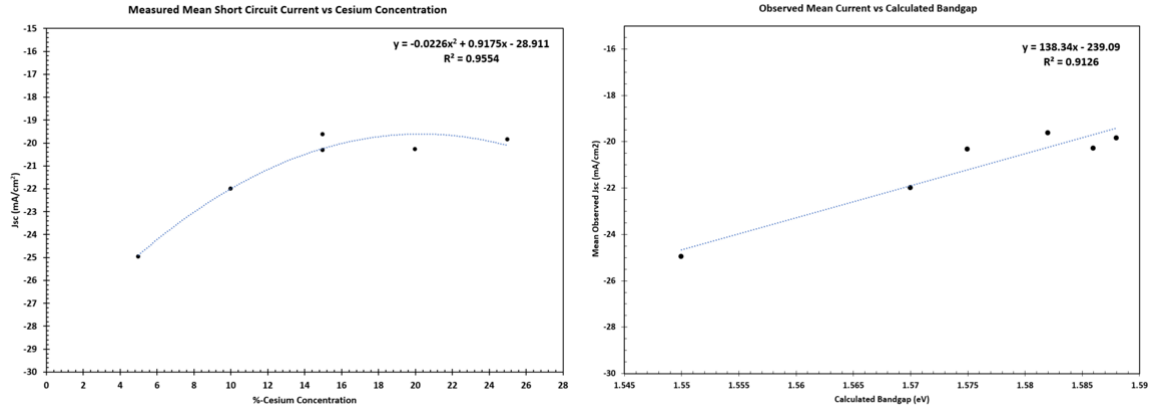


Figure 5-52: A) Short Circuit Current vs Cesium Concentration, B) Short circuit vs Bandgap.

The remaining phenomena for the current performance is the dependence on thickness. The perovskite is a solar material and material thickness will effect current as the more material phonons can penetrate, the more current that can be produced.

Figure 5-53 shows the measured current of the alloy devices against the alloy device thickness. There is a strong dependence (second order) on thickness, although these are linear relationships as FA content effects performance as well.

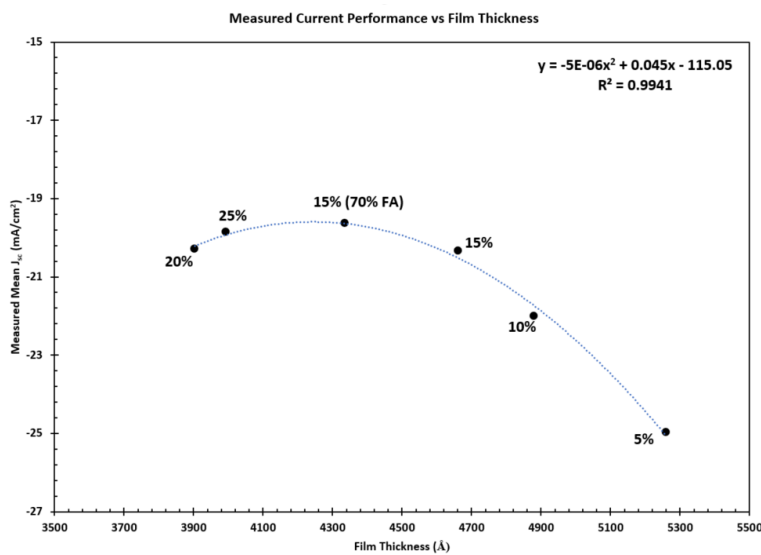
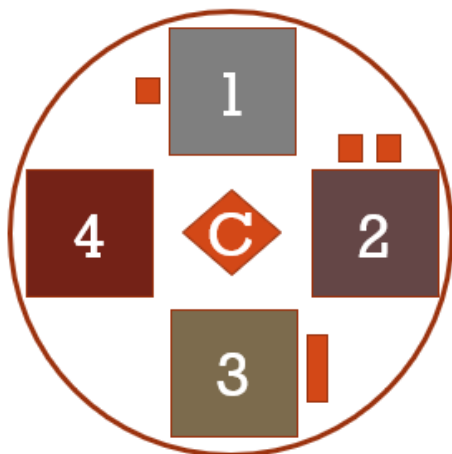


Figure 5-53: Alloy current vs thickness, graph shows importance on layer thickness.

#### 5.4.8 XPS Data

The XPS data were measured over a course of several weeks. A few mishaps with the instrument required some maintenance intervention. The earlier samples, the detector appears to be more sensitive to the peaks and peaks shapes are much more defined. The latest data, the peaks are a little smaller, but can be measured.

Samples were placed on a metal carrier as shown below in figure 5-54. The samples were mounted to the metal carrier using double sided tape. Additional tape was used to indicate which sample was which for analysis. The center of the metal carrier was left empty and was used to calibrate the system for run to run matching using the carbon found in stainless steel. Samples loaded into the XPS system were not baked to 150°C per the SOP, but rather left in the load lock to pump down to base prior to moving into the transfer system. This usually took several hours to achieve, however, prevented any thermal degradation to the samples (MAPBI).



*Figure 5-54: XPS Sample holder showing layout of samples 1-4 and the center position for run to run alignments.*

Samples were calibrated to shifts in the detector from run to run and within run by looking for the carbon found in the stainless steel in the center of the metal carrier as shown above. The presence of iron and the lack of lead in the XPS signal indicated that the x-rays were hitting the center and not the samples and was checked for each run. Despite two maintenance events on the XPS between sample acquisition, the total deviation between the center carbon was 1.9eV over a ~8-week period.

The corrected XPS data are presented below. As can be seen, the sensitivity (counts) dropped after the second maintenance on the XPS which required opening the system for maintenance. A second axis is used on some of the data to better define the peaks in the group chart. The 0% cesium sample is a one-step acetate adduct MAPbI sample and is included only as a reference point.

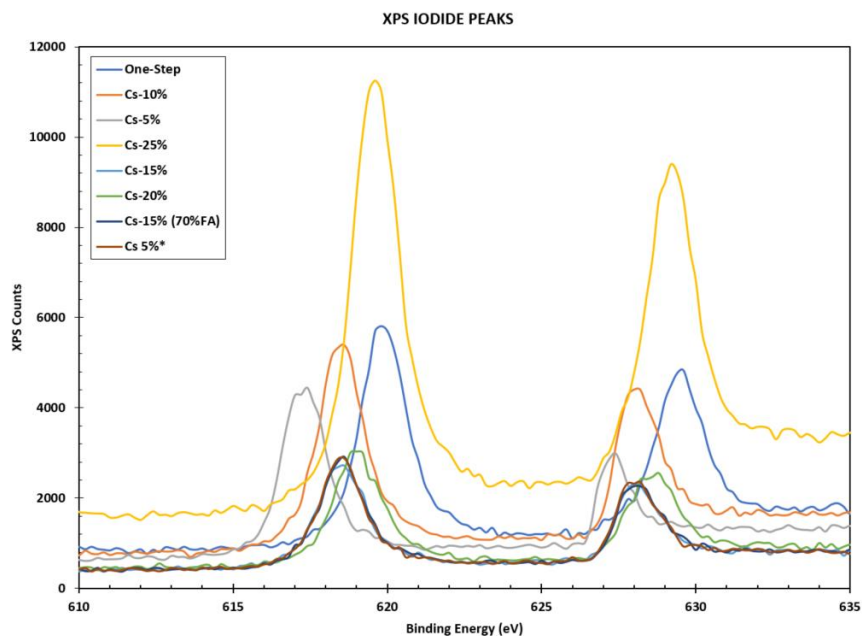


Figure 5-55: XPS results for the iodide peaks in the perovskite alloys.

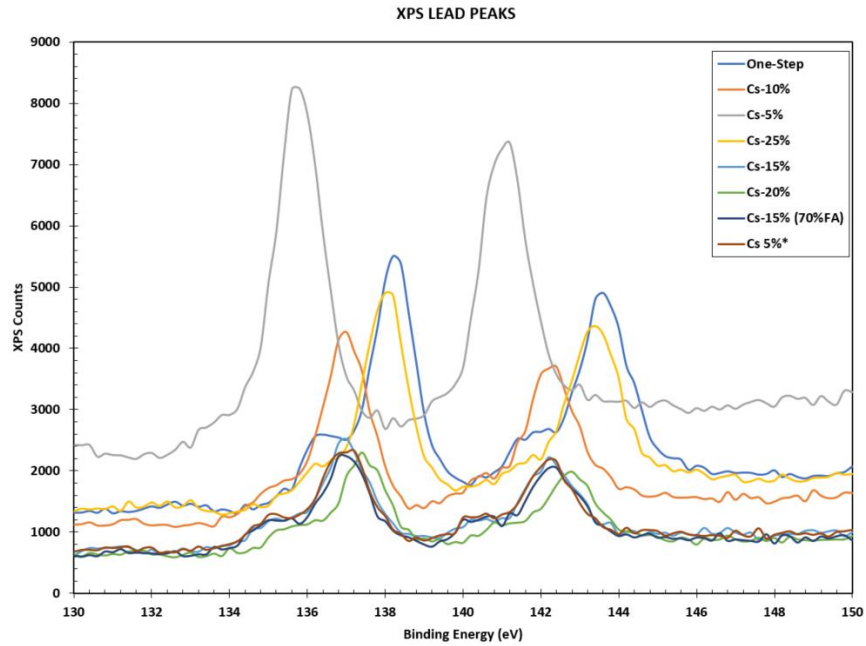


Figure 5-56: XPS results for the lead peaks in the perovskite alloys.

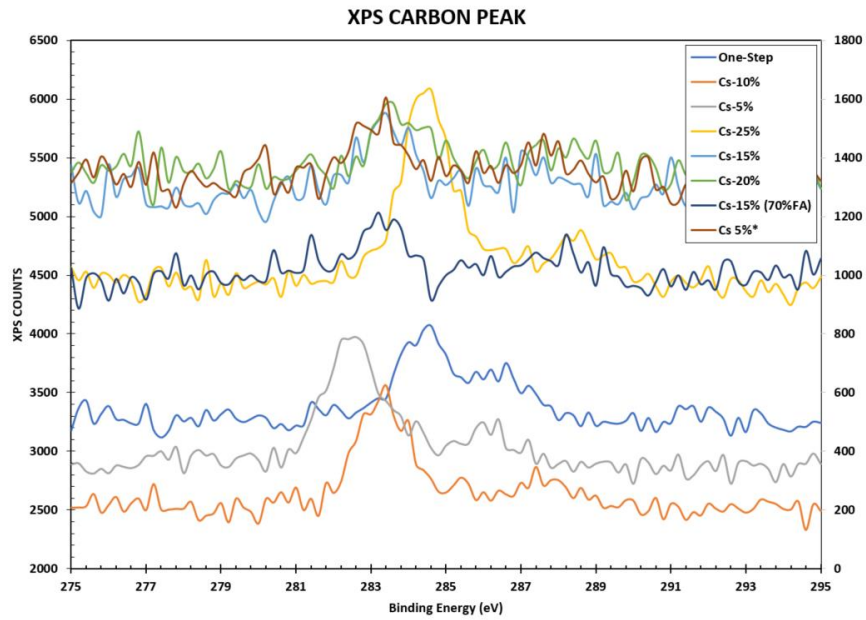


Figure 5-57: XPS results for the carbon peak in the perovskite alloys.

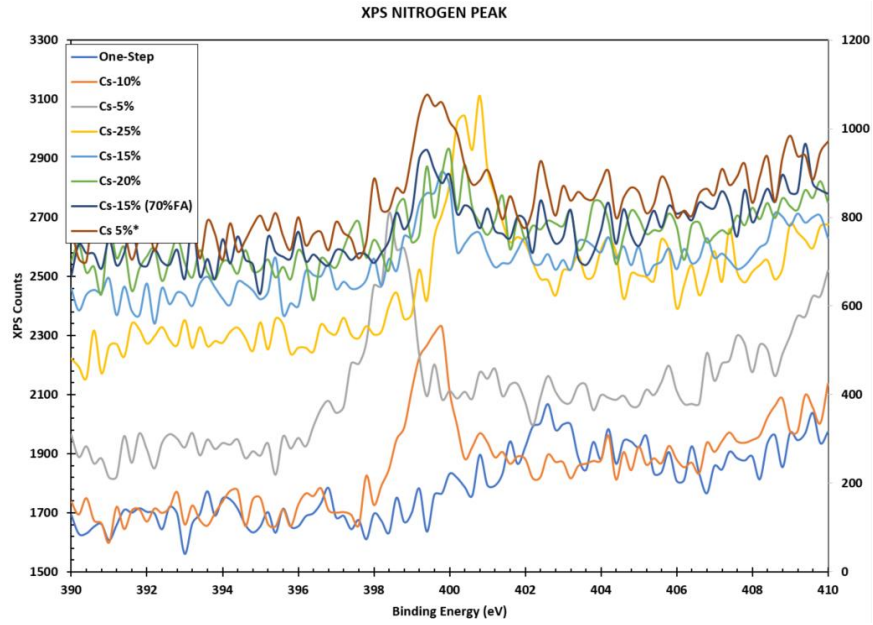


Figure 5-58: XPS results for the nitrogen peak in the perovskite alloys.

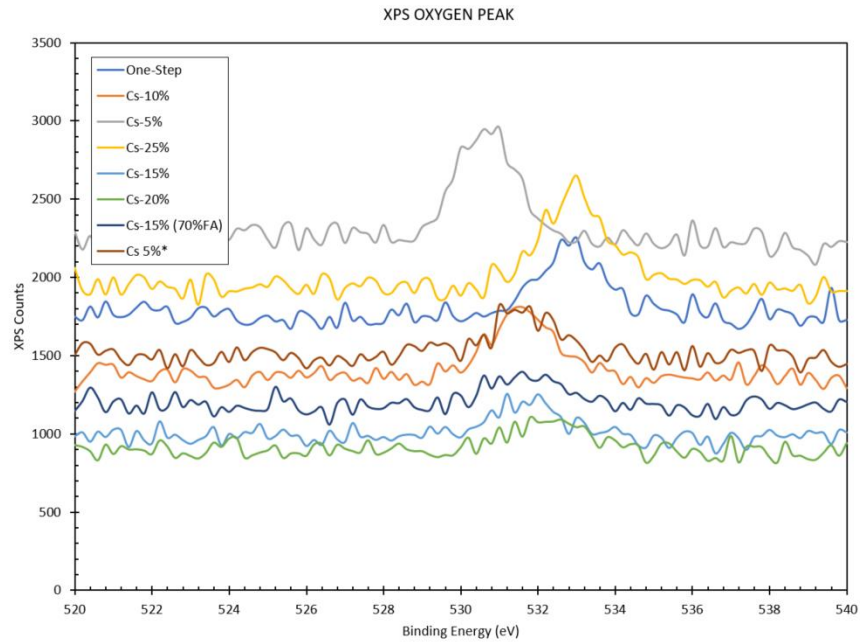


Figure 5-59: XPS results for the oxygen peak in the perovskite alloys.

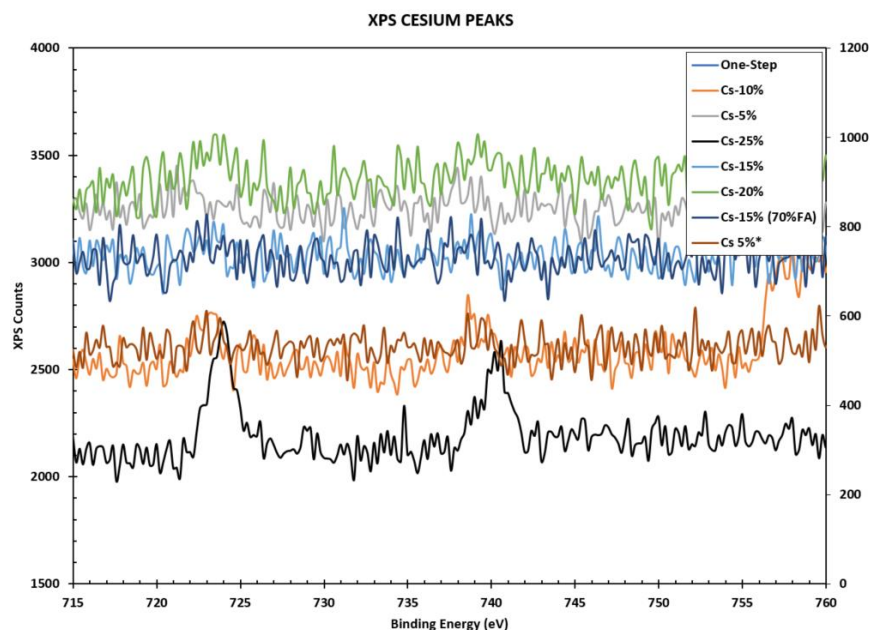


Figure 5-60: XPS results for the cesium peaks in the perovskite alloys.

Reviewing the XPS spectra, there is a difference in both the peak location and for the lead, iodide and cesium, a difference in the separation between the peaks (orbitals). One note, cesium was incredibly hard to resolve, data from cesium was based on high points in the approximate area of the spectrum where it was expected to be found. As a result, confidence in the cesium data should be regarded as low. Again, the trouble with prolonged exposure to X-rays is sample degradation[128]. None was observed during measurements and was verified by reimaging old samples and not observing any shifts.

Trends were observed for the lead, iodide nitrogen and cesium binding energies. These trends are good observations as these atoms are what interacts together to form the crystal lattice[13]. As can be observed for alloy systems, increasing the cesium concentration, increases the binding energy for all four crystal lattice participants and are shown in figure 5-61, 5-62, 5-63 and 5-64.

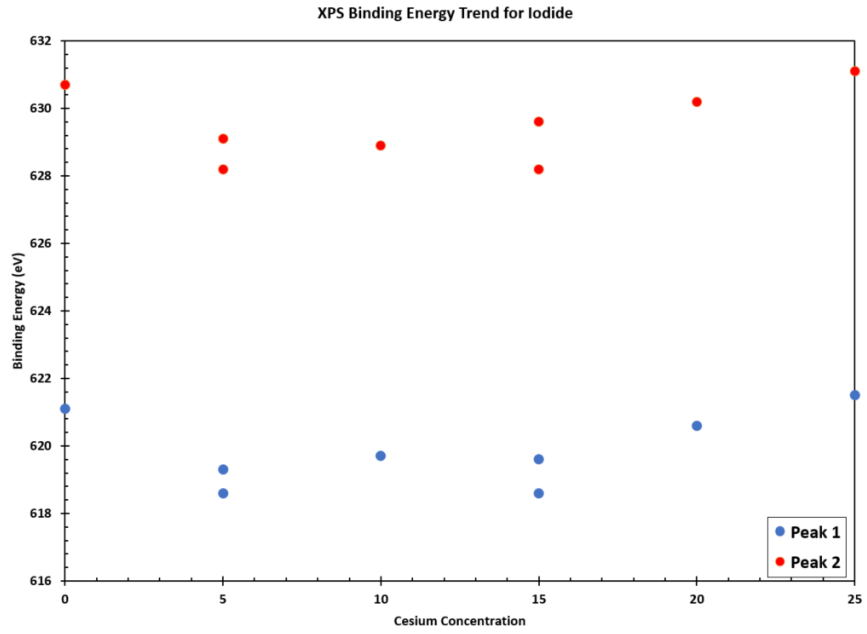


Figure 5-61: Binding energy trend for iodide as a function of cesium concentration.

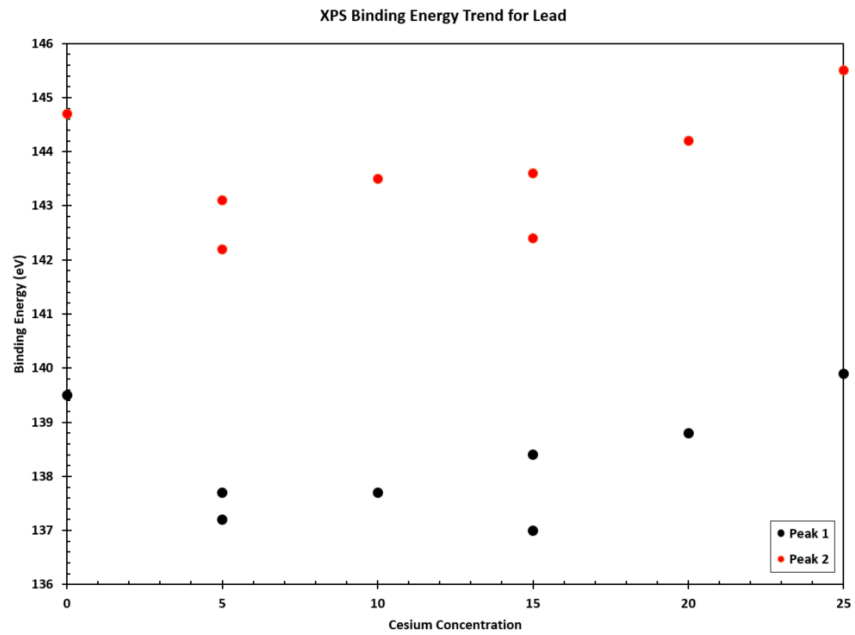


Figure 5-62: Binding energy trend for lead as a function of cesium concentration.

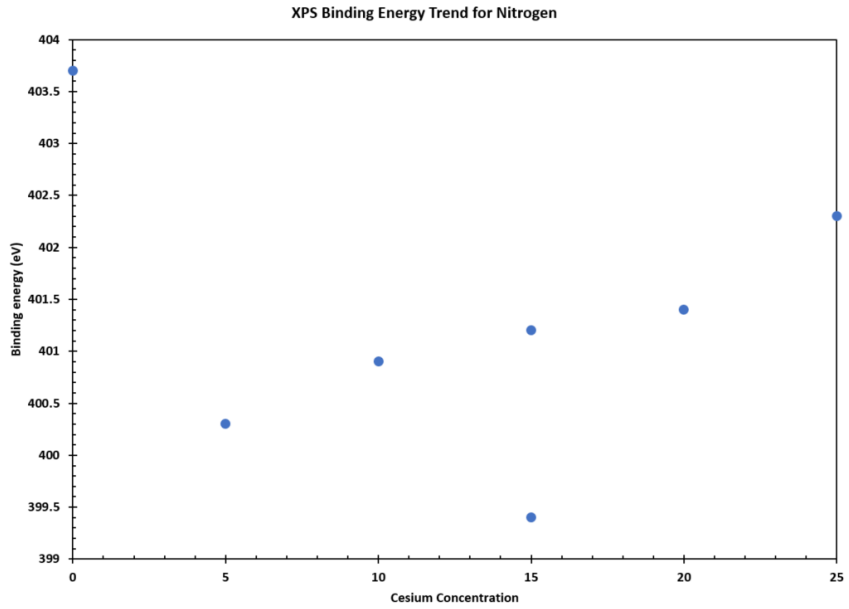


Figure 5-63: Binding energy trend for nitrogen as a function of cesium concentration.

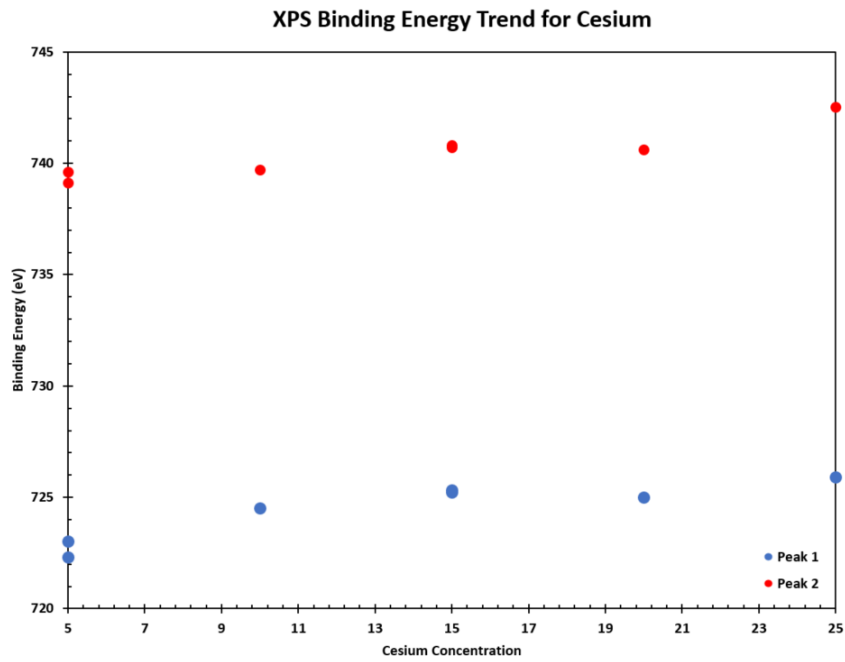


Figure 5-64: Binding energy trend for cesium as a function of cesium concentration.

The nitrogen trend was a bit surprising to observe as there are three nitrogen atoms (two in the FA and one in the MA), however, the increasing cesium concentration still pushed the binding energies to higher values. The trend for the cesium binding energy is also apparent, albeit less confidence in this trend is warranted as stated previously.

The next set of figures deal with the energy differences between the doublet peaks found in iodide, lead and cesium. For cesium and iodide, these energies are associated with the  $3d_{3/2}$  and  $3d_{5/2}$  orbitals and for lead these are the peaks for the  $4f_{5/2}$  and  $4f_{7/2}$  orbitals.

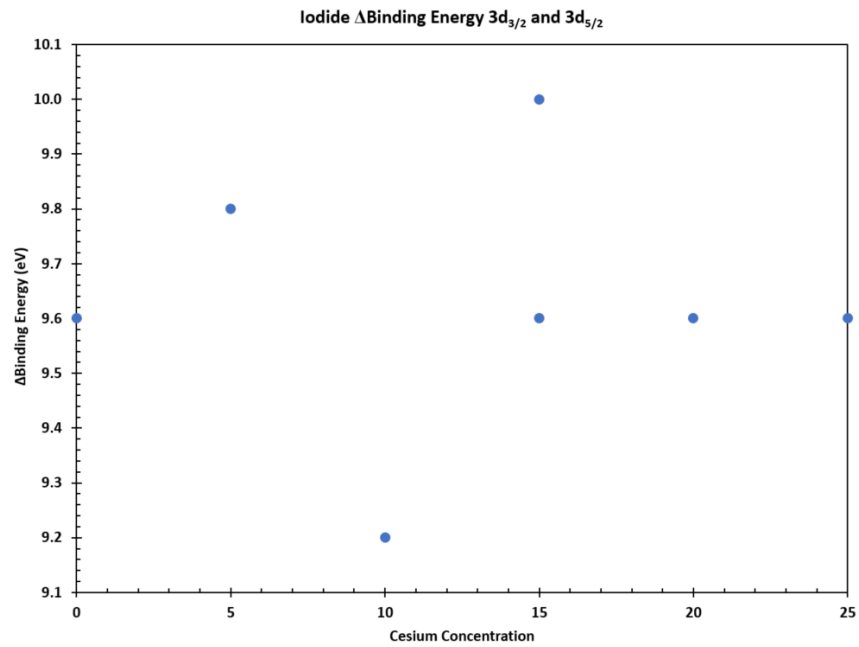


Figure 5-65: Iodide binding energy.

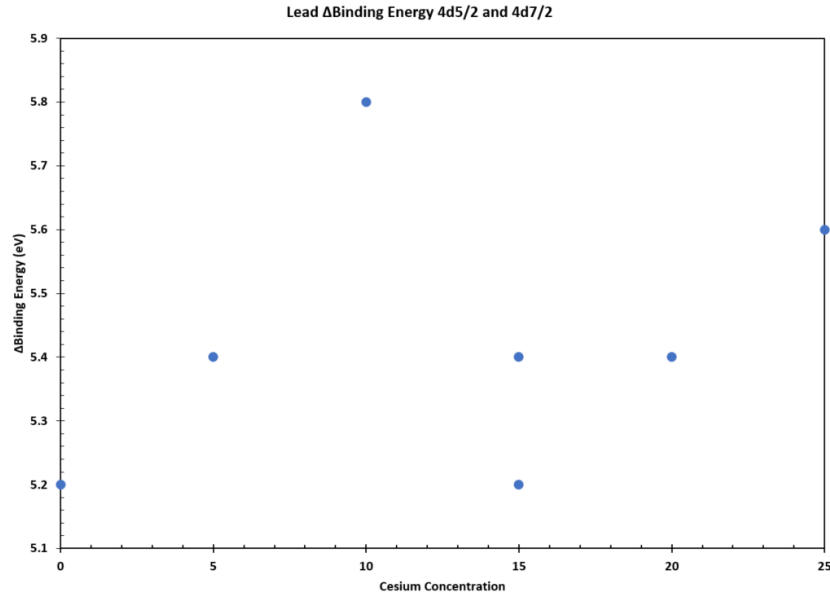


Figure 5-66: Lead binding energy.

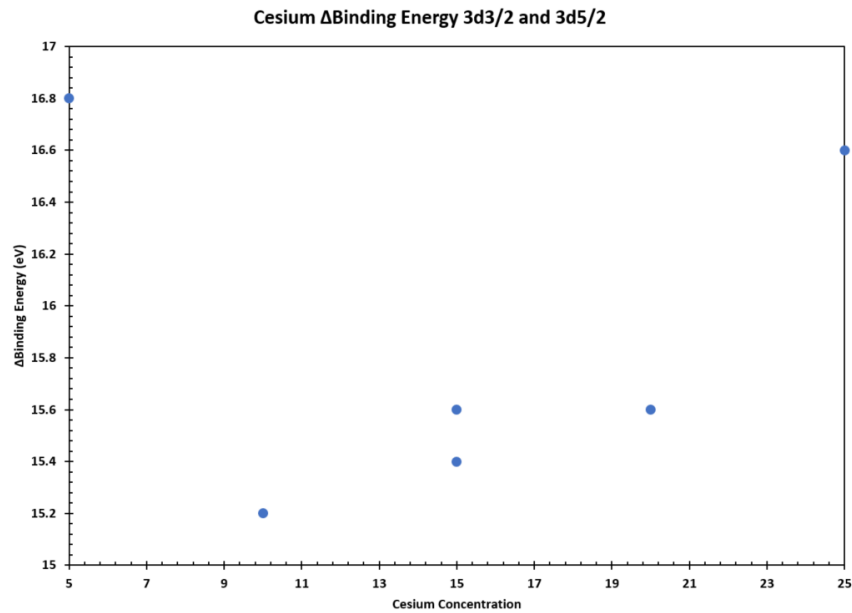


Figure 5-67: Binding energy gap of cesium.

The binding energy gap for each of the cation crystal lattice components differed than what was reported in literature for 'naked' systems. The observed binding energy

difference for lead was 5 eV, for iodide it was 11 eV and for cesium 14 eV [170].

Reviewing the data, the energy difference increased for the cesium and lead and decreased for the iodide. This is a finding supported by the arrangement of the crystal lattice, the two cations are contributing electrons to the lattice, hence the energy in the outer shells increases to keep additional electrons from being lost. For the anion (iodide) the addition of the electron in the lattice indicates a relaxing of the binding energies as the excess electron is added to the orbital.

Nitrogen experiences a slight chemical shift from 398 eV into the 400-402 eV range. Nitrogen also experiences the largest chemical shift of the cations. This could indicate that nitrogen is giving up its electron to the crystal structure, resulting in a tighter bond for the remaining electrons. Alternatively, the nitrogen electron is in the 1s shell and is tightly held due to proximity of the orbital to the nucleus.

In general, for nitrogen, the chemical shift observed matches well with the observed lattice spacing, that is the greater the lattice spacing, the greater the chemical shift. The other crystal lattice participants do not have a clear trend and the chemical shifts seen with iodide, lead and cesium are flat in terms of relationship with the lattice constants. The nitrogen is associated with the MA and FA cations which are modeled to be 'free floating' within the crystal lattice[55][13], thus the general increase in binding energy with an increasing crystal lattice size could be related with the nitrogen being able to hold on to its electron better due to a larger distance from the iodide.

The IV data ( $J_{sc}$ ) trends are also an indication that it is the nitrogen electron contributing to the current as  $J_{sc}$  gets higher with smaller lattice sizes, which is a loose function of cesium concentration. Since the binding energy change with the other lattice atoms are small in relation to nitrogen, this could be the reason behind the current increase with increasing nitrogen concentration. With two nitrogen atoms interacting with the lattice, further study is needed.

The carbon XPS trends are shown in figure 5-68. There is not a trend observed. The carbon peak is at 285eV[170] and the data reflects a tight grouping around that value. As the carbon atom is not interacting with the crystal lattice, this finding is not extraordinary.

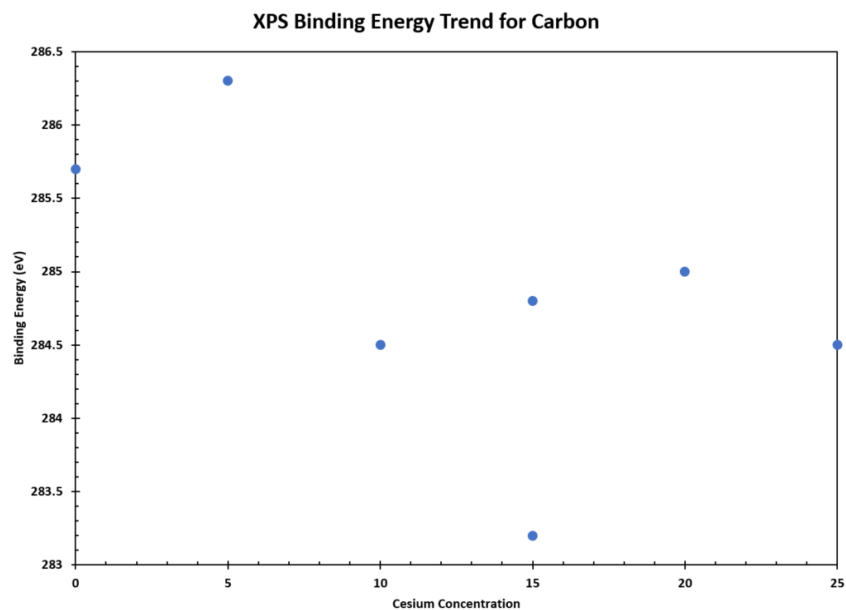


Figure 5-68: Carbon XPS trend.

Oxygen was also observed in the samples as seen in figure 5-69. XPS was also performed for silicon and sulfur to test whether the oxygen observed was from the glass

substrate. Neither silicon or sulfur was observed to be present. The oxygen observed is theorized to be passivating the grain boundaries of the crystal and thus interacting with the lead and cesium. The perovskite films are deposited in a O<sub>2</sub> and H<sub>2</sub>O free atmosphere, however the bare film must be measured and there is no current way to prevent exposure to atmosphere, hence the grain boundary passivation. FTIR measurements could provide more information, however, the detector does not measure in the range to verify Cs-O and Pb-O bonds [171] [172].

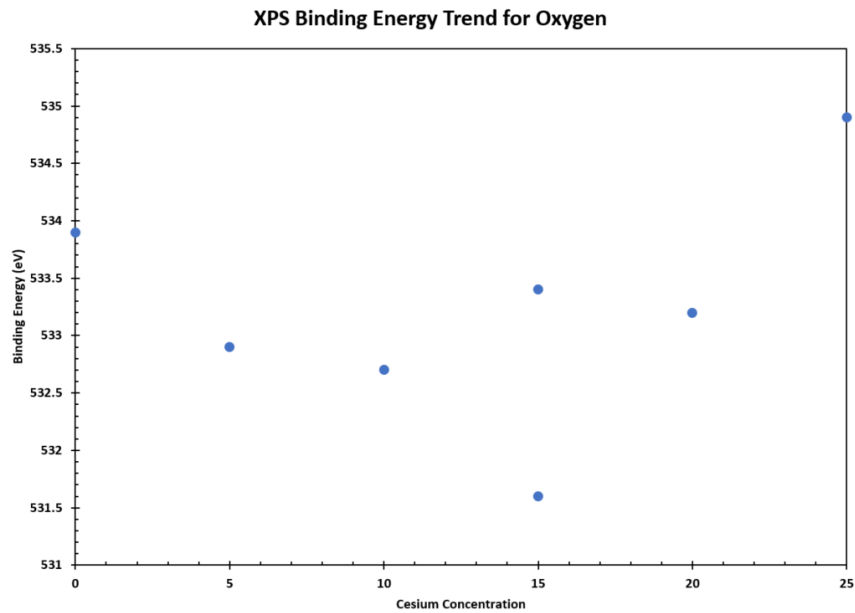


Figure 5-69: XPS trend for oxygen.

In summary, the XPS data revealed much about the alloy systems. There was a slight trend in the data based on cesium concentration for the cations and anions in the crystal lattice. The large deviation and chemical shift for nitrogen indicates that potentially the nitrogen electron is contributing to the enhanced current characteristics

observed in the IV data. This trend is initiated by the larger cesium atom creating larger lattice spacing allowing the nitrogen to keep a better hold on its electron.

### 5.5 Measurement Discussion

Based on the results of crystal sizes and surface roughness (table 5-7) there are two observations. The first is there is no obvious trend with surface roughness or surface coverage. All alloys appear to have coated the surface with equal ease. The second observation is that there is a slight trend in crystal sizes and Cs concentration and that is as Cs concentration increases, the crystal sizes shrink.

*Table 5-7: Crystal sizes and surface roughness summary from AFM results.*

<b>%Cs Content</b>	<b>Surface Roughness Ra (nm)</b>	<b>Crystal Diameter (nm)</b>
5	16.2	218.5
10	13.4	168.8
15	17.0	133.9
20	14.3	124.5
25	20.8	137.5

To grow a crystal, three basic steps are needed: supersaturation of the solution, nucleation and finally crystal growth[173]. Within these basic steps, many factors can effect crystal growth such as solubility, the number of nucleation sites, mechanical agitation, temperature, pressure, pH, viscosity, density, conductivity, dielectric constant, the coefficient of expansion and the time allowed to grow[173] [174]. As can be imagined, the crystal growth kinetics are complicated with over a dozen parameters all effecting how the crystal grows.

Fortunately, we can eliminate some of the differences between these alloy systems. All films grown for AFM were done on a layer of PEDOT:PSS (as well as bare glass) all prepared at the same time, this allows us to assume that the number of nucleation sites are the same for each alloy. Next, each system was deposited using the same process recipe, therefore, time, mechanical agitation, temperature and pressure were all the same. This leaves pH, viscosity, density, conductivity, dielectric constant, and the coefficient of expansion as the factors that could explain the differences in crystal sizes observed.

The growth of crystals requires a starting point. The Gibbs-Thomson equation is the fundamental equation for nucleation events [173][175]:

$$k_B T \ln \left( \frac{c}{c^*} \right) = \frac{2\sigma V}{r} \quad (5-9)$$

Where  $k_B$  is Boltzmann's constant,  $T$  the temperature,  $c$  is the actual concentration,  $c^*$  is the equilibrium concentration,  $\sigma$  is the surface energy and  $V$  is the volume of the growth. If we continue to the Gibbs energy of formation we have the energy of formation for the critical nucleus as [173][175]:

$$\Delta G^* = \frac{16\pi\sigma^3 T_0^2}{3kTL(\Delta T)^2} \quad (5-10)$$

Where  $L$  is the molecule and is related to the heat of fusion of a molecule. The other terms in equation 5-10 are constants and not associated with the alloy type. Together equations 5-9 and 5-10 apply to the nucleation of a seed crystal to which further growth will occur. Neither apply to the ultimate size the crystal will grow to. To

investigate that further, two paths need to be elucidated further. The first path is that the crystals have an equal number of nucleation sites to which to spawn a perovskite crystal. This path assumes then that ultimate growth is then controlled by diffusion of the solute into the crystal. This model is shown in figure 5-70.

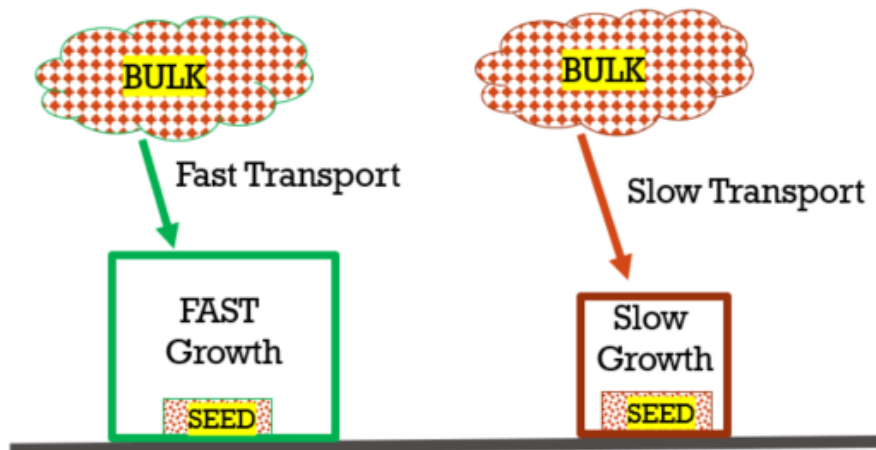


Figure 5-70: Growth of crystals based on transport kinetics.

The second pathway implies that there is a different number of nucleation sites with smaller crystals having more nucleation centers which results in smaller crystals grown as the smaller crystals remove solute from the bulk diminishing the chance that any large crystals will result. The model for this growth is shown in figure 5-71. An alternative to this pathway is a smaller number of nucleation sites further apart than in the first pathway. Growth kinetics then are limited by the ability of the solute to transport to the seed crystal and grow prior to solvent removal. However, this pathway would give poor surface coverage and that is not observed in the AFM or SEM measurements and as a result, can be eliminated.

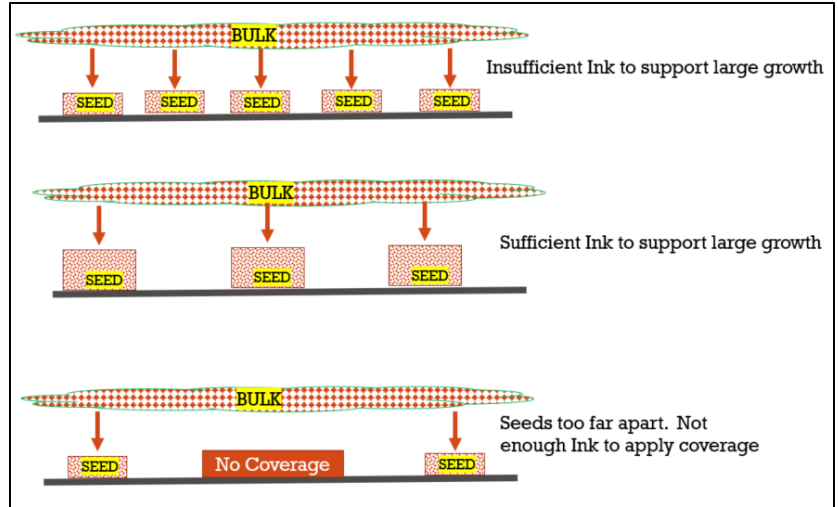


Figure 5-71: Growth model for crystals based on nucleation sites number and spacing.

To begin the analysis, elimination of one or more models is required. Equation 5-10 seems to be the most logical place to start an analysis. As mentioned prior, the only value within equation 5-10 is the dependence on the latent heat of formation. Reviewing literature for other systems indicates that there can be considerable differences in latent heats based on alloy concentrations [176] indicating that information is required to evaluate whether some of the alloys have more favorable situations.

To calculate the latent heats, the use of the Neumann-Kopp rule is needed and is given by the following relationships[176][177]:

If a solid compound can be described as:



then the heat capacity becomes

$$C_{pm}(A_aB_bC_cD_dE_e(s) = aAC_{pm}(s) + bBC_{pm}(s) + cCC_{pm}(s) + dDC_{pm}(s) + eEC_{pm}(s) \quad (5-12)$$

The beauty of this relationship is that it estimates the heat capacity of the alloy based on the contributions of the individual components to the alloy. Since our perovskite is built on the following:

$$xCs(s) + yMA(s) + zFA(s) + Pb(s) + 3I(s) = Cs_xMA_yFA_zPbI_3(s); \text{ where } (x + y + z = 1) \quad (5-13)$$

The use of Neumann-Kopp rule can be applied to estimate the heat capacities and the latent heat of formation. It should be noted that there can be considerable error in the use of Neumann-Kopp [176][177], however in the case of perovskite systems, these alloys do not phase change from liquid to solid but rather tend to decompose with constituents leaving the solid phase via the gas phase and leaving the remaining in other forms such as  $PbI_2$  and CsI salts. Unfortunately, the main problem with using Neumann-Kopp remains the unknown values for the organic cations and for the final alloy.

Luckily, we can apply a Born-Haber cycle to the components and gain an understanding of stability as well [178]. From work of Zheng and Rubel [178], we can calculate some values to help gain some insight on the role of the cation in the alloy. To do so, one assumption is needed and that is how to calculate the molecularization energy for the alloy. Zheng and Rubel provide molecularization energy for the pure phase  $CsPbI$ ,  $MAPbI$  and  $FAPbI$  perovskite materials. Borrowing from the Neumann-Kopp rule and applying those to the molecularization energy based on the percentages

of each phase, we can approximate the molecularization energy for each phase. The results of those calculations are in table 5-8.

*Table 5-8: Calculated energies.*

<b>Species (ions)</b>	<b>Ionization Energy <math>\Delta H_{ion,1/2}</math> (eV)[178]</b>	<b>Compound</b>	<b>Molecularization Energy <math>\Delta H_{mo}</math> (eV)[178]</b>
MA+	4.2	MAPbI3	5.66
PbI3-	-4.19	CsPbI3	5.72
Cs+	3.85	FAPbI3	5.4
FA+	3.97		
<b>Alloy</b>	<b>Ionization Energy Difference <math>\Delta H_{ion}</math> (eV)</b>	<b>Molecularization Energy <math>\Delta H_{mo}</math> (eV)</b>	<b>Potential Lattice Energy <math>\Delta H_{latt} + \Delta H_r</math> (eV)</b>
MAPbI3	0.01 [178]	-	-
FAPbI3	-0.22 [178]	-	-
CsPbI3	-0.34 [178]	-	-
5%	-0.1915	5.455	5.2635
10%	-0.209	5.458	5.249
15%	-0.2265	5.461	5.2345
20%	-0.221	5.49	5.269
25%	-0.2385	5.493	5.2545
15%	-0.2035	5.487	5.2835

Reviewing the data in table 5-8, one thing that stands out is that the potential lattice energies are very much the same. Reviewing the potential heats of reaction from Zheng and Rubel and applying the Neumann-Kopp rule to those, the differences between the most energetic and least energetic reaction is only about 16%. Going back to the original mechanism pathway for crystal size and equation 5-10, the latent heat of formation which is related to the values listed here are very similar to each of the alloys under investigation. The estimated ~16% difference in heats of reaction, which is

dominated by the most abundant species in the alloy (FA) are close enough in value to update the pathway models seen in figure 5-71 and to eliminate the differences seen in crystal sizes (~43%) based on the number of nucleation sites as the energy difference is not large enough to favor one alloy system.

The next investigation is to determine the reason for the difference in crystal sizes is to examine the transport of solute (fast vs slow) to the crystal as seen in figure 5-70. The transport of solute is governed by the diffusion rates of the species in solution:

$$v_t = \sqrt{\frac{3k_B T}{\pi m}} \quad (5-14)$$

where  $k_B$  is Boltzmann coefficient,  $T$  is temperature and  $m$  is the mass. This can be simplified into:

$$\text{diffusion rate} = K \sqrt{\frac{T}{m}} \quad (5-15)$$

Where  $K$  depends on the area and geometric factors under which the diffusion is occurring. Since the systems are at the same temperature and geometry of the resulting crystals are the same, a simple rule of thumb can be used to judge the differences in diffusion rates and is given by:

$$\frac{\text{Diffusion Rate A}}{\text{Diffusion Rate B}} = \sqrt{\frac{m_B}{m_A}} \quad (5-16)$$

This gives a simple expression in which the diffusion rate, that is the amount of material being delivered to the crystal is depended upon the mass of the species. To

help elaborate this, table 5-9, lists the mass of the cation alloy (the Cs, MA and FA) portion as the lead and iodide diffusion rates should be the same, the rate of the alloy cations should dictate transport and building of a crystal.

*Table 5-9: Cation Alloy Masses*

<b>Alloy System</b>	<b>Alloy Cation Mass (g/mol)</b>
5% Cs	47.504
10% Cs	52.546
15% Cs	57.588
15% Cs (70% FA)	56.289
20% Cs	61.331
25% Cs	66.373

Reviewing the crystal sizes in relation to the alloy cation mass, a strong relationship between the cation mass and resulting size is revealed. The larger crystal sizes had smaller cation masses, allowing for faster diffusion rates from the bulk to the crystal. The slower diffusion rates would also explain the additional peaks in the XRD spectra for the higher Cs content alloys as this would indicate insufficient time to transport to the growing crystal, leaving unreacted ink salts. Thinner films are also observed, which given the same molar ratio starting point would indicate that material is not being converted into perovskite.

The last factor that the cation selection could have on crystal formation is in relation to the evaporation rate of the solvent (4:1 ratio of DMF to DMSO). If the cation effects the evaporation rate of the solvent it will serve to influence the time under which the diffusion takes place. There are 7 factors influence evaporation rates, they

are concentration of the solvent in atmosphere, other substances in the atmosphere, flow rates of atmosphere, pressure, surface area, temperature of the substrate and inter-molecular forces. Of these 7 factors, the first 6 factors are the same for each system. This leaves the inter-molecular forces as the determining factor that can influence solvent evaporation rates alloy system to alloy system.

To determine the influence on the evaporation rate, much data is needed. Unfortunately, the ink systems are too complicated to take advantage of several models that can estimate some of interactions such as the Pitzer parameters, the three-characteristic-parameter correlation (TCPC) or even a simplified two parameter system [179][180]. All these models are for evaluating electrolyte solutions, that is a single salt in a single solvent. Our system consists of two solvents and four salts.

However, we can use a small subset of the models to estimate the interactions of the cations to determine how much of an impact they might have on the evaporation rate. The solvation energy influences the evaporation rate [181] [182]. The two major influences in the solvation energy are the atomic radii and atomic charges[183]. We have the mean activity coefficient for a single salt as [179]:

$$\ln\gamma_{\pm} = \ln\gamma_{\pm}^{PDH} + \ln\gamma_{\pm}^{SV} \quad (5-17)$$

Where

$$\ln\gamma_{\pm}^{PDH} = -|z_{+} \dots z_{-}| A_{\phi} \left[ \frac{I^{1/2}}{1+bI^{1/2}} + \frac{2}{b} \ln(1 + bI^{1/2}) \right] \quad (5-18)$$

And

$$A_{\phi} = \frac{1}{3} (2\pi L d_w)^{\frac{1}{2}} \left( \frac{e^2}{DkT} \right)^{3/2} \quad (5-19)$$

Here  $A_{\phi}$  is the Debye-Hückel constant which is  $\sim 0.392$  at room temp.  $D$  is the static dielectric constant (in Kelvin),  $L$  is Avogadro's number,  $d_w$  is density of the solvent (DMF-DMSO),  $k$  is Boltzmann constant,  $e$  is the electronic charge and  $z_i$  are the charge numbers on the cation and anion. The parameter  $b$  is the distance parameter of closet approach of the ions in solvent. This is an adjustable parameter in the model as this is unknown and is adjusted to fit data.

The remaining parameter is  $I$ , which is given by equation 5-7 above and is the ionic strength of the cations in solution.

The other half of the model is given by:

$$\ln \gamma_{\pm}^{SV} = \frac{S}{T} \frac{I^{2n}}{v_+ + v_-} \quad (5-20)$$

Here  $S$  is a model parameter known as the solvation parameter and is adjusted to fit data,  $T$  is temperature and  $v_i$  are the stoichiometric coefficients of the cation and anion in the solvent.

From the work of Ge and Wang[179], they were able to reduce the equation to two model parameter in which  $S$  and  $b$  can be fitted to the data. However, if we review the equations from above we can see that there is a strong dependence on ionic strength as it appears in both relations in equation 5-17. We can then make the approximation that solvation energy is proportional to ionic strength. The ionic strengths were calculated in table 5-8 and these strengths for each system are very

consistent. Based on this, we can assume that the evaporation rate of the solvent from each of the alloy inks are essentially the same.

## 5.6 Summary

In reviewing the data on the cation systems several things are apparent and are directly related to the choice of cation.

**BANDGAP:** Cation selection was also shown to influence the bandgap of the alloy. Higher cesium concentrations were observed to have higher bandgaps in the UV-Vis data. The overall electronegativity of the cation species was shown to be related to the bandgap. XPS data showed a similar trend with outer orbitals of cation/anion species shifting to higher energies with cesium concentration. The higher binding energies would require more energy to free an electron, so the data is consistent with the XPS data. The KPFM also showed a general increase in the work potential. While the work potential and the bandgap are not the same, they are related.

**CURRENT:** Current was seen to differ between the alloy concentrations. The 5% cesium had the best (statistical outlier) when compared to the other alloys. Current did have an inverse relationship with cesium concentration, however the role of FA concentration also effected the relationship. XPS data showed the influence of the nitrogen atom in the cations and higher chemical shift implying that the nitrogen atoms of the cations might be contributing the current availability.

**FILM THICKNESS:** Film thickness was shown to have a relationship with the dipole moment of the cation. Larger dipole moments resulted in thicker films under

similar processing conditions. This is driven by the larger viscosity relationships caused by the larger dipole-dipole interactions within the inks.

VOLTAGE ( $V_{oc}$ ): No relationship was seen with the  $V_{oc}$ . KPFM did show a relationship of increasing work potentials with cesium concentration, however that trend was not observed in the  $V_{oc}$  measurements. This could be due to the increasing mismatch between the PEDOT:PSS energy levels and the perovskite alloy (bandgap) or just the poor nature of the PEDOT:PSS interface. However, XRD data did show extraneous peaks with higher cesium concentration indicating that unreacted precursors could still be present in the film affecting the  $V_{oc}$  measurements, which is also supported by the overall thinner alloys at higher cesium concentration despite same mass/molar ratios in the ink.

CRYSTAL SIZE: Crystal sizes were shown to be a primarily a function of diffusion characteristics, with a minor role of the cation ionic strengths. The larger alloy cations of the higher cesium concentration alloys had a much larger effective mass than the lower alloy cations, 40% more, which translated into the bulk of the size difference between the alloy crystals. More study on the ink systems is needed to complete the study, however, the role of ionic strength of the cations also contributed to the crystal sizes seen.

## 6. INTERFACES

Perovskite films are a wonderful solar absorber, however, they are not without their challenges. The alloy systems studied here are just one solution to the stability issues facing perovskite materials. The other large obstacle facing perovskite materials is the interfaces of the materials in contact with the perovskite.

In this chapter, a review of past work done on a MAPBI system grown on a ZnO hole transport layer as well as the challenges found in the lifetime testing of the alloy samples in regard to PEDOT:PSS will be provided.

### 6.1 Zinc Oxide

The work in this section was the first work done on perovskites by this researcher at Texas State University. This work was published and is shown in figure 6-1. This work was done in 2015 and was published in 2016. Work was pioneering in the use of what we termed ‘Restricted Volume Solvent Annealing’ (RVSA). This concept was then used later by other researches and coined ‘solvent recycling’.

THE JOURNAL OF  
PHYSICAL CHEMISTRY C

Article

pubs.acs.org/JPC

#### Reliable Annealing of $\text{CH}_3\text{NH}_3\text{PbI}_3$ Films Deposited on ZnO

Christopher Manspecker,<sup>†</sup> Patrick Scruggs,<sup>‡</sup> Jonathan Preiss,<sup>‡</sup> Dmitry A. Lyashenko,<sup>†</sup>  
and Alex A. Zakhidov<sup>\*,†,‡</sup>

<sup>†</sup>Materials Science, Engineering, and Commercialization and <sup>‡</sup>Department of Physics, Texas State University, San Marcos, Texas 78666, United States

*Figure 6-1: Work done at Texas State and published in the Journal of Physical Chemistry C [9].*

### 6.1.1 Background

Perovskites are a sandwich of transport layers, metals, transparent conductive oxides and the perovskites layer. In early work on perovskite systems, zinc oxide (ZnO) was a promising electron transport layer as it had a large band gap (3.3eV), high electron mobility ( $> 1\text{cm}^2/(\text{Vs})$ ) and was easily deposited onto substrates[9]. However, ZnO perovskite systems suffered from decomposition at low temperatures ( $\sim 90^\circ$ ) which is a problem as fielded solar panel arrays can experience temperatures of nearly  $120^\circ\text{C}$ . In addition, there was debate on the decomposition mechanism and whether HI was a catalyst in the decomposition pathway. The work shown in this paper is a brief overview and the focus of which was to look at ways to prevent the decomposition as well as characterize the species seen in the decomposition products.

### 6.1.2 Devices

The devices under investigation in this early work were n-i-p devices and the structure is shown in figure 6-2. The ZnO was deposited via spin coating from a 12 wt. % water dispersion of ZnO nanoparticles. The perovskite was deposited via a twostep method where a 1M  $\text{PbI}_2$  in DMF solution was deposited followed by a 10mg/mL MAI in IPA and allowed to sit for 5 minutes and then spun coated dry. Samples were then annealed on a hot plate and the difference in annealing methods being an experimental method. The perovskite film was then coated using an ink of 2,2',7,7'-tetrakis(N,N-di-4methoxyphenylamino)-9,9'-spirobifluorene (Spiro-OMeTAD) that was doped. The Spiro-OMeTAD was doped by adding bis(trifluoromethane)sulfonimide lithium salt (Li-

TFSI) solution. The film stack was then capped with a silver anode. The film stack is shown in figure 6-2.

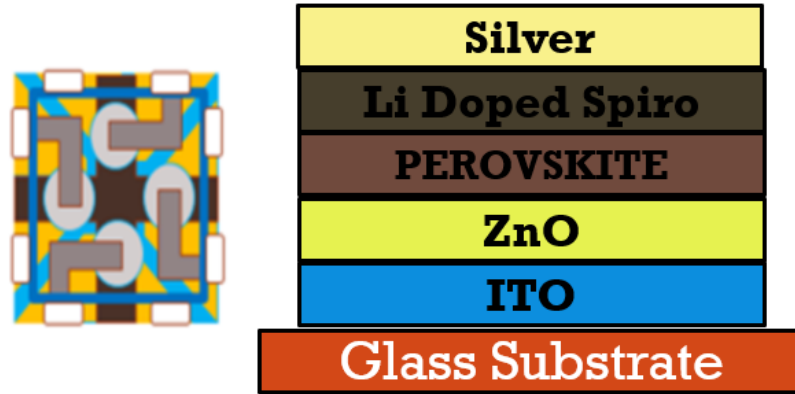


Figure 6-2: The n-i-p structure for ZnO perovskite.

### 6.1.3 Annealing

As stated earlier, the annealing step for the perovskite was differentiated as shown in the figure 6-3. The annealing methods differed only in whether one was open to atmosphere (denoted open volume annealing) or closed to atmosphere (denoted restricted volume solvent annealing). It should be noted that all annealing steps took place within a controlled atmosphere glove box with 0ppm water and 0ppm O<sub>2</sub>.

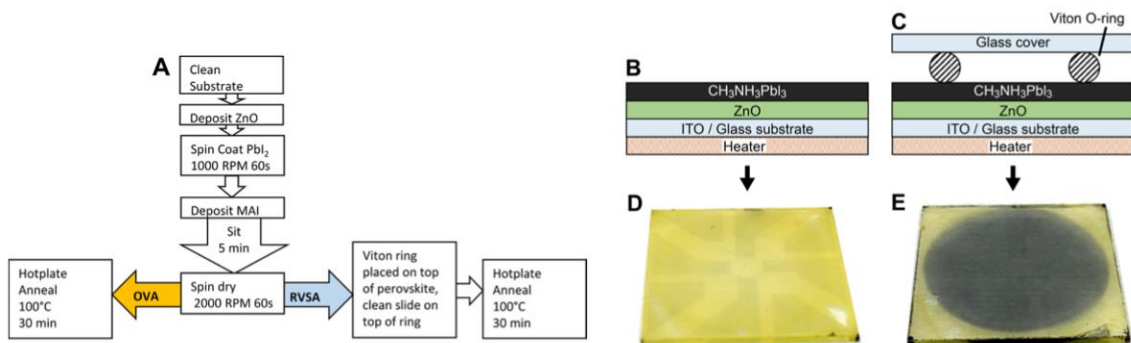


Figure 6-3: Annealing schema for the ZnO taken from work[9].

#### 6.1.4 Metrology

The samples were subjected to the same metrology tools and regimens found elsewhere in this work as FTIR, SEM/EDS, and IV measurements. The only difference was the use of a Bruker D8 powder XRD tool to measure the XRD spectra.

The driving method behind this paper was the use of FTIR to characterize the decomposition as well as the discovery of the RVSA annealing method. FTIR was used to determine the decomposition products from the film. However, there was not a convenient way to measure the decomposition products from the thin film, given the volume of gas expected and the air currents moving byproducts from the surface. Thus, there was a need to 'cap' the head space above the perovskite layer to investigate for gaseous species such as the organic portion of the perovskite.

It was known that the decomposed perovskite samples had an XRD pattern of standard  $\text{PbI}_2$ . This would indicate that the organic portion of the crystal was leaving the sample. Furthermore, since no reports of a reversible reaction has been published, the organic portion of the perovskite crystal must be leaving the substrate as the reaction was not reversible even if with the soaking of the sample with solvent to help facilitate movement and crystal growth. Thus, it was theorized that the organics were leaving the sample in a gaseous form as seen in figure 6-4. The gaseous nature of the decomposition products meant that it would be possible to sample the volume above the perovskite using FTIR to determine the decomposition species.

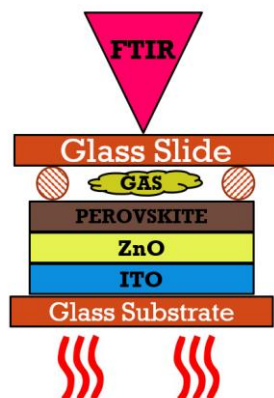


Figure 6-4: FTIR sample setup schematic.

A few samples were prepared ahead of time as well as examining various ways to anneal samples, or to drive out the residual solvent, which was thought to contribute to the mobility of potential mechanisms to unravel the perovskite crystal. The resulting test structure appears in figure 6-4.

To test using the FTIR, some modifications had to be made. The first was a blank indium tin oxide (ITO) substrate (no pattern) was modified and a pair of leads were soldered to the ITO side. A power supply was then used to supply a current to the ITO which in turn heated up. By controlling the input current, it was possible to control the temperature of the glass slide. This was then used as a small form heater. The second was that the ATR window on the FTIR was used as the glass cover slide so the whole sample was upside down on the FTIR system. The setup is shown in figure 6-5.

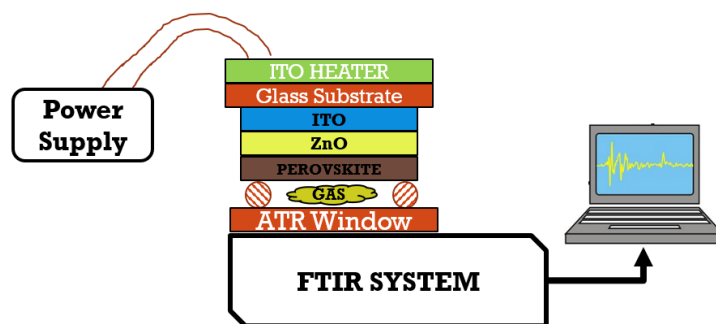


Figure 6-5: FTIR experimental setup for collection of data in reference [9].

The FTIR system then collected data every 60-90 seconds depending upon the scan settings and the skill of the researcher. The FTIR took static scans, meaning the ‘time resolved’ scans had to be done manually via the use of a stop watch.

Results are found in the above-mentioned paper. The FTIR showed remarkable stability for the RVSA samples when compared to open volume annealing (OVA) and other types of annealing. FTIR also showed the possibility of residual solvent being driven out of the film as well as N-H, O-H, C-H and C-OH bond stretching. The FTIR did not find any HI spectra, however, the HI might have remained in the substrate.

#### 6.1.5 Conclusions

It was shown that RVSA had the opportunity to prolong the life of perovskite materials deposited upon ZnO. Others have used similar methods after such as Numata [184], Mahmud [185] and Zhou[186] which all built on work done here at Texas State based on the RVSA method.

## 6.2 PEDOT:PSS Poisoning

### 6.2.1 Overview

This is a review of the poisoning of PEDOT:PSS surfaces for samples coated with PEDOT:PSS and not immediately coated with perovskite. The data reviewed shows the issues involved with sample preparation as well as que times, that is the length of time a process step can be delayed prior to further processing without a yield impact. Data presented here may be applicable to other hole transport layers (HTL) such as TiO<sub>2</sub>, ZnO and CuO, the last of which is undergoing development at Texas State.

### 6.2.2 Background PEDOT:PSS

PEDOT:PSS is an electroactive polymer which has a conductivity ability close that of many metals and is shown in figure 6-6. The thin films of PEDOT:PSS as deposited are thin (~35nm) and are transparent to light. The lab at Texas State University uses a PEDOT:PSS layer as a hole transport layer. The PEDOT:PSS is a dispersion of the polymer in water. While the layer has some advantages and many disadvantages, our primary use of PEDOT:PSS is the inexpensive nature of the material, the ease of deposition via spin coater and as seen above, does not promote decomposition as ZnO does. While differences in p-i-n or n-i-p structures dictate the starting point for perovskite deposition, the preparation of the surface is important for quality film deposition[10]. The PEDOT:PSS layer provides a good growth layer for perovskite growth.

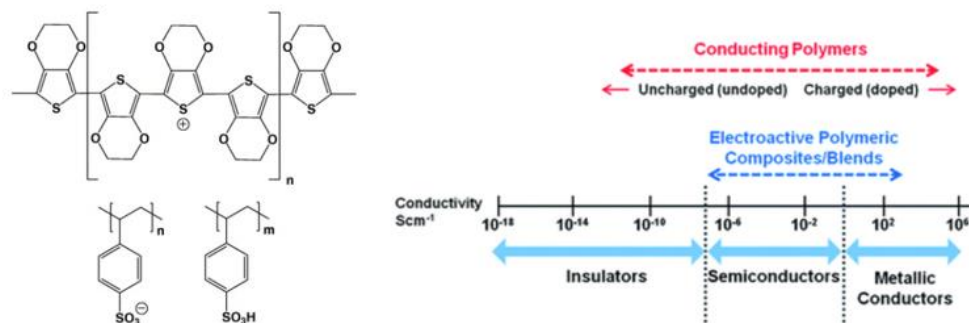


Figure 6-6: The structure of PEDOT:PSS[187] and the conductivity of PEDOT:PSS compares to metals[188].

### 6.2.3 PEDOT:PSS Deposition and Storage

PEDOT:PSS is spin coated to the desired thickness and annealed at 145°C for at least 10 minutes. This drives off water from the film which can be an issue with interfaces as well as contribution to perovskite decomposition. It has been observed that PEDOT:PSS coated samples that had a time lag (>12hrs) between PEDOT:PSS deposition and perovskite deposition had performance issues. The storage location (which is related to que time) of PEDOT:PSS contributes to the device performance and gives an indication of the interface importance.

### 6.2.4 Mass Change

To test for changes related to storage or que times, samples were prepared and spun coated with PEDOT:PSS at the same time. All the samples were weighed on a mass balance after deposition and annealing. The samples were then split into two groups and half the samples were then stored in a sample box and placed in the glovebox (humidity and oxygen-controlled environment, 0ppm) and a fume hood in ambient

conditions. Figure 6-7 shows the results after 24 hours of storage. The samples stored in the glovebox show a decrease in mass, while samples stored in the fume hood, an uncontrolled atmosphere, show an increase in mass.

It is theorized that the increase in mass was a result of the absorption of water and other gases from atmosphere. The substrates stored in the glovebox did not see the increase in mass and the resulting loss of mass was probable due in part to a vacuum step purge step required before entering the glove box which could have removed additional water from the samples.

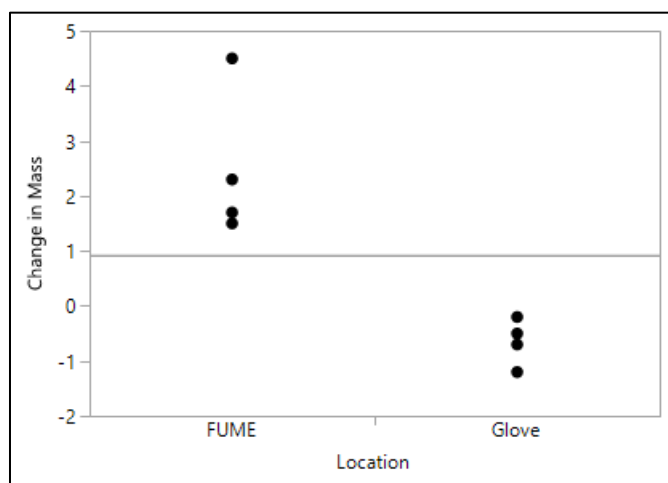


Figure 6-7: Change in mass of slides stored in fume hood and glovebox.

The next step in identifying the effects of que time and theorized water uptake was to create some devices under different que time conditions and are found in table 6-1. There were five different groups of devices created. The 'fresh' sample was made up the day of the test. All other devices were stored for 24hrs prior to the next step. The 'regen' samples were reheated to 145°C for 10min, essentially repeating the annealing step post PEDOT:PSS deposition.

Table 6-1: PEDOT:PSS test matrix

Sample	Que Time	Location	Regenerated
Fresh	0	None	N/A
Fume	24hr	Fume hood	None
Fume-Regen	24hr	Fume hood	145°C for 10min
Glove	24hr	Glovebox	None
Glove-Regen	24hr	Glovebox	145°C for 10min

Figure 6-8 shows the difference in efficiency measured from these samples. Results show that PEDOT:PSS stored in air for 24 hours had a large drop in efficiency and could not be regenerated to fresh sample conditions. Results also showed that PEDOT:PSS stored inside the glove box in a controlled atmosphere also suffered from a loss in efficiency, however, performance could returned as observed on the Fresh samples performance by repeating the annealing steps at 145°C for 10min.

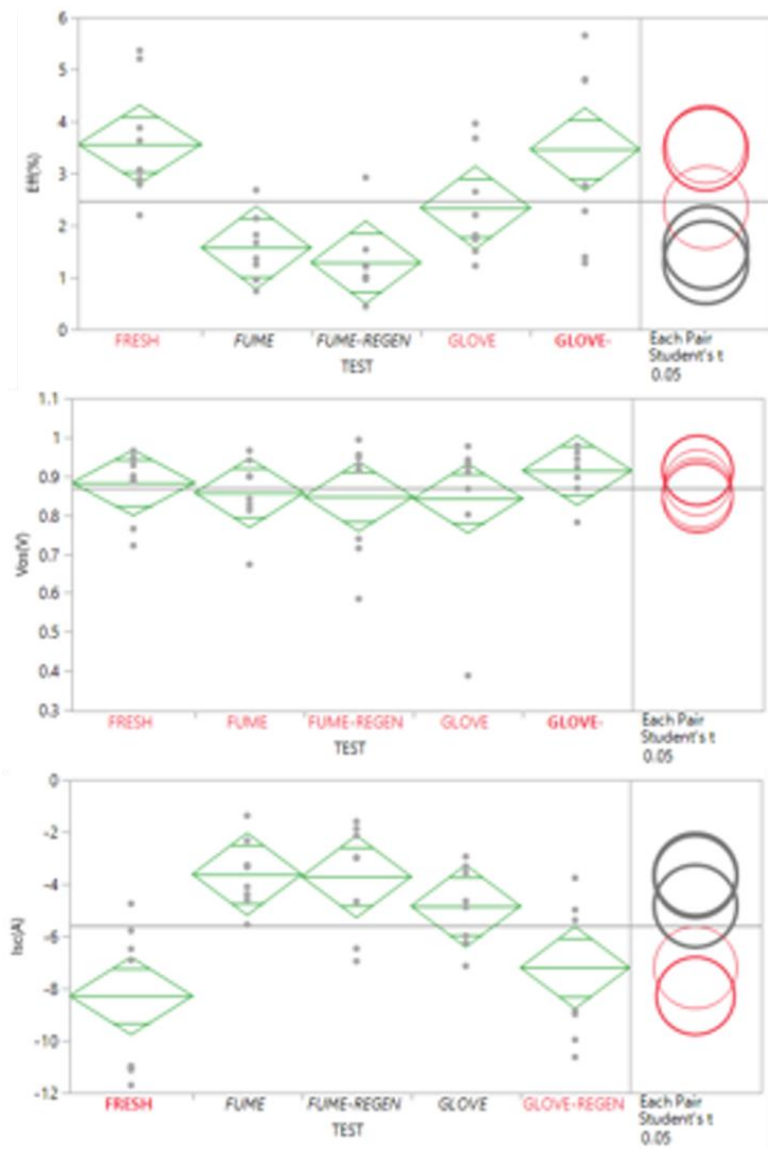


Figure 6-8: Analysis of samples, top to bottom, EFF, Voc and Isc.

Figure 6-9 shows why there is a reduction in efficiency and it is a drop in measured current. The  $V_{oc}$  remains essentially the same for all samples, however the  $I_{sc}$  shows a dramatic loss across the samples. It is hypothesized that the PEDOT:PSS is acting as a sponge and the water from the atmosphere or the solvents in the glove box are forming a barrier to hole transport on the sample. This is supported by loss of  $I_{sc}$

seen in the samples. It should be noted that no wetting differences were seen in the perovskite spin coating on any of the samples.

The 'REGEN' samples were heated to 145°C for 10min, which mimics the anneal step post PEDOT:PSS deposition. Results show that PEDOT:PSS stored in air for 24 hours had a large drop in efficiency and could not be regenerated to fresh sample conditions under the conditions of the experiment. Results also showed that PEDOT:PSS stored inside the glove box in a controlled atmosphere also suffered from a loss in efficiency, however, performance could be returned to Fresh sample performance by repeating the annealing steps at 145°C for 10min. It is hypothesized that the PEDOT:PSS is acting as a sponge and the water from the atmosphere or the solvents in the glove box are forming a barrier to hole transport on the sample. This is supported by loss of  $I_{sc}$  seen in the samples. Furthermore the inability to regenerate the PEDOT:PSS points to oxidation of the PEDOT:PSS layer which is supported by the inability to regenerate the layer via heating [189]–[191].

Most would agree that any ETL or HTL left in atmosphere would perform differently based on oxygen or water absorption, especially if untreated prior to next deposition steps. However, the HTL stored inside a H<sub>2</sub>O and O<sub>2</sub> free atmosphere (less than 1ppm) in which a solvent trap was in operation also performed worse. This indicates that the HTL surface is also susceptible to solvent influences if not treated (reheated).

This simple test shows the importance of the interface when depositing or growing perovskite films. Both the incorporation of oxygen, water and/or additional solvents had similar effects in reducing the efficiency of the device by interfering with current extraction.

This also has implications for industrial scale production as poisoning of the growth layer can affect yield and efficiency of devices that are not manufactured in a continuous flow process. This can increase the cost of manufacturing as continuous flow processes require 24-7 staffing or the creation of safe staging points for process material to avoid shifting process yields.

#### 6.2.5 PEDOT:PSS Poisoning Summary

PEDOT:PSS preparation and storage conditions were reviewed for their influence on que time considerations for device preparation. Data shows a dramatic drop in performance for devices stored for at least 24hrs prior to continuation of device preparation. In addition, samples stored in air could not be regenerated to freshly prepared conditions while those samples stored in an inert atmosphere could be restored to fresh performance. At the current time, PEDOT:PSS is the only HTL in wide use at Texas State, but the development of CuO HTL needs to proceed with the caution as gas and water absorption on that surface could affect device performance if que times are not observed.

### 6.3 Lifetime

The next step on the journey of interfaces comes from the investigation of lifetime measurements. For this test sequence, full devices were manufactured as mentioned earlier in the text and encapsulated. High performing devices (high PCE) were then selected for lifetime testing. The lifetime testing that took place was done under AM1.5G illumination as the device was biased and held at  $V_{oc}$ . The IV curve was measured every 60seconds for the first 10 minutes and thereafter the IV was performed every 10 minutes. The device was biased constantly based on last measurement.

This test schema was designed and inspired by the work of Sergie Tretiak's group at Los Alamos National Labs [81],[192]. The basis of the work concerns the polarons charge carriers found in perovskites. Since hybrid perovskites are using organic molecules which contains dipoles, under a constant bias, these dipoles should align[192]. As the dipoles align, these create trap zones for the current as shown in figure 6-9.

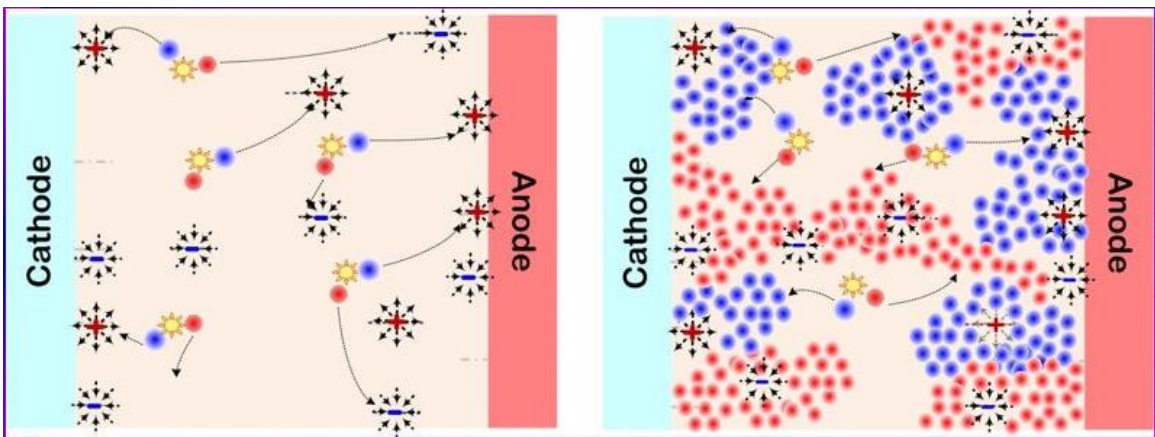


Figure 6-9: Left, polarons under no bias experience no dipole resistance, Right panel, under bias induced dipole resistance [192].

The modeling predicts that the addition of cesium into the alloy of perovskites should reduce the ability of the perovskite to form the charge trapping regions under constant biasing as cesium has no dipole. The initial data from LANL as shown in figure 6-10, seems to support that assumption.

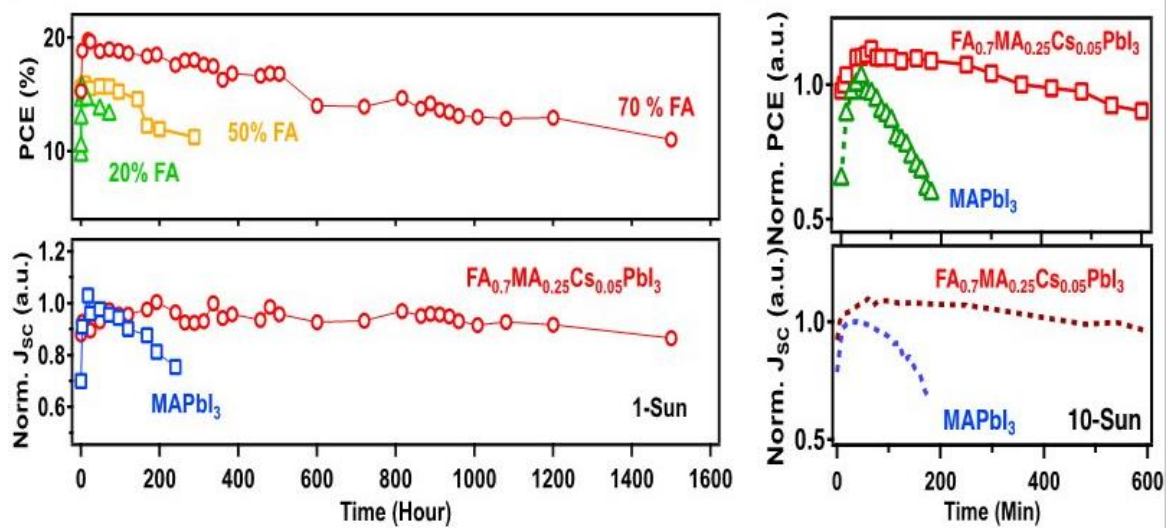


Figure 6-10: Lifetime data showing cesium compounds (no dipole) performing better than dipole alloys [192].

This lead to the lifetime testing of the alloy perovskites. The current die off observed in LANL data would indicate that devices with higher cesium content should have longer current production times, i.e. the normalized current (initial current over current current) should stay near one.

### 6.3.1 Results of Lifetime Testing

Figure 6-12 shows the result of several alloy compositions as well as MAPBI samples. As can be seen, there appears to be no reason to the madness in the results. In the tests conducted here, MAPBI outperformed the other alloy samples which

contradicts the data from LANL. Further testing showed that the PEDOT:PSS layer was the more problematic layer than the perovskite layer.

As temperature stability is a known issue for perovskites, understanding the temperature conditions of the test were required. Samples were kept under AM1.5G conditions for many hours and since the IV testing apparatus at Texas State is not temperature controlled, the increase in temperature could affect the measurements as well as degrade the films. Figure 6-11 shows the temperature ramp of devices under test. Devices under test quickly ramp in temperature from room temperature ( $\sim 30^{\circ}\text{C}$ ) to as much as  $60^{\circ}\text{C}$  in about 10 minutes as measured via an IR temperature probe. Maximum temperature observed was the  $70^{\circ}\text{C}$  seen in figure 6-11, however, random measurements of devices under test showed typical temperatures between  $60^{\circ}$  and  $65^{\circ}\text{C}$ . These observed temperatures are well below the decomposition temperatures of MAPBI [193][194] or any of the reported alloys[149] as well as not high enough to damage the PEDOT:PSS layer [195] which is annealed at  $145^{\circ}\text{C}$ .

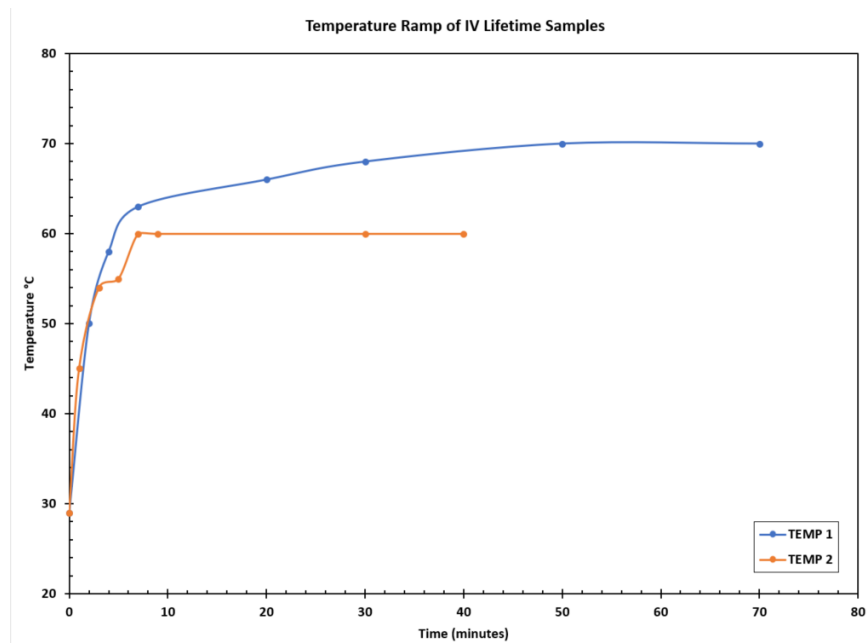


Figure 6-11: Temperature Ramp of Lifetime Testing IV devices.

The IV lifetimes were measured for a variety of different systems. To better align data, that is make up for the differences in parameters based on actual built in performance differences, the parameters were normalized to the initial value (parameter value at time = 0), thus it is possible for some values to have a normalized value greater than 1. All IV parameters were normalized,  $V_{oc}$ , Eff,  $J_{sc}$  and FF, in this way.

Figure 6-12 shows the normalized lifetime measurement for current. As can be seen, the best performing data is the one-step MAPBI perovskite (0% cesium and 0% FA). The worse performing systems were the 10% and 15% cesium devices.

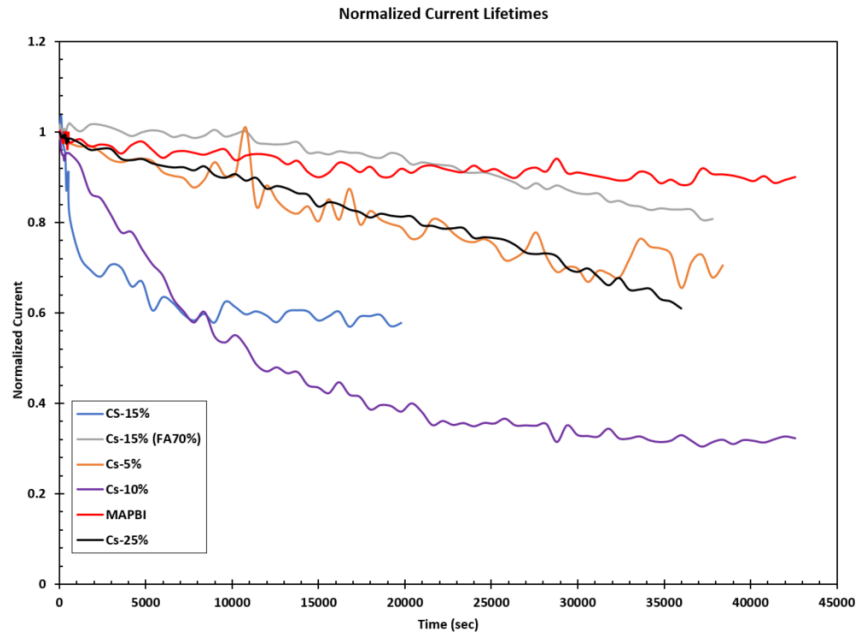


Figure 6-12: Normalized lifetime current decay for the different alloys including MAPBI samples.

The most surprising data appears in the  $V_{oc}$  lifetimes and are reported in figure 6-13. In almost each alloy, the  $V_{oc}$  did not decay rather stayed constant or even increased as the lifetime progressed. The only exception was the MAPBI system which saw a  $\sim 20\%$  decay in the  $V_{oc}$  over the course of data logging.

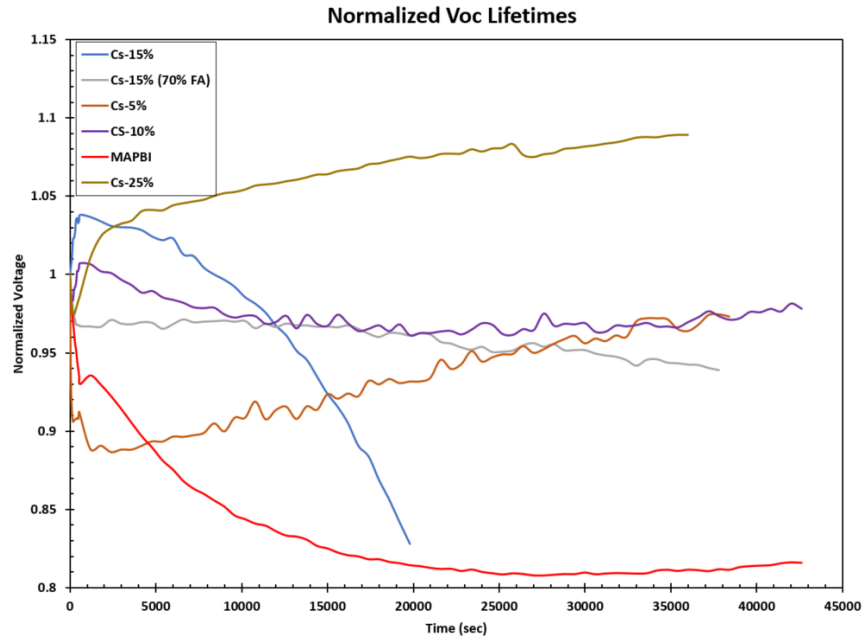


Figure 6-13: Normalized Lifetime Voc for the alloy samples and MAPBI.

With the  $V_{oc}$  gaining or remaining the same during the course of testing, the efficiency lifetime curves resemble the current lifetime curves and follow the same drop efficiency as the would be expected with a drop in measured current. The efficiency data is shown in figure 6-14.

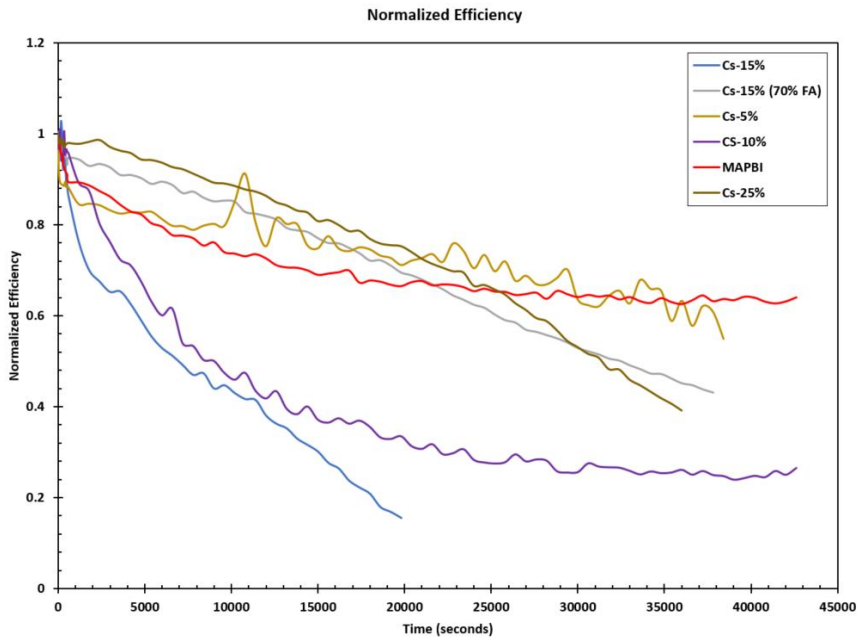


Figure 6-14: Normalized efficiencies for the alloy samples and MAPBI.

The normalized lifetime fill factor is shown in figure 6-15. In general, the fill factor decreases as the current drops as all parameters are related. In particular the current die off drove this parameter as well.

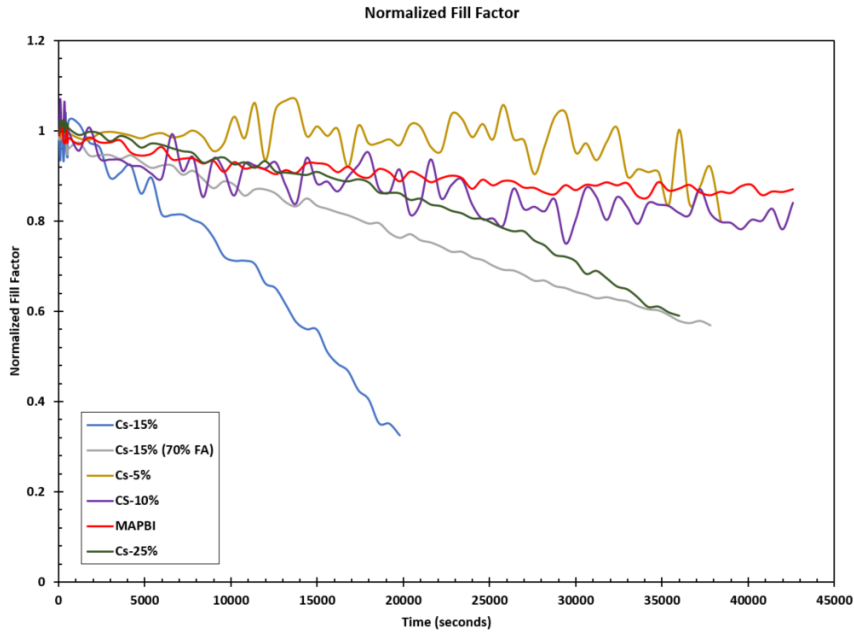


Figure 6-15: Normalized Fill Factor for the alloy samples and MAPBI.

However, what is hidden in the fill factor data is the shape of the curve. The curve shape, especially towards the end part of the lifetime testing took on two different shapes and are shown in figures 6-16 and 6-17.

The first decay curves are shown in figure 6-16. The notable feature here is that the IV curve retains the hockey stick shape and what the change in curves observed is caused by a general reduction in current. These curves would agree with polaron entrapment hypothesis[192] as the continued biasing of the device reduces current output.

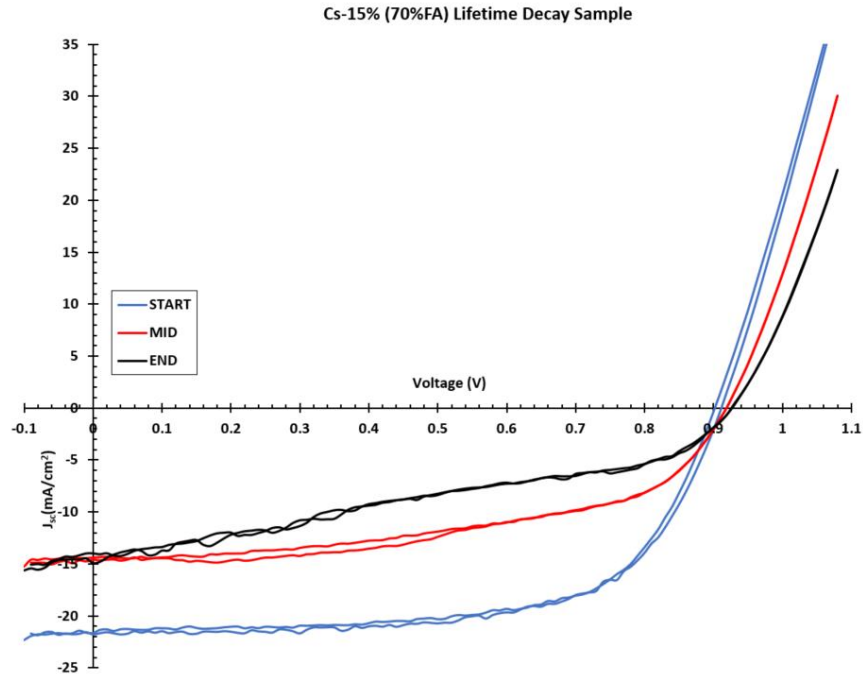


Figure 6-16: Decay of sample showing no interface breakdown, just dipole induced current loss.

The second decay is shown in figure 6-17 and it shows the loss of hockey shape ideal IV curve which is shown in figure 6-17 by the Start curve. As time progresses, the curve begins to have a lazy 'S' shape. The change in shape of the IV curve is due to a change in the shunt and series resistance of the solar cell. A decrease in the shunt resistance is typically also accompanied by a loss in  $V_{oc}$ , however, no change in  $V_{oc}$  is observed. We can then conclude that the shape change is caused by an increase in the series resistance.

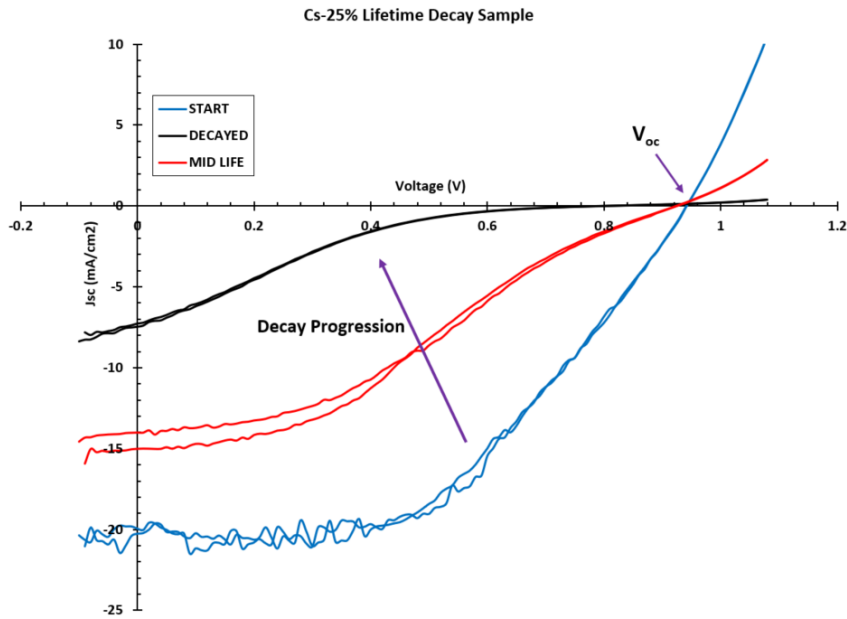


Figure 6-17: Decay IV curves of samples undergoing interface (PEDOT:PSS) break down.

An increase in the series resistance can come from several interfaces, the metal, the HTL and the ETL layers. In this case, the series resistance increase is coming from a degradation of the PEDOT:PSS. The discovery of the integrity issues with the PEDOT:PSS was discovered by accident when the labs at Texas State began using PEDOT:PSS from a new supplier. Samples made with the new PEDOT:PSS performed the same as PEDOT:PSS from the old supplier, however, longevity/stability of the layer device suffered as encapsulated devices despite being stored inside a solvent, oxygen and water free environment showed marked degradation in performance when tested the next day.

These devices showed traits of the MID-LIFE curves, despite being in storage for less than 12 hours. This was a marked change from the old PEDOT:PSS supplier where encapsulated samples could be stored for weeks with no measured change in

performance. Since the only change to the device stacks was the new PEDOT:PSS layer, this made the problem layer readily available to identify.

To combat the PEDOT:PSS integrity issue, the PEDOT:PSS layer was annealed for 60 minutes to drive out the water from the sample as PEDOT:PSS is a water suspension. The additional annealing time also gave insight onto why the layer was decomposing, water. Under the extreme lifetime testing, the water remaining in the PEDOT:PSS layer might be migrating to the interface with the perovskite and poisoning the interface in much the same way the bare interface was experiencing.

The PEDOT:PSS problem, which manifests despite vendor under lifetime testing, is that devices on the same substrate could have markedly different lifetimes despite being separated by a few millimeters. Thus, the only real conclusions from the lifetime testing of devices built with PEDOT:PSS as a HTL is that PEDOT:PSS is a poor material to conduct long term stress testing on.

One key take away of the lifetime testing, despite the problems with PEDOT:PSS is that observed hysteresis did not change much over the course of the lifetime testing. In fact, it was observed with all alloys and the MAPBI device that hysteresis present on the initial scan tended to get better as lifetime testing progressed. This is consistent with observations by others[196].

## 7. SCALABILITY SLOT DIE WORK

### 7.1 Overview

Texas State University and nTact Inc (FAS Holdings Group) were awarded an SBIR Phase I grant (award #1721884) for \$225,000 for “Scalable fabrication of stable perovskite solar panels using slot-die coating technique”. Work was to transfer a spin coated perovskite process on glass to on a flexible substrate with a slot die coater. Program was to realize 20% efficiency, a power-to-weight ratio 1kW/kg with a manufacturing cost of less than \$0.30/W.

### 7.2 Background

Perovskite solar devices have many advantages over traditional thin film solar cells. The main potential of perovskite solar devices is the low cost and ease of production. Perovskites hold that potential due to the possibility of using roll to roll processing techniques.

The current problem is, most perovskite devices and processes have been developed using spin coaters. Spin coaters have the advantage of low cost and ease; however, spin coaters cannot scale to meet the roll to roll challenge or large-scale production needs.

To solve the production throughput needs and low production costs, slot die can meet that need. Slot die extrudes the perovskite onto the substrate. To make the switch, several challenges are needed to be solved:

- Atmospheric and ambient conditions
- Solvent removal
- Annealing conditions
- Reliability
- Uniformity
- Ink formulation

Presented here are the preliminary results for slot-die coater from a one-step ink using a  $\text{PbI}_2$ -MAI-MAAc ink formulation.

### 7.3 Air Spin Coated

#### 7.3.1 Ink formulation

Texas State University has several different ink formulations for device creation and are shown in table 7-1.

*Table 7-1: Ink formulations.*

<b>INK</b>	<b>Step One</b>	<b>Step Two</b>	<b>Best Eff</b>
Two Step ( $\text{PbI}_2$ )	$\text{PbI}_2$	MAI	12%
Two Step (MAAc)	$\text{PbI}_2$ + MAAc	MAI	15%
One Step (MAAc)	$\text{PbI}_2$ + MAAc + MAI	---	16%
Alloy w/Solvent Wash	$\text{PbI}_2$ + MAI + FAI + CsI	Chlorobenzene	17%

From the table, the Alloy formulation results in the best efficiency for devices. However, the complexity for doing a second deposition step on a slot die coater is has additional technical challenges. The Alloy ink requires a chlorobenzene wash in fast succession or the perovskite crystal formulation suffers, and the efficiency drops. This is

not a problem for the other two processes that require a second deposition step. The slot die coater that is available at nTact has only one deposition 'chamber', meaning that a one-step deposition technique is needed, especially since the changeover from one ink to another ink was time consuming.

Based on these limitations and brief time for access to the slot die (the slot die unit whose data is reported here was available for 3 days as it was destined for another customer), the decision was made to use the one-step ink using MAAc.

Technical challenge for one step  $\text{PbI}_2$ -MAI-MAAc ink is that all depositions are done in an oxygen and humidity-controlled glovebox. While this ink has the best results when annealed in ambient, no work was performed on spin coating in ambient conditions.

Figure 7-1. shows the difference in device parameters based on one step  $\text{PbI}_2$ -MAI-MAAc ink. The only difference between the two device groupings is the spin coat step for the perovskites. Ambient conditions were  $\sim 73^\circ\text{F}$  and 55%RH. All devices were annealed in ambient and mixed for the evaporator depositions. Results show an almost 4x decrease in efficiency performance based on perovskite deposition conditions, driven by both a dramatic decrease in  $J_{sc}$  and  $V_{oc}$ .

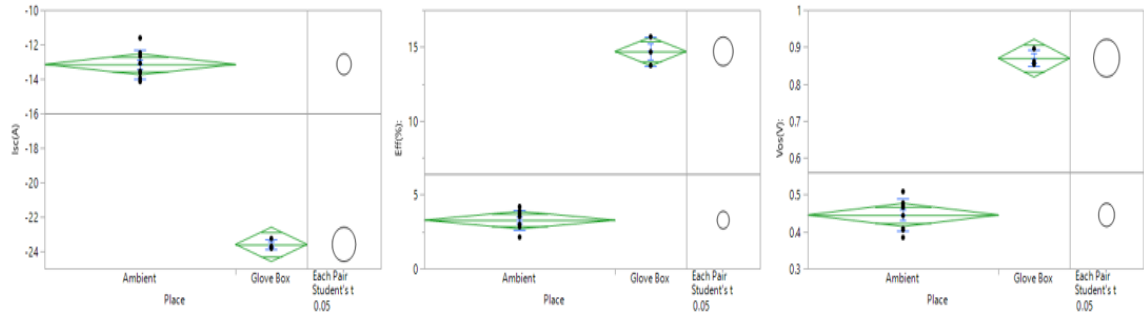


Figure 7-1: Difference in device parameters on one step 1:1:1  $PbI_2:MAI:MAAc$  ink spun coated in ambient and glove box conditions. Results from left to right are  $I_{sc}$ , EFF and  $V_{oc}$ .

The next step in ink development was to adjust the ratio of the MAAc in the ink. Ratios were investigated were 1.0, 0.75, 0.5 and 0.25, and the ambient conditions changed <16%RH due to the weather conditions outside (cold and dry). Devices were spun coated with these new ink concentrations and annealed. The 0.25 and 0.5 molar concentration MAAc films went white upon removal from the spin coater. The 0.25 and 0.5 inks both produced a poor film as seen by the eye. The 0.75 ink had a fairly good film, but after annealing looked poor. The 1.0 ink was yellow after the deposition (they typically turn brown during the spin cast) and turned black on the hot plate. The decision was made based on visual aspect of the films to not produce devices as non-typical films (0.25, 0.5, and 0.75 inks) had such a poor visual appearance.

The next task was to repeat the previous experiment of 1.0, 0.75, 0.5 and 0.25 molar MAAc concentrations in ambient with a relative humidity <16% RH. The new technique was using a hot casting method where the substrates are heated to 145°C and then placed into the spin coater onto a special substrate holder to prevent cooling

from the vacuum chuck. Results are shown in figure 7-2. All devices were less than 2% compared to the typical results of ~15%.

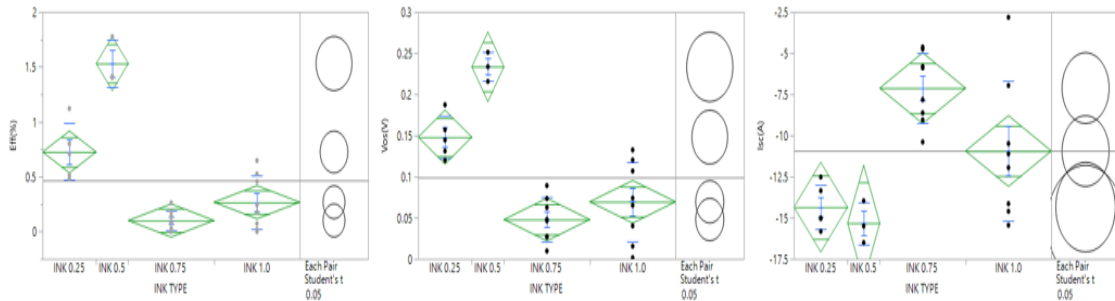


Figure 7-2: Ambient inks solar device characteristics with different molar ratios of MAAC. From left to right, EFF, Voc and Isc.

Next step was the examine the other ratio and examine the MAI concentration.

This was determined to be the next step based on the visual evidence from the earlier tests, mainly the turning of the samples to white prior to annealing. It was theorized that water in the atmosphere is reacting with the MAI in the ink/sample which is causing incomplete conversion and the poor results. To combat the reduction of MAI, the molar concentration was increased. The relative humidity during ambient conditions during these testing conditions were 30%RH.

Included in the next steps, a few other parameters were added, including hot casting, dynamic and static deposition methods as well as a IPA wash to try and prevent water incorporation into the film. The higher MAI concentration of MAI showed some promise on deposition. The MAI concentration for these tests were 1.5 and 2.0 molar. The higher MAI molar concentration still resulted in white films off the spin coater to anneal step, but annealing did show dark films with promising aspects. As an aside, the

heavy MAI concentration films also showed a dark red film upon annealing which was seen in previous work. Furthermore, if the anneal step was prolonged for 90 minutes and or increased the temperature towards 145°C the films became black and showed signs of being a viable path for the inks. The best performing device was at 8.76% efficiency, 0.793V and 26.675A and the curve is shown in figure 7-3. Based on these results, the higher concentration MAI were chosen for use in slot die.

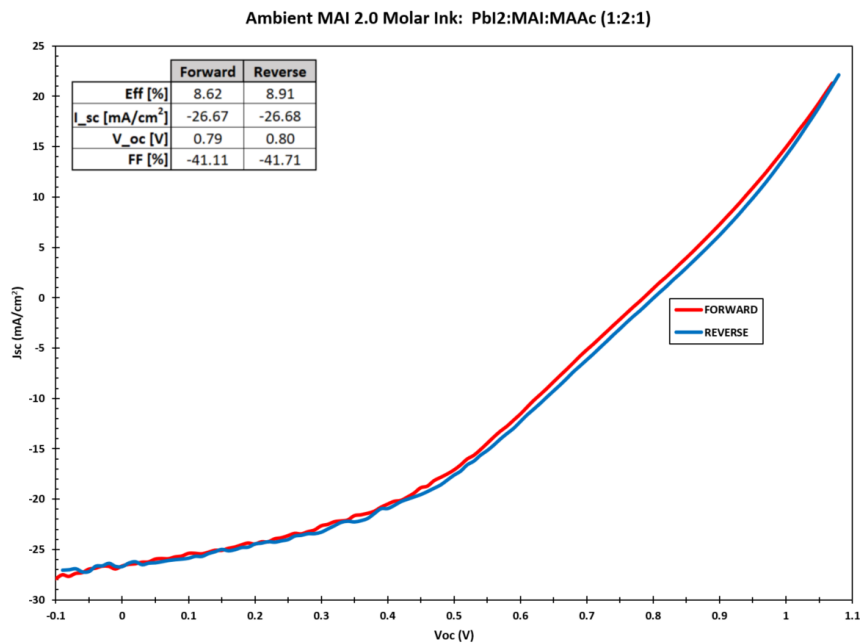


Figure 7-3: Best ambient 2.0 MAI concentration Device.

## 7.4 Slot Die Overview

Slot die work was done at nTact's Dallas location. The slot die coater has several components and are shown in figure 7-4 and are different than a spin coater. The first difference is ink dispenser which is a syringe filled with the ink. Both the volume delivered, and the speed of the volume can be controlled. The slot die is a special nozzle that requires special geometry and design. The slot die was not adjusted but can

be adjusted on different systems. The slot die is typically setup to deliver a specified width with a certain thickness range. The other parameter on the slot die is the distance above the substrate. The stage supports the substrate and is held in place with a vacuum and can be heated to 70°C. The stage movement is also controlled including acceleration to final velocity, velocity and travel range. Some slot die coaters also have air blades which deliver a metered gas flow ( $N_2$ , CDA or other gas) to the substrate which can assist with solvent evaporation, this air flow can be heated. The unit used for the ambient investigation did not have an air blade installed. Other options can add a second slot die and air blade for multiple depositions and that might be an option on a future unit for use at Texas State. The other option available at nTact is a portable glovebox which can be backfilled with clean dry air (CDA) which can drive the relative humidity to less than 5%.

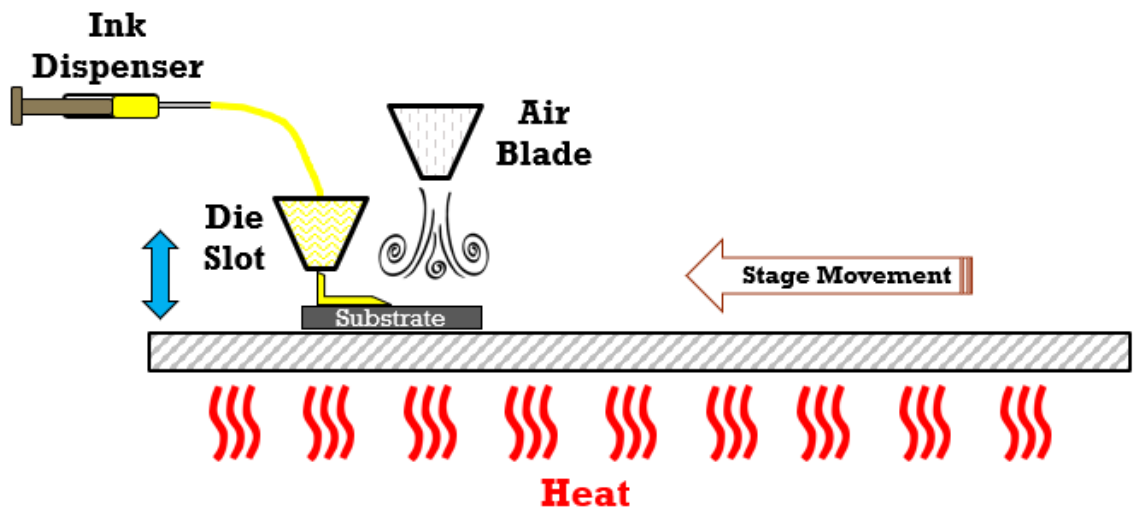


Figure 7-4: A typical Slot Die Coater. This was used to deposit films seen here, except air blade was not installed.

For use at nTact, 2" slides were used and were prepared the day before. For use, 16 slides were cleaned and coated with PEDOT:PSS as normal. Other slides were cleaned for possible use at nTact if needed. Maximum length of time between PEDOT:PSS deposition and perovskite deposition were 48hrs. As shown in section 6.2, PEDOT:PSS exposed to ambient conditions absorbs water from the air and causes poor results with devices. In addition, there was a delay of 24 hours post deposition from nTact's deposition and device creation at Texas State which is another source of device deviation. Consequently, no devices were made with these samples as results are predicted to be poor.

## 7.5 Tests at nTact

The system was setup to handle the 2" samples. The first ink used for setup and first runs was the 1:2:1  $\text{PbI}_2$ :MAI:MAAc ink. The stage was setup to move at 40mm/sec and was not adjusted for these samples. Dispense rate was varied from 2.5 $\mu\text{l}$  to 5.0 $\mu\text{l}$  and the thickness measured on a profilometer at nTact showed thickness of 1500nm to 450nm. Non-coated glass slides needed an UV treatment to improve wetting of the glass substrates. The ink needed to be poured in the syringe and not drawn into the syringe as drawing into the syringe creates bubbles in the ink and those are transferred to the substrates and results in micro holes. The 1:2:1  $\text{PbI}_2$ :MAI:MAAc ink was used up in the setup of the slot die for substrates and the ink. As a result, the remaining ink was used to deposit on substrates which was done the next day. The test matrix is shown in table 7-2. The only ink not used was the 1:1.5:1 ratio ink.

Table 7-2: Test matrix of initial samples done at nTact.

Sample	INK	Dispense (µl/sec)	Travel Rate (mm/sec)	Lift Off (mm)	Chuck temp	Ambient	Comment
Sample #1	1:1.75:1	2.5	40	5	60°	Yes	Bare Glass
Sample #2	1:1.75:1	2.5	40	5	60°	Yes	Bare Glass
Sample #3	1:1.75:1	3	40	10	60°	Yes	Bare Glass
Sample #4	1:1.75:1	3	40	10	60°	Yes	PEDOT
Sample #5	1:1.75:1	3	40	10	60°	Yes	T/S of 'tab' issue at end
Sample #6	1:1.75:1	3	40	10	60°	Yes	T/S of 'tab' issue at end
Sample #7	1:1.75:1	2.5	40	5	60°	Yes	
Sample #8	1:1.75:1	3.5	40	5	60°	Yes	
Sample #9	1:1.75:1	3.5	40	5	60°	Yes	fast move to hot plate
Sample #10	1:1:1	2.5	40	5	60°	Yes	
Sample #11	1:1:1	3.5	40	5	60°	Yes	
Sample #12	1:1:1	2.5	40	5	60°	8%RH	
Sample #13	1:1:1	2.5	40	5	60°	8%RH	Trashed sample
Sample #14	1:1:1	3.5	40	5	60°	8%RH	
Sample #15	1:1:1	2.5	40	5	30°	Yes	
Sample #16	1:1:1	3	40	5	30°	Yes	
Sample #17	1:1:1	3.5	40	5	30°	Yes	
Flexible	1:1:1	5	40	5	30°	Yes	annealed with air gun

The samples done in table 7-2 were then measured at Texas State University for thickness, bandgap and conversion via profilometer, UV-VIS and XRD. Figure 7-5 shows the thickness results for the samples as a function of dispense rate. Thickness trends from the data show thickness trends with dispense rate, chuck temp and relative humidity. The higher the dispense rate, the thicker the film; the drier the ambient conditions, the higher the temperature the thicker the film.

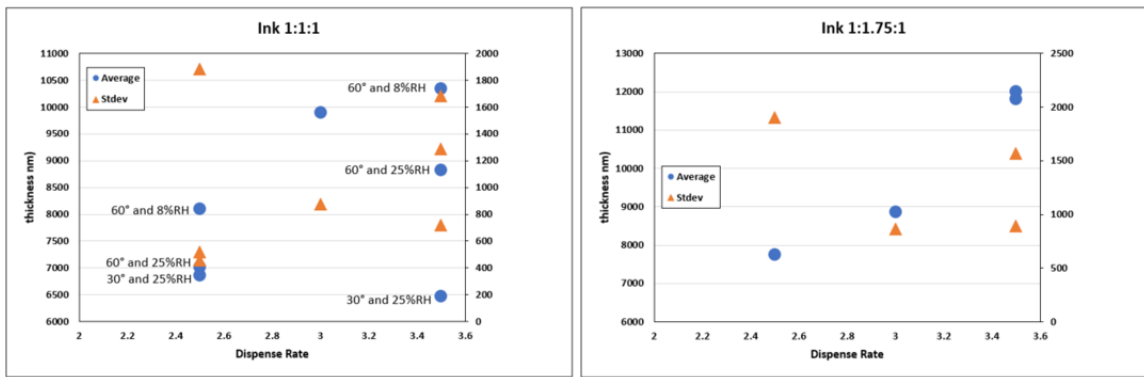


Figure 7-5: Thickness trends for the different inks versus the dispense rate. Included is the high standard deviation along the right axis.

The films also have a large standard deviation indicating the films are not uniform and can be seen visually as seen in figure 7-5. The samples also have a high lip along the edge. The 'tab' portion seen at the bottom of the perovskite (figure 7-6) stripe is a result of the slot die deposition ending and that area was not used in thickness measurements.

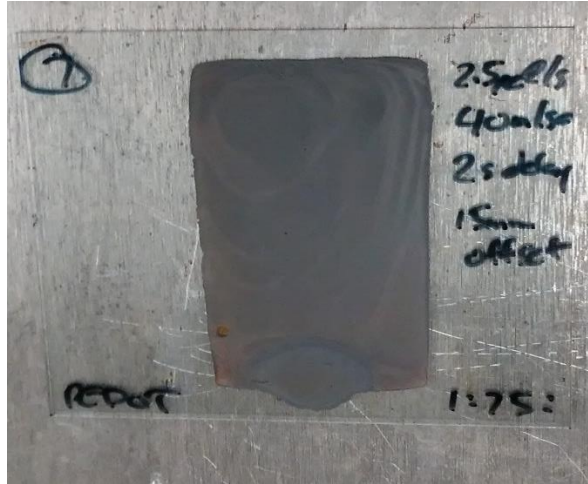


Figure 7-6: Visual result of the sample with wood grain due to thickness non-uniformity.

UV-VIS was performed at Texas State and the data is shown in figure 7-7. The data is broken up according to inks, however, the bandgap all seem to align to the same value around 782nm which corresponds to a bandgap of  $\sim 1.59\text{eV}$ . The films were all deposited on ITO patterned 2" substrates. All samples have good agreement and given the time delay and uncontrolled storage conditions, the data is in good agreement.

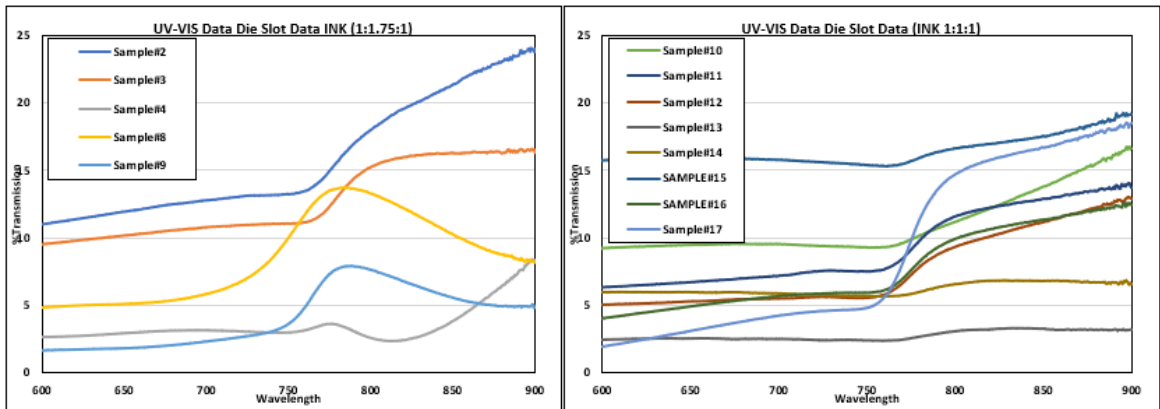


Figure 7-7: UV-VIS data for the different inks and samples performed at nTact. UV data shows good agreement, indicating perovskite formation.

## 7.6 XRD Data

XRD data was done at Texas State on all the samples. Results are shown in figure 7-8 and 7-9. The data shows good conversion to perovskite. For the 1:1:1 ink, the  $\text{PbI}_2$  peak (a  $2\theta \sim 12^\circ$ ) gets larger for thicker films at the lower dispense rate and gets larger for the for thinner films at the higher dispense rate. This indicates that the higher volume of dispense rate ( $3.5\mu\text{l}/\text{sec}$ ) which results in thicker films has better conversion rates to perovskite. The opposite was observed with the  $2.5\mu\text{l}/\text{sec}$  dispense rates. The indication from this is that the excess solvent aids in conversion to perovskite for these slot die deposited films. It should be noted that the  $\text{PbI}_2$  peak appears shifted higher.

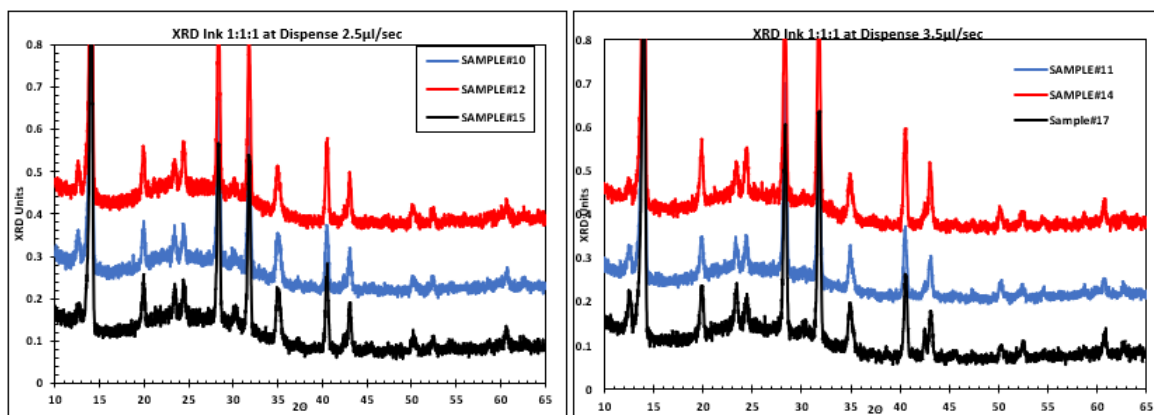


Figure 7-8: XRD data for the 1:1:1 ink at the different dispense rates. Thicker samples are in red, thinnest is black.

The XRD results for the 1:1.75:1 ink shows good results for the perovskite. All films showed a  $\text{PbI}_2$  peak (a  $2\theta \sim 12^\circ$ ) in the correct location and there was no correlation was seen based on film thickness or dispense rate for these films except for sample #4 (blue in both frames of figure 7-9). Sample #4 was a dispense rate of  $3.0\mu\text{l}/\text{sec}$  and a heated chuck. This XRD pattern shows complete conversion. One note

to the XRD patterns is that these films were deposited 24 hours prior and not stored in an inert environment. Thus, the PbI<sub>2</sub> peaks can be due to decomposition products and not conversion rates. Once the slot die system is available at Texas State, a confirmation of decomposition or incomplete conversion can be attained.

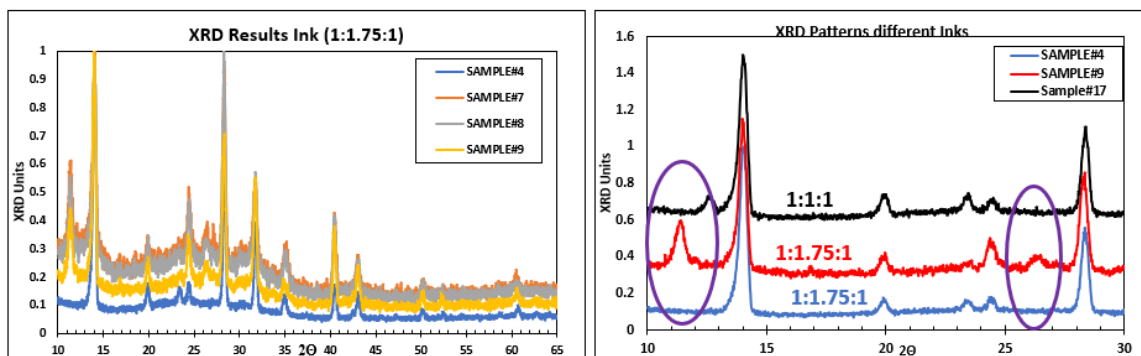
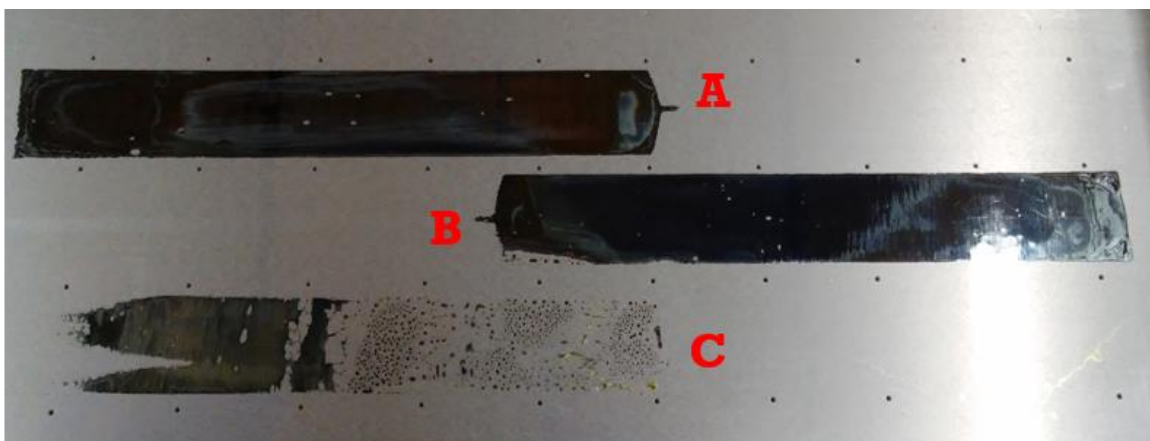


Figure 7-9: XRD Data for the 1:1.75:1 at different dispense rates left and the difference in apparent PbI<sub>2</sub> peak shown in purple circle on the right.

## 7.7 Flexible Substrate

The last test was to deposit perovskite onto a flexible substrate. Unfortunately, the flexible substrate used could not be positively determined as the packaging material was removed by the janitorial staff while testing was undergoing. The flexible substrate and results are shown in figure 7-10. The first deposition is seen in figure 7-10-C. The resulting film was very poor, showed pooling of deposited film due to poor wetting on the flexible film. The second film (figure 7-10-B) had better coverage but investigating the image in 8-10-B, the far right of the image shows wipe marks (stripping from top to bottom) on the image indicating poor substrate preparation. The flexible substrates were prepped with IPA and the wipe marks are clearly seen. Better IPA wipe and the resulting film is seen in figure 7-10-A. The holes seen in the film are theorized to be the

result of bubbles in the ink. The chuck was at room temperature and these films were annealed using an CDA gun blowing gently across the films, no heat. Further investigation into flexible substrates will be done once a slot die system is available at Texas State.



*Figure 7-10: Flexible substrate. A: Good coverage with holes resulting from bubbles in ink. B) the same conditions as A with poor surface preparation and C poor and untreated surface.*

## 7.8 Scalability Discussion

The initial results from the slot die coater were promising. The films deposited via slot die behaved differently than the spin coated slides in that the none of the visual characteristics or defects were observed. None of the films turned white or red. Films were yellow on deposition and turned black on annealing on a hot plate at 120°C. Ambient conditions were room temperature with a relative humidity of ~25% during the testing.

One observation from the deposition was that the as deposited films were much thicker than the spin coated films as the solvent is not driven off by the spin action. It is

hypothesized that the additional solvent in the slot die films prevented water incorporation into the film preventing the red or white color seen between spin coater and hot plate on spin coated samples. This initially can be seen as an advantage as the as deposited films didn't show the observed defect pathways of water incorporation. However, the tradeoff is the excess solvent causes the nonuniformity of thickness seen in figure 7-6 and figure 7-10. The nonuniformity issue could be mitigated by the application of an air blade, however that option was not available at the time.

The other promising discovery from the initial slot die films is that ability to anneal the films at low temperatures on the chuck which can be heated to 60°C. The use of an air gun also annealed films on the flexible substrates which were deposited on a 30°C chuck. The air flow was slight (no measurement available for the flow rate), but a simple back and forth movement across the as deposited film, the films were annealed and with favorable results as seen in figure 7-10. However, it was also observed that the air gun could also affect the uniformity problems seen as the solvent is blown around randomly. Again, the air blade option could negate uniformity issues, by supplying a constant air flow rate (as well as the potential to be heated). In addition, the use of a portable glove box which drove ambient relative humidity conditions from 25% to less than 5% showed no measurable differences in film parameters observed here.

XRD and UV-VIS data also showed good films. The time delay and undesirable conditions could be the reason for the  $PbI_2$  peaks in the XRD films. There is an interesting mystery on the XRD peaks seen in figure 7-9 between the different inks and further investigation will further elucidate the origin of the shift observed.

## 7.9 Scalability Summary

In support of an NSF SBIR award number #1721884, 'Scalable fabrication of stable perovskite solar panels using slot-die coating technique' measurements of perovskite films deposited via slot die coater available from nTact. Pework was done at Texas State to find a viable one step ink that could be transferred from a spin coat process to a slot die process. Pework showed that films with an increased MAI molar concentration performed better in ambient conditions.

Films were then deposited at nTact's facilities in Dallas. Films coated were observed to be visually better than films spun coated prior during ink development. Films slot die coated were observed to have thicknesses in the range of typical device thickness as deposited at nTact, however, the thickness measurements were high in standard deviation, meaning the films were non-uniform. Further measurements on all deposited films performed at Texas State showed thicknesses much higher than typical films (450nm vs 700nm and higher) as well as the high nonuniformity. Other measurements using XRD and UV-VIS showed initial good film parameters.

The addition of an air blade and further ink development and deposition parameters could lead to a reliable uniform film deposited via a slot die coater. Further work should occur in 2018 at Texas State which will allow devices to be better characterized and evaluated.

## 8. CONCLUSIONS AND FUTURE WORK

### 8.1 Introduction

This section covers the conclusions based on this work as well as possible next steps in research on these types of devices. The conclusions reached here shed good light on the role of the cation in the hybrid structure as well as the role of interfaces and ambient processing conditions.

The interesting thing about hybrid perovskites at this point in time is that these devices are very new and have a wide range of possible next steps and research focus. In fact, an entire dissertation can be filled with possible next steps. The ones presented here, therefore, should be thought here are just a small sample of possible next steps.

### 8.2 Conclusions

This work has resulted in several findings that are will help future researchers understand not only the role of the cation in hybrid perovskite materials, but as well as some of the processing conditions that are related to perovskite performance as a material for solar devices.

#### 8.2.1 The Cation

The cation choice in perovskite materials has a direct impact on the thermal and structural stability of the resulting crystal lattice. In addition, the following was observed in the work presented here:

- The Cation's role in the perovskite is related to its ionic strength when compared to other cations. A Cation with a higher ionic strength will see the

following overall trend when used in the same device, film stack and processing conditions (spin coat recipe)

- A decrease in bandgap. The effect of the ionic strength of the cation was observed to have a small effect on the bandgap as measured with UV-Vis.
  - An increase in film thickness was observed via profilometry.
  - An increase in crystal sizes was observed via AFM and SEM.
  - A decrease in the work function of the material was seen via KPFM.
  - A general increase in the performance of the final solar cell via the use of IV testing.
- The cation's crystal sizes were observed to be based on kinetics of the system. The larger cation mass as well as the ionic strength all contributed to the diffusion rate (large mass had slower diffusion rates) and the stronger ionic natures lead to longer evaporation times for the solvent allowing for longer diffusion times. Together, the smaller mass and ionic strength allowed for larger crystals.

#### 8.2.2 Formamidinium

- Formamidinium is a poor candidate for use as a solar perovskite material. The  $\alpha$ -phase, which is the desired cubic state for solar performance, is not thermal stable and prefers to transition to the  $\delta$ -phase which results in a considerable loss in IV performance. While the bare film can be readily regenerated into the  $\alpha$ -phase as witnessed by UV-Vis measurements, a functioning device cannot be

recovered without loss of the device. This could be from the high thermal expansion coefficient causing delamination with the film stack or some other problems with the film stack due to the 150°C+ temperature required to regenerate the  $\alpha$ -phase. The use of pure formamidinium is therefore only recommended in operational places where the temperature will remain high enough to assure  $\alpha$ -phase stays present.

### 8.2.3 PEDOT:PSS

- PEDOT:PSS is not a long term stable hole transport layer especially when the perovskite films are under stress.
  - The first observation was that PEDOT:PSS layers needed to be used (coated with perovskite) in a reasonable amount of time (<4 hours) or the film will absorb water as well as oxidize in ambient conditions.
  - PEDOT:PSS not used quickly, needs to be stored in a water, oxygen and solvent free atmosphere or device performance will suffer.
  - PEDOT:PSS layers had a tendency to fail under lifetime testing (devices biased at  $V_{oc}$  and kept under constant illumination during testing period).  
The failure mechanism observed via the IV curves was an increase in  $R_{series}$ , which implies a failure occurring within the PEDOT:PSS layer.  
More research is needed to elucidate the exact nature of the failure mechanism.

#### 8.2.4 Slot Die

- Slot die deposition of the perovskite films look very promising. Visual, XRD, UV-Vis and profilometer measurements of perovskite films deposited via slot die show good conversions, proper bandgaps and thick films.
  - Inks developed for glove box spin coating depositions were modified for use in slot die. Films deposited via slot die in ambient showed none of the visual problems observed when inks are deposited are spin coated in ambient.
  - The thick nature of the films indicates that the excess solvent and thickness might be providing a solvent vapor layer above the precipitating perovskite crystal which inhibits water and oxygen incorporation into the film.
  - Slot die coated material also showed the ability to develop perovskite films without the need for elevated temperature annealing steps.

#### 8.2.5 Ambient Conditions

- Ambient conditions are significant to perovskite crystal growth. Perovskite films and devices manufactured under different ambient conditions had a statistical difference between devices.
  - Temperature: crystals grown at elevated ambient temperatures showed larger crystal sizes, thicker films and poorer performance than films grown at reduced temperatures.

- Pressure: crystals grown at higher ambient pressures showed smaller crystal sizes, thicker films and better overall performance than films grown at lower pressures.
- Solvent Vapor concentration: Crystals grown in higher excess solvent concentrations, where the solvent concentration is the same solvent used in the ink, show thinner films, smaller crystals and better performance than films grown under no excess solvent conditions.
- All trends show that conditions that inhibit solvent evaporation from the film results in better device performance.

## 8.3 Future Work

### 8.3.1 Hole Transport Layer

The first and obvious step is to examine the hole transport layer currently used in the p-i-n structure used at Texas State. PEDOT:PSS is the current hole transport layer, but as presented here, it is not a very stable layer. For long term use, a better more stable layer will be needed.

The first possibility is the use of tin oxide (SnO). Texas State has the ability to deposit ALD layers of SnO in the cleanroom. The use of SnO can improve device efficiency and the effect of the different transport layer on the cation and perovskite performance can be measured much as it was used here.

A second research method is the use of CuO as a transport layer. Current work is underway to examine using CuO and hope is in the near future, this transport layer will

return good results. Again, a smaller research project focusing on the effects of CuO on perovskite layers can be done.

The third approach is to return to the zinc oxide transport layer. While it is known that ZnO and the MAPbI perovskite are not a thermally stable system, the use of an alloy such as  $MA_xFA_yCs_zPbI_3$  (where  $x+y+z = 1$ ) might mitigate the decomposition pathways currently seen in MAPbI films. An example of this would be the use of chromium in stainless steel, where a small amount prevents the movement of iron atoms which leads to rust.

### 8.3.2 Electron Transport Layer

In an effort towards slot die production and scalable production runs, an alternative way to deposit BCP needs to be found. Currently this ETL is deposited via the evaporator. Finding a non-vacuum assisted technology to help would help make perovskite solar cells more commercially viable. One potential route might be to co-dissolve the BCP and C60 compounds together and spin coat them. This could be done via one ink or a second ink provided the solvent in the second ink did not cause problems with the prior layers. Currently, chlorobenzene is used to dissolve C60 for spin casting.

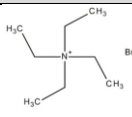
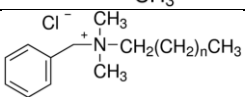
### 8.3.3 The Perovskite

Examination of the grain boundaries. Devices can be isolated from oxygen incorporation at Texas State labs by isolation and encapsulation prior to measurement. However, bare films will be exposed to ambient conditions. The exposure could be influencing the measurements as oxygen is being incorporated into the films as revealed

by the XPS measurements. Further works is needed to reveal if oxygen (or another passivation method) is detrimental to the system (prior to encapsulation) or if oxygen incorporation is skewing measurement analysis of bare perovskite films.

Alternative cations: Ethyl ammonium (EA)[197] has recently been shown as a cation for perovskites. Examining the role of this cation as well as alloys of EA, MA, FA and Cs could add to more information on cation performance. Higher order chains such as butylamine can also be researched into increasing the stability of the perovskite. Other possible candidates are shown in table 8-1. The only real requirement for the cation remains steric restrictions on size, ionic charge (+1) and solubility in current solvents.

*Table 8-1: Possible cation choices. Chemical structure from Sigma-Aldrich.*

Compound	Structure	Notes
Tetraethylammonium bromide Or Tetraethylammonium iodide		Symmetrical
Cetrimonium	$\text{H}_3\text{C}(\text{H}_2\text{C})_{15}-\text{N}^+(\text{CH}_3)_2-\text{Br}^-$	Long chains could hinder growth
Benzalkonium chloride		Aromatic ring could be steric interference
Butylamine	$\text{H}_3\text{C}-\text{CH}_2-\text{CH}_2-\text{CH}_2-\text{NH}_2$	Used in creating 2D structures[198]

One-Step Systems: The acetate adducts works well with both formamidinium acetate and methylammonium acetate and making perovskites of  $\text{MA}_{(1-x)}\text{FA}_x\text{PbI}_3$  compositions.

The exact role of the acetate needs to be elucidated as devices made with acetates

perform better. Also, as the alloys of cesium are promising, developing an ink that uses one of the acetates (or both) needs to be investigated as well. As seen in the scalability section, the acetate-based inks performed well with the slot die coater and would be a good ambient processing step.

## APPENDIX

The material found in these appendixes are intended to either supplement this work in a related effort not directly associated with the role of cations. Topics found in these appendixes:

Appendix A: Device Targeting

Appendix B: Deposition Technique

Appendix C: Design of Experiments and Statistics

Appendix D: Ambient environmental factors and their influence on perovskite formation kinetics

Appendix E: Best Device

## Appendix A: Device Targeting

### Introduction to Device Targeting

In this work the layer stack was optimized to obtain maximum performance from the devices. As seen in figure A-1, the solar device is made up of many different layers; the substrate, the transparent oxide, the hole transport layer (HTL), the perovskite, the electron transport layer (ETL) and finally the metal electrode. The substrate, transparent oxide and aluminum thicknesses are not a factor in device performance as the metal layer needs to be just thick enough to conduct and the substrate and transparent oxide are prefabricated to thickness. Obviously, a transparent oxide that is too thick will fail to be transparent enough or too thin will fail to conduct carriers effectively. The metal also has a minimum thickness as well as the metal must connect the layer stack and the ITO pad as seen in figure A-1, too thin of a metal layer and the Aluminum “L” will not make a good contact for testing.

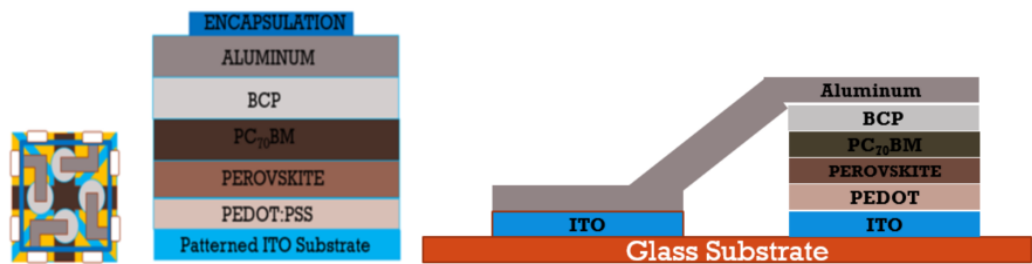


Figure A-1: Film Stack of the device, from left to right, cartoon of the device, the layer stack, the layer stack as deposited for testing.

The remaining layers were then targeted to find the best layer thickness and conditions for the device performance. These layers were the PEDOT:PSS, PC<sub>70</sub>BM and BCP thickness and conditions.

#### PC<sub>70</sub>BM Thickness

PC<sub>70</sub>BM is used as an electron transport layer (ETL). PC<sub>70</sub>BM is a fullerene compound and was discussed earlier in the main text. For use in this work, the thickness of PC<sub>70</sub>BM was of interest. A transport layer (ETL or HTL) needs to have a few characteristics to be considered a good layer. These are typically: high transparency to incoming light, good charge collection, compatible bandgap and have a good film qualities[199][200]. It should be noted that the architecture of the device, p-i-n or n-i-p will determine which transport layer needs to be transparent as only the transport layer prior to the perovskite needs to be transparent. In fact, there can be some material design on the back-transport layer to help improve efficiency by using plasmonic centers that could reflect back some non-absorbing incoming photons from the perovskite layer, back into the perovskite increasing the possibility of absorption increasing efficiency.

The PC<sub>70</sub>BM is a solid and is widely available from many manufactures. To use in this test, the PC<sub>70</sub>BM was dissolved in chlorobenzene to a concentration of 20mg/mL. The solution is kept wrapped and away from light to prevent any possible degradation. The PC<sub>70</sub>BM solution is spin coated and annealed at 80°C for 20 min. Unlike perovskite, the anneal step here is to remove the solvent and not grow crystals or attributes to the thin film parameters. As a result, the only parameter that effects the output of solar cell is

the thickness of the resulting film. To control the thickness, the spin rate was varied.

Results are shown in figures A-2, A-3 and A-4.

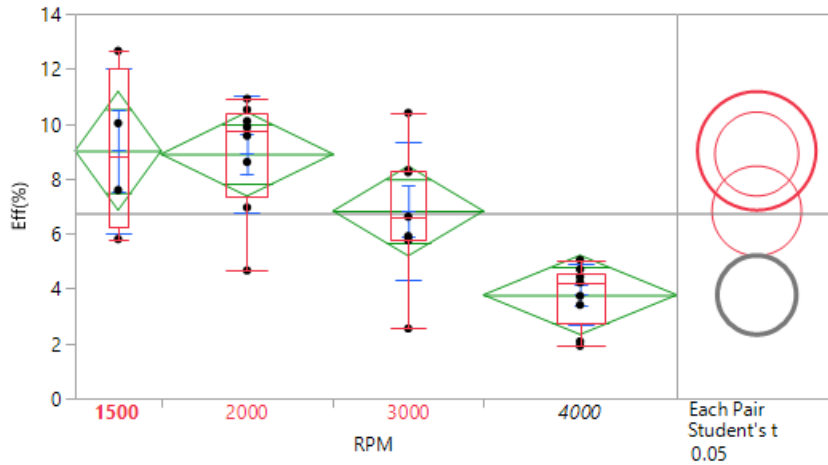


Figure A-2: Efficiency of devices based on thickness (spin rate) of PC<sub>70</sub>BM.

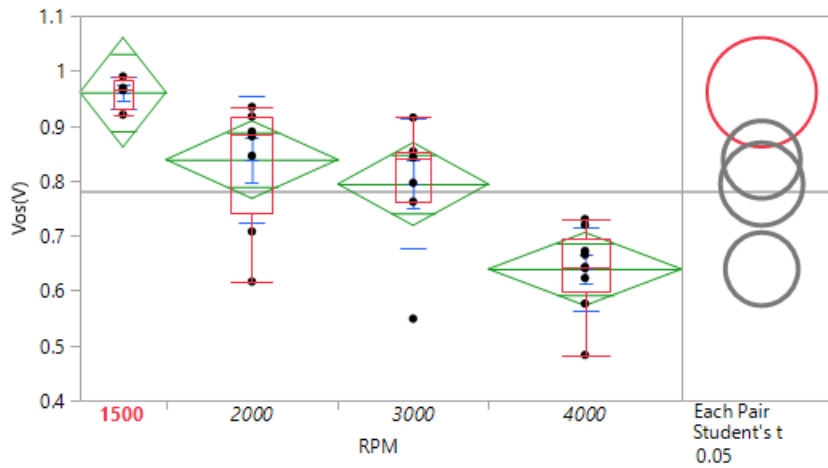


Figure A-3: Open voltage of devices based on thickness (spin rate) of PC<sub>70</sub>BM.

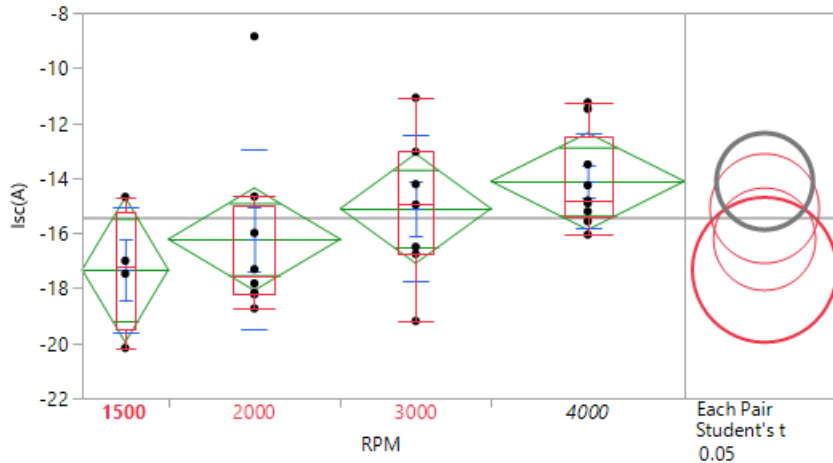


Figure A-4: Short current of devices based on thickness (spin rate) of PC<sub>70</sub>BM.

Reviewing the data in figures A-2, A-3 and A-4, the thicker film produced the best results. Efficiency for the 1500RPM devices were the highest, however, they were similar to the 2000RPM and 3000RPM results. The short circuit current ( $J_{sc}$ ) performance are well matched for the 1500RPM, 2000RPM and 3000RPM. However, for both efficiency and  $J_{sc}$ , the thicker film (1500RPM) performed better. Where the separation was found was in the  $V_{oc}$ , with the 1500RPM devices being statistically different than the other systems. As a result, the 1500RPM system performed the best for the PC<sub>70</sub>BM.

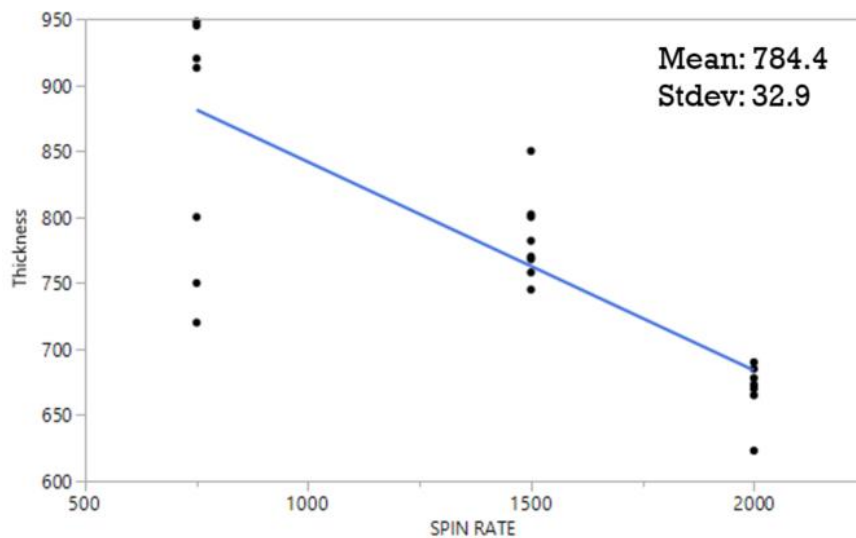


Figure A-5: Thickness of the PC<sub>70</sub>BM film fitted to the spin rate, the 1500RPM film has a mean thickness of 784.4Å.

Figure A-5 shows the thickness and the linear fit of the film versus the spin coat rate. To determine thickness, several samples were produced on bare silicon glass slides substrates. The substrates were then coated with PC<sub>70</sub>BM and were scratched with a knife to bare glass and then a profilometer was used to measure thickness of the resulting trenches. As can be seen in figure A-5, the spin coater gives a linear fit of film thickness to spin speed and that linear relationship is seen on all the films used in this work.

Figure A-5 also shows some of the problems with the spin coating at lower spin speeds and that is the non-uniformity of the resulting film. The non-uniformity can be seen in the data spread for the 750RPM thickness data. Spin coating works well for, but the resulting films are a function of the viscosity of the ink used. Thus, for a low enough value of the spin speed, the ink will not coat properly, and the beginning of the non-

uniformity region is below 1000RPM for the 20mg/mL PC<sub>70</sub>BM in chlorobenzene as indicated by the thickness data.

### BCP Thickness

Bathocuproine (BCP) is a second electron transport layer. As mentioned previously, BCP has a unique role in that it fills the voids in the PC<sub>70</sub>BM layer. Since the BCP needs to fill the voids created by the large PC<sub>70</sub>BM molecules, one can predict that there is a minimum thickness needed to fill the holes as well as create the top layer that binds with the metal layer.

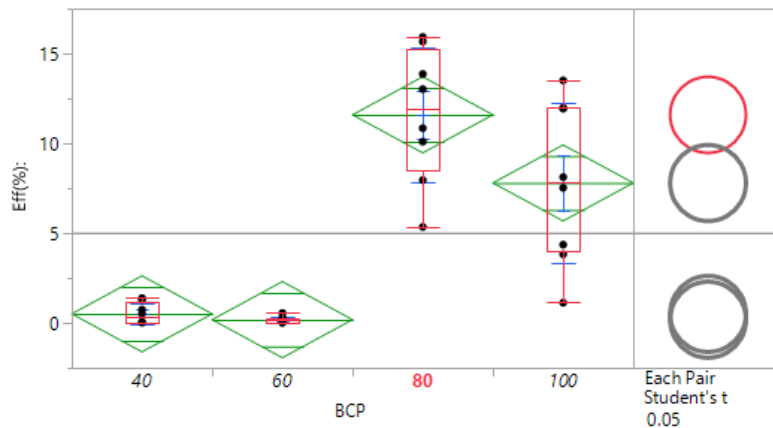


Figure A-6: BCP Skew results for Efficiency.

Figure A-6 shows the results of the BCP thickness skew for efficiency. As can be seen, the BCP target thickness of 60Å and 40Å results in non-functioning devices, indicating that this thickness is too thin to properly create a functioning device. The rapid falloff of device performance also indicates a process cliff where a minimum thickness is needed to assure functioning devices. The 80Å BCP performed the best, however, if some of the lower performing 100Å BCP devices are removed, these devices

would have performed closer to the 80Å, however, the best performing devices was the 80Å in terms of efficiency.

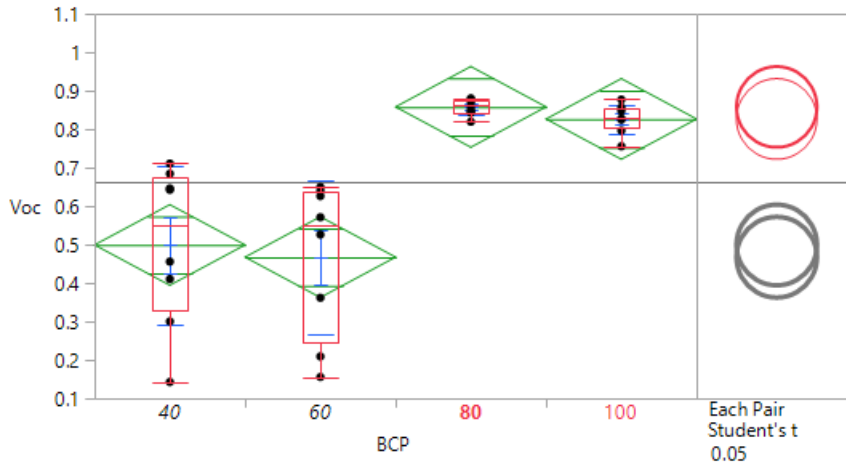


Figure A-7: BCP skew open circuit voltage results.

Figure A-7 shows the voltage results for this experiment. Again, the thin BCP devices performed poorly. As can be seen in figure A-7, the Voc measurements for the devices were statistically equivalent for the 80Å and 100Å devices, with the 80Å owning a slight performance advantage in terms of higher Voc and lower standard deviation for the test. The 40Å and 60Å devices showed poor performance with a high a standard deviation for Voc. It should be noted, that despite the high Voc marks for the 40Å and 60Å devices, the IV curves were not indicative of a solar device and shown in figure A-9. All devices for the 40Å and 60Å devices had similar curves and these devices had behavior close to a diode. Figure A-9 also has the best performing 80Å device as a comparison.

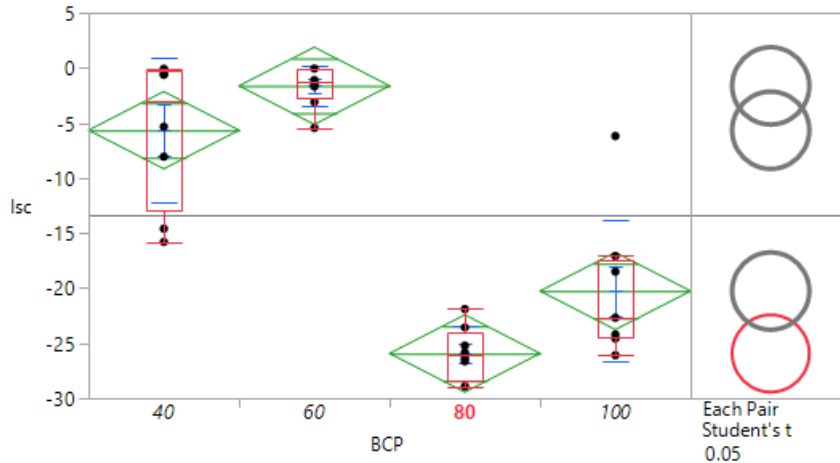


Figure A-8: BCP skew results for short circuit current.

Figure A-8 shows the results of the current measurements. Here the best performing device is clear, and the current performance is what makes the 80Å device the best. The 80Å device efficiency performance is driven by the current performance. Films above 100Å appear to begin to decrease current flow but doesn't appear to be a process cliff as it was for thinner BCP films.

One take away from the BCP thickness skew is the severe drop in process performance with thin BCP films. Considering the 'noise' in process controls for BCP deposition, researchers need to be careful in using the QCM measurement system and to closely monitor deposition rates. If a spike in the QCM deposition is observed, additional BCP deposition should be undertaken to assure target thickness is achieved or exceeded as data presented here indicates that being thinner is more a risk to device performance than being thick for BCP thicknesses. Figure A-10 shows a typical noisy BCP deposition rate monitor on the Trovato evaporation system. The noisy channel persists despite rewiring, replacement and swapping of sensor heads. There is a

potential for an upper spike to register as a spike in material deposition leading to a potential thinner film.

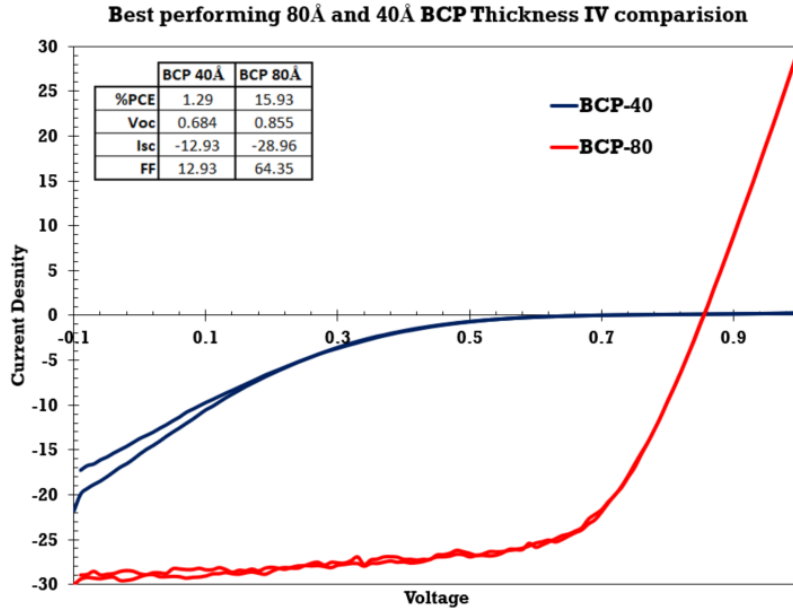


Figure A-9: IV curve difference between best performing devices and a poorer performing device split.

#### PEDOT:PSS Thickness

PEDOT:PSS is the hole transport layer (HTL) used in this work. PEDOT:PSS is a polymer that has excellent transport properties. Since we are using a p-i-n junction configuration, the PEDOT:PSS layer needs to be transparent to allow light to pass through it into the perovskite layer. PEDOT:PSS does have excellent transport properties, it does have some disadvantages when compared to other HTLs and like many organic compounds, tends to degrade upon exposure to UV.

However, for the purposes here, PEDOT:PSS is a good choice for hole transport as it is inexpensive, easy to coat and provides an excellent growth layer for the

perovskite. The other HTLs that was tried was zinc oxide (ZnO) (section 6.1) and currently tin oxide (SnO) and copper oxide are being investigated to improve transport properties and increase efficiencies.

In this work, PEDOT:PSS is coated via a spin coater on top of the ITO patterned glass. The thickness is controlled via the spin coating and does have a good linear relationship as shown in figure A-10.

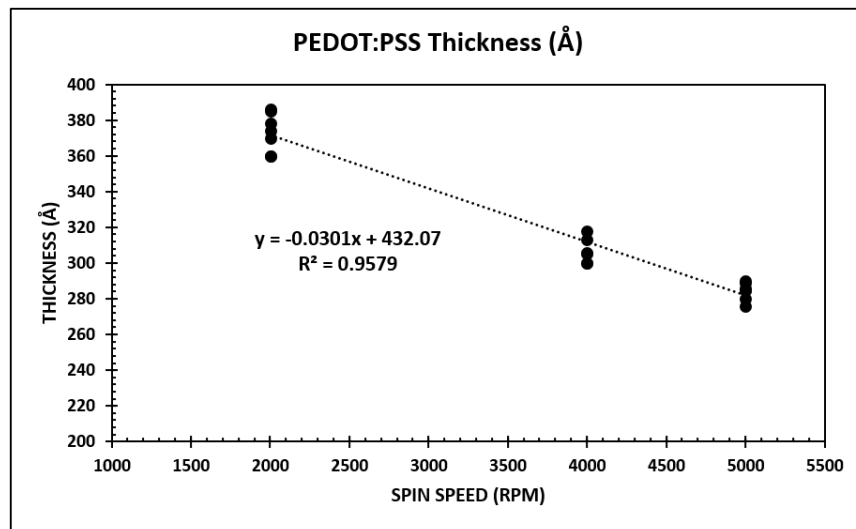


Figure A-10: PEDOT:PSS Thickness vs spin speed.

The PEDOT:PSS thickness was varied via spin coating speeds and the efficiency data is shown in figure A-11. As can be seen, there was not much difference in efficiencies as measured by this test. The 4000RPM test did show less efficient devices in this skew despite being the most used thickness prior to this test. Given the general lack of difference in device performance at a thinner and thicker PEDOT:PSS thickness it would appear that PEDOT:PSS thickness, while important, has little influence on device output.

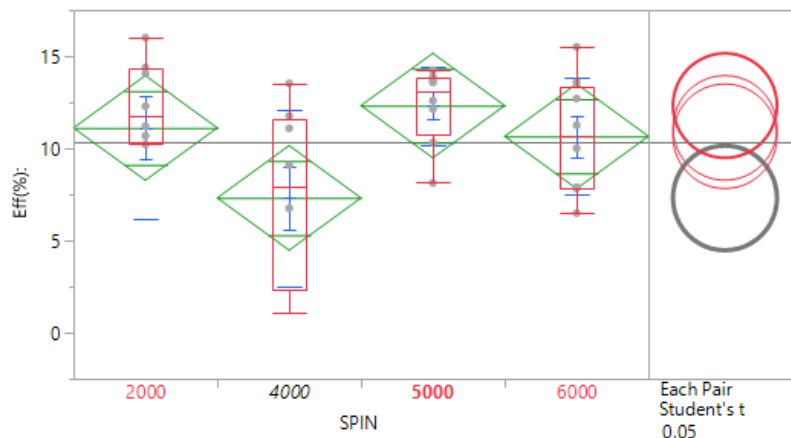


Figure A-11: PEDOT:PSS Thickness skew efficiency results.

The Voc measurements are shown in figure A-12. Again, results are fairly flat and are statistically equivalent for these tests. The thinner films (higher spin rates) show slightly better performance for Voc, but as the PEDOT:PSS thins, the variability of results begin to grow. It should be noted that while equivalent, the thickest film performed the worst.

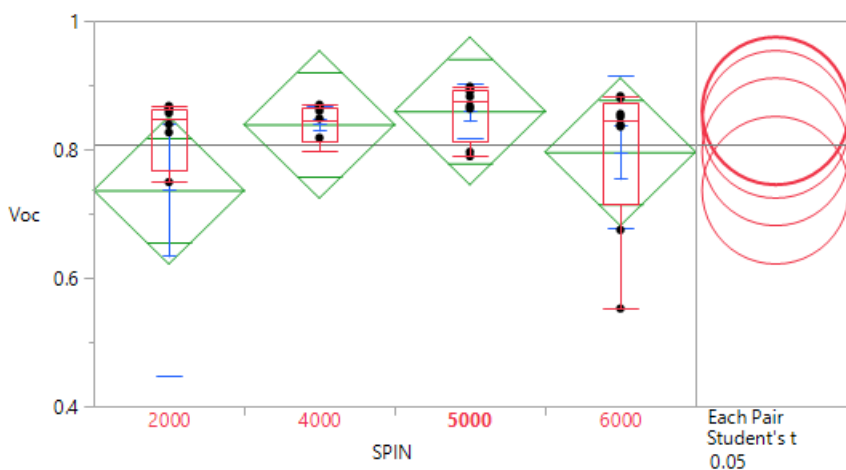


Figure A-12: Voc performance from PEDOT:PSS spin coat thickness skew.

Figure A-13 shows the results of the current skew on the thickness of PEDOT:PSS. Again, not much statistically different about the performance based on these results. The 5000RPM samples performed the best here as well. The thickest film did have some very high current values, but also had a high variability in the results, which made the 5000RPM film perform better overall (less variability).

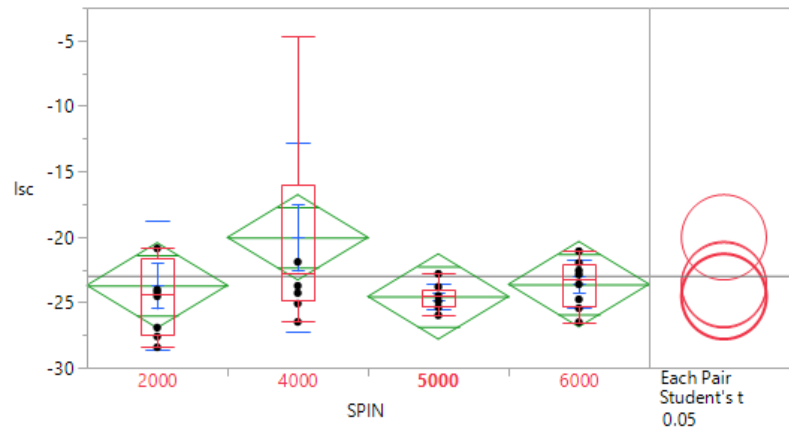


Figure A-13: Current results from PEDOT:PSS thickness skew.

These results from the PEDOT:PSS skew show not much difference in device performance despite a 3X difference in spin speed from thinnest to thickest film. Examining figure A-11 shows why there is such minor difference in observed values for efficiency, current and voltage.

Figure A-11 shows that there is simply not enough difference in measured thicknesses despite the large differences in spin speeds. The thinnest films are predicted to have a thickness of  $\sim 250\text{\AA}$  and the thickest  $\sim 370\text{\AA}$ . This represents a  $\sim 50\%$  difference in film thicknesses and it could be for the given perovskite structure, this difference is not great enough to cause any large variabilities in device performance.

Contrast the PEDOT:PSS 50% thickness skew with the BCP, which was  $\sim 2.5x$  (250%) difference in thickness and the PC<sub>70</sub>BM thickness which were predicted to be 777Å to 260Å and almost  $\sim 3x$  (300%) difference in thin film thickness. It then becomes more understandable that the PEDOT:PSS thickness skew would have a less observed effect on the device performance.

Again, it should be noted that reduction in spin speeds below 1000RPM leads to poor substrate coating (thicker films) and since PEDOT:PSS is coating a ITO patterned device structure, the thinner films then have trouble getting coating the islands of ITO (where it is needed) as opposed to being in the trenches of glass. One of the purposes of the PEDOT:PSS coating is that it serves as a planarizing film to allow for better deposition of perovskite in the next step.

#### Appendix A Conclusion

The hole and electron transport layers film thicknesses were skewed to show the results of different film thicknesses on device performance. For the Electron transport layers, which are deposited upon the perovskite, the thickness of the observed films were greater than for the hole transport layers. As a result, the ETL thicknesses showed a relationship with device performance and ETL layers. The PC<sub>70</sub>BM needed a minimum thickness to be effective and thinner films causing worse performance. Thicker films were limited due to poor coating of the PC<sub>70</sub>BM solution. To overcome this problem, different solutions can be made (higher concentration) to allow thicker films to be coated onto the devices. This will be left for later.

Bathocuproine thin film showed a process cliff, where thin films resulted in non-yielding devices and the thicker films showing good results, with the middle film performing the best. Further film targeting can easily be done as BCP thickness was controlled via the evaporator. However, given the process cliff and thicker films (above 100) performance, the current target of 80 will be close to the best.

## Appendix B: Deposition Technique

### Appendix B Overview

The information in this section is related to the challenges associated with the deposition techniques of perovskites via spin coater. While spin coater technology is well understood [ref], that general understanding is challenged when depositing perovskites as crystal formation and diffusion kinetics are also taking place at the same time.

This section also contains information on dynamic and static deposition techniques and the challenge of the former when considering the crystal formation kinetics.

### Perovskite Deposition Technique

There are three spin deposition techniques for perovskite formation, single-step and two-step and solvent engineering, which is a modification of the two-step deposition technique and can be found in table B-1. The one step deposition technique, while having challenges, is the more process friendly of the three and generally follows general spin coating techniques and principles. The remaining two-step and solvent engineering steps are more complicated and are a challenge for perovskite formation on spin coaters.

Table B-1: One and two step ink systems.

Ink Type	Ink System	1st Dep	2nd Dep	Anneal	Comments
One Step	Traditional	PbI <sub>2</sub> :MAI PbI <sub>2</sub> :FAI	N/A	100°C	
	Acetate System	PbI <sub>2</sub> -MAI-MAAc	N/A	100°C	Anneal in ambient
Two Step	Traditional	PbI <sub>2</sub> PbI <sub>2</sub>	MAI FAI	100°C	
	Acetate System	PbI <sub>2</sub> -MAAc PbI <sub>2</sub> -MAAc PbI <sub>2</sub> -FAAc PbI <sub>2</sub> -FAAc	MAI FAI MAI FAI	100°C	First dep does not need to be annealed
	Alloy	PbI <sub>2</sub> :MAI:FAI:Csl	Chlorobenzene	100°C	Chlorobenzene is added <10sec left in first dep

In addition to the ink systems found in table B-1, there is another complication and that is the deposition style, static or dynamic. For static deposition styles, the ink is deposited onto the substrate, allowed to spread and then the spin portion of the deposition begins. In a dynamic spin coat system, the substrate is spinning at speed when the ink is deposited, thus the substrate was in motion during deposition. The dynamic or static technique can be used for all systems with one exception. The alloy system can be static or dynamic on the first ink deposition, however the second step must be done while the substrate is spinning to take advantage of the solvent engineering method.

### Spin Coating

Spin coating is a well understood technology [153], [154]. Spin coating is used to deposit thin films uniformly and inexpensively. Spin coating can be broken up into

several phases, fluid dispense, spin up, fluid flow and evaporation [153], [154] and are seen in figure B-1.

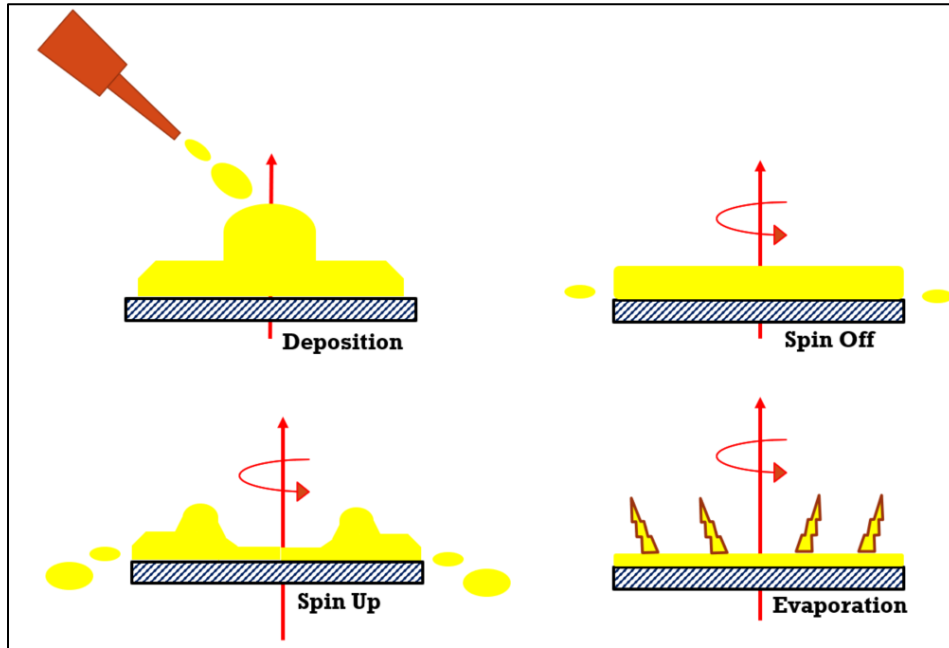


Figure B-1: Spin Coating phases: Deposition, Spin Up, Spin Off and Evaporation.

All these phases are important and while there are many different parameters that affect the final film thickness outcome the two driving parameters are spin speed and fluid (ink) viscosity. That relationship can be seen in the following relationships[153],[154]:

$$\frac{h(t)}{h_o} = \sqrt{\frac{3\eta}{2\rho\omega^2 h_o^2}} \quad (\text{B-1})$$

Where  $h(t)$  is final film thickness at time  $t$ ,  $h_o$  is the initial film thickness,  $\eta$  is absolute viscosity,  $\rho$  is the fluid density and  $\omega$  is the angular velocity [153],[154]:

$$h(t) = 3 \left[ \frac{3C^3(t)\vartheta_o\phi}{2(1-C_o(t))\omega^2} \right]^{1/3} \quad (\text{B-2})$$

Where  $h(t)$  is final film thickness at time  $t$ ,  $C(t)$  is the concentration of the solids at  $t$ ,  $C_0$  is initial solid concentration,  $\varphi$  is the liquid evaporation rate and  $\nu$  is the kinetic viscosity ( $\nu = \eta/\rho$ ). The difference between the two expressions is evaporation rate which is found in equation B-2. Both expressions are ignoring the shear stress of spin coating in an atmosphere and any effects of Newtonian and non-Newtonian fluids. However, examining equation B-1, we see that the expression is dimensionless and can be simplified into:

$$H \sim \tau^{-1/2} \quad (\text{B-3})$$

Where  $H$  is  $h(t)/h_0$  and has same relationship as in equation B-1. If the other factors such as Newtonian fluid dynamics and avoiding further expression and, the dimensionless final thickness behaves as [153]:

$$H \sim \tau^{-1} \quad (\text{B-4})$$

Comparing the final thickness expressions in equations B-3 and B-4, it can be seen that spin coating in air results in a thinner film as a result of evaporation and shear effects of the atmosphere and the liquid [153],[154].

It should be noted that nowhere in the relationships and equations for spin coating are the reaction kinetics accounted for. Most spin coating models as described by the relationships above are for describing the creation of thin films that take place without reactions. These models need to be adjusted for the deposition techniques such as two step and alloy methods.

For single step inks and depositions, the reaction rates can be described by those equations as seen above. However, the expressions become more complex with time.

The values for the liquid evaporation rate ( $\phi$ ) and the kinetic viscosity ( $\nu$ ) will no longer be constant but will rather be functions of time. A further complication is that rates of formation of perovskite also effect evaporation rates as the crystallite sizes can impede diffusion of the solvent to the top surface which reduces the evaporation rate.

However, the crystallite size growth is modeled by an independent set of conditions based on nucleation sites, therefore if crystals grow from the bottom interface will have no impact on evaporation rates as the crystals will push the solvent (ink) towards the top surface where it can freely evaporate. If, however, the crystals form at the top surface and grow toward the back interface and move down with the solvent (ink) level, the crystals can impede the evaporation rate and can trap residual solvent (ink) at the back interface.

The following adjustments to the expressions above are needed to consider the perovskite formation for a single step ink deposition:

$$\rho(t) = \rho_{ink} + \rho_{crystal}(t) + \rho_{ink}(t) \quad (B-5)$$

$$\eta(t) = \eta_{ink} + \eta_{crystal}(t) + \eta_{ink}(t) \quad (B-6)$$

$$\phi(t) = \phi_{ink} + \Delta\phi_{ink}(t) \quad (B-7)$$

For the expressions in equations B-5, B-6 and B-7, the terms  $\phi_{ink}$ ,  $\eta_{ink}$  and  $\rho_{ink}$  are all the initial values for the ink prior to deposition. The terms  $\eta_{crystal}(t)$  and  $\rho_{crystal}(t)$  refer to the changes in the ink related to perovskite crystal formation. The creation of perovskite crystals in the ink will change the volume as well as well as the viscosity of the fluid. The remaining terms in equations B-5 and B-6 refer to the changes in the solvent due to the loss of fluid and crystals. The other term in equation B-7 is the

change in evaporation rate due to the crystal formation and the impact on solvent diffusion rates.

Examining the new expressions in equations B-5, B-6 and B-7 is that for single step deposition inks these can still be reduced to a constant provided the ink contains equal molar ratios needed for the final product. As the perovskite crystals are forming (precipitating from solution) the values of in B-5, B-6 and B-7 can be considered constant for equal molarity inks as the loss of material from the ink to the crystal does not change the composition of ink during crystal formation. However, for those with non-molar ratio inks, the loss of ink material to the crystal will have a greater impact on the values in B-5, B-6 and B-7.

For the alloy systems, the evaporation rate changes as:

$$\phi(t) = \phi_{ink} + \Delta\phi_{ink}(t) \quad \langle t = 0, t = t_1 \rangle \quad (\text{B-8})$$

$$\phi(t) = \phi_{solvent} \quad \langle t = t_1, t = t_2 \rangle \quad (\text{B-9})$$

$$\phi(t) = \Delta\phi_{ink}(t) \quad \langle t = t_2, t = t \rangle \quad (\text{B-10})$$

The evaporation rate depends on the same conditions as listed above. However, the addition of a solvent wash during the deposition process changes the evaporation rate. Prior to the addition the evaporation rate behaves the same way as in the single step systems. Once the solvent wash is added, the evaporation rate for the ink stops as the solvent wash creates a cap on the top interface and the only evaporation is that of the added solvent.

The additional benefit of the solvent engineering method with a solvent wash is a cooling effect on the film. Evaporation is a cooling effect as energy is removed from

the system to allow the liquid to enter the gas phase which then has a cooling effect [201] on the film. Unlike the deposition process in which the volume of ink deposited has negligible effect on the final film thickness, the volume of the solvent wash will have an effect as the greater volume/mass of solvent added will remove more heat from the substrate and film as more energy is needed to remove the solvent. Furthermore, the speed of application of the solvent wash also effects the thin film as a faster deposition rate was observed to hop or bounce across the perovskite surface as well as form the visual rings seen.

For two-step inks, the expressions become much more complicated. The first step of a two-step deposition, the standard expressions for thin films deposited via spin coater all apply with little to no modifications. However, the second step however a much more complicated process than what is described by the expressions above. As shown in figure B-2-A, the second deposition step must perform an additional step and that is diffuse into the underlying scaffold layer. This diffusion must happen in both the depth and radial direction while the material is being spin off. For a static spin technique, the delay after the application of the second ink allows the ink to spread uniformly due to good surface contact. This allows the ink to spreading and the additional ink material can then diffuse down into the scaffolding layer prior to the spin. Results from static spinning are more reproducible as seen in figure B-3.

The second application is to use dynamic spin coat for the second ink. The ink undergoes diffusion and spreading while at the same time reacting and evaporating from the surface. The consequence of the dynamic spin coating on a second step

system is shown in figure B-2-B and that are unreacted areas randomly distributed in the active layer.

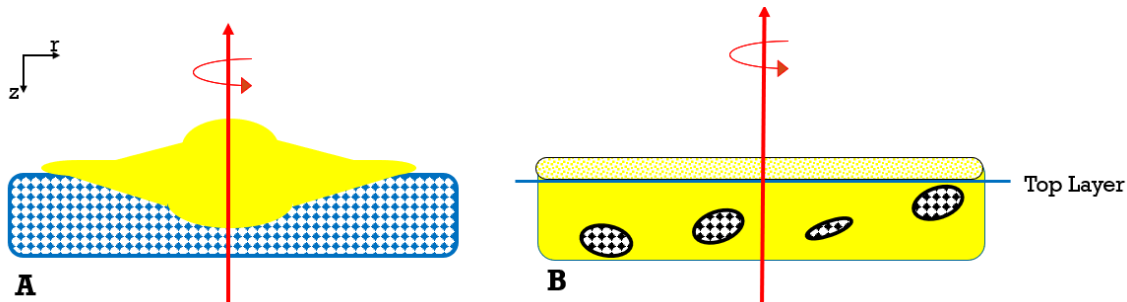


Figure B-2: Issues with a two-step deposition, A) Diffusion into and radial on a sample and B) areas of unreacted material.

The second application is to use dynamic spin coat for the second ink. The ink must then undergo diffusion and spreading while at the same time reacting and evaporating from the surface. The inevitable consequence of the dynamic spin coating on a second step system is shown in figure B-2-B and that are regions within the scaffold layer that either does not react with the ink or reacts and prevents material from diffusing through the crystal. The results are the same, these devices contain regions of scaffold layers surrounded by perovskite crystal layers. These regions help explain the worse standard deviations seen within and between device to device as shown in figure B-3. Examining figure B-3, the best device was during a dynamic spin, however the standard deviation for efficiencies were almost 2x the static deposition technique allowing the static deposition devices to outperform the dynamic deposition. The standard deviations got much worse for the  $I_{sc}$  and  $V_{oc}$  approaching near 3x. The dynamic devices also had better current performance, however the  $V_{oc}$  are lower which would indicate a poorer crystal formation.

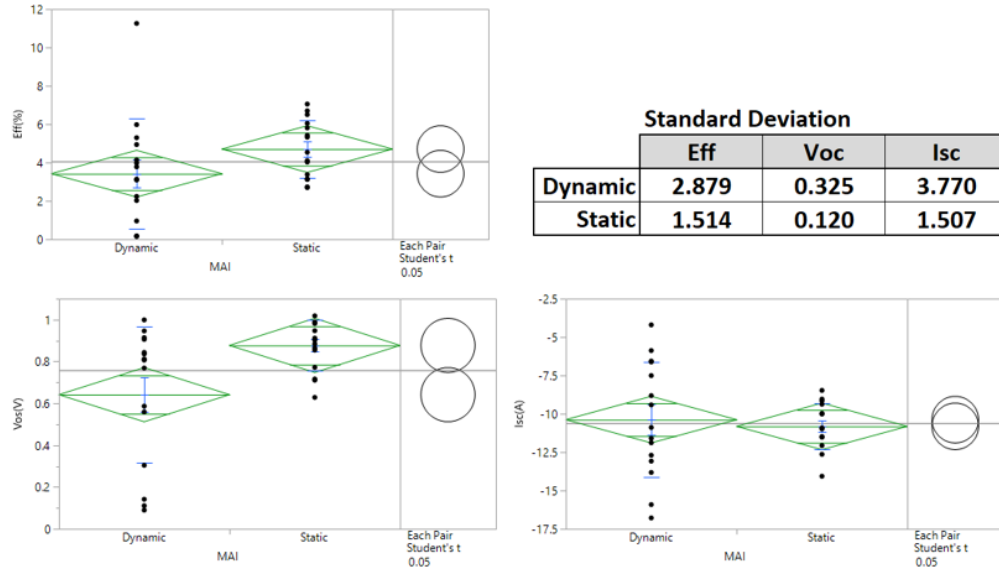


Figure B-3: Performance of devices based on dynamic vs static deposition. Data is for two step deposition PbI<sub>2</sub> followed by MAI.

Figure B-4-A shows the device layout for structures built at Texas State, which consist of 4 solar devices with an active area of 6.5mm<sup>2</sup> all in a growth area of ~1cm<sup>2</sup> in the center of the glass substrate. There are thus four devices on each sample that should see the exact same conditions. Having a large standard deviation due to a spin coating technique is further evidence of incomplete conversion due to the diffusion and reaction kinetics found in a two-step ink.

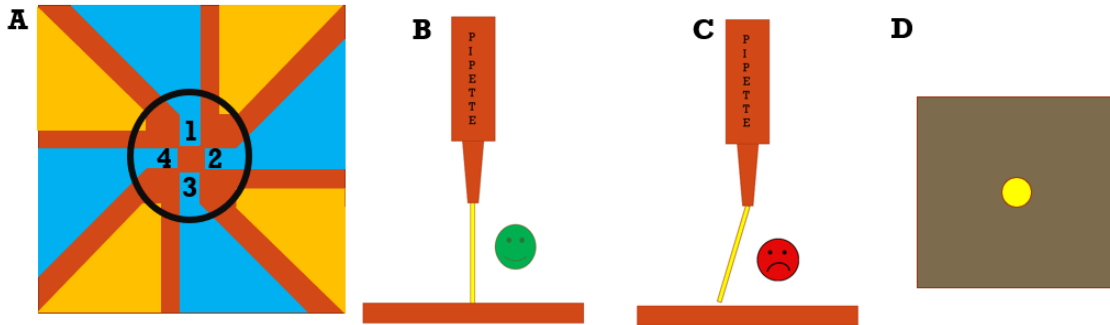


Figure B-4: A) Pin wheel design and the 4 devices. B) Good pipette delivery of ink. C) Poor pipette delivery of ink. D) Hole in perovskite film due to poor pipette delivery or bad centering.

### Other Issues

In addition to the challenges of the dynamic spin, there were several other issues unique to Texas State that are contributing to the high standard deviation in those samples. The first is the centering of the sample. The samples are placed on a vacuum chuck manually and as a result are not centered to the spin. In addition, the application of ink is also done by hand and can be off center further still. Both these subtle errors create more problems for the dynamic spin, the worse of which is a center hole as shown in figure B-4-D.

Next, the delivery of ink via a pipette also has challenges. Pipettes tips were designed to transfer controlled volumes of liquid, not dispense ink onto a spin coater, and a frequent problem seen was the errant dispense of the ink off to the side (figure B-4-B and C) which has the same result, a hole as seen in figure B-4-D. Since there is method to predict a pipette tip will dispense errantly, this is another source of variation in the process.

Lastly, MAI (and FAI) deposition requires the use of new pipette tips. The dispense of MAI in IPA (or FAI in IPA) from the pipette results in white residue that can be clearly seen in the pipette. It was common practice to reuse tips for dispensing inks, however, the longer the tip remained in use, the higher the chances that the white residue would transfer to the substrate and result in poor devices.

#### Prevention

To combat these problem, several changes were made. The first was to stop the use of dynamic deposition and instead rely on static deposition processes. The static deposition process has the advantage of allowing the ink to be placed in the center of the sample and to pool and spread out prior to spin start. This helps reduce the lateral diffusion and thin out described above. In addition, a new chuck was introduced which centered the substrate in the spin coater in a consistent manner via the use of notches and not vacuum. The centering of the sample allows for better uniformity on the slide as the centripetal force is more uniform. Visually, no further swirls were visually observed, and film thickness became more uniform which was pulled from the efficiency data not having an overall trend based on position.

Lastly, pipette tips were replaced after each deposition. The results on from this change was that films had less defects spin coated related defects which can be a source of nonuniformity in the perovskite crystal. Figure B-5 shows common spin coating defects and table B-2 shows common solutions.

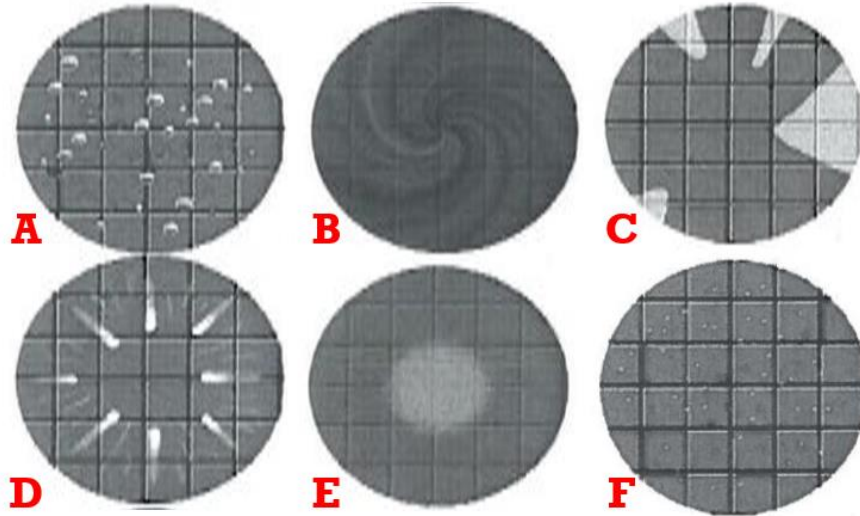


Figure B-5: Common spin coating defects. A) Air bubbles on surface, B) Swirl patterns, C) Insufficient Ink, D) Comets, streaks or flares, E) Chuck mark or dispense problem and F) Pinholes.[154],[202].

Table B-1: Types of defects and potential causes. Adapted from [154], [202].

Defect	Cause
Air Bubbles	Air bubbles in ink, bad dispense tip
Swirl Patterns	Fast acceleration, exhaust problems, ink not centered
Insufficient Ink	Not enough ink
Comets, Streaks or Flares	Particles in ink, ink not centered, speed issues, exhaust issues
Chuck mark	Vacuum chuck mark (cooling), off center deposition
Pinholes	Air bubbles, particles

While these changes helped reduce process variation, spin coating of perovskite devices remain a challenge. Together with items discussed in section 6.2 and in appendixes B and D the sources of process variation in solar device processes from spin coating were reduced.

## Appendix C: Design of Experiments and Statistics

### Introduction to DOE

In this work the design of experiments (DOE) was to be used as a fast way to path find the best performing devices with the least amount of effort and expense. However, the method proved to not be useful in this effort due to the high incidence of variability in the process. This appendix will review the concepts of DOE and list out some of the problems associated with the approach for spin cast perovskite solar cells.

### Design of Experiment

Design of experiment is a testing method that uses variation under controlled conditions to test whether the controlled conditions had an effect on the variation observed. Said another way, it is a systematic approach to looking for cause and effect in a process. DOE differs from other experimental approaches as it allows more than one variable to be changed at once without loss in information. The traditional approach is known as the one factor at time (OFAT). Not only does this allow the DOE to have less testing requirements than OFAT, it also provides more information.

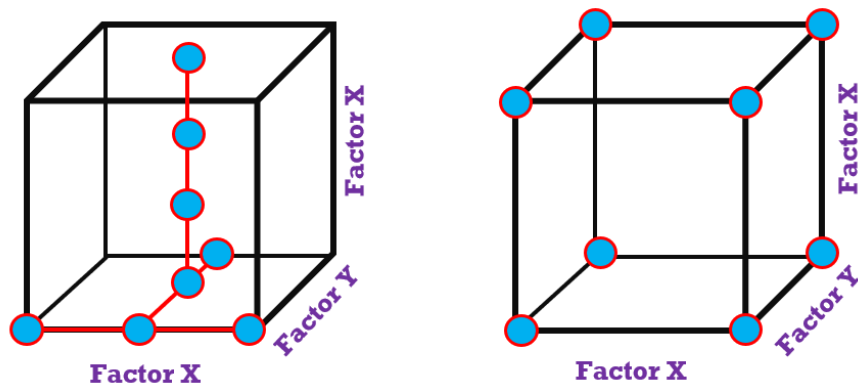


Figure C-1: DOE vs OFAT in design space for a 3-factor test, OFAT is the left panel, DOE the right.

An example of this concept between of more information and less testing is highlighted by the example shown in figure C-1. In Figure C-1, there are three testing factors (the variables to change) and can be represented visually in 3D as a cube. The OFAT approach gives the results shown in the left panel of figure C-1. Since one factor is changed at a time, the experimenter is confined to changes along the red lines in x, y and z factors. The DOE experimenter is not confined by the limitations of the given values of any of the factors. The experimenter chooses the highest and lowest values for factors which results in a cube seen on the left of figure C-1. The volume of the cone given by the OFAT lines is less than the volume of the cube given by DOE and this gives more information about the process and experimental space than the cone.

In addition, a properly designed DOE also allows higher order relationships to be calculated. In the OFAT method, no higher order relationships can be determined other than pair wise relationships and are limited to variation in x, y and z. The DOE on the other hand allows all the variables to be compared at once which gives rise to higher order relationships, such that x, y, z are known as well as xy, xz, yz and xyz relationships. DOE can do this as the mathematics that supports the generation of the higher order relationships are built into the model for a factorial design and that math to build higher order relationships in OFAT is not possible.

#### DOE Principles

DOE is based on a statistical approach to collecting data. This statistical approach allows the use of mathematical tools to help evaluate the data and develop relationships between variables as well higher order relationships. To accomplish this

task there are three principles that need to be addressed to have a good statistical model and meaningful results using DOE. These are, replication, randomization and blocking [203]. Replication is the repeating of the basic experiment and is important for two reasons. Replication is important in that repeating the same tests allows for the experimental error to be calculated and secondly it provides more information on the effect of a variable on the outcome if a sample mean is used as a response.

Randomization is a hallmark of statistical processes and testing. In DOE randomization is another important concept as statistical methods are based on measurements and errors being independently and random variables[203]. The easiest way to randomize is to conduct the experiments in a random order thereby reducing the effect seen from unknown factors on the test. For example

The last concept is the idea of blocking. Blocking is an experimental method used to increase precision. Precision is a statistical concept that refers to the amount of variability in a process and by increasing precision, the variability is reduced. Blocking is essentially combining factors together, for example gender and age are very common but also material batches. Blocking also has an advantage in that it can control nuisance factors. Nuisance factors are variables that affect the outcome of your observation but are either hard to control or impossible to control. Examples of nuisance factors are material batches, day vs night, and the shift or people conducting the experiment. By blocking what you cannot control, you can turn the problem into a factor in your experiment as blocks can be analyzed as well.

## Statistics Used

In this work the other statistical tests that were used were mean ( $\bar{x}$ ), standard deviation ( $\sigma$ ) and least significant difference (LSD). The first two are very commonly used and a good measure of the device performance and spread in that performance.

The sample mean is given by:

$$\bar{x} = \frac{\sum_{i=1}^n x}{n} \quad (\text{C-11})$$

Where n is the number of data points and x is the value of each of the n data points.

Standard deviation is given by:

$$\sigma^2 = \frac{\sum_{i=1}^n (x_i - \bar{x})^2}{n-1} \quad (\text{C-12})$$

Where again, n is the number of data points and  $\bar{x}$  is the mean and  $x_i$  is the value of each data point.

Together the mean and standard deviation are the two most common statistical values reported. The mean indicates the central tendency of the values observed and the standard deviation indicates how much spread is seen in that data. For this work, the means were important, but only in maximizing the efficiency, short circuit current, open circuit voltage and fill factors. The standard deviation was more so interesting in establishing how well devices performed under the same experimental conditions. Large standard deviations indicated that problems existed with the device manufacture and indicated that other factors were at work in the ultimate device performance.

The other statistical test that was performed was the ‘each pair student t’ test that was performed in JMP. This test uses the LSD method for determining a difference in each of the population’s means which indicates that there is a statistical probability that the two means are statistically different. The LSD method is based on the null hypothesis test that two means are the same which is statistic speak for a test that determines if two means are different by statistically showing the two means are not the same.

To determine the LSD, we first need to introduce a new statistical measure known as the mean square error ( $MS_E$ ) which is given by the equation:

$$MS_E = \frac{\sum_{i=1}^a [\sum_{j=1}^n (y_{ij} - \bar{y}_i)^2]}{N - a} \quad (C-13)$$

Where a is the number of factors being tested, n is the number of measurements at each factor and N is the total number of observations given by  $N = a * n$ . This value is then applied to the t statistic:

$$t_o = \frac{\bar{y}_i - \bar{y}_j}{\sqrt{MS_E \left( \frac{1}{n_i} + \frac{1}{n_j} \right)}} \quad (C-14)$$

The t statistic is a measure of the difference of a hypothesized value versus the standard error. What it measures in this work are two values the same when compared to the standard error, i.e. can we observe a difference between two values given the error in our observations. This allows efficiency, currents, voltages and fill factors to be tested for statistical differences.

The t-statistic is usually kept in a table form and is based on two further values known as  $t_{\alpha/2}$  and  $N-a$ .  $N$  is the total number of observations (tests) and  $t_{\alpha/2}$  is the confidence level for the test. For these calculations, the default value for  $t_{\alpha/2}$  is 0.025, which is a confidence level of 95%. All the confidence level means is that if the test shows a difference in two observed values, that difference is true 95% of the time.

The 95% confidence level is what was used in industry the current researcher fled. Values for engineering related testing usually ranged from 85% to 98% with the two most common being 90% and 95%. Reasons for these values are only dictated by the amount of risk an organization wishes to take.

We now arrive at the LSD expression:

$$LSD = t_{\alpha/2, N-a} \sqrt{MS_E \left( \frac{1}{n_i} + \frac{1}{n_j} \right)} \quad (C-15)$$

This expression is then calculated for each test observation. The use of JMP greatly improves the researcher's ability to quickly and accurately perform these calculations and tests. JMP Pro 13.0.0 is a statistical software program that assists with all things statistical such as hypothesis testing, statistical value calculation, graphing and DOE matrix creation. In addition, JMP makes use of visuals to demonstrate some basic statistics as well as the student t (LSD) test results in a graphical form as seen in figure C-2.

## Plots

In figure C-2, there are two panels. In each panel there is data represented by the vertical lines of black dots. The black dots are the individual data point values in the overall group represented by the categories on the x-axis (16%RH, 20%RH and 26%RH). The red boxes are the standard box and whisker plots which represent the mean and standard deviation. The box plot's center line is the mean value and the box is the representation of the standard deviation, such that samples with larger boxes have larger variation in the observed value. The green diamonds are each data set's LSD value.

The grey and red circles are a visual representation of the t-test results. In figure C-2-A, all circles are red, this represents that these two groups are statistically the same per the student t (LSD) test. The result in figure C-2-B is that two circles are both red and one circle that is grey, the overlapping circles are both statistically the same while the grey is considered statistically different. The bold red lines and x-axis categories are there to show you which group you have selected (20%RH in figure C-2-A and 26%RH in figure C-2-B) is only bold to show you which group you are testing and the red values are those that match your selected item or grey showing a mismatch.

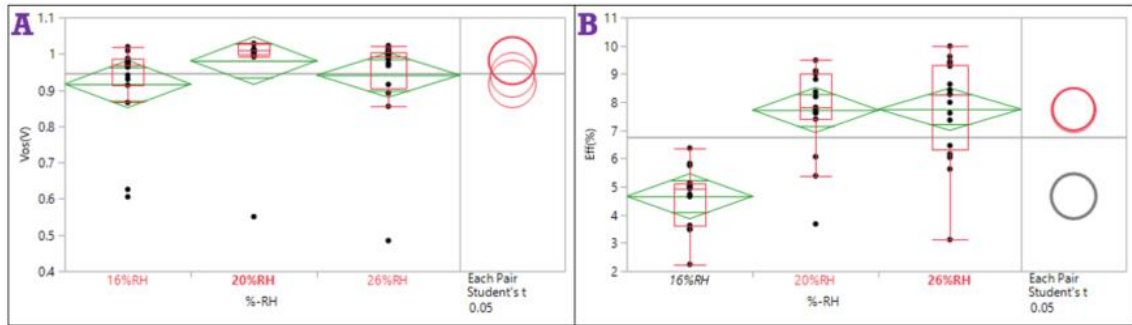


Figure C-2: Example of a JMP output graph. group. A) Red overlapping circles indicating statistically equivalent data; B) Non-overlapping circles (red and grey) indicating statistical different populations.

## Data

As highlighted previously, the test structure used has four devices on each substrate. In addition, the evaporator step of the deposition process (used for aluminum deposition, bathocuproine and  $C_{60}$ ) can handle 4 substrates at a time. This gives 16 devices per batch, which is also the minimum number of data points to have a meaningful statistical test. Figure C-3 shows the relationship for testing for significance for a sample size of 16 and the difference that can be seen as well as the power of the test.

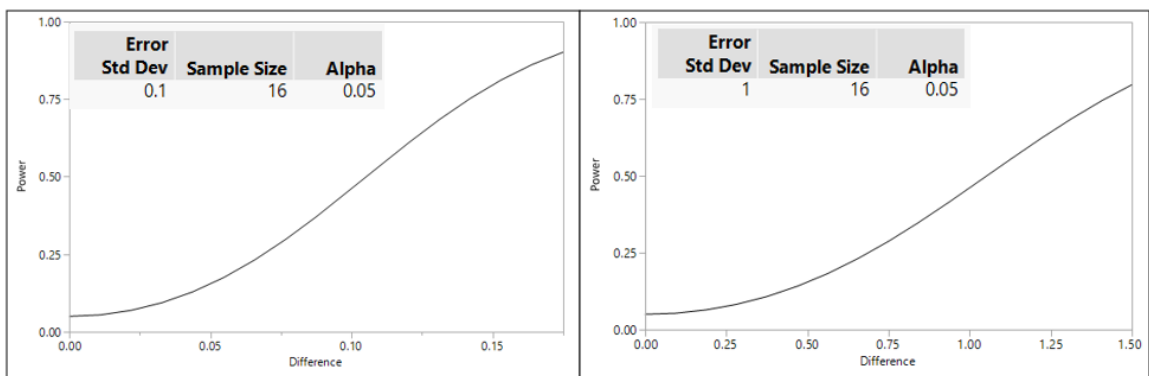


Figure C-3: Power, sample size and difference.

Power is the ability of a statistical test to return useful information on the test result. Essentially, the graphs in figure C-3 are showing that the power of the test are worse for smaller differences in the mean. This implies that there is more error in determining that two means are different with the current sample size. It also should follow, that as the number of samples increases, the power of the test also increases. The data collected in here are meeting the requirement for a good statistical testing for differences at 16 samples.

#### DOE Failure

As mentioned before, DOE was to be the primary tool for pathfinding perovskite devices. The initial hope was that the four devices on each sample would yield consistently enough to make tests between various factors viable such that each evaporator run could yield 4 tests. The evaporator use is a form of blocking since each of the deposition rates for aluminum, C60, and BCP were different batch to batch.

The perovskite structure was thought to be a function of:

$$\text{Perovskite} = f(\text{ink}, \text{dep technique}, \text{anneal temp}, \text{anneal time}, \text{spin rate}) \quad (\text{C-16})$$

However, it was determined that these were not the only factors contributing to perovskite performance. In fact, perovskite is a function of those in equation C-16, but also:

$$\text{Perovskite} = f(\text{ambient temp}, \text{ambient pressure}, \text{ink age}, \text{PEDOT age}, \%RH) \quad (\text{C-17})$$

Of these new factors, only PEDOT age and %RH could be controlled reliably on each test. Ambient temperature and pressure could not be controlled. Ink age could be controlled, however, there was some limitations on creating new inks every few days that introduced slight variations in the concentration and ratios of the precursors.

As seen in appendix D, ambient factors have just as much influence on the device performance as any of the controlled factors. This requires changes to the testing program as day to day pressure swings (weather systems) and temperature were contributing to equally to test results.

#### Appendix C Summary

Statistics are valuable way to measure differences in results. Used in this work, statistics were used to look for differences in perovskite solar device performance levels as a result of changes in the perovskite manufacturing techniques. DOE was initially tried to make quicker work of targeting optimal devices, however, too many non-controllable factors were equally contributing to device performance.

In the end, the use of least significant difference (LSD) techniques were used to show optimal results from a slew of different factor levels. The differences in day to day levels were found to be unsurmountable to effectively use DOE techniques.

## Appendix D: Ambient environmental factors and their influence on perovskite formation kinetics.

This appendix is the preliminary text of a paper addressing the ambient environmental factors that influence perovskite performance. The paper focuses on the 5% cesium alloy as it was the favorite at NREL. Texas State University's One-Step ink is also featured.

### Introduction to Ambient

Perovskite solar cells hold the promise of inexpensive solar energy via a combination of high efficiency devices created with inexpensive production methods. Since the first photovoltaic device was identified a short time ago, much research focus has been applied to study of hybrid inorganic and organic perovskite solar systems. Current efficiencies are exceeding 25% and much work has been done focusing on the stability issues of the perovskites in a solar cell. In addition, a plethora of electron and hole transport layers have been used to both improve efficiencies and address some of the stability issues [10].

Spin casting remains the favorite deposition due to its ease and low cost. As a result, much effort is being applied to the development of various kinds of inks to create a stable and efficient perovskite layer. At the moment, there are two broad techniques for creating a perovskite film, one step ink and two step inks. Included in the one step inks are those inks using adducts like MAAC, acids, bases and co-solvents. For two step inks, these include scaffolding (for example using PbI<sub>2</sub>-MAAC) as well as solvent

engineering methods that require the deposition of a co-solvent to aid in film development.

Regardless of the ink type, the general discussion that is generally occurring is on the type of forces interacting within the ink solution during deposition. One model that is being presented is that perovskite formation is dictated by intermolecular exchange and the rate of which this occurs influences film characteristics. The other model is the solvent removal rate which states that the film characteristics is being dictated by the rate of removal of the solvent from the film.

The two most popular solvents used for perovskite inks are DMF and DMSO. Both DMF and DMSO are polar solvents, with DMF having a dipole moment of 3.86D and DMSO one at 3.96D, which are both larger values than for water which has a dipole moment of 1.84D. In solution these polar solvents are thought to form complexes with the ionic salts that constitute the inks [204].

Missing from the conversation is the effect of ambient conditions on the perovskite formation. As will be investigated here, the role of the ambient conditions contributes a larger role in the formation of high quality perovskite films than is generally regarded.

In this study the effects of the ambient conditions of humidity, temperature, pressure, and solvent concentration will be explored, and their effect device performance will be explored. It will be shown that the influence of ambient conditions

contributes to the true device performance in such a way as to suggest that the solvent removal rate model is the dominate factor in perovskite performance.

## Materials Methods

An inverted planar p-i-n perovskite solar cell structure was used as a test vehicle and is shown previously in figure A-1. For this work, the effects of environmental conditions and the influence on the resulting perovskite solar cell are of interest, not the ultimate efficiency of the device. The data for each data point was taken from the same ink compositions and typically made the same day. Data for each run was also taken on the same day.

In each case, the same inks were used to make the test devices unless otherwise noted. Two different perovskite deposition methods were investigated, and both are spin coated as this is the current deposition of choice for a majority of the work reported. The perovskite was deposited using a single ink via an adduct method, Texas State's one-step method and the other using solvent engineering using a promising perovskite alloy resulting in a  $\text{MA}_{0.15}\text{FA}_{0.8}\text{Cs}_{0.5}\text{PbI}_3$ . In each system under investigation, results are reported and contrasted within the chosen film. Thus, this isn't a review of the best performing film, but a look at the factors influencing film performance.

The samples were prepatterned ITO glass substrates from and were cleaned using in an ultra-sonic tank of a 10% concentration of DECONIX in DI water mix for 20 minutes. Samples were rinsed well using DI water and blown dry using  $\text{CO}_2$  gas.

Samples were heated on a hot plate to 120°C for 10 minutes. Samples were then plasma treated with an O<sub>2</sub> plasma for 10 minutes.

A 30nm film of PEDOT:PSS deposited via spin coating done in atmosphere and annealed at 145°C. The samples were then transferred to a LC Technologies N<sub>2</sub> glovebox where the O<sub>2</sub> and H<sub>2</sub>O levels are less controlled to less than 1ppm. Perovskite inks were prepared in and deposited inside the N<sub>2</sub> glovebox via spin coater. Samples annealed at relative humidities other than 0% were removed from the glove box and placed into a separate relative humidity-controlled glove box, without O<sub>2</sub> removal.

Temperature tests were done inside the LC Technologies N<sub>2</sub> glovebox spin coating glove box and were done using a room heater and monitoring the temperature near the spin coater and annealing hotplate. The heater was turned off prior to deposition to remove the fan component blowing N<sub>2</sub> around the glovebox and altering results. Temperature remained constant during deposition and annealing (~15 minutes) which was done inside the glovebox on a hotplate.

Pressure tests were done inside the LC Technologies N<sub>2</sub> glovebox and using the pressure control system on the LC Technologies glove box. Movement inside the glovebox was minimized to prevent pressure fluctuations during deposition and annealing. The pressure range was limited due to the potential damage from elevated pressures to the glovebox. Maximum pressures available was 14 mbarr above ambient conditions are were constant during deposition and annealing.

Solvent tests were done inside the LC Technologies N<sub>2</sub> glovebox as well. To simulate a higher solvent concentration, cleanroom wipes were cut into ~25mm x 75mm strips and soaked with ~1mL of 4:1 DMF:DMSO solvent. These were placed in the bowl of the spin coater as well as near the hotplate. The soaked strips remained wetted during the duration of the spin coat and anneal. Once the elevated solvent tests were complete, the strips were removed from the glovebox and a 15min N<sub>2</sub> purge was performed on the glovebox, removing the additional solvent concentration.

Samples were then placed into an evaporator where they received 40nm of C<sub>60</sub>, 8nm of bathocuproine (BCP) and 100nm of aluminum. Samples were then encapsulated via an automated encapsulator and then immediately tested were done using an Oriel solar simulator and results captured using a Keithley 2400 source-meter. JMP software was used to determine statistical differences noted here.

#### Annealing Conditions (Humidity)

Humidity and water is a challenge for perovskite materials as the MAPbI<sub>3</sub> systems tend to decompose with exposure to water [205], [206]. However, it has been shown that exposure to elevated relative humidity increases the performance of the perovskite layer [5], [6]. Results performed using a two-step adduct method, two-step PbI<sub>2</sub> method, and a solvent engineering alloy inks all show improved efficiency performance with increases in relative humidity.

A review of the data from a selected system, and seen in the other systems, is an increase in the  $J_{sc}$  as a result of the annealing performed in elevated relative humidity conditions. The  $V_{oc}$  shows almost no change indicating that the effect of the relative humidity is an increasing the current output from the device. In addition, the fill factor for these devices did not show any trend. Thus, the gains in the efficiency was directly related the gains in the  $J_{sc}$ . Figure D-1 shows the efficiency curve of devices annealed at different relative humidity levels.

However, there is a relative humidity level that is most beneficial to the devices and above that level, there is a device performance roll off, again driven by  $J_{sc}$ .

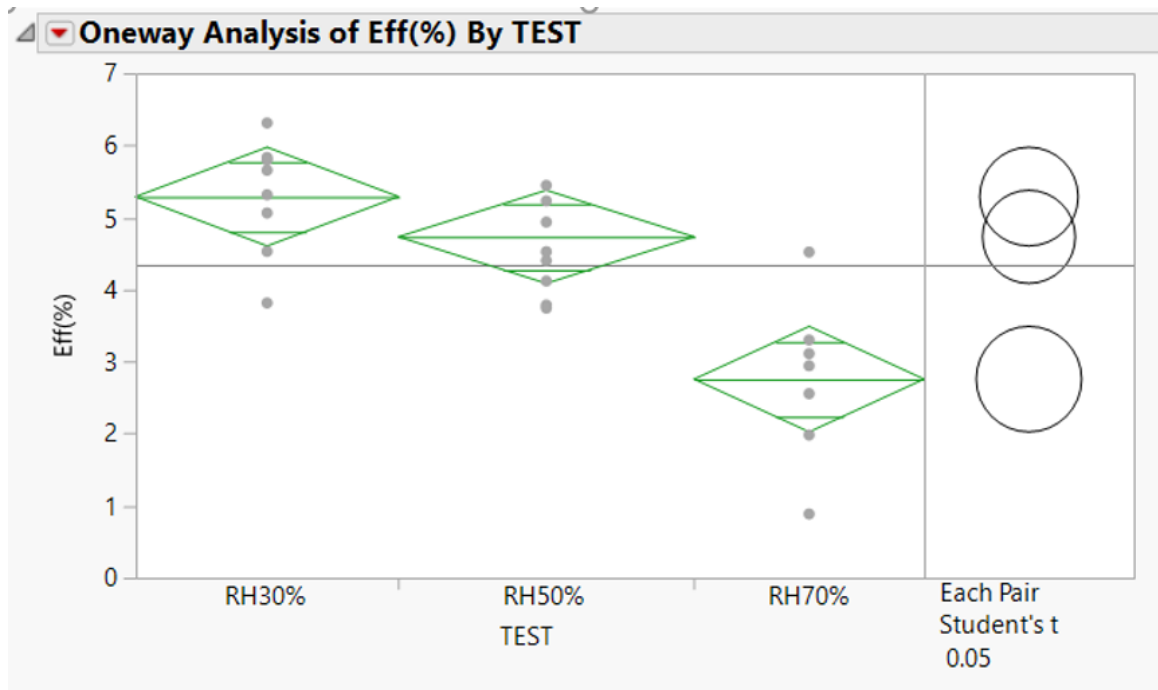


Figure D-1: Efficiency dependency on %RH levels for one-step MAPBI films.

## Temperature

In most typical perovskite work, the temperature of concern is either the temperature of the annealing step post deposition or in the case of hot casting, the temperature of the ink and substrate. However, ambient temperature is also a factor during the perovskite deposition step.

Tests conducted on the solvent engineering deposition step shows that there is a clear difference between the performance of perovskite solar cells with cooler ambient temperatures than with warmer temperatures. Two different test matrices were used comparing systems at 27°C, 32°C and 37°C, with 27°C being the ambient condition inside the N<sub>2</sub> glovebox.

Results show a difference in performance that differs as the temperature increases, with the higher temperature data showing a drop off in efficiency performance as seen in figure D-2. In fact, the lowest temperature samples show a statistical difference from the 5°C and 10°C samples. In both instances, there was a slight drop in measured values of  $V_{oc}$  and  $J_{sc}$  for the higher temperatures.

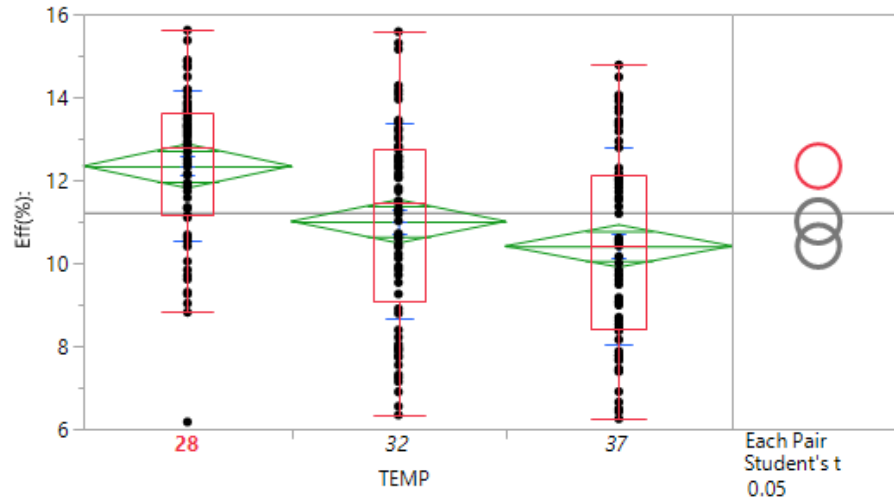


Figure D-2: Efficiency measurements from the 5% alloy at a temperature skew.

Figure D-3 shows the current performance of the solvent engineered 5% cesium sample temperature skew. The current performance are statistically matched, however, the higher temperature samples had a higher standard deviation than the other samples.

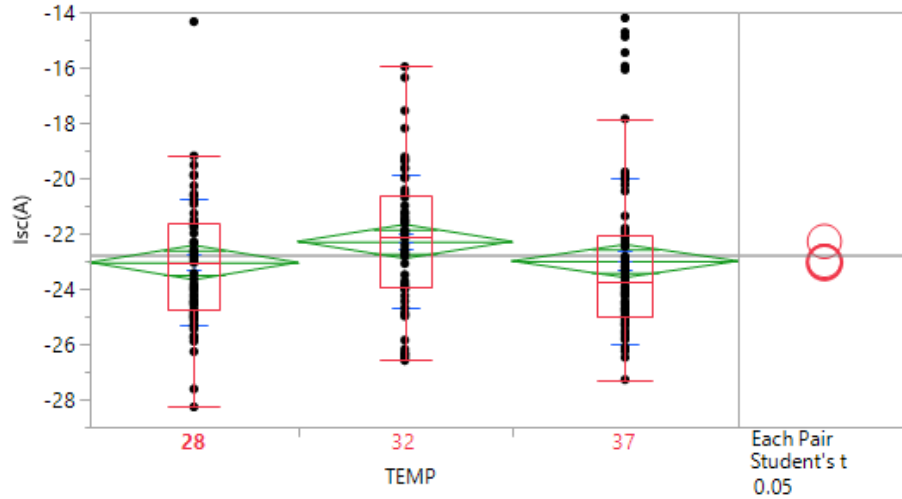


Figure D-3:  $I_{sc}$  measurements from the 5% alloy at a temperature skew.

Lastly, figure D-4 shows the  $V_{oc}$  performance. As can be seen, the efficiency performance is driven by the low temperature samples and is statistically different from the other samples. Also, notice that the standard deviation of the samples increased with each temperature step.

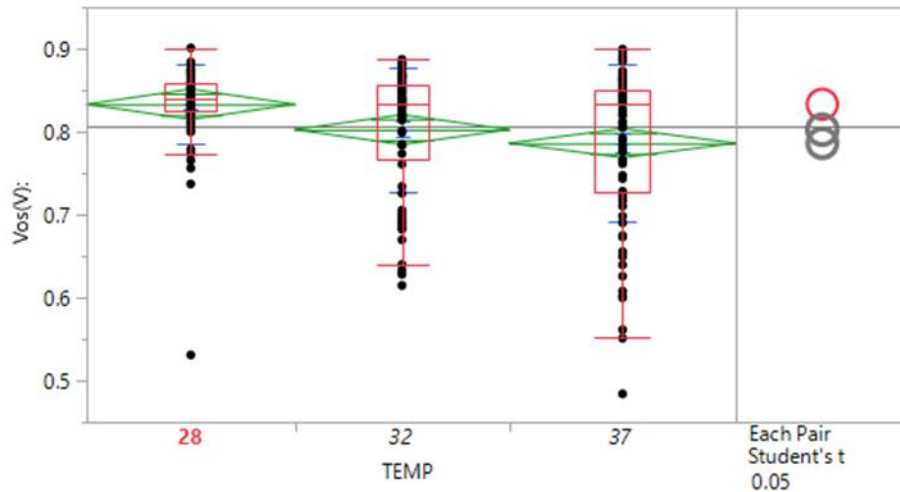


Figure D-4:  $V_{oc}$  measurements from the 5% alloy at a temperature skew.

AFM was performed on bare films processed in the same temperature conditions. Those results are shown in figure D-5. The AFM results show a trend in both the thickness and crystal sizes observed under different ambient conditions. The increase in temperature shows an increase in film thickness as well as the crystal sizes.

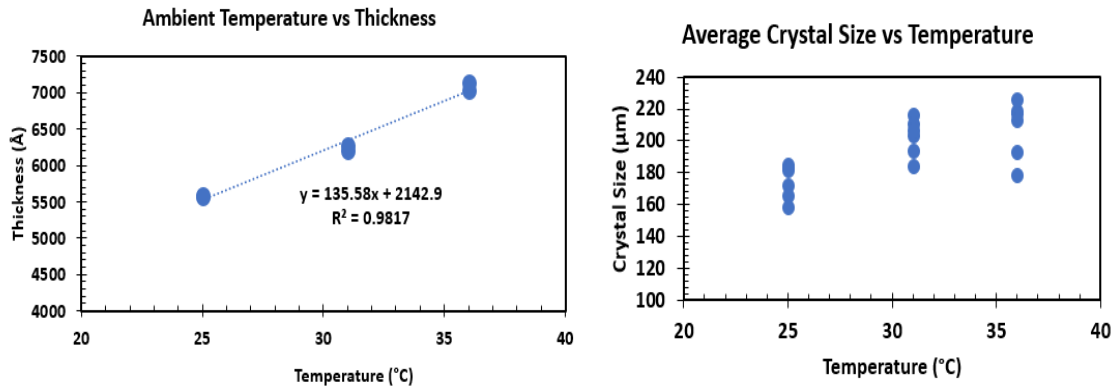


Figure D-5: Ambient temperature effects on thickness and crystal sizes.

### Solvent Concentration

For most deposition processes, the solvent concentration of concern is the solvent concentration either in the ink or in the engineering solvent step. Since solvent concentrations are hard to measure and require specialized equipment, they are typically not reported. However, ambient solvent concentration has a dramatic effect on the performance of the perovskite solar cells.

The efficiency of the samples created in excess solvent atmosphere are shown in figure D-6. The samples appear to have the same efficiency, with the higher solvent

concentration atmosphere performing slightly better, but having a higher data spread.

This could be due to the solvent evaporating from the wetted wipes.

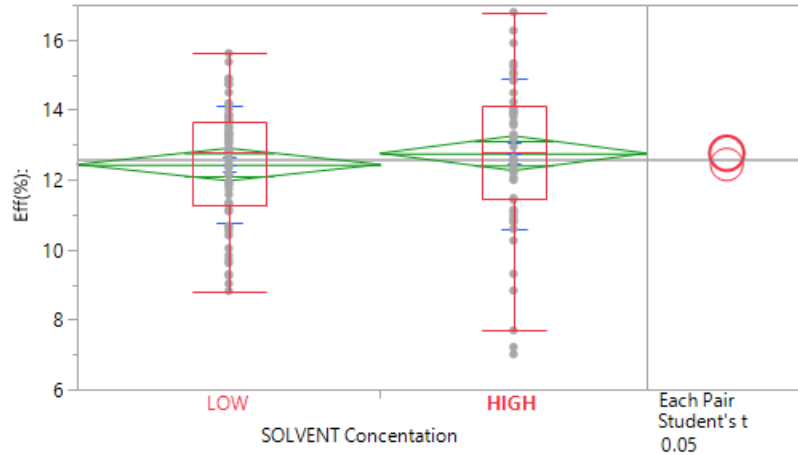


Figure D-6: Solvent atmosphere and effect on efficiency.

Figure D-7 shows that there is a statistical difference for the current performance for these samples. Samples in the high solvent atmosphere had lower standard deviation between the samples and a better over all current density.

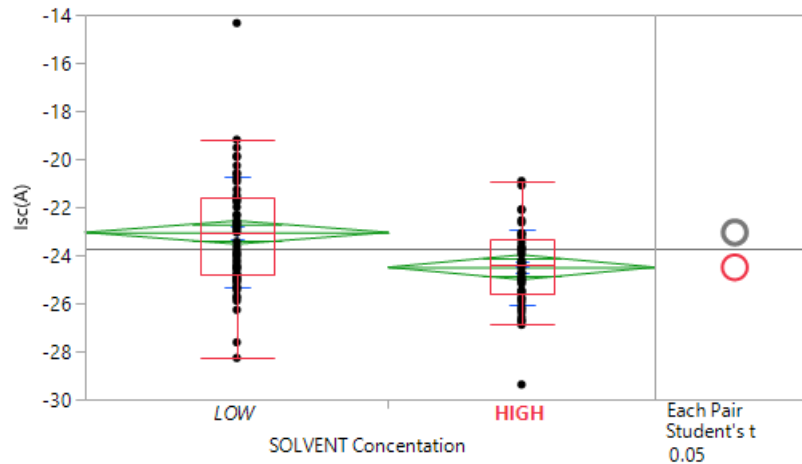


Figure D-7: Current performance of the solvent samples.

Figure D-8 shows the open circuit voltage performance and again there is a statistical difference between the high and low solvent concentration samples, with the high solvent concentration samples performing better.

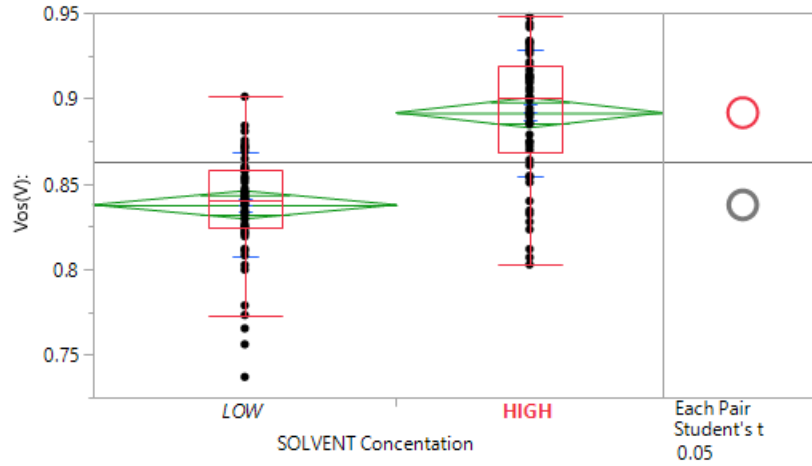


Figure D-8: Open Circuit Voltage performance based on solvent concentration in ambient.

AFM was also done on the perovskite films deposited under different solvent concentrations and the data is shown in figure D-9. The AFM results show that with increasing the solvent concentration, the resulting films are thinner and the crystals smaller.

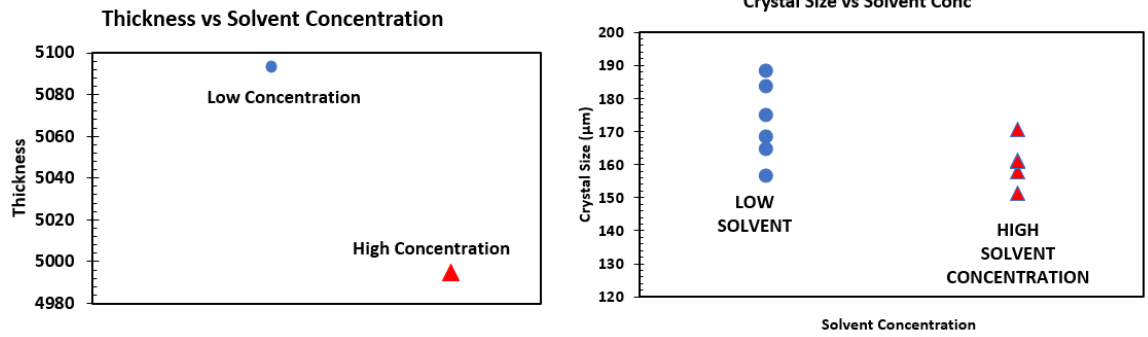


Figure D-9: Ambient solvent concentrations and the effect on film thickness and crystal sizes.

### Pressure Influences

The last ambient condition that was varied was the pressure. Samples saw a difference of about 9mbar between the low pressure and high-pressure tests. It should be noted, pressures reported are gauge pressures and are above laboratory pressures as the tests were conducted inside a pressurized N<sub>2</sub> glovebox.

Figure D-10 shows the performance of the devices based on the pressure skew. The higher pressure (+9mbarr) samples have a statistical difference in performance and are the better result.

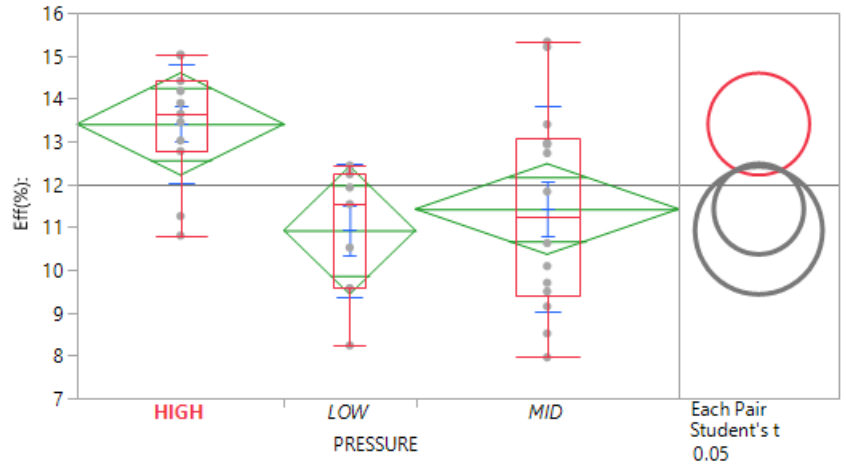


Figure D-10: Pressure skew data for efficiency.

Figure D-11 shows the performance of the alloy device under the increased pressure. While not statistically different, the  $V_{oc}$  performs better under the higher pressure.

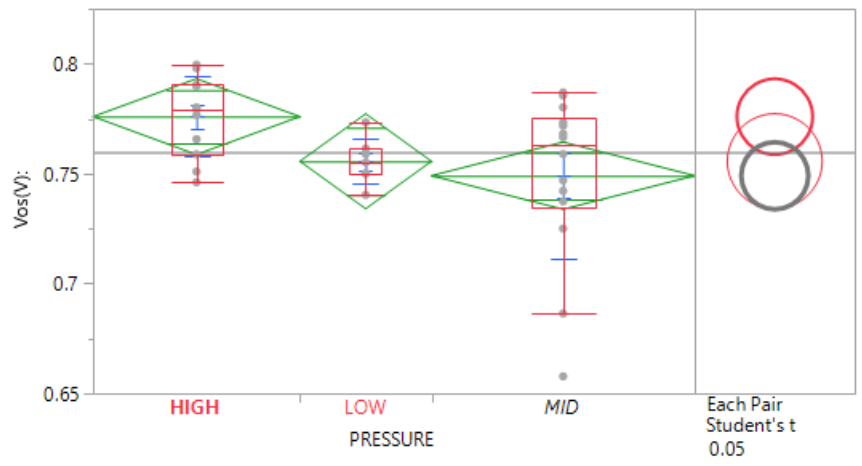


Figure D-111: Open circuit voltage pressure skew performance.

Finally, figure D-12 shows the current performance of the alloy samples. There again is not a statistical difference between all pressure settings, but the higher-pressure levels have better current performance.

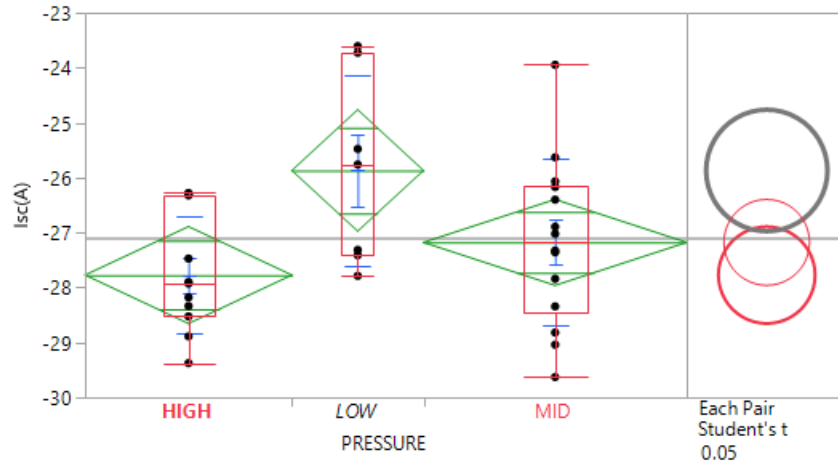


Figure D-12: Alloy current performance based on pressure.

AFM was also done on the ambient pressure skew samples and that data is shown in figure D-13. The results show a difference in measured crystal sizes and film thickness. A smaller crystal size with higher pressure was observed as well as a slightly thicker film.

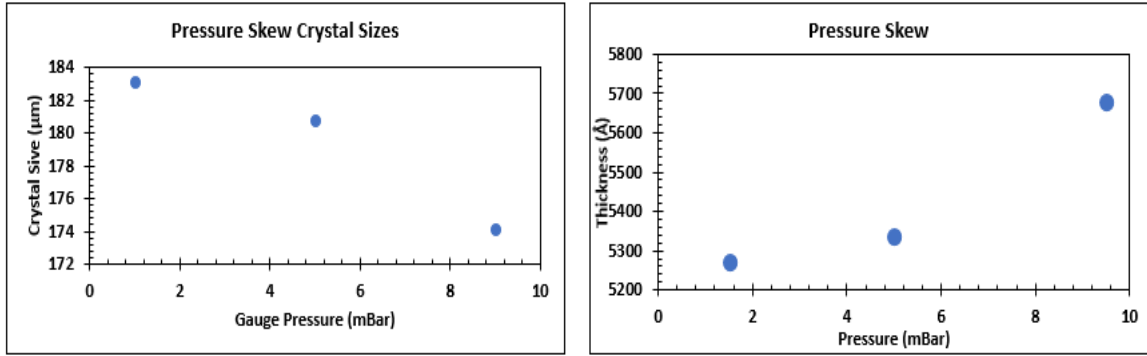


Figure D-13: Ambient pressure conditions and the relationship with crystal size and film thickness.

### Discussion

The results show that ambient conditions consisting of relative humidity, ambient solvent vapor concentrations, temperature and pressure are all factors influencing the performance of the perovskite system. In each case, the ambient condition that would retard solvent evaporation from the perovskite performed better. Increases in relative humidity reduce the ability of solvents to evaporate into air, so does lower temperatures, higher pressures and increased solvent vapor concentrations.

These results also align well with research on the use of additives and solvent engineering to control evaporation rates.

The Langmuir equation for evaporation rate gives us:

$$\frac{dM}{dt} = (p_v - p_{solvent}) \sqrt{\frac{m}{2\pi kT}} \quad (D-18)$$

Where  $p_v$  is the vapor pressure of the liquid,  $p_p$  is the partial pressure of the vapor in the gas,  $T$  is the temperature of the liquid. For the perovskite systems under investigation,  $p_v$  and  $T$  are constant and can be considered to be constant. Thus, the rate is depended upon the partial pressure of the vapor in the gas. Using the ideal gas, the partial pressure of the solvent becomes depended on atmospheric temperature, ( $T_{air}$ ), atmospheric pressure ( $P_{air}$ ) and the molar fractions of solvent ( $n_{solvent}$ ) and water ( $n_{H2O}$ ) in the atmosphere.

$$p_{solvent} = f(P_{air}, T_{air}, n_{solvent}, n_{H2O}) \quad (D-19)$$

In our case, the partial pressure of the solvent in ambient atmosphere is reduced under conditions of lower temperature, higher pressure, excess solvent vapors and water vapors which all contribute to lower the evaporation rate.

These results also disagree with the findings in section 6 and the longer the solvent evaporation rates. Since these are homogenous systems, the difference in the rate of evaporation might be pointing to a different mechanism within a similar cation system. All films showed smaller crystals and better performance with ambient conditions that would promote longer evaporation times such as lower temperatures, higher ambient solvent vapor concentration and higher pressures. It could be that the slower evaporation rate leads to smaller, but better ordered crystals with less defects. However, most study is needed.

## Solvent Removal Rate

Reviewing the data gathered in investigating the effects of pressure, solvent concentrations, humidity levels and temperature gives further information on the growth processes for perovskite crystals and can lead to a better model of perovskite growth.

There are two models of crystal growth, solvent removal rate vs intramolecular exchange. Solvent removal rate model [209][210] [211], as the name implies, believes the crystal growth is a function of the rate of removal of the solvent such as DMF or DMSO from the perovskite film. The second model says the growth rate is determined by the rate of exchange between the MAI and solvent molecules [212] [213].

The exchange rate model presented by [213] has good supporting evidence indicated by the dependence on more than one factor (time and temperature) during annealing that is determining the crystal and conversion factor. In further support of the exchange model poly(vinylidene fluoride-co-hexafluoropropylene) (PVDF-HFP) as an additive that they theorized reduced the rate of the exchange rate between the solvent (DMSO) and MAI[214] . The use of PVDF-HFP resulted in uniform coverage and increased crystal sizes.

A review of an FTIR scan of the first step of two step ink deposition process is needed on a working FTIR. Examining the regions of the FTIR for DMF bond stretches will indicate whether there is potential for a complex. FTIR work done (terrible spectra)

does show either residual DMF or a complex of  $PbI_2$ -DMF molecules are present at least in the first step of the deposition process.

Keeping with the  $PbI_2$  and  $MAPbI_3$  films, we will examine the intramolecular exchange mechanism using  $MAPbI_3$  films as an example for this class of materials. However, the same mechanisms are found on hybrid perovskites containing formamidinium, cesium, alloys of as well as mixed halides. The intramolecular exchange as proposed states that a complex of  $PbI_2$ -DMF needs to react with MAI:



However, this is not a true intramolecular exchange reaction. A true intramolecular exchange reaction has the form:



This is since an intramolecular exchange reaction involves the atoms on the same molecule as seen in the Smiles rearrangement [215][216], the Dieckmann condensation reaction[217] and the Madelung synthesis reactions [218] for examples. Thus, a MAI: $PbI_2$ :DMF complex must then exist in the ink (for one-step systems) or the complex must quickly form during the second step of a two-step ink process prior to the removal of the solvent.

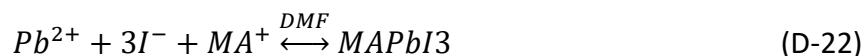
The MAI: $PbI_2$ :DMF complex is then needed for proper reaction for a true intramolecular reaction to take place. The two-step ink would require fast kinetics

favoring the of formation of the complex which then favors the formation of the complex over the perovskite (equation D-21).

If the formation of the MAI:PbI<sub>2</sub>:DMF complex is not taking place rapidly during a two-step ink deposition process, then multiple reaction mechanisms involving complexes are taking place, one of which is not an *intramolecular* reaction but an *intermolecular* exchange reaction is occurring. Regardless of the complex, DMF appears on both sides of the reaction and is in excess. The removal of DMF or any solvent from the system would not favor the complex nor the perovskite formation and should not have an influence on the outcome.

For proper perovskite formation we need to anneal the system. This supplies energy to the reaction and could drive the reactions in favor of perovskite formation as seen in equations D-20 and D-21. However, if the inks are heated, especially the one-step inks, this should prompt perovskite crystals to precipitate out of the inks as the excess energy would favor perovskite formation. Currently, none of these are effects are observed.

However, for the molecular exchange theory to be the dominate mechanism those mechanisms outlined above should contribute to film quality as determined by efficiency measurements. In the case of the findings presented here, the film parameters defined as efficiency,  $J_{sc}$ ,  $V_{oc}$  and fill factor are dominated by the solvent removal rate and not the intramolecular exchange rate. The proposed reaction mechanism is shown below and reported by others[219]:



This reaction has a favorable heat of formation calculated to be ~371.6kJ/mol [219] with other halide systems with more favorable formation heats.

In each of the systems defined here, the same inks, substrate temperatures and annealing conditions were used. The only factor that changed between study groups was the ambient conditions of pressure, temperature, solvent vapor concentration and relative humidity. These factors all influence the partial pressure of the solvent and directly influences the evaporation rate, hence the removal rate from the film. The favorable heats of formation of perovskites are what drives the formation of the crystal from the solvent solution. As the solvent is removed, the perovskite is formed.

The finding is not surprising, many of the additives and solvent engineering techniques used are all effecting the solvent removal rate from the film and have been reported. However, the simple changes to the ambient conditions demonstrated here, have had similar effect on device performance as some of these techniques. These all point to solvent removal rate from the inks as the dominating device performance metric for highly efficient perovskite devices.

These findings should serve as a caution for future of perovskite solar cells. The projected ease of manufacturing is an underlying assumption of the cost advantage of perovskites solar cells versus other thin film technologies [220][221]. However, results shown here are should challenge that assumption as these conditions presented here

are not uncommon that can easily occur when a weather system moves through an area. The significant differences in output based on just pressure and relative humidity changes should be troublesome news for companies attempting to use atmospheric deposition equipment to make consistent yielding perovskite solar cells.

#### Appendix D Conclusion

In this section of work, process conditions influencing the performance of perovskite films were characterized. The ambient conditions of temperature, pressure, solvent concentration, and relative humidity were used to determine the efficiency of the resulting perovskite solar cell. Furthermore, using these ambient conditions the mechanism of quality perovskite layers was elucidated. The data presented here indicates that the solvent removal rate is the underlining mechanism driving efficiency in perovskite films rather than an intramolecular exchange. Solvent removal rate was shown to be depended upon ambient conditions and in each case, the slower removal rate (evaporation) resulted in a higher quality film as determined by IV-curves. These results were consistent across a combination of different deposition methods, including one-step inks, adduct methods, two-step inks and solvent engineering perovskite growth methods. Results here can indicate that controlled ambient conditions have as much influence on the performance of the perovskite film as additives and solvent engineering approaches.

## Appendix E: Best Device

The following is the IV curve and statistics for the best performing device based on efficiency during the testing period. The device was a 5% alloy cesium ( $\text{MA}_{0.15}\text{FA}_{0.8}\text{Cs}_{0.05}\text{PbI}_3$ ) and the IV curve is shown below in figure E-1.

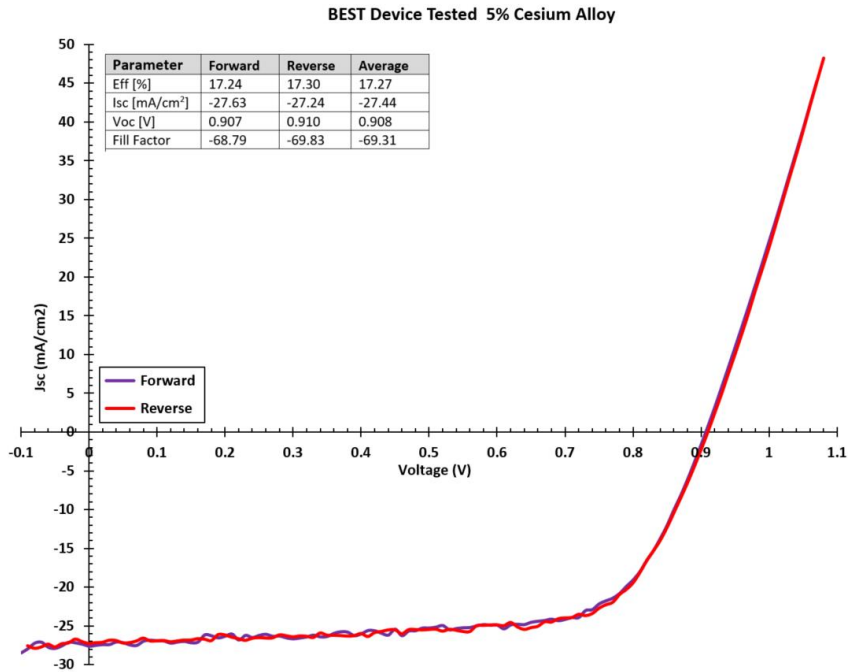


Figure E-1: Best performing device for this work. IV curve is of 5% cesium alloy.

This device was made with freshly prepared inks and no other notable changes to the device structures. The device performed the best mostly from the high  $V_{oc}$  measured. Also note the lack of hysteresis in the curve, a characteristic of most devices tested. The performance parameters are summarized in table E-1.

Table E-1: Summary of best device performance parameters.

Parameter	Forward	Reverse	Average
Eff [%]	17.24	17.30	17.27
Isc [mA/cm <sup>2</sup> ]	-27.63	-27.24	-27.44
Voc [V]	0.907	0.910	0.908
Fill Factor	-68.79	-69.83	-69.31

Of note, this sample (#6) had four other devices, the next highest average efficiency was 12.96% followed by 9.62% and a finally a non-yielding device. The other 5% alloy device made at the same time also had high efficiency devices of 16.41%, 16.38%, 15.09% and a non-yielding device. The high spread in the measured values was one of the challenges in this work.

## REFERENCES

- [1] Becquerel, "Mémoire sur les effets électriques produits sous l'influence des rayons solaires," *Comptes Rendus des Séances Hebd.*, vol. 9, pp. 561–567, 1839.
- [2] A. Einstein, "Über einen die Erzeugung und Verwandlung des Lichtes betreffenden heuristischen Gesichtspunkt," *Ann. Phys.*, vol. 17, no. 132, 1905.
- [3] NREL, "[http://www.nrel.gov/pv/assets/images/efficiency\\_chart.jpg](http://www.nrel.gov/pv/assets/images/efficiency_chart.jpg)," November, 2016. .
- [4] L. Katz *et al.*, "The perovskite history : More than 60 years of research from the discovery of ferroelectricity to colossal magnetoresistance via high T C superconductivity.," *Prog. Solid State Chem.*, vol. 35, pp. 171–173, 2007.
- [5] M. Johnsson and P. Lemmens, "Perovskites and thin films — crystallography and chemistry," *J. Phys. Condens. Matter*, vol. 20, no. 26, pp. 0–6, 2008.
- [6] M. I. Saidaminov *et al.*, "High-quality bulk hybrid perovskite single crystals within minutes by inverse temperature crystallization," *Nat. Commun.*, vol. 6, no. May, 2015.
- [7] NREL, "<http://www.nrel.gov/news/press/2015/21588>. Accessed Oct 2015.," 2015. .
- [8] H. Post, "[http://www.huffingtonpost.com/clayton-b-cornell/perovskite-solar-cell-key\\_b\\_11069628.html](http://www.huffingtonpost.com/clayton-b-cornell/perovskite-solar-cell-key_b_11069628.html). Accessed November 2016.," 2016.

- [9] C. Manspecker, P. Scruggs, J. Preiss, D. A. Lyashenko, and A. Zakhidov, "Reliable Annealing of CH<sub>3</sub>NH<sub>3</sub>PbI<sub>3</sub> Films Deposited on ZnO," *J. Phys. Chem. C*, vol. 120, no. 12, pp. 6377–6382, Mar. 2016.
- [10] C. Manspecker, S. Venkatesan, A. Zakhidov, and K. S. Martirosyan, "Role of interface in stability of perovskite solar cells," *Curr. Opin. Chem. Eng.*, vol. 15, pp. 1–7, 2016.
- [11] F. Li *et al.*, "Piezoelectric Activity in Perovskite Ferroelectric Crystals," *IEEE Trans. Ultrason. Ferroelectr. Freq. Control*, vol. 62, no. 1, pp. 18–32, 2015.
- [12] B. V Lotsch, "New Light on an Old Story : Perovskites Go Solar," *Angew. Chem. Int. Ed. Engl.*, vol. 53, no. 3, pp. 635–637, 2014.
- [13] T. Baikie *et al.*, "A combined single crystal neutron/X-ray diffraction and solid-state nuclear magnetic resonance study of the hybrid perovskite CH<sub>3</sub>NH<sub>3</sub>PbX<sub>3</sub> (X = I, Br and Cl)," *J. Mater. Chem. A Mater. energy Sustain.*, vol. 3, pp. 9298–9307, 2015.
- [14] W. Peng *et al.*, "Engineering of CH<sub>3</sub>NH<sub>3</sub>PbI<sub>3</sub> Perovskite Crystals by Alloying Large Organic Cations for Enhanced Thermal Stability and Transport Properties," *Angew. Chemie Int. Ed.*, Jul. 2016.
- [15] V. C. Albert Titus, Maurice Cheung, *Photodiodes - World Activities in 2011*. InTech, 2011.

- [16] C. Wehrenfennig, G. E. Eperon, M. B. Johnston, H. J. Snaith, and L. M. Herz, "High Charge Carrier Mobilities and Lifetimes in Organolead Trihalide Perovskites," *Adv. Mater.*, pp. 1584–1589, 2014.
- [17] D. Bi, N. Pellet, and J. Lewin, "Formation of Stable Mixed Guanidinium – Methylammonium Phases with Exceptionally Long Carrier Lifetimes for High-Efficiency Lead Iodide-Based Perovskite Photovoltaics," *J. Am. Chem. Soc.*, 2018.
- [18] W. Ning *et al.*, "Long Electron – Hole Diffusion Length in High-Quality Lead-Free Double Perovskite Films," *Adv. Funct. Mater.*, vol. 1706246, pp. 1–6, 2018.
- [19] L. M. Herz, "Charge-Carrier Mobilities in Metal Halide Perovskites: Fundamental Mechanisms and Limits," *ACS Energy Lett.*, vol. 2, pp. 1539–1548, 2017.
- [20] L. Wang, "The Nature of Electron Mobility in Hybrid Perovskite  $\text{CH}_3\text{NH}_3\text{PbI}_3$ ," *Nano Lett.*, vol. 17, pp. 3646–3654, 2017.
- [21] K. Huang *et al.*, "Stability and carrier mobility of organic-inorganic hybrid perovskite  $\text{CH}_3\text{NH}_3\text{PbI}_3$  in two-dimensional limit Stability and carrier mobility of organic-inorganic hybrid perovskite  $\text{CH}_3\text{NH}_3\text{PbI}_3$  in two-dimensional limit," *J. Chem. Phys.*, vol. 164703, no. 147, 2017.
- [22] S. Shrestha, G. J. Matt, A. Osvet, D. Niesner, R. Hock, and C. J. Brabec, "Assessing Temperature Dependence of Drift Mobility in Methylammonium Lead Iodide Perovskite Single Crystals," *J. Phys. Chem. A*, vol. 122, pp. 5935–5939, 2018.

- [23] O. Malyk and S. Syrotyuk, "New scheme for calculating the kinetic coefficients in CdTe based on first-principle wave function," *Comput. Mater. Sci.*, vol. 139, pp. 387–394, 2017.
- [24] I. Turkevych, R. Grill, J. Franc, and E. Belas, "High-temperature electron and hole mobility in CdTe," *Semicond. Sci. Technol.*, vol. 17, no. 10, pp. 2–5, 2002.
- [25] P. Scajev, S. Miasojedovas, A. Mekys, K. Lynn, S. Swain, and K. Jarasiunas, "Excitation-dependent carrier lifetime and diffusion length in bulk CdTe determined by time-resolved optical pump-probe techniques," *J. Appl. Phys.*, vol. 123, no. 2, 2018.
- [26] T. A. Gessert, R. Dhere, J. Duenow, D. Kuciauskas, A. Kanevce, and J. Bergeson, "Comparison of Minority Carrier Lifetime Measurements in Superstrate and Substrate CdTe PV Devices," in *Presented at the 37th IEEE Photovoltaic Specialists Conference (PVSC 37)*, 2011.
- [27] L. Hexin, Z. Daming, and L. Jiang, "Effects of Annealing on CuInGaSe<sub>2</sub> Solar Cell Prepared by Magnetron Sputtering," *Proc. ASME 2011 Int. Mech. Eng. Congr. Expo. IMECE2011*, vol. IMECE2011-, pp. 1–7, 2011.
- [28] A. Morales-acevedo, "A Simple Model of Graded Band-Gap CuInGaSe<sub>2</sub> Solar Cells," *Energy Procedia*, vol. 2, no. 1, pp. 169–176, 2010.
- [29] R. Scheer, "Towards an electronic model for CuIn<sub>1-x</sub>Ga<sub>x</sub>Se<sub>2</sub> solar cells," *Thin Solid Films*, vol. 519, pp. 7472–7475, 2011.

- [30] M. Maiberg, C. Spindler, E. Jarzembowski, and R. Scheer, "Electrical characterization of Cu ( In , Ga ) Se 2 -solar cells by voltage dependent time-resolved photoluminescence," *Thin Solid Films*, vol. 582, pp. 379–382, 2015.
- [31] J. Lee *et al.*, "Drift-mobility characterization of silicon thin- film solar cells using photocapitance," *J. Non. Cryst. Solids*, vol. 358, no. 17, pp. 2194–2197, 2012.
- [32] E. A. Schiff, "Hole mobilities and the physics of amorphous silicon solar cells," *J. Non. Cryst. Solids*, vol. 352, pp. 1087–1092, 2006.
- [33] A. R. Moore and A. R. Moore, "Electron and hole drift mobility in amorphous silicon Electron and hole drift mobility in amorphous silicon," *Appl. Phys. Lett.*, vol. 762, no. 31, 1997.
- [34] H. Okamoto *et al.*, "Mobility lifetime product and interface property in amorphous silicon solar cells," *J. Appl. Phys.*, vol. 3236, no. 54, 1983.
- [35] L. Derbali, A. Zarroug, and H. Ezzaouia, "Minority carrier lifetime and efficiency improvement of multicrystalline silicon solar cells by two-step process," *Renew. Energy*, vol. 77, pp. 331–337, 2015.
- [36] T. Trupke, T. Puzzer, W. Warta, and S. W. Glunz, "Diffusion lengths of silicon solar cells from luminescence images," *J. Appl. Phys.*, vol. 101, pp. 1–11, 2007.
- [37] W. Walukiewicz, J. Lagowski, L. Jastrzebski, and H. C. Gatos, "Minority-carrier mobility in p -type GaAs," *J. Appl. Phys.*, vol. 5040, no. 50, pp. 43–46, 1979.

- [38] L. Pfeiffer *et al.*, "Electron mobilities exceeding  $10^7$  cm<sup>2</sup> / Vs in modulation-doped GaAs Electron mobilities exceeding  $10^7$  cm<sup>2</sup> / V sin modulation .. doped GaAs," *Appl. Phys. Lett.*, vol. 1888, no. 55, pp. 67–70, 1989.
- [39] K. Takeda, A. Taguchi, E. Ohta, M. Sakata, and G. Gap, "Hole mobility of GaAs, GaP, and Ga<sub>1-x</sub>P<sub>x</sub> mixed-compound semiconductors," *Phys. Rev. B*, vol. 32, no. 2, 1985.
- [40] M. Niemeyer, J. Ohlmann, A. W. Walker, P. Kleinschmidt, R. Lang, and T. Hannappel, "Minority carrier diffusion length , lifetime and mobility in p-type GaAs and GaInAs," *J. Appl. Phys.*, vol. 115702, no. 122, 2017.
- [41] J. Nelson, *The Physics of Solar Cells*, 1st ed. London: Imperial College Press, 2005.
- [42] S. Fonash, *Solar Cell Device Physics*, 2nd ed. Oxford, UK: Academic Press, 2010.
- [43] E. Neier, R. Ugarte, N. Rady, S. Venkatesan, T. Hudnall, and A. Zakhidov, "Solution-processed organic light-emitting diodes with emission from a doublet exciton; using (2,4,6-trichlorophenyl)methyl as emitter," *Org. Electron.*, vol. 44, pp. 126–131, 2017.
- [44] Image, "Solar Energy Distribution." [Online]. Available: <http://geologycafe.com/oceans/chapter8.html>.

- [45] T. Hoiium, "Why Solar Panel Efficiency Matters More Than You Think," *The Motley Fool*, 2015. [Online]. Available: <https://www.fool.com/investing/general/2015/01/31/why-solar-panel-efficiency-matters-more-than-you-t.aspx>.
- [46] W. Shockley and H. J. Queisser, "Detailed Balance Limit of Efficiency of p-n Junction Solar Cells," *J. Appl. Phys.*, vol. 32, pp. 510–519, 1961.
- [47] Image, "Current Dependence on Bandgap," [www.pveducation.org/ko](http://www.pveducation.org/ko), 2018. [Online]. Available: [www.pveducation.org/ko](http://www.pveducation.org/ko). [Accessed: 20-Aug-2002].
- [48] F. Panzer, C. Li, T. Meier, A. Köhler, and S. Huettnner, "Impact of Structural Dynamics on the Optical Properties of Methylammonium Lead Iodide Perovskites," *Adv. Energy Mater.*, vol. 3, pp. 1–11, 2017.
- [49] Y. Jiang, M. A. Green, R. Sheng, and A. Ho-baillie, "Room temperature optical properties of organic – inorganic lead halide perovskites," *Sol. Energy Mater. Sol. Cells*, vol. 137, pp. 253–257, 2015.
- [50] G. E. Eperon, S. D. Stranks, C. Menelaou, M. B. Johnston, L. M. Herz, and H. J. Snaith, "Environmental Science Formamidinium lead trihalide : a broadly tunable perovskite for efficient planar heterojunction solar," *Energy Environ. Sci.*, vol. 7, pp. 982–988, 2014.

- [51] H. Yuan *et al.*, "Photoluminescence Blinking of Single-Crystal Methylammonium Lead Iodide Perovskite Nanorods Induced by Surface Traps," *ACS Omega*, vol. 1, pp. 148–159, 2016.
- [52] T. Tachikawa, I. Karimata, and Y. Kobori, "Surface Charge Trapping in Organolead Halide Perovskites Explored by Single-Particle Photoluminescence Imaging," *J. Phys. Chem. Lett.*, vol. 6, pp. 3195–3201, 2015.
- [53] Y. Tian *et al.*, "Giant Photoluminescence Blinking of Perovskite Nanocrystals Reveals Single-Trap Control of Luminescence Giant Photoluminescence Blinking of Perovskite Nanocrystals Reveals Single- Trap Control of Luminescence," *Nano Lett.*, 2015.
- [54] M. Kato, T. Fujiseki, T. Miyadera, T. Sugita, S. Fujimoto, and M. Tamakoshi, "Universal rules for visible-light absorption in hybrid perovskite materials," *J. Appl. Phys.*, vol. 115501, no. 121, 2017.
- [55] W. Yin, T. Shi, and Y. Yan, "Superior Photovoltaic Properties of Lead Halide Perovskites : Insights from First-Principles Theory," *J. Phys. Chem. C*, vol. 119, pp. 5253–5264, 2015.
- [56] S. M. H. Qaid *et al.*, "Band-gap tuning of lead halide perovskite using a single step spin-coating deposition process," *Mater. Lett.*, vol. 164, pp. 498–501, 2016.
- [57] D. P. Mcmeekin *et al.*, "A mixed-cation lead mixed-halide perovskite absorber for tandem solar cells," *Science (80-. )*, vol. 351, pp. 151–155, 2016.

- [58] B. Zhang, J. Yan, J. Wang, and Y. Chen, "Effect of the modulating of organic content on optical properties of single-crystal perovskite," *Opt. Mater. (Amst)*., vol. 62, pp. 273–278, 2016.
- [59] B. Putz, B. Völker, C. Semprimoschnig, and M. J. Cordill, "Microelectronic Engineering Influence of extreme thermal cycling on metal-polymer interfaces," *Microelectron. Eng.*, vol. 167, pp. 17–22, 2017.
- [60] H. Zhou, "Effects of deposition methods and processing techniques on band gap , interband electronic transitions , and optical absorption in perovskite," *Appl. Phys. Express*, vol. 11906, no. June, 2017.
- [61] D. H. Fabini *et al.*, "Reentrant Structural and Optical Properties and Large Positive Thermal Expansion in Perovskite Formamidinium Lead Iodide," *Angew. Chemie Int. Ed.*, no. 55, pp. 1–6, 2016.
- [62] Q. Han *et al.*, "Single Crystal Formamidinium Lead Iodide (FAPbI<sub>3</sub>): Insight into the Structural, Optical, and Electrical Properties," *Adv. Mater.*, p. n/a-n/a, Jan. 2016.
- [63] I. Levchuk *et al.*, "Brightly Luminescent and Color-Tunable Formamidinium Lead Halide Perovskite FAPbX<sub>3</sub> (X = Cl, Br, I) Colloidal Nanocrystals," *Nano Lett.*, vol. 3, no. 17, pp. 2765–2770, 2017.

- [64] B. M. B. Slimi, M. Mollar, I. Ben Assaker, I. Kriaa, R. Chtourou, "Perovskite FA1-xMAxPbI3 for solar cells: film formation and properties," *Energy Procedia*, vol. 102, pp. 87–95, 2016.
- [65] N. Pellet *et al.*, "Mixed-Organic-Cation Perovskite Photovoltaics for Enhanced Solar- Light Harvesting," *Angew. Chemie*, vol. 126, pp. 3215–3221, 2014.
- [66] H. Uratani and K. Yamashita, "Charge Carrier Trapping at Surface Defects of Perovskite Solar Cell Absorbers: A First-Principles Study," 2017.
- [67] Z. Liu, J. Hu, H. Jiao, L. Li, G. Zheng, and Y. Chen, "Chemical Reduction of Intrinsic Defects in Thicker Heterojunction Planar Perovskite Solar Cells," vol. 1606774, pp. 1–8, 2017.
- [68] J. Ye *et al.*, "Effective and reproducible method for preparing low defects perovskite film toward highly photoelectric properties with large fill factor by shaping capping layer," *Sol. Energy*, vol. 136, pp. 505–514, 2016.
- [69] M. Bokdam *et al.*, "Role of Polar Phonons in the Photo Excited State of Metal Halide Perovskites," *Nat. Publ. Gr.*, pp. 1–9.
- [70] W. Tress, J. P. Correa Baena, M. Saliba, A. Abate, and M. Graetzel, "Inverted Current-Voltage Hysteresis in Mixed Perovskite Solar Cells: Polarization, Energy Barriers, and Defect Recombination," *Adv. Energy Mater.*, Jul. 2016.

- [71] B. P. Uberuaga and L. J. Vernon, "Interstitial and vacancy mediated transport mechanisms in perovskites : A comparison of chemistry and potentials," *Solid State Ionics*, vol. 253, pp. 18–26, 2013.
- [72] A. Ram *et al.*, "Nonlinear Carrier Interactions in Lead Halide Perovskites and the Role of Defects," 2016.
- [73] M. K. N. and M. G. W. Tress, N. Marinovaa, T. Moehla, S. M. Zakeeruddina, "Understanding the rate-dependent J-V hysteresis, slow time component, and aging in CH<sub>3</sub>NH<sub>3</sub>PbI<sub>3</sub> perovskite solar cells: the role of a compensated electric field," *Energy Environ. Sci.*, 2015.
- [74] A. J. Pearson, "Structure formation and evolution in semiconductor films for perovskite and organic photovoltaics," *J. Mater. R*, no. 10, 2017.
- [75] M. Saliba, W. Zhang, M. De Bastiani, and A. Petrozza, "Charge selective contacts, mobile ions and anomalous hysteresis in organic–inorganic perovskite solar cells," *Mater. Horizons*, vol. 2, pp. 315–322, 2015.
- [76] H. J. Snaith *et al.*, "Anomalous Hysteresis in Perovskite Solar Cells," *J. Phys. Chem. Lett.*, vol. 5, no. iii, pp. 1511–1515, 2014.
- [77] J. M. Frost and A. Walsh, "What Is Moving in Hybrid Halide Perovskite Solar Cells?," *Acc. Chem. Res.*, vol. 49, no. 3, pp. 528–535, Feb. 2016.
- [78] A. Shahini and K. Abbasian, "Charge Carriers and Excitons Transport in an Organic Solar Cell-Theory and Simulation," vol. 8, no. 4, pp. 435–443, 2012.

- [79] X.-Y. Zhu and V. Podzorov, "Charge carriers in hybrid-organic–inorganic lead-halide perovskites might be protected as large polarons," *J. Phys. Chem. Lett.*, vol. 6, no. 23, pp. 4758–4761, Nov. 2015.
- [80] T. Chen *et al.*, "Origin of long lifetime of band-edge charge carriers in organic – inorganic lead iodide perovskites," vol. 114, no. 29, pp. 7519–7524, 2017.
- [81] A. J. Neukirch *et al.*, "Polaron stabilization by cooperative lattice distortion and cation rotations in hybrid perovskite materials.," *Nano Lett.*, May 2016.
- [82] C. C. Stoumpos, M. G. Kanatzidis, P. Mante, and A. Yartsev, "Electron–acoustic phonon coupling in single crystal CH<sub>3</sub>NH<sub>3</sub>PbI<sub>3</sub> perovskites revealed by coherent acoustic phonons," *Nat. Commun.*, vol. 8, pp. 1–7, 2017.
- [83] T. Ivanovska, C. Dionigi, E. Mosconi, F. De Angelis, and F. Liscio, "Long-Lived Photoinduced Polarons in Organohalide Perovskites," 2017.
- [84] A. Mahmud *et al.*, "Enhanced stability of low temperature processed perovskite solar cells via augmented polaronic intensity of hole transporting layer," vol. 889, no. 12, pp. 882–889, 2016.
- [85] C. Sima, C. Grigoriu, and S. Antohe, "Comparison of the dye-sensitized solar cells performances based on transparent conductive ITO and FTO," *Thin Solid Films*, vol. 519, no. 2, pp. 595–597, 2010.

- [86] W. Choi, D. Kwak, C. Park, and Y. Sung, "Characterization of Transparent Conductive ITO, ITiO, and FTO Films for Application in Photoelectrochemical Cells Delivered by Ingenta to ;," *J. Nanosci. Nanotechnol.*, vol. 12, no. 4, pp. 3394–3397, 2012.
- [87] Q. Qiao, J. Beck, R. Lumpkin, and J. Pretko, "A comparison of fluorine tin oxide and indium tin oxide as the transparent electrode for P3OT / TiO<sub>2</sub> solar cells," *Sol. Energy Mater. Sol. Cells*, vol. 90, pp. 1034–1040, 2006.
- [88] W. Baek *et al.*, "Use of fluorine-doped tin oxide instead of indium tin oxide in highly efficient air-fabricated inverted polymer solar cells Use of fluorine-doped tin oxide instead of indium tin oxide in highly efficient air-fabricated inverted polymer solar cells," *Appl. Phys. Lett.*, vol. 133506, no. 96, 2010.
- [89] G. Adam *et al.*, "Solution processed perovskite solar cells using highly conductive PEDOT : PSS interfacial layer," *Sol. Energy Mater. Sol. Cells*, vol. 157, pp. 318–325, 2016.
- [90] Q. Wang, C. Chueh, M. Eslamian, and A. K. Jen, "Modulation of PEDOT : PSS pH for Efficient Inverted Perovskite Solar Cells with Reduced Potential Loss and Enhanced Stability," *Appl. Mater. Interfaces*, vol. 8, pp. 32068–32076, 2016.
- [91] W. Sun *et al.*, "An ammonia modified PEDOT:PSS for interfacial engineering in inverted planar perovskite solar cells," *Org. Electron.*, 2017.

- [92] P.-W. Liang, C.-C. Chueh, S. T. Williams, and A. K.-Y. Jen, "Roles of Fullerene-Based Interlayers in Enhancing the Performance of Organometal Perovskite Thin-Film Solar Cells," *Adv. Energy Mater.*, vol. 5, no. 10, p. n/a-n/a, 2015.
- [93] S. D. Stranks and H. J. Snaith, "Metal-halide perovskites for photovoltaic and light-emitting devices," *Nat. Publ. Gr.*, vol. 10, no. 5, pp. 391–402, 2015.
- [94] J. Xu *et al.*, "Perovskite–fullerene hybrid materials suppress hysteresis in planar diodes," *Nat. Commun.*, vol. 6, no. May, pp. 1–8, 2015.
- [95] and L.-S. L. Da-Xing Yuan, Xiao-Dong Yuan, Qing-Yang Xu, Mei-Feng Xu, Xiao-Bo Shi, Zhao-Kui Wang, "Solution-Processed Bathocuproine Cathode Interfacial Layer for High-Performance Bromine-Iodine Perovskite Solar Cells," *R. Soc. Chem.*, vol. 17, no. 40, pp. 26653–26658, 2015.
- [96] Y. Wang *et al.*, "BCP as Additive for Solution-Processed PCBM Electron Transport Layer in Efficient Planar," *IEEE J. Photovoltaics*, vol. 7, no. 2, pp. 550–557, 2017.
- [97] J. Liu *et al.*, "Understanding the Role of the Electron-Transport Layer in Highly Efficient Planar Perovskite Solar Cells," *ChemPhysChem*, vol. 18, pp. 617–625, 2017.
- [98] Y. Cheng *et al.*, "Decomposition of Organometal Halide Perovskite Films on Zinc Oxide Nanoparticles," *ACS Appl. Mater. Interfaces*, vol. 7, no. 36, pp. 19986–19993, Aug. 2015.

- [99] W. Zhang *et al.*, "Ultrasoft organic–inorganic perovskite thin-film formation and crystallization for efficient planar heterojunction solar cells," *Nat. Commun.*, vol. 6, p. 6142, Jan. 2015.
- [100] W. Ke *et al.*, "Employing Lead Thiocyanate Additive to Reduce the Hysteresis and Boost the Fill Factor of Planar Perovskite Solar Cells," *Adv. Mater.*, vol. 28, no. 26, pp. 5214–5221, 2016.
- [101] H. Kim and N. Park, "Parameters Affecting I–V Hysteresis of CH<sub>3</sub>NH<sub>3</sub>PbI<sub>3</sub> Perovskite Solar Cells: Effects of Perovskite Crystal Size and Mesoporous TiO<sub>2</sub> Layer," *J. Phys. Chem. Lett.*, vol. 5, pp. 2927–2934, 2014.
- [102] B. Chen, M. Yang, S. Priya, and K. Zhu, "Origin of J-V Hysteresis in Perovskite Solar Cells," *J. Phys. Chem. Lett.*, vol. 7, pp. 905–917, 2016.
- [103] Y. Hou *et al.*, "Inverted, Environmentally Stable Perovskite Solar Cell with a Novel Low-Cost and Water-Free PEDOT Hole-Extraction Layer," *Adv. Energy Mater.*, pp. 1–7, 2015.
- [104] H. Aitdads, S. Bouzit, L. Nkhaili, A. Elkissani, and A. Outzourhit, "Solar Energy Materials & Solar Cells Structural, optical and electrical properties of planar mixed perovskite halides / Al-doped Zinc oxide solar cells," *Sol. Energy Mater. Sol. Cells*, vol. 148, pp. 30–33, 2016.

- [105] S. Chen, L. Lei, S. Yang, Y. Liu, and Z. Wang, "Characterization of Perovskite Obtained from Two-Step Deposition on Mesoporous Titania," *ACS Appl. Mater. Interfaces*, vol. 46, no. 7, pp. 25770–25776, 2015.
- [106] L. Yang, J. Wang, and W. W. Leung, "Lead Iodide Thin Film Crystallization Control for High-Performance and Stable Solution-Processed Perovskite Solar Cells," *Appl. Mater. Interfaces*, vol. 7, pp. 14614–14619, 2015.
- [107] Y. Shi *et al.*, "CH<sub>3</sub>NH<sub>3</sub>PbI<sub>3</sub> and CH<sub>3</sub>NH<sub>3</sub> PbI<sub>3-x</sub>Cl<sub>x</sub> in Planar or Mesoporous Perovskite Solar Cells : Comprehensive Insight into the Dependence of Performance on Architecture," *J. Phys. Chem. C*, vol. 119, pp. 15868–15873, 2015.
- [108] T. D. R. Zhihua Xu, Kevin Weeks, "Perovskite Solar Cells," *Brookhaven National Laboratory*, 2015. [Online]. Available: [https://www.bnl.gov/education/static/VFP/colloquium/xu\\_colloquium2015.pdf%0A](https://www.bnl.gov/education/static/VFP/colloquium/xu_colloquium2015.pdf%0A).
- [109] M. D. McGehee, "PEROVSKITE SOLAR CELLS Continuing to soar," *Nat. Publ. Gr.*, vol. 13, no. 9, pp. 845–846, 2014.
- [110] N. Ali *et al.*, "Advances in nanostructured thin film materials for solar cell applications," *Renew. Sustain. Energy Rev.*, vol. 59, pp. 726–737, 2016.
- [111] R. J. Sutton *et al.*, "Bandgap-Tunable Cesium Lead Halide Perovskites with High Thermal Stability for Efficient Solar Cells," *Adv. Energy Mater.*, vol. 6, no. 8, pp. 1–6, 2016.

- [112] H. C. Weerasinghe, Y. Dkhissi, A. D. Scully, R. A. Caruso, and Y. Cheng, "Encapsulation for improving the lifetime of flexible perovskite solar cells," *Nano Energy*, vol. 18, pp. 118–125, 2015.
- [113] F. Bella *et al.*, "Improving efficiency and stability of perovskite solar cells with photocurable fluoropolymers," *Science (80-. )*, vol. 354, pp. 203–206, 2016.
- [114] J. Xie, X. Yu, X. Sun, J. Huang, Y. Zhang, and M. Lei, "Nano Energy Improved performance and air stability of planar perovskite solar cells via interfacial engineering using a fullerene amine interlayer," *Nano Energy*, vol. 28, pp. 330–337, 2016.
- [115] B. Koo *et al.*, "Pyrite-Based Bi-Functional Layer for Long-Term Stability and High-Performance of Organo-Lead Halide Perovskite Solar Cells," *Adv. Funct. Mater.*, vol. 26, pp. 5400–5407, 2016.
- [116] C. Chiang and C. Wu, "Film Grain-Size Related Long-Term Stability of Inverted Perovskite Solar Cells," *ChemSusChem*, vol. 9, pp. 2666–2672, 2016.
- [117] G. Migan, "Study of the operating temperature of a PV module Solar PV physics," *Univeristy Lund*, p. 4, 2013.
- [118] P. M. Segado, J. Carretero, and M. Sidrach-de-cardona, "Models to predict the operating temperature of different photovoltaic modules in outdoor conditions," *Prog. Photovoltaics Res. Appl.*, vol. 23, no. 10, pp. 1267–1282, 2015.

- [119] P. Bhatt *et al.*, “Investigating the charge carrier transport within the hole-transport material free perovskite solar cell processed in ambient air,” *Sol. Energy Mater. Sol. Cells*, vol. 140, pp. 320–327, 2015.
- [120] D. H. Sin, H. Ko, S. B. Jo, M. Kim, G. Y. Bae, and K. Cho, “Decoupling Charge Transfer and Transport at Polymeric Hole Transport Layer in Perovskite Solar Cells,” *ACS*, vol. 8, no. 10, pp. 6546–6553, 2016.
- [121] L. Dan, H. Zhang, L. Hao, and Y. Shen, “Effect of Hole Transport Layer in Planar Inverted Perovskite Solar Cells,” *Chem. Lett.*, vol. 45, pp. 89–91, 2016.
- [122] N. Cheng *et al.*, “Enhanced performance in hole transport material free perovskite solar cells via morphology control of Pbl<sub>2</sub> film by solvent treatment,” *J. Power Sources*, vol. 319, pp. 111–115, 2016.
- [123] T. Singh, J. Singh, and T. Miyasaka, “Role of Metal Oxide Electron-Transport Layer Modification on the Stability of High Performing Perovskite Solar Cells,” *ChemSusChem*, vol. 9, no. 18, pp. 2559–2566, 2016.
- [124] J. Pascual, I. Kosta, T. T. Ngo, A. Chuvilin, and G. Cabanero, “Electron Transport Layer-Free Solar Cells Based on Perovskite – Fullerene Blend Films with Enhanced Performance and Stability,” *ChemSusChem*, vol. 9, no. 18, pp. 2679–2685, 2016.
- [125] H. Chen and S. Yang, “High-quality perovskite in thick scaffold : a core issue for hole transport material-free perovskite solar cells,” *Sci. Bull.*, 2016.

- [126] H. Yuan *et al.*, "Degradation of Methylammonium Lead Iodide Perovskite Structures through Light and Electron Beam Driven Ion Migration," *J. Phys. Chem. Lett.*, p. acs.jpcllett.5b02828, Jan. 2016.
- [127] Y. Li, X. Xu, C. Wang, and Y. Gao, "Light Induced Degradation of CH<sub>3</sub>NH<sub>3</sub>PbI<sub>3</sub> Hybrid Perovskite Thin Film," *J. Phys. Chem. C*, vol. 121, no. 7, 2017.
- [128] K. Motoki *et al.*, "Degradation of CH<sub>3</sub>NH<sub>3</sub>PbI<sub>3</sub> perovskite due to soft x-ray irradiation as analyzed by an x-ray photoelectron spectroscopy time-dependent measurement method," *J. Appl. Phys.*, vol. 121, no. 8, 2017.
- [129] Images, "FTIR Images," <https://www.slideshare.net/aishuanju/ftir-45012578>, 2018. [Online]. Available: <https://www.slideshare.net/aishuanju/ftir-45012578%0A>. [Accessed: 20-Aug-2002].
- [130] Image, "Image: Electron Beam Spectrum Generation," [https://upload.wikimedia.org/wikipedia/commons/4/49/Electron\\_Interaction\\_with\\_Matter.svg](https://upload.wikimedia.org/wikipedia/commons/4/49/Electron_Interaction_with_Matter.svg), 2018. [Online]. Available: [https://upload.wikimedia.org/wikipedia/commons/4/49/Electron\\_Interaction\\_with\\_Matter.svg%0A](https://upload.wikimedia.org/wikipedia/commons/4/49/Electron_Interaction_with_Matter.svg%0A).
- [131] JEOL, "Image: SEM Operational Cutaway," <https://www.jeol.co.jp/en/science/epma.html>, 2018. [Online]. Available: <https://www.jeol.co.jp/en/science/epma.html%0A>. [Accessed: 20-Aug-2002].

- [132] R. Guinebretiere, *X-Ray Diffraction by Polycrystalline Materials*, Online. London, UK: Wiley Online Library, 2007.
- [133] Bruker, "Bruker DektakXT Stylus Profiler User Manual." Bruker, P/N 980-365, p. 83, 2011.
- [134] G. Gauglitz and D. Moore, *Handbook of Spectroscopy*, 2nd ed. Weinheim: WILEY-VCH Verlag, 2014.
- [135] Image, "Image: UV-VIS System Cutaway," <https://orgspectroscopyint.blogspot.com/p/basics-of-uv-visible-spectroscopy.html>, 2018. [Online].
- [136] J. Watts, *An Introduction to Surface Analysis by XPS and AES*, Online. Chichester, West Sussex, England ; New York: John Wiley, 2003.
- [137] S. Hofmann, *Auger- and x-ray photoelectron spectroscopy in materials science*, Online. Berlin, Heidelberg: Springer, 2013.
- [138] U. of Maryland, "Image: XPS Operational Theory," 2018. [Online]. Available: <http://www.chem.umd.edu/sharedinstrumentation/surface-analysis-center%0A>.
- [139] Image, "XPS System Cutaway," 2018. [Online]. Available: <http://www.assignmentpoint.com/science/physics/photoemission-spectroscopy.html%0A>.

- [140] G. Group, "Solar Cells Market to surpass US\$100 billion by 2024.," *PR Newswire US*, 2018. [Online]. Available:  
<http://link.galegroup.com.libproxy.txstate.edu/apps/doc/A531056348/BIC?u=txshrcad2550&sid=BIC&xid=3140afc3>. [Accessed: 20-May-2018].
- [141] D. A. Barber, "Energy Trend," *www.pv.energytrend.com*, 2012. [Online]. Available:  
[http://pv.energytrend.com/research/Portable\\_PV\\_Power\\_Market\\_20120131.html%0A](http://pv.energytrend.com/research/Portable_PV_Power_Market_20120131.html%0A).
- [142] N. Thompson and J. Ballen, "First Solar," *MIT Manag. Sloan Sch.*, vol. 17–181, pp. 1–33, 2017.
- [143] Heimbuch, "TreeHugger," *www.treehugger.com*, 2009. [Online]. Available:  
<http://www.treehugger.com/clean-technology/off-grid-charging-for-cell-phones-is-a-23-billion-industry-video.html%0A>.
- [144] C. Neiger, "Bad News for Apple and Samsung: Mobile Phone Upgrade Cycles are Slowing," *The Mptley Fool*, 2016. [Online]. Available:  
<https://www.fool.com/investing/general/2016/04/20/bad-news-for-apple-and-samsung-mobile-phone-upgrad.aspx>.
- [145] M. T. Weller, O. J. Weber, J. M. Frost, and A. Walsh, "Cubic perovskite structure of black formamidinium lead iodide,  $\alpha$ -[HC(NH<sub>2</sub>)<sub>2</sub>]PbI<sub>3</sub>, at 298 K," *J. Phys. Chem. Lett.*, vol. 6, pp. 3209–3212, Aug. 2015.

- [146] M. Saliba *et al.*, “Cesium-containing triple cation perovskite solar cells: improved stability, reproducibility and high efficiency,” *Energy Environ. Sci.*, no. 6, 2016.
- [147] E. Article, G. Kieslich, S. Sun, and A. K. Cheetham, “An extended Tolerance Factor approach for organic – inorganic perovskites †,” *Chem. Sci.*, vol. 6, pp. 3430–3433, 2015.
- [148] J. H. Jensen and J. C. Kromann, “The Molecule Calculator: A Web Application for Fast Quantum Mechanics-Based Estimation of Molecular Properties,” *Journal of Chemical Education*, 2013. [Online]. Available: <http://molcalc.org>.
- [149] M. Saliba *et al.*, “Cesium-containing triple cation perovskite solar cells: improved stability, reproducibility and high efficiency,” *Energy Environ. Sci.*, vol. 9, no. 6, pp. 1989–1997, 2016.
- [150] Y. Wang *et al.*, “Nano Energy Stitching triple cation perovskite by a mixed anti-solvent process for high performance perovskite solar cells,” *Nano Energy*, vol. 39, no. July, pp. 616–625, 2017.
- [151] Martin Stolterfoht *et al.*, “Approaching the fill factor Shockley–Queisser limit in stable, dopant-free triple cation perovskite solar cells,” *Energy Environ. Sci.*, vol. 10, no. 6, pp. 1530–1539, 2017.
- [152] R. Zhang *et al.*, “Theoretical lifetime extraction and experimental demonstration of stable cesium-containing tri-cation perovskite solar cells with high efficiency,” *Electrochim. Acta*, vol. 265, pp. 98–106, 2018.

- [153] B. Parija and S. Panigrahi, "Fundamental understanding and modeling of spin coating process : A review," *Indian J. Phys.*, vol. 83, no. 4, pp. 493–502, 2009.
- [154] T. Schneller and R. Waser, *Chemical Solution Deposition of Functional Oxide Thin Films*. New York, New York, USA: Springer-Verlag Wien, 2013.
- [155] G. Jones and M. Dole, "THE VISCOSITY OF AQUEOUS SOLUTIONS OF STRONG ELECTROLYTES WITH SPECIAL REFERENCE TO BARIUM CHLORIDE," *J. Am. Chem. Soc.*, vol. 51, no. 10, pp. 2950–2964, 1929.
- [156] T. Xiao and X. Song, "A molecular Debye-Hückel theory and its applications," *J. Chem. Phys.*, vol. 104104, no. 135, pp. 1–14, 2011.
- [157] A. B. Nikumbh and R. C. Bhujbal, "Apparent molar volumes and viscosity B-coefficients of sodium salicylate in different solvent systems at different temperatures.," *Int. J. Sci. Eng. Res.*, vol. 5, no. 7, pp. 138–146, 2014.
- [158] Y. Marcus, "Viscosity B Coefficients of Ions in Solution," *Chem. Rev.*, vol. 95, pp. 2695–2724, 1995.
- [159] G. M. Kontogeorgis, B. Maribo-mogensen, and K. Thomsen, "Fluid Phase Equilibria The Debye-Hückel theory and its importance in modeling electrolyte solutions," *Fluid Phase Equilib.*, vol. 462, pp. 130–152, 2018.
- [160] T. Oku, "Crystal Structures of CH<sub>3</sub>NH<sub>3</sub>PbI<sub>3</sub> and Related Perovskite Compounds Used for Solar Cells," in *Solar Cells- New Approaches and Reviews*, InTechOpen, 2015, pp. 77–101.

- [161] L. Xie *et al.*, "Understanding the Cubic Phase Stabilization and Crystallization Kinetics in Mixed Cations and Halides Perovskite Single Crystals," *J. Am. Chem. Soc.*, vol. 139, pp. 17–20, 2017.
- [162] J. Gong, P. Guo, S. E. Benjamin, P. G. Van Patten, R. D. Schaller, and T. Xu, "Cation engineering on lead iodide perovskites for stable and high-performance photovoltaic applications," *J. Energy Chem.*, vol. 0, pp. 1–23, 2018.
- [163] H. Gil-bernal, M. L. Zambrano, and J. C. Arce, "Quantum-Chemical-Aided Design of Copolymers With Tailored Bandgaps and Effective Masses : The Role of Composition," *Int. J. Quantum Chem.*, vol. 110, pp. 2522–2531, 2010.
- [164] J. Baedi, S. Gholampur, and F. Mircholi, "The study of the electronic properties of  $\text{Bi}_0.5\text{Na}_0.5\text{TiO}_3$  , their structures," *Opt. Mater. (Amst).*, vol. 67, pp. 44–51, 2017.
- [165] A. Zakhidov, "Tailoring nucleation and grain growth by changing the precursor phase ratio for efficient organic lead halide perovskite optoelectronic," *J. Mater. Chem. C*, vol. 5, pp. 10114–10121, 2017.
- [166] NREL, "National Renewable Energy Laboratory (NREL) Hands On Photovoltaic Experience (H.O.P.E.)." 2017.
- [167] W. Hu *et al.*, "Copper iodide-PEDOT : PSS double hole transport layers for improved efficiency and stability in perovskite solar cells," *J. Photochem. Photobiol. A Chem.*, vol. 357, pp. 36–40, 2018.

- [168] C. Zuo and L. Ding, "Solution-Processed Cu<sub>2</sub>O and CuO as Hole Transport Materials for Efficient Perovskite Solar Cells," *Small*, no. 41, pp. 5528–5532, 2015.
- [169] Y. Liang, Y. Wang, C. Mu, S. Wang, X. Wang, and D. Xu, "Achieving High Open-Circuit Voltages up to 1.57 V in Hole-Transport-Material-Free MAPbBr<sub>3</sub> Solar Cells with Carbon Electrodes," *Adv. Energy Mater.*, vol. 1701159, pp. 1–6, 2018.
- [170] J. Moulder, W. Stickle, P. Sobol, and K. Bomben, *Handbook of X-Ray Photoelectron Spectroscopy*. Eden Prairie: Physical Electronics, Inc, 1992.
- [171] J. Senvaitiene, J. Smirnova, A. Beganskiene, and A. Kareiva, "XRD and FTIR Characterisation of Lead Oxide-Based Pigments and Glazes," *Acta Chim. Slov.*, vol. 54, pp. 185–193, 2007.
- [172] P. Technology, "Sorption studies of cesium on TiO<sub>2</sub> – SiO<sub>2</sub> mixed gel spheres," *Sep. Purif. Technol.*, vol. 47, pp. 96–104, 2006.
- [173] G. Dhanaraj, K. Byrappa, V. Prasad, and M. Dudley, Eds., *Handbook of Crystal Growth*. Springer, 2010.
- [174] D. Li, M. Nielsen, J. Lee, C. Frandsen, J. Banfield, and J. De Yoreo, "Direction-Specific Interactions," *Science (80-. )*, vol. 336, no. May, pp. 1014–1019, 2012.
- [175] M. Science, B. Engineering, and T. Place, "A kinetic model for crystal growth from aqueous solution in the presence of impurity," *J. Cryst.*, vol. 152, pp. 203–208, 1995.

- [176] W. J. Yao and N. Wang, "Latent heats of fusion and crystallization behaviors of Co – Si binary alloys," *J. Alloys Compd.*, vol. 487, pp. 354–357, 2009.
- [177] D. Sedmidubsk, "Application of Neumann – Kopp rule for the estimation of heat capacity of mixed oxides," *Thermochim. Acta*, vol. 497, pp. 7–13, 2010.
- [178] C. Zheng and O. Rubel, "Ionization Energy as a Stability Criterion for Halide Perovskites," *J. Phys. Chem. C*, vol. 121, pp. 11977–11984, 2017.
- [179] X. Ge and X. Wang, "A Simple Two-Parameter Correlation Model for Aqueous Electrolyte Solutions across a Wide Range of Temperature," *J. Chem. Eng. Data*, vol. 54, pp. 179–186, 2009.
- [180] X. Ge, M. Zhang, M. Guo, and X. Wang, "Correlation and Prediction of Thermodynamic Properties of Nonaqueous Electrolytes by the Modified TCPC Model," *J. Chem. Eng. Data*, vol. 54, no. 2, pp. 149–159, 2008.
- [181] M. Labowsky, J. B. Fenn, and J. F. De, "A continuum model for ion evaporation from a drop : effect of curvature and charge on ion solvation energy," *Anal. Chim. Acta*, vol. 406, pp. 105–118, 2000.
- [182] V. M. Gun, R. Nasiri, and S. S. Sazhin, "Effects of the surroundings and conformerisation of n-dodecane molecules on evaporation / condensation processes Effects of the surroundings and conformerisation of n -dodecane molecules on evaporation / condensation processes," *J. Chem. Phys.*, vol. 34502, no. 142, 2015.

- [183] X. Yang, H. Lei, P. Gao, D. G. Thomas, D. L. Mobley, and N. A. Baker, "Atomic Radius and Charge Parameter Uncertainty in Biomolecular Solvation Energy Calculations," *J. Chem. Theory Comput.*, no. 14, pp. 759–767, 2018.
- [184] Y. Numata, A. Kogo, Y. Udagawa, and H. Kunugita, "Controlled Crystal Grain Growth in Mixed Cation- Halide Perovskite by Evaporated Solvent Vapor Recycling Method for High Efficiency Solar Cells," *Appl. Mater. Interfaces*, vol. 9, no. 22, 2017.
- [185] A. Mahmud *et al.*, "Controlled nucleation assisted restricted volume solvent annealing for stable perovskite solar cell," *Sol. Energy Mater. Sol. Cells*, vol. 167, no. March, pp. 70–86, 2017.
- [186] Y. Zhou, M. Yang, W. Wu, A. L. Vasiliev, K. Zhu, and N. P. Padture, "Room-temperature crystallization of hybrid-perovskite thin films via solvent–solvent extraction for high-performance solar cells," *J. Mater. Chem. A Mater. energy Sustain.*, vol. 3, pp. 8178–8184, 2015.
- [187] S. Timpanaro, M. Kemerink, F. Touwslager, M. De Kok, and S. Schrader, "Morphology and conductivity of PEDOT/PSS films studied by scanning–tunneling microscopy," *Chem. Phys. Lett.*, vol. 394, pp. 339–343, 2004.
- [188] G. Kaur, R. Adhikari, P. Cass, M. Bown, and P. Gunatillake, "Electrically conductive polymers and composites for biomedical applications," *RSC Adv.*, vol. 5, no. 47, pp. 37553–37567, 2015.

- [189] J. S. Teguh, T. Chien, and E. K. L. Yeow, "Effect of charge accumulation on the stability of PEDOT : PSS during device operation," *Chem. Phys. Lett.*, vol. 607, pp. 52–56, 2014.
- [190] E. Voroshazi, B. Verreet, A. Buri, R. Müller, D. Di, and P. Heremans, "Influence of cathode oxidation via the hole extraction layer in polymer : fullerene solar cells," *Org. Electron.*, vol. 12, no. 5, pp. 736–744, 2011.
- [191] L. Zhang, H. Deng, S. Liu, Q. Zhang, F. Chen, and Q. Fu, "Enhanced thermoelectric properties of PEDOT : PSS films via a novel two-step treatment," *RSC Adv.*, vol. 5, pp. 105592–105599, 2015.
- [192] H. Tsai *et al.*, "Light-induced lattice expansion leads to high-efficiency perovskite solar cells," *Science (80-. )*, vol. 360, no. 6384, pp. 67–70, 2018.
- [193] T. Leijtens, G. E. Eperon, N. K. Noel, S. N. Habisreutinger, A. Petrozza, and H. J. Snaith, "Stability of Metal Halide Perovskite Solar Cells," *Adv. Energy Mater.*, vol. 5, p. 1500963, Sep. 2015.
- [194] E. Smecca *et al.*, "Stability of solution-processed MAPbI<sub>3</sub> and FAPbI<sub>3</sub> layers," *Phys. Chem. Chem. Phys.*, vol. 18, pp. 13413–13422, 2016.
- [195] S. Střiteský *et al.*, "Printing inks of electroactive polymer PEDOT:PSS: The study of biocompatibility, stability, and electrical properties," *J. Biomed. Mater. Research*, vol. 106, no. 4, pp. 1121–1128, 2018.

- [196] X. Deng, X. Wen, J. Zheng, T. Young, C. Fai, and J. Lau, "Dynamic study of the light soaking effect on perovskite solar cells by in-situ photoluminescence microscopy," *Nano Energy*, vol. 46, no. February, pp. 356–364, 2018.
- [197] A. Dhar, P. Maiti, A. Dey, S. Roy, P. Paul, and R. Vekariya, "Fabrication and characterization of next generation nano-structured organo-lead halide-based perovskite solar cell," *Ionics (Kiel)*, vol. 24, no. 4, pp. 1227–1233, 2018.
- [198] Z. Wu *et al.*, "Alloying n-Butylamine into CsPbBr<sub>3</sub> to Design an Unprecedented Two-dimensional Bilayered Perovskite Ferroelectric.," *Angew. Chem. Int. Ed. Engl.*, vol. 57, pp. 1–5, 2018.
- [199] W. T. and L. L. Hao Lu, Yulong Ma, Bangkai Gu, "Identifying the optimum thickness of electron transport layers for highly efficient perovskite planar solar cells," *J. Mater. Chem.*, no. 32, 2015.
- [200] M. Firdaus, M. Noh, H. Teh, and R. Daik, "The architecture of the electron transport layer for a perovskite solar cell," *J. Mater. Chem. C*, vol. 6, pp. 682–712, 2018.
- [201] B. Halasz, "A general mathematical of evaporative cooling model devices," *Rev. Gen. Therm.*, vol. 37, no. 4, pp. 245–255, 1998.
- [202] U. of Louisville, "Spin coating defects," no. October. p. 4, 2013.
- [203] D. C. Montgomery, *Design and Analysis of Experiments*, 4th ed. New York, New York, USA: John Wiley & Sons, Inc., 1996.

- [204] R. Szostak *et al.*, "Understanding perovskite formation through the intramolecular exchange method in ambient conditions," *J. Photonics Energy*, vol. 7, no. 2, pp. 22002-1-22002-14, 2017.
- [205] D. Wang, M. Wright, N. K. Elumalai, and A. Uddin, "Stability of perovskite solar cells," *Sol. Energy Mater. Sol. Cells*, vol. 147, pp. 255-275, 2016.
- [206] C. Wang, C. Zhang, Y. Huang, S. Tong, H. Wu, and J. Zhang, "Degradation behavior of planar heterojunction CH<sub>3</sub>NH<sub>3</sub>PbI<sub>3</sub> perovskite solar cells," *Synth. Met.*, vol. 227, pp. 43-51, 2017.
- [207] H. Gao *et al.*, "Nucleation and Crystal Growth of Organic – Inorganic Lead Halide Perovskites under Different Relative Humidity," 2015.
- [208] G. Wang, D. Liu, D. Zhou, K. Alameh, B. Ding, and Q. L. Song, "Efficient perovskite solar cell fabricated in ambient air using one-step spin-coating," *R. Soc. Chem.*, vol. 6, no. 49, pp. 43299-43303, 2016.
- [209] Z. Xiao, Q. Dong, C. Bi, Y. Shao, Y. Yuan, and J. Huang, "Solvent Annealing of Perovskite-Induced Crystal Growth for Photovoltaic-Device Efficiency Enhancement," *Adv. Mater.*, vol. 26, no. 37, pp. 6503-6509, 2014.
- [210] N. J. Jeon, J. H. Noh, Y. C. Kim, W. S. Yang, S. Ryu, and S. Il Seok, "Solvent engineering for high-performance inorganic-organic hybrid perovskite solar cells," *Nat. Ma*, no. July, pp. 1-7, 2014.

- [211] C. Fei, L. Guo, B. Li, R. Zhang, H. Fu, and J. Tian, "Nano Energy Controlled growth of textured perovskite films towards high performance solar cells," *Nano Energy*, vol. 27, pp. 17–26, 2016.
- [212] T. Zhang, M. Long, K. Yan, M. Qin, X. Lu, and X. Zeng, "Crystallinity Preservation and Ion Migration Suppression through Dual Ion Exchange Strategy for Stable Mixed Perovskite Solar Cells," *Adv. Energy Mater.*, vol. 1700118, pp. 1–10, 2017.
- [213] and Y. Y. Yaoguang Rong, Zhongji Tang, Yufeng Zhao, Xin Zhong, Swaminathan Venkatesan, Harrison Graham, Matthew Patton, Yan Jing, Arnold M. Guloy, "Solvent Engineering Towards Controlled Grain Growth in Perovskite Planar Heterojunction Solar Cells," *Nanoscale*, vol. 7, pp. 10595–10599, 2015.
- [214] S. Zhang, Y. Lu, B. Lin, Y. Zhu, K. Zhang, and N. Yuan, "PVDF-HFP additive for visible-light-semi-transparent perovskite films yielding enhanced photovoltaic performance," *Sol. Energy Mater. Sol. Cells*, vol. 170, no. May, pp. 178–186, 2017.
- [215] A. R. P. Henderson, J. R. Kosowan, and T. E. Wood, "Truce-Smiles rearrangement," *Can. J. Chem.*, vol. 95, no. 5, pp. 1–64, 2017.
- [216] I. Allart-simon, S. Gérard, and J. Sapi, "Radical Smiles Rearrangement : An Update," *Molecules*, vol. 21, no. 7, pp. 878–888, 2016.
- [217] J. J. Li, *Name Reactions: A Collection of Detailed Mechanisms and Synthetic Applications Fifth Edition*. Springer, 2014.
- [218] J. J. Li, *Name Reactions in Heterocyclic Chemistry*. Wiley-Interscience, 2004.

- [219] J. C. Thermodynamics *et al.*, "Thermodynamics of formation of hybrid perovskite-type methylammonium lead halides," *J. Chem. Thermodyn.*, vol. 116, pp. 253–258, 2018.
- [220] M. Cai, Y. Wu, H. Chen, X. Yang, Y. Qiang, and L. Han, "Cost-Performance Analysis of Perovskite Solar Modules," *Adv. Sci.*, vol. 4, p. 1600269, 2017.
- [221] Z. Song *et al.*, "Environmental Science module manufacturing with low-cost materials and techniques †," *Energy Environ. Sci.*, 2017.